

University of the Western Cape

Faculty of Natural Sciences

Department of Physics & Astronomy



**Nuclear structure studies in the $A=136$
region using transfer reactions**

Bernadette M. Rebeiro

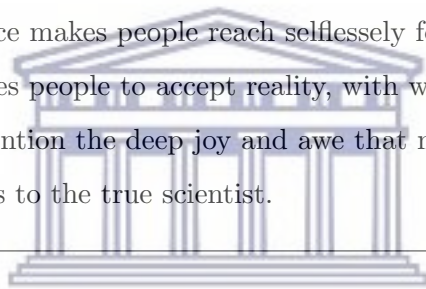


UNIVERSITY of the
WESTERN CAPE

A thesis submitted in partial fulfillment for the degree of
Doctorate of Philosophy in Physics

2018

Science makes people reach selflessly for truth and objectivity; it teaches people to accept reality, with wonder and admiration, not to mention the deep joy and awe that natural order of things brings to the true scientist.



Lise Meitner

UNIVERSITY *of the*
WESTERN CAPE

Declaration

I declare that NUCLEAR STRUCTURE STUDIES IN $A = 136$ REGION USING TRANSFER REACTIONS is my own work, that it has not been submitted for any degree or examination in any other university and that all sources I have used or quoted have been indicated and acknowledged by complete references.



Bernadette M. Rebeiro

December 2018

Signature:

UNIVERSITY *of the*
WESTERN CAPE

To my nephew, Chason D'Souza.

“Grow in wonder and awe for it's still magic even if you know how it was done.”



UNIVERSITY *of the*
WESTERN CAPE

Acknowledgements

As this thesis is finally ready for submission I would like to thank everyone whose help, support and encouragement has made this a reality.

My biggest gratitude is of course towards my supervisor, Smarajit Triambak for giving me this opportunity, for supporting me throughout my research career, for believing in my abilities, for giving me numerous opportunities to present my work at national and international conferences and workshops, for being an awesome mentor as well as the biggest critic of my work. This list is endless but working with you over these N number of years has been a pleasure and a great learning opportunity.

I definitely cannot thank Philip Adsley enough for all the discussions I've had with him, for the ungodly times I've emailed him with a question and received an answer swiftly, for reading my thesis and giving me feedback and also for checking up on me periodically.

I would also like to thank Robbie Lindsay, Paul Garrett, Gordon Ball and Nico Orce for all the helpful discussions about my analysis and DWBA calculations and Gordon Ball for the useful suggestions on the thesis write up as well. I am very grateful for your time and expertise. I also thank Ian Thompson for helping me out with FRESCO and Alex Brown for the helpful discussions on the shell model calculations.

I would also like to thank Alfredo Galindo-Uribarri for giving me the opportunity to attend the Institute of Nuclear Theory's workshop on Nuclear ab initio Theories and Neutrino Physics. This gave me the chance to meet and learn from some of the experts of the field and further improve this work.

I thank my long distance friend, Christina Burbadge for answering all the questions

I've had related to this analysis.

How can I forget Shirese Constant, Rudy Maart, Sikelela Mqhayi, Mogammad Kamedien and specially Angela Adams for helping me with all my administrative work thus making my life so much easier here. Also, I would like to say a special thanks to Angela, Shirese and Lynndle for the incredible hospitality they showed me in making me feel at home when I was new to South Africa. I would also like to thank Reggie Madjoe for all the light-hearted chats and coffee we have shared and everyone in the department for making me feel welcome and so much a part of this place. UWC physics will be missed fondly.

I reserve a special place for Leah Koskimaki for her encouraging words and for always understanding and supporting me and sometimes when I've needed it the most. Thanks to both, you and Smarajit for letting me be a part of your family.

A special thanks to Bhivek Singh, Mohamed Kamil, Jespere Ondze, Justice Mukhweho, Craig Vyfers and Zandile Mabika with whom I've spent such a large part of my time in UWC. Thank you all for your friendships over these past years. A special thanks to Mohamed for proof-reading my thesis when time wasn't on my side. Thanks also to all the wonderful friends I have made here, Sinovuyo Tanci, Lola Afolayan, Sfiso Khanyile, Bako Audu, Natasha Peterson, Elijah Akakpo, Freedom Maibane, Israel Hlatshwayo and so many others. You guys have added the life to these years.

How can I not say thanks to Kushal Kapoor for all our coffee pe charche and for lightening my mood during stressful times. My gratitudes also to Rakesh Dubey for all his help and support. I would also like to thank Estelle and Callie for all the wonderful braais and hikes we did together and for the times when you were my home away from home.

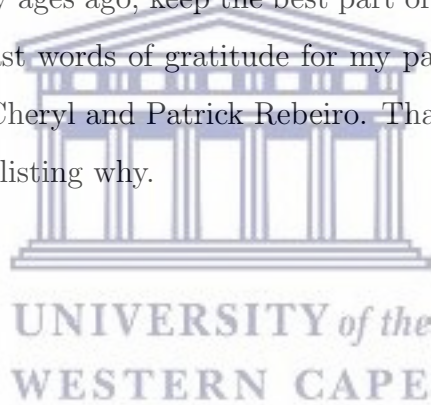
A very special thanks to all my friends back home, Sudeshna Sarmah, Nisha Rani, Rojeeta Devi, Khushboo, Mansi Sharma, Neeraj Kumar, William Britto, Gaurish Sal-

gaonkar, Nagendra Prabhakar, Nanddeep Nasnodkar and Priyanka Bhende. You guys have been my steady waters over the years, friends that I could always turn to. A special shout out to William for checking up on me regularly since I left Goa.

Going back to where this all started, my school and college teachers, Ninette D'Souza and Bosco Lawrence were the reason why I pursued physics. Thank you for being such wonderful teachers and always encouraging us to go beyond. On the same note, I have to thank Brajesh Choudhary, Deepak Samuel and Naba Mondal for introducing me to the field of neutrino physics.

A special thanks to Massimiliano Marchisone for having to put up with the worst of me while I was writing this thesis but never complaining and for always being so understanding. Now that this thesis is done, I'll be nicer and irritate you more.

My father once said, many ages ago, keep the best part of the watermelon for the last and hence I reserve my last words of gratitude for my parents Diogo and Esperanca Rebeiro and my siblings Cheryl and Patrick Rebeiro. Thank you for everything, for I won't do justice if I start listing why.



Abstract

This thesis describes research work undertaken to study neutron pairing correlations in ^{136}Ba via the $^{138}\text{Ba}(p, t)$ pair transfer reaction and to perform high-precision spectroscopy of low-lying states in ^{136}Cs using the $^{138}\text{Ba}(d, \alpha)$ reaction. The aim of this project was to provide useful spectroscopic information relevant for matrix element calculations of ^{136}Xe neutrinoless double beta decay. This work is relevant because neutrinoless double beta decays are standard-model-forbidden lepton number violating processes, which if observed, would establish the Majorana nature of the neutrinos and also determine the absolute mass scale of the light Majorana neutrinos.

Our experiments show a significant fragmentation of the two-neutron transfer (p, t) strength to excited 0^+ states in ^{136}Ba , which could significantly affect future matrix element calculations. Additionally we obtain information on ~ 65 new states in ^{136}Cs observed in this work. It is anticipated that these new information will play a vital role in improving the precision of calculated matrix elements for ^{136}Xe double beta decays.

Contents

1	Massive Neutrinos and Double Beta Decays	3
1.1	Introduction	3
1.1.1	Chirality of weak interactions	5
1.1.2	Nuclear beta decays	10
1.2	Massive neutrinos and double beta decays	11
1.2.1	Neutrino mass terms	13
1.3	Neutrinoless double beta decay	16
1.4	Nuclear Matrix Elements for $0\nu\beta\beta$ decays	18
1.5	Reducing the uncertainty on NME's	20
1.6	Status of $^{136}\text{Xe}\rightarrow^{136}\text{Ba}$ $\beta\beta$ decay experiments	25
1.6.1	Information on ^{136}Cs intermediate states	28
2	Direct Nuclear Reactions as a Probe of Nuclear Structure	31
2.1	General non-relativistic scattering theory	32
2.2	Two Nucleon Transfer Reactions	40
2.2.1	Two nucleon transfer reaction as a probe to study nuclear structure	43
2.2.2	The (\mathbf{d}, α) reaction	44
2.2.3	The (\mathbf{p}, \mathbf{t}) reaction	45
2.3	Pairing interactions and two-neutron transfer reactions	46
2.4	Implication of pairing correlations on neutrinoless double beta decay matrix elements	48

Status of pairing correlations in the $\beta\beta$ decay nuclei	49
3 Experimental Setup	51
3.1 Overview of the Experiments	51
3.2 Experimental Facility	51
3.3 Q3D Magnetic Spectrometer	54
3.4 Focal-Plane Detector	55
3.5 Experimental details	57
3.5.1 $^{138}\text{Ba}(p, t)^{136}\text{Ba}$	57
3.5.2 $^{138}\text{Ba}(d, \alpha)^{136}\text{Cs}$	58
4 Data Analysis	59
4.1 Particle Identification	59
4.2 Peak fitting	60
4.3 Energy calibration	60
4.3.1 Effective excitation energy transformations	61
4.3.2 Corrections due to energy loss in targets	64
4.3.3 Uncertainties on effective excitation energy	66
4.4 Cross Section Calculation	67
4.4.1 Elastic scattering	68
Choosing the optical model parameters	68
Estimating the correct target thickness	69
4.4.2 Beam particle normalization	70
4.4.3 Dead time corrections	70
4.4.4 Dark current correction	71
4.4.5 Solid Angle Estimation	71
4.4.6 Slit offset calibration	72
4.4.7 Uncertainties in Cross-Section	74
4.5 DWBA Calculation	74
4.5.1 DWUCK4	74

4.6	Identification of impurities	76
5	$^{138}\text{Ba}(p, t)^{136}\text{Ba}$ Results	79
5.1	Energy Calibration	79
5.2	Elastic scattering	85
5.3	DWBA Calculations	85
5.3.1	$J^\pi = 0^+$ states	89
5.3.2	$J^\pi = 1^-$ states	91
5.3.3	$J^\pi = 2^+$ states	92
5.3.4	$J^\pi = 3^-$ states	94
5.3.5	$J^\pi = 4^+$ states	94
5.3.6	$J^\pi = 5^-$ states	95
5.3.7	$J^\pi = 6^+$ states	96
5.3.8	$J^\pi = 7^-$ states	96
5.3.9	Tentative assignments	96
5.3.10	Indefinite assignments	101
5.4	Neutron pairing correlations in ^{136}Ba	101
6	$^{138}\text{Ba}(d, \alpha)^{136}\text{Cs}$ Results	103
6.1	Energy Calibration	103
6.2	Elastic scattering	105
6.3	DWBA Calculations	107
6.4	J^π Assignments	114
6.4.1	Natural Parity States	115
	$J^\pi = 1^-$ states	115
	$J^\pi = 2^+$ states	115
	$J^\pi = 3^-$ states	115
	$J^\pi = 4^+$ states	115
	$J^\pi = 5^-$ states	115
6.4.2	Unnatural Parity Assignments	116

6.4.3	Tentative J^π Assignments	116
6.4.4	Indefinite Assignments	118
7	Conclusions and Future Work	119
A	Relativistic Kinematics	122
B	Description of DWUCK4 input file used for DWBA Analysis	126
C	$^{138}\text{Ba}(p, t)^{136}\text{Ba}$ Angular distributions	130
D	$^{138}\text{Ba}(d, \alpha)^{136}\text{Cs}$ Angular distributions	144
	Bibliography	154



List of Figures

1.1	Neutrino mass hierarchy obtained from solar and atmospheric oscillation data. The color coding shows the proportion of each flavor eigenstate in the respective mass eigenstates [14].	13
1.2	The mass parabolas for $A = 136$ nuclei. ^{136}Xe is stable against ordinary beta-decay but unstable against double beta-decay. Figure extracted from Ref. [18].	16
1.3	Left panel: $2\nu\beta\beta$ decay. Right panel : $0\nu\beta\beta$ decay.	17
1.4	Neutrinoless double beta-decay matrix elements for various isotopes calculated using different methods. Figure obtained from Ref [26].	19
1.5	Cutaway view of the EXO-200 setup [70]	27
1.6	Schematic representation of the KamLAND-ZEN detector. At the center of the detector is the 3.08 m balloon filled with enriched ^{136}Xe [68].	28
1.7	$\langle m_{\beta\beta} \rangle$ as a function of the lightest neutrino mass. The shaded regions for the normal hierarchy (NH) and the inverted hierarchy (IH) are the current limits set by neutrino oscillation experiments. The horizontal blue band is the current 90% C.L. limits on $\langle m_{\beta\beta} \rangle$ set by the KamLAND-Zen experiment [66]. Currently, KamLAND-ZEN provides the most stringent limit on the masses of light Majorana neutrinos.	29
1.8	Triton spectrum from the $^{136}\text{Xe}(^3\text{He}, t)^{136}\text{Cs}$ reaction, observed with the the Grand Raiden Spectrometer at RCNP. Figure extracted from Ref. [48].	29

2.1	Quantum mechanical description of scattering. An incident plane wave results in a spherical scattered wave due to the scattering potential. For a detector placed at an angle θ with respect to the direction of the incident particles, $k_{out} = k_{\beta}$ is the momentum of the scattered wave in the reaction channel β while $k_{in} = k_{\alpha}$ is the incident momentum of $\Psi_{initial}$. Picture taken from Ref. [90].	33
3.1	The tandem Van de Graff accelerator hall at MLL. The tandem is shown in orange and the analyzing magnet is painted blue.	52
3.2	Schematic representation of the Stern-Gerlach ion source at the MLL. Adapted from Ref [141].	53
3.3	A schematic representation of the MP tandem accelerator used at MLL. . .	54
3.4	Schematic of the Q3D spectrometer	55
3.5	Cartoon depicting the response the of the cathode-strip detector to a charged particle interaction. Figure obtained from Ref. [145].	56
3.6	Cross sectional schematic view of the focal plane detector taken from Ref. [145]	57
4.1	Particle identification spectra - left panel: $\Delta E - \Delta E_1$, partial energy loss of the ejectiles in the two proportional counters. Right panel: $\Delta E - E$ spectrum from the second proportional counter and the plastic scintillator. In the $\Delta E - E$ spectra it is difficult to distinguish between the protons from $^{138}\text{Ba}(d, p)$ and deuterons from $^{138}\text{Ba}(d, d)$ as the energy deposited by these two ejectiles is very similar. However the tritons from $^{138}\text{Ba}(d, t)$ have comparatively less energy and thus higher energy loss (compared to the deuterons and protons) and thus the left blob in the right figure. The energy loss information from the $\Delta E - E$ spectra can then be easily used to deduce the position of the tritons in the $\Delta E - \Delta E_1$ spectrum.	60
4.2	A sample fit to the uncalibrated 1866 keV peak in ^{136}Ba . The lineshape function is the convolution of a Gaussian with a low energy exponential tail on a flat background.	61

4.3	Least squared fit to energy loss values obtained from SRIM [151] for α particles passing through a $^{94}\text{MoO}_3$ target. The lowest order polynomial that adequately describe the SRIM output values within the required energy range was found to be 4. This procedure was repeated for all the charged particle-target combinations encountered in this analysis.	65
4.4	A schematic representation depicting the path of the charged particles through the target material. Assuming the reaction occurs at the center of the target, the projectile with energy E passes through the backing and half the target material where it loses energy $E - E_{loss}$. The resulting ejectile with energy E_{new} then passes through the other half of the target where it additionally loses energy $(E_{new} - E'_{loss})$ before it is detected at the focal plane.	66
4.5	Schematic representation of the Q3D opening with the slits.	72
4.6	Linear fit to the ratio of dead-time corrected elastic peak area over <i>Scaler1</i> as a function of different x-slit width.	73
5.1	Excitation energy spectrum for ^{136}Ba at $\theta_{lab} = 15^\circ$. The triton spectra were collected at 4 different momentum settings up to 4.6 MeV. All the 0^+ states identified from this experiment are indicated. The red arrows indicate new states observed in this work.	80
5.2	Energy calibrations for the $^{138}\text{Ba}(p, t)$ reaction at 4 different momentum bites. The small x and y uncertainties are included in the image. The first three bites were calibrated using known excitation energies in ^{136}Ba . The 4 th bite is calibrated using ^{134}Ba excitation energies that were extracted using the procedure described in Section 4.3.	81

5.3	Experimental elastic scattering angular distributions for 23 MeV protons on ^{138}Ba compared with DWBA angular distribution. Global proton optical model parameters used are from Becchetti and Greenlees (BG) [154], Koning and Delaroche (KD) [155], Varner <i>et al.</i> [156], Menet <i>et al.</i> [157] and Walter and Guss (WG) [158]. The proton OMP that best reproduces the elastic scattering data is the one by Varner <i>et al.</i> [156]. This OMP is further used in the DWBA analysis.	86
5.4	DWBA angular distributions from DWUCK4 for the ground state using different triton optical model parameters. The OMP from Li <i>et al.</i> (LLC) [159] results in a better fit to the data compared to the one recommended by Becchetti and Greenlees (BG) [160].	87
5.5	0^+ states populated in this (p, t) reaction. The measured cross-sections are compared to normalized DWBA curves.	102
6.1	Focal plane spectra at $\theta_{\text{lab}} = 10^\circ$ for $^{138}\text{Ba}(d, \alpha)$ (bottom), $^{94}\text{Mo}(d, \alpha)$ and $^{92}\text{Zr}(d, \alpha)$ (top) reactions. The three spectra were obtained with the same field settings. The red labels (in the top panel) mark the excitation energies (in keV) of ^{92}Nb [149] while black labels mark well known ^{90}Y states [150]. In the $^{138}\text{Ba}(d, \alpha)$ spectrum, the blue labels are for the previously known states and all the other peaks are new states identified in this work. Some of the most prominent ones are labeled in red.	104
6.2	Energy calibration for $^{138}\text{Ba}(d, \alpha)^{136}\text{Cs}$ reaction using effective excitation energies from $^{92}\text{Zr}(d, \alpha)^{90}\text{Y}$ and $^{94}\text{Mo}(d, \alpha)^{92}\text{Nb}$	105
6.3	Experimental elastic scattering angular distributions for 22 MeV deuterons on ^{138}Ba , compared with DWBA cross sections. The global deuteron OMPs used for comparison are An and Cai [178], Han <i>et al.</i> [179], Bojowald <i>et al.</i> [180] and Perey <i>et al.</i> [181]. The deuteron OMP that best reproduces the data is the one provided by An and Cai [178].	106

6.4	$^{136}\text{Ba}(\alpha, \alpha)$ elastic scattering data obtained from Ref. [184] compared to theoretical DWBA elastic scattering cross sections obtained using DWUCK4 that used α OMP sets from Refs. [183–185, 188]. Clearly the α OMP set recommended by Ref. [184] best reproduces the experimental data.	107
6.5	$^{140}\text{Ce}(\alpha, \alpha)$ (top) and $^{130}\text{Te}(\alpha, \alpha)$ (bottom) elastic scattering data obtained from Refs. [186, 187] compared with our DWBA calculations using the optical model parameter sets of Ref [183–185].	108
B.1	Sample DWUCK4 input file for $L = 3$ transfer in $^{138}\text{Ba}(p, t)^{136}\text{Ba}$ reaction and $L = 4$ in $^{138}\text{Ba}(d, \alpha)^{136}\text{Cs}$. For the purpose of illustration, the various input blocks are labeled. Description of each block is provided in the text.	126



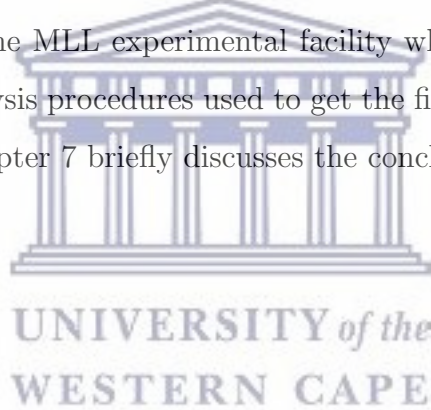
Introduction

Ever since Pauli postulated the existence of neutrinos, observing neutrinos and studying their properties has been an exciting field of research. This is mainly because neutrinos are massive (with their masses being many orders of magnitude smaller than the masses of the other elementary fermions) and their cross sections for interaction with matter are minuscule ($\sigma \sim 10^{-44} \text{ cm}^2$). Additionally, neutrinos are also the only neutral elementary fermions. Their massive and electrically neutral nature opens up the possibility of neutrinos being their own antiparticles, i.e. they are Majorana fermions. Currently, there is a lot of experimental activity underway all over the world to establish the Majorana nature of neutrinos. This is because the most popular explanation for the smallness of the neutrino masses is based on the assumption that lepton number is violated at large scale ($\sim 10^{15} \text{ GeV}$) [1]. If this were the case, then neutrinos *would have* to be Majorana particles. A clear-cut validation of the Majorana nature of neutrinos would be the observation of neutrinoless double beta ($0\nu\beta\beta$) decay, which can only be probed in a handful of nuclei.

The motivation of this thesis is to study the structure of $A = 136$ nuclei that are relevant for the $0\nu\beta\beta$ decay of $^{136}\text{Xe} \rightarrow ^{136}\text{Ba}$. We accomplished this using the $^{138}\text{Ba}(p, t)$ and $^{138}\text{Ba}(d, \alpha)$ two nucleon transfer reactions. The motivation for the $^{138}\text{Ba}(p, t)$ reaction was to study neutron pairing correlations in ^{136}Ba . We also used the $^{138}\text{Ba}(d, \alpha)$ reaction to achieve a high resolution spectroscopy of low-lying states in ^{136}Cs . The latter reaction is not particularly selective and can produce higher spin states due to the large momentum mismatch between the incoming deuteron and outgoing alpha particles. The (p, t) reaction on the other hand selectively produces natural parity states with low orbital angular

momentum transfer. It is hoped that these spectroscopic information will be beneficial to constrain $0\nu\beta\beta$ decay matrix element calculations for the special case of ^{136}Xe .

This thesis is divided into 7 chapters. In Chapter 1 I give a brief description of weak interactions in the context of massive neutrinos. I follow this with a discussion on neutrinoless double beta decays with emphasis on the challenges faced in calculating $\beta\beta$ decay matrix elements. I also discuss briefly nuclear structure information that can be used to improve or constrain these calculations, before concluding the chapter by bringing to the reader's notice why neutrinoless double beta decay of ^{136}Xe is interesting. In Chapter 2 I briefly discuss direct nuclear reactions in the context of the (d, α) and (p, t) reactions as special cases. One section is dedicated to the discussion of pairing correlations and its implication for $0\nu\beta\beta$ matrix elements. I conclude the chapter with a discussion on the status of pairing correlation studies in several double beta decay candidates. In Chapters 3 and 4, I describe the MLL experimental facility where the experiments were performed and the data analysis procedures used to get the final results, which are discussed in Chapters 5 and 6. Chapter 7 briefly discusses the conclusions and future directions.



1 | Massive Neutrinos and Double Beta Decays

I have done a terrible thing, I have postulated a particle that cannot be detected

Wolfgang Pauli

1.1 Introduction

The standard model of particle physics [2] describes fundamental particles and their interactions using a renormalizable field theory, which is based on a $SU(3) \times SU(2) \times U(1)$ gauge symmetry. Its formalism classifies elementary particles (and their antiparticles) in three generations of spin-1/2 quarks and leptons, such that the interactions between the fermions are mediated via the exchange of spin-1 gauge bosons. This classification is depicted below.

$$\begin{pmatrix} u \\ d \end{pmatrix}, \quad \begin{pmatrix} c \\ s \end{pmatrix}, \quad \begin{pmatrix} t \\ b \end{pmatrix} \quad \text{quarks} \tag{1.1}$$
$$\begin{pmatrix} \nu_e \\ e^- \end{pmatrix}, \quad \begin{pmatrix} \nu_\mu \\ \mu^- \end{pmatrix}, \quad \begin{pmatrix} \nu_\tau \\ \tau^- \end{pmatrix} \quad \text{leptons}$$

The quarks interact via the strong, electromagnetic and weak interactions while the leptons experience only the electromagnetic and weak forces. The spin-1 force carriers for the electromagnetic, weak and strong interactions are the photons, W^\pm , Z^0 bosons and

the gluons respectively. The photons and gluons are massless, while the W^\pm , Z^0 bosons are extremely massive ($M_{W^\pm} \sim 80$ GeV, $M_Z \sim 90$ GeV). The large masses of the weak interaction bosons is due to a spontaneous breaking of the local $SU(2) \times U(1)$ gauge symmetry via the Higgs mechanism [3]. This further leads to the requirement of at least one additional spin-0 scalar (Higgs) boson.

Below are listed some of the crowning achievements of the standard model.

1. It incorporates the theory of Quantum Chromodynamics (QCD), within which the inherent $SU(3)$ symmetry is unbroken (leading to massless gluons), with an additional quantum number called ‘color’ assigned for the quarks. The color charge for quarks and gluons naturally explains the short-ranged nature of the strong interaction. Furthermore, since the gluons also interact among themselves, in addition to the usual quark-gluon couplings, observed QCD phenomena (such as quark confinement) are natural consequences of the model.
2. It successfully unified the electromagnetic and weak interactions in an ‘electro-weak’ theory, while correctly predicting the masses of the W^\pm , Z^0 bosons and the existence of the top and charm quarks, in addition to the Higgs boson [2,3].
3. Most importantly, the Higgs field that generates the masses of the W^\pm and Z^0 bosons (while causing the photons to remain massless) is also sufficient to explain the mass generation of the quarks and charged leptons.

Despite the above, and having withstood stringent experimental probes over several years, the standard model still has several limitations. Some of the most important ones concern the properties of the neutral leptons (the neutrinos) listed in Eq. (1.1). Unlike the charged leptons, neutrinos only participate in weak interactions and have very small (unknown) masses which makes them difficult to detect experimentally. Before delving into a discussion on neutrino properties, it is important to briefly discuss some salient features of the theory of weak interactions, which is a vital component of the standard electroweak model.

1.1.1 Chirality of weak interactions

We first take into consideration that quarks and leptons are spin-1/2 fermions and are thus best described by 4-component Dirac fields (or spinors). Using the notation where $\hbar = c = 1$, the Dirac equation for spin-1/2 fermions is

$$(\vec{\alpha} \cdot \vec{p} + \beta m) \Psi = H \Psi \quad (1.2)$$

where,

$$\vec{\alpha} = \begin{pmatrix} 0 & \vec{\sigma} \\ \vec{\sigma} & 0 \end{pmatrix}, \quad \beta = \begin{pmatrix} I & 0 \\ 0 & -I \end{pmatrix}. \quad (1.3)$$

The equation can be written in a more succinct form by introducing the 4 gamma matrices $\gamma^\mu \equiv (\beta, \beta \vec{\alpha})$, so that it reduces to

$$(i\gamma^\mu \partial_\mu - m)\Psi = 0, \quad (1.4)$$

where Ψ is a 4-component column vector (for each spin projection, corresponding to both positive and negative energy solutions), given that the gamma matrices satisfy the anticommutation relation

$$\{\gamma^\mu, \gamma^\nu\} = 2g^{\mu\nu}. \quad (1.5)$$

The adjoint of Dirac equation is written as

$$i\partial_\mu \bar{\Psi} \gamma^\mu + m \bar{\Psi} = 0, \quad (1.6)$$

where $\bar{\Psi} \equiv \Psi^\dagger \gamma^0$ is the Hermitian conjugate of Ψ . The free particle plane-wave solutions of the Dirac equation are well known

$$\Psi(x) = u(p)e^{-ip_\mu x^\mu}, \quad (1.7)$$

where the $u(p)$ solve the momentum space equation

$$(\gamma^\mu p_\mu - m)u(p) = 0. \quad (1.8)$$

Eq. (1.8) can easily be solved to obtain the positive energy solutions [4]

$$\Psi(x) = \sqrt{\frac{E+m}{2E}} \begin{pmatrix} \chi^\pm \\ \frac{\vec{\sigma} \cdot \vec{p}}{|E|+m} \chi^\pm \end{pmatrix} e^{-ip_\mu x^\mu}, \quad (1.9)$$

and the negative energy solutions [4]

$$\Psi(x) = \sqrt{\frac{E+m}{2E}} \begin{pmatrix} \frac{-\vec{\sigma} \cdot \vec{p}}{|E|+m} \chi^\pm \\ \chi^\pm \end{pmatrix} e^{ip_\mu x^\mu}, \quad (1.10)$$

where χ^\pm are two-component Pauli spinors representing spin up and spin down states respectively. It is important to note at this point that the negative energy solutions of the Dirac equation are actually as positive energy antiparticle solutions in the Feynman-Stückelberg interpretation [5]. In fact, the $E < 0$ solution correctly describes a particle moving backwards in time [5]. This is equivalent to an antiparticle with $E > 0$ moving forward in time. The $\sqrt{\frac{E+m}{2E}}$ ‘normalization’ term in Eqs. (1.9) and (1.10) arises from two contributions. One is from the equation of continuity for a relativistic wave equation, which shows that the probability density per unit volume is proportional to twice the total energy (i.e. there are $2E$ particles per unit volume). The other $\sqrt{E+m}$ term is simply the normalization for $u(p)$.

The antiparticle solution shown in Eq. 1.10 can be expressed in simpler terminology as,

$$\Psi(x) = v(p)e^{ip_\mu x^\mu} = v(p) e^{i(Et - \vec{p} \cdot \vec{x})}. \quad (1.11)$$

which satisfies the Dirac equation for antiparticles

$$(\gamma^\mu p_\mu + m)v(p) = 0. \quad (1.12)$$

The above complements Eq. (1.8). The relativistic equations for spin-1/2 particles and antiparticles can be written in a more compact form using the Feynman slash notation ($\not{p} = \gamma^\mu p_\mu$)

$$\begin{aligned}(\not{p} - m)u(p) &= 0 \\ (\not{p} - m)v(p) &= 0.\end{aligned}\tag{1.13}$$

Likewise, the Dirac equation for an electron in an electromagnetic field is,

$$(i\not{\partial} - e\mathcal{A} - m)\Psi = 0,\tag{1.14}$$

where $\not{\partial} = \gamma^\mu \partial_\mu$ and Ψ includes both the positive and negative energy solutions. In order to represent the negative energy solutions as positive energy solutions of the positrons, one needs to define a charge conjugation operation,

$$\widehat{C}\Psi = \Psi^c,\tag{1.15}$$

where Ψ represents a particle state and Ψ^c is its corresponding antiparticle state, both with positive energies. The antiparticle state should ideally satisfy a similar equation

$$(i\not{\partial} + e\mathcal{A} - m)\Psi^c = 0.\tag{1.16}$$

It can easily be shown [4] that Ψ^c is a solution of Eq. (1.16) if

$$\Psi^c = \widehat{C}\gamma^0\Psi^* = \widehat{C}\bar{\Psi}^T,\tag{1.17}$$

where a suitable choice for the charge conjugation operator is $\widehat{C} = i\gamma^2\gamma^0$ [4, 5].

The case of massless fermions

In the limit as $m \rightarrow 0$, $E \rightarrow \pm|\vec{p}|$. Therefore, for massless spin-1/2 particles, Eq. (1.9) reduces to

$$\Psi(x) = \frac{1}{\sqrt{2}} \begin{pmatrix} \chi^\pm \\ \vec{\sigma} \cdot \hat{p} \chi^\pm \end{pmatrix} e^{-ip_\mu x^\mu}.\tag{1.18}$$

Here it is important to define a new observable called helicity, given by the operator

$$\hat{H} = \vec{\sigma} \cdot \hat{p}, \quad (1.19)$$

whose eigenvalues quantify the two projections of the particle's intrinsic spin along its direction of momentum. A particle with positive helicity has its spin aligned along the direction of its motion (is a right-handed particle) and vice versa. Defining a helicity eigenstate is essential as it is not possible to define the rest frame of a massless particle (which moves with velocity c) to quantify its spin projections. However, it is also important to note that helicity is not a Lorentz invariant quantity for massive particles.

In order to better understand helicity eigenstates, a more convenient representation is the Weyl (or chiral) representation for α and β matrices [5]

$$\vec{\alpha} = \begin{pmatrix} -\vec{\sigma} & 0 \\ 0 & \vec{\sigma} \end{pmatrix}, \quad \beta = \begin{pmatrix} 0 & I \\ I & 0 \end{pmatrix}. \quad (1.20)$$

Similarly as before, the 4-component solutions can be written as two 2-component spinors for both $E > 0$ and $E < 0$ solutions

$$\Psi = \begin{pmatrix} \chi \\ \phi \end{pmatrix}. \quad (1.21)$$

Then for $m = 0$, the Dirac equation leads to two uncoupled equations

$$-\vec{\sigma} \cdot \vec{p} \chi = E \chi, \quad (1.22)$$

$$\vec{\sigma} \cdot \vec{p} \phi = E \phi. \quad (1.23)$$

The positive energy solution of Eq. (1.22) satisfies,

$$\vec{\sigma} \cdot \hat{p} = -\chi, \quad (1.24)$$

while the negative energy solution satisfies

$$\vec{\sigma} \cdot (-\hat{p}) = \chi. \quad (1.25)$$

Translating this to antiparticles means that Eq. (1.24) describes a left-handed particle (with negative helicity), while Eq. (1.25) describes a right-handed antiparticle (moving backwards in time). Similarly, Eq. (1.23) describes a left-handed antiparticle and right-handed particle. Based on the above, one can define the chirality operator

$$\gamma^5 \equiv i\gamma^0\gamma^1\gamma^2\gamma^3 = \begin{pmatrix} -I & 0 \\ 0 & I \end{pmatrix} \quad (1.26)$$

and the left and right chirality eigenstates $\Psi_L = \begin{pmatrix} \chi \\ 0 \end{pmatrix}$ and $\Psi_R = \begin{pmatrix} 0 \\ \phi \end{pmatrix}$

so that

$$\gamma^5 \begin{pmatrix} \chi \\ 0 \end{pmatrix} = - \begin{pmatrix} \chi \\ 0 \end{pmatrix} \quad (1.27)$$

corresponds to left-handed fermions, while

$$\gamma^5 \begin{pmatrix} 0 \\ \phi \end{pmatrix} = \begin{pmatrix} 0 \\ \phi \end{pmatrix} \quad (1.28)$$

corresponds to right-handed fermions. In the extreme relativistic limit the γ^5 operator is the same as the helicity operator (1.19). However, as noted previously, helicity is not a relativistically invariant quantity for massive fermions. In order to remove the reference frame dependence in describing the ‘handedness’ of a massive fermion, one has to resort to the projection operator

$$P = \frac{1}{2} (\mathbb{1} \mp \gamma^5), \quad (1.29)$$

which projects out the left or right handed components of a general spinor

$$\Psi = \Psi_L + \Psi_R = \begin{pmatrix} \chi \\ \phi \end{pmatrix} \quad (1.30)$$

1.1.2 Nuclear beta decays

The standard model assumes that nuclear beta decays (and other weak decays) are caused by purely $V - A$ (vector–axial vector) interactions. In such processes, the leptons interact via charged current weak interactions, where the interaction is described as a combination of only γ^μ and $\gamma^\mu\gamma_5$ bilinear terms. This is because overwhelming experimental evidence shows that parity is maximally violated in weak interactions and that neutrinos are left-handed particles [3,6].

In a field theoretical description, the weak interaction Hamiltonian for semi-leptonic processes (such as nuclear beta decays) is written as a four-point current-current interaction

$$H_W = \frac{G_F}{\sqrt{2}} J_\mu J^{\mu\dagger}, \quad (1.31)$$

considering that the W bosons are extremely massive. In the above, G_F is the universal Fermi coupling constant and the charged weak current contains the sum of both hadronic and leptonic components, which further satisfy maximal parity violation (and the fact that neutrinos are experimentally observed to be left-handed). For the description of the simplest semi-leptonic β -decay (i.e. neutron decay), the hadronic current can be written (analogous to the electromagnetic current) as

$$J_{had}^\mu = \bar{\phi}_p (g_V \gamma^\mu - g_A \gamma^\mu \gamma_5) \phi_n, \quad (1.32)$$

where g_V and g_A are the vector and axial-vector form factors. Similarly, the leptonic current is

$$J_{lep}^\mu = \bar{\phi}_e \gamma^\mu (1 - \gamma_5) \phi_{\nu_e}, \quad (1.33)$$

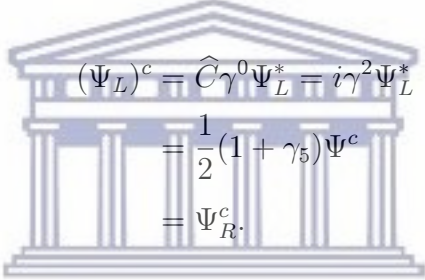
Here, the ϕ 's represent the quantum field operators describing the particles involved in the decay. In the allowed approximation for β decays, the vector and axial-vector components of weak interaction (γ^μ and $\gamma^\mu\gamma_5$) reduce to the usual Fermi and Gamow-Teller transition operators (τ^\pm and $\vec{\sigma}\tau^\pm$) in the non-relativistic limit. Based on the above, one can generate left-handed neutrino fields using the projection operation on a general neutrino state Ψ_{ν_e} by the operation

$$\nu_{eL} = \frac{1}{2}(1 - \gamma_5)\Psi_{\nu_e} . \quad (1.34)$$

Therefore, the most general leptonic current for left-handed particle fields can be written as

$$J_{lep}^\mu = 2(\bar{e}_L\gamma^\mu\nu_{eL} + \bar{\mu}_L\gamma^\mu\nu_{\mu L} + \bar{\tau}_L\gamma^\mu\nu_{\tau L}), \quad (1.35)$$

which includes the muon and tau sectors of the weak interaction as well. The fields of the antiparticles are generated by the charge conjugation operation



$$\begin{aligned} (\Psi_L)^c &= \widehat{C}\gamma^0\Psi_L^* = i\gamma^2\Psi_L^* \\ &= \frac{1}{2}(1 + \gamma_5)\Psi^c \\ &= \Psi_R^c. \end{aligned} \quad (1.36)$$

The above clearly shows that the handedness of antiparticles are opposite to those of the particles. Therefore antineutrinos are right-handed. As a result of Eq. (1.36) the standard model classification of elementary particles (shown in Eq.(1.1)) gets modified slightly, so that the quark and lepton doublets only include left-chiral fields for particles. In this representation the right-handed fields for the charged fermions are only part of the $SU(2)$ singlet [4].

1.2 Massive neutrinos and double beta decays

Until the late 1990's, the standard model assumed that neutrinos were massless fermions. However, there were indications much earlier (based on solar neutrino flux measurements) that neutrinos could in fact have finite masses [7]. The 'solar neutrino problem' [8] sug-

gested that the deficit of the observed solar neutrinos is because the neutrinos change flavor while in flight. This phenomenon is called neutrino oscillation, as previously suggested by Pontecorvo, Maki, Nakagawa and Sakata [1]. To date, the observation of neutrino oscillations in several independent experiments such as Super Kamiokande [9, 10], SNO [8], GALLEX [11], SAGE [12], K2K [13], etc, has confirmed that neutrinos do indeed change flavor from one eigenstate to another in flight. This is only possible if neutrinos have mass. These results imply that the left-handed neutrino fields ν_L do not represent states with a definite mass. The flavor eigenstates that participate in weak interactions are in fact mixtures of the mass eigenstates, given by

$$\begin{pmatrix} \nu_e \\ \nu_\mu \\ \nu_\tau \end{pmatrix} = \begin{pmatrix} U_{e1} & U_{e2} & U_{e3} \\ U_{\mu1} & U_{\mu2} & U_{\mu3} \\ U_{\tau1} & U_{\tau2} & U_{\tau3} \end{pmatrix} \begin{pmatrix} \nu_1 \\ \nu_2 \\ \nu_3 \end{pmatrix}. \quad (1.37)$$

The 3×3 unitary matrix shown above is the Pontecorvo-Maki-Nakagawa-Sakata (PMNS) [1] neutrino mixing matrix. The probability that the flavor changes from $\nu_l \rightarrow \nu_{l'}$ after a time t is (assuming only 3 generations of neutrinos)

$$P(\nu_l \rightarrow \nu_{l'}) = \sum_{i=1}^3 |U_{li}|^2 |U_{l'i}|^2 + \sum_{j \neq i} U_{li} U_{l'j} U_{l'i}^* U_{lj}^* \exp\left(\frac{-i(m_i^2 - m_j^2)t}{2p}\right), \quad (1.38)$$

where p is the momentum of the neutrino ν_l , with $p \gg m_i$. Clearly this probability oscillates as a function of time. Here $m_i^2 - m_j^2 = \Delta m_{ij}^2$ is the mass squared difference for the two neutrinos involved in the oscillation. As evident from Eq. (1.38), neutrino oscillation measurements can only determine the mass squared differences for the neutrinos and not their absolute masses. Recent solar and atmospheric neutrino oscillation experiments have shown that $\Delta m_{12}^2 \ll \Delta m_{13}^2 \approx \Delta m_{23}^2$ [8]. Furthermore, since the atmospheric neutrino experiments only give the absolute value of Δm_{13}^2 (or Δm_{23}^2), it is not clear if the third eigenstate is much heavier or lighter than the former two. Thus the neutrino mass splittings can be of two types, the normal or inverted hierarchy, as shown in Fig. 1.1.

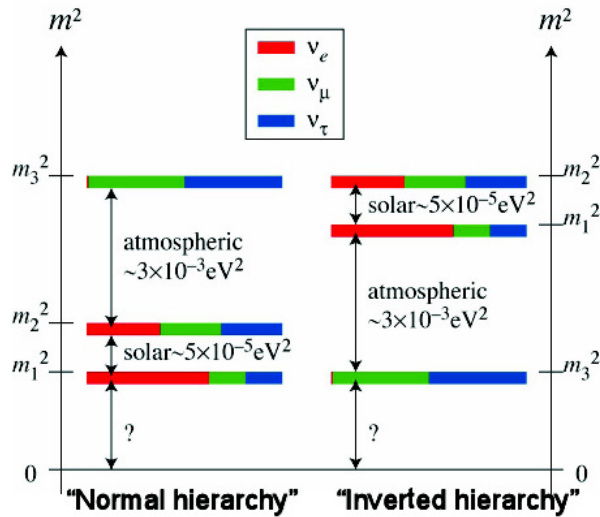


Figure 1.1: Neutrino mass hierarchy obtained from solar and atmospheric oscillation data. The color coding shows the proportion of each flavor eigenstate in the respective mass eigenstates [14].

1.2.1 Neutrino mass terms

Prior to the discovery of neutrino oscillations, the standard model electroweak Lagrangian included the neutrino fields on a similar footing as the quarks and charged leptons. However there was one fundamental difference. The other fermion masses were generated via Yukawa couplings of the fields to the Higgs doublet. The mass terms in the Lagrangian were constructed using both left-handed and right-handed chiral fields. Since experimental evidence showed the absence of right-handed neutrinos, the neutrino mass term could not be constructed similarly. The neutrino fields had no right-handed singlet components, which naturally explained massless neutrinos in the standard model.

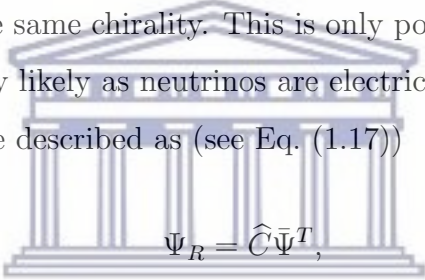
With the discovery of neutrino oscillations clearly a new explanation was required to describe the generation of neutrino masses. In the simplest modification to the minimal standard model, massive neutrinos can be generated similarly as it was done for the charged fermions. This introduces *sterile* right-handed neutrino fields as $SU(2)$ singlets. Assuming that the neutrino fields satisfy the Dirac equation, they can be described by the Lagrangian

$$\mathcal{L} = \bar{\nu} (i\gamma^\mu \partial_\mu - m_D) \nu , \quad (1.39)$$

where $m_D \bar{\nu} \nu$ is called the Dirac mass term. In the presence of neutrino fields of both chiralities, the mass term is simply

$$\mathcal{L}_{mass} = -m_D(\bar{\nu}_L \nu_R + \bar{\nu}_R \nu_L) , \quad (1.40)$$

which requires four neutrino chirality solutions (as expected by the Dirac equation), two of which are sterile. The right-handed sterile fields only give the neutrinos masses, they do not couple with the weak interaction and are not realized experimentally otherwise. Although the Dirac mass term conserves lepton number, its formalism is unsatisfactory. For example, if the neutrino mass generation mechanism were similar to the charged fermions, the extreme smallness of the neutrino mass compared to the others would require an unnaturally weak Yukawa coupling to the Higgs field. A second alternative was proposed by Ettore Majorana, who suggested to build a mass term with only two active neutrino fields, both of the same chirality. This is only possible if the neutrino is its own antiparticle which is highly likely as neutrinos are electrically neutral. In this case, since a right-handed field can be described as (see Eq. (1.17))



$$\Psi_R = \hat{C} \bar{\Psi}^T, \quad (1.41)$$

the Majorana neutrino field can be expressed similarly as in Eq. 1.30

$$\begin{aligned} \nu &= \nu_L + \nu_R \\ &= \nu_L + \hat{C} \bar{\nu}^T \\ &= \nu_L + \nu_L^c . \end{aligned} \quad (1.42)$$

Then clearly $\nu^c = \nu_L^c + \nu_L = \nu$. Therefore a Majorana fermion is its own antiparticle. The Majorana mass term can thus be constructed from purely left-handed or right-handed fields without having to invoke sterile neutrinos,

$$\mathcal{L}_{mass} = -\frac{1}{2} m_L (\bar{\nu}_L^c \nu_L + \bar{\nu}_L \nu_L^c) . \quad (1.43)$$

The above clearly couples neutrinos to antineutrinos, which can be viewed as the creation of two particles, thereby leading to violating of lepton number by $\Delta L = 2$. Therefore Majorana neutrinos would lead to a rare (yet-to-be-observed) lepton number violating process called neutrinoless double beta decay which is described in Sect. 1.3. However, the Majorana mass term in Eq. (1.43) unfortunately violates the $SU(2)_L \times U(1)$ gauge symmetry of the standard model.

A very appealing alternative to explain the smallness of neutrino masses uses both Dirac and Majorana terms, where the Lagrangian has both left-handed and right-handed fields,

$$\mathcal{L}_{mass} = -\frac{1}{2} \begin{pmatrix} \bar{\nu}_L & \overline{(\nu_R)^c} \end{pmatrix} \begin{pmatrix} m_L & m_D \\ m_D & m_R \end{pmatrix} \begin{pmatrix} (\nu_L)^c \\ \nu_R \end{pmatrix} + h.c. \quad (1.44)$$

Diagonalizing the 2×2 mass matrix shown above, one arrives at the solutions

$$m_{1,2} = \frac{1}{2} \left[(m_L + m_R) \pm \sqrt{(m_L - m_R)^2 + 4m_D^2} \right]. \quad (1.45)$$

Due to the breaking of the gauge symmetry mentioned above, one can set $m_L = 0$. Further assuming $m_R \gg m_D$, it is easy to see that

$$m_1 = \frac{m_D^2}{m_R} \quad (1.46)$$

and

$$m_2 = m_R \left(1 + \frac{m_D^2}{m_R^2} \right) \approx m_R. \quad (1.47)$$

Clearly, such a prescription ensures that the large value of m_R suppresses the mass of the light neutrino. This is called the see-saw mechanism [1], which naturally explains the smallness of neutrino masses. It requires neutrinos to be Majorana particles and the additional existence of an extremely heavy right-handed neutrino.

1.3 Neutrinoless double beta decay

Double beta-decay is a rare process that can occur in only ~ 35 naturally occurring radioactive isotopes. One such example is ^{136}Xe $\beta\beta$ decay to ^{136}Ba , shown in Fig. 1.2, where the intermediate nucleus is ^{136}Cs . The pairing energy between like nucleons makes the even-even parent more bound, thus energetically forbidding a single beta decay to the odd-odd intermediate nucleus. However, a two-neutrino double beta decay ($2\nu\beta\beta$) to the grand-daughter is still energetically favorable and would occur with the emission of two electrons and two neutrinos. This would effectively lead to two neutrons converting to two protons, with the emission of 4 leptons as the final product. The $2\nu\beta\beta$ decay mode does not violate any conservation laws and is a standard-model-allowed second-order transition. The decay can occur irrespective of whether the neutrinos are Dirac or Majorana type. However, such decays are highly suppressed due phase space considerations, with lifetimes of the order of $10^{19} - 10^{22}$ yrs [15–17].

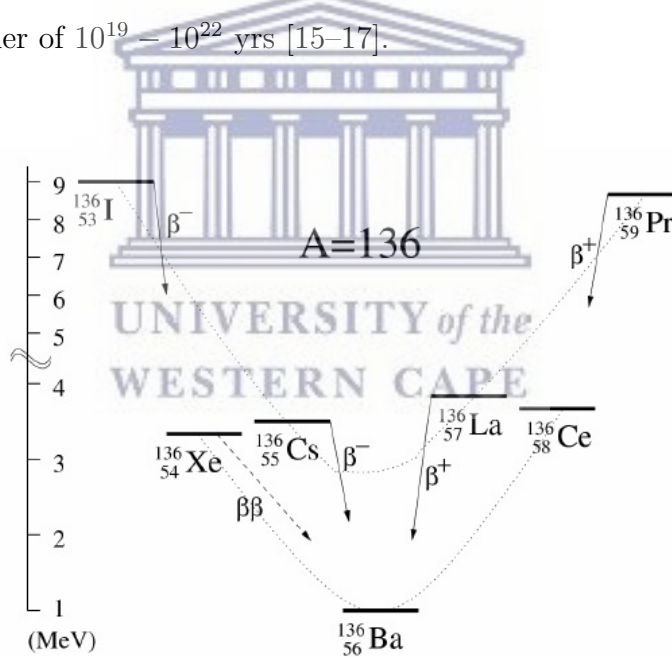


Figure 1.2: The mass parabolas for $A = 136$ nuclei. ^{136}Xe is stable against ordinary beta-decay but unstable against double beta-decay. Figure extracted from Ref. [18].

The massive nature of neutrinos opens up another possibility, the $0\nu\beta\beta$ decay mode with no neutrino emission. As mentioned previously, this is the (only) way one can ascertain

directly the Majorana nature of neutrinos. Unlike the $2\nu\beta\beta$ decay mode, where the phase space is $\sim Q^{11}$, $0\nu\beta\beta$ decays are not limited by phase space ($\sim Q^5$). But they are lepton number violating and standard-model-forbidden. Both these decay modes are shown in the Feynman diagrams in Fig. 1.3.

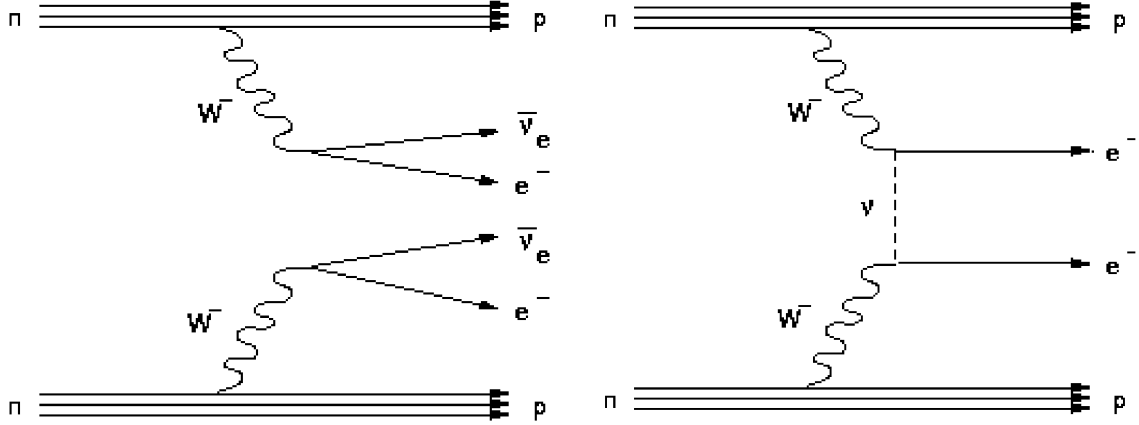


Figure 1.3: Left panel: $2\nu\beta\beta$ decay. Right panel : $0\nu\beta\beta$ decay.

The assumption that massive Majorana neutrinos would cause $0\nu\beta\beta$ decays is one of the best motivated examples to search for physics beyond the standard model (BSM). Although all postulated BSM theories require neutrinos to be Majorana particles, there are several possible mechanisms that could cause $0\nu\beta\beta$ decays [19–22]. These include the exchange of light or heavy Majorana neutrinos [21], presence of right-handed weak interactions [23] or exotic interactions from R-parity violating SUSY models [24]. By far the standard interpretation adopted (and preferred) by theorists is the one that involves the mediation of light Majorana neutrinos. In general, the rate of a $0\nu\beta\beta$ decay depends on contributions from all the possible lepton number violating mechanisms

$$[T_{1/2}^{0\nu}]^{-1} = \sum_i G_i^{0\nu}(Q, Z) |M_i^{0\nu} \eta_i|^2. \quad (1.48)$$

where $G^{0\nu}(Q, Z)$ is a phase-space factor, $|M_i^{0\nu}|$ are the nuclear matrix elements (NME) for the decay and η_i are the LNV parameters that depend on the mechanism driving the process. If we assume that the dominant mechanism responsible for the decay is mediated by the exchange of light left-handed Majorana neutrinos, the η parameter in Eq. (1.48)

reduces to [1]

$$\eta = \frac{\langle m_{\beta\beta} \rangle}{m_e}, \quad (1.49)$$

where, $m_{\beta\beta} = \sum_{k=1}^3 m_k U_{ek}^2$ is the effective Majorana mass of the electron neutrino. The U_{ek} are elements of the PMNS mixing matrix described earlier in this chapter, m_k are the light Majorana neutrino mass eigenvalues and m_e the electron mass. The $0\nu\beta\beta$ -decay half-life can then be expressed as,

$$[T_{1/2}^{0\nu}]^{-1} = G^{0\nu}(Q, Z) |M^{0\nu}|^2 \left(\frac{\langle m_{\beta\beta} \rangle}{m_e} \right)^2. \quad (1.50)$$

If $0\nu\beta\beta$ decays were observed, the Schechter-Valle theorem (also called the Black Box theorem) [17, 22, 25] ensures that the neutrinos have to be Majorana fermions regardless of the mechanism driving the decay. However, to get any further information on the LNV parameters driving the decay (such as $\langle m_{\beta\beta} \rangle$), one needs an accurate computation of the nuclear matrix elements (NMEs) for the decay. To date there have been several approaches undertaken by theorists world wide to evaluate these NMEs. As shown in Fig. 1.4, currently there exists significant disparity in calculated values for several cases depending on the method used. This is briefly overviewed in the section below, with an emphasis on two of the most popular approaches.

1.4 Nuclear Matrix Elements for $0\nu\beta\beta$ decays

The nuclear matrix elements are calculated using different theoretical methods, the Quasi-particle Random Phase Approximation (QRPA) [27–31], Interacting Shell Model (ISM) [32, 33], projected Hartree-Fock Bogoluibov (P-HBF) [34] method, Interacting Boson Model (IMB) [35], and by Energy Density Functional Method (EDF) [36]. The difference in these methods lie in their choice of valence space used, correlations included between the nucleons and in the way the equations of motion for the effective Hamiltonian H_{eff} are solved. Current status of the $0\nu\beta\beta$ decay NME calculated using these approaches is shown in Fig. 1.4. Of all the above, the ones most widely used are the Interacting Shell Model (ISM) and Quasiparticle Random Phase Approximation (QRPA). These two approaches

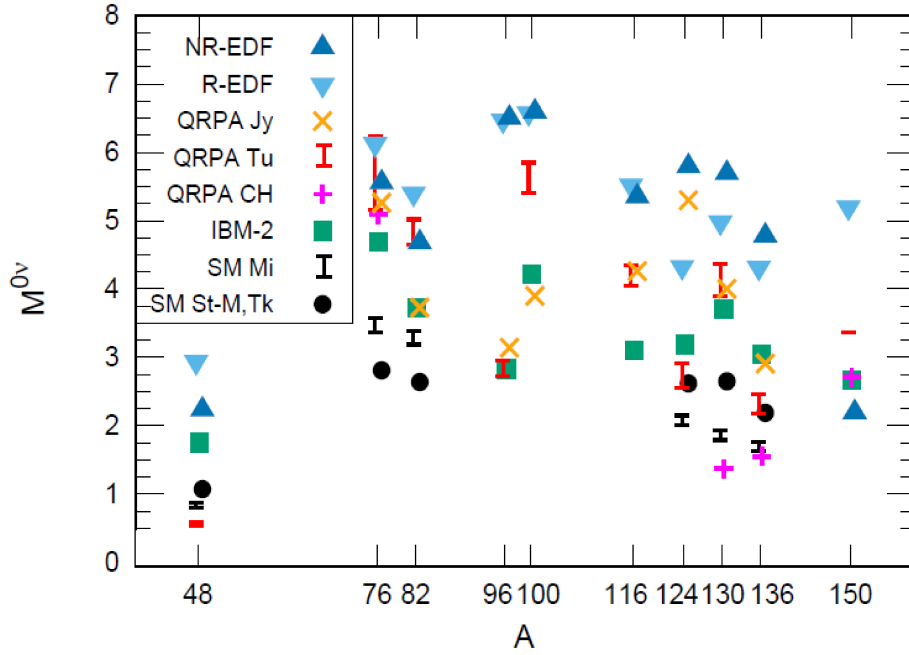


Figure 1.4: Neutrinoless double beta-decay matrix elements for various isotopes calculated using different methods. Figure obtained from Ref [26].

are discussed below.

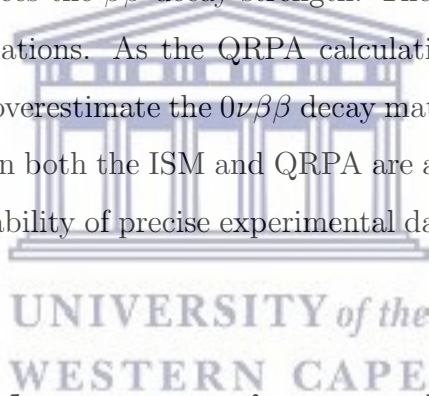
The Interacting Shell Model (ISM)

The shell model has been widely used to describe the properties of medium and heavy mass nuclei [26, 37, 38]. The effective nuclear interaction H_{eff} used in the shell model is initialized by fitting the bare nucleon-nucleon interaction to two-nucleon scattering data [26]. The model utilizes a valence space that comprises of active nucleons occupying only a few single particle states outside the Fermi surface. However, the effective Hamiltonian for this configuration space is exactly diagonalized, resulting in shell model states that account for all correlations between the valence nucleons. As a result, the shell model can quite accurately describe the ground state properties of the nuclei and low-lying excitation energy spectra [26, 37, 38]. The model also quite successfully reproduces the experimental single β and $2\nu\beta\beta$ decay rates if the strength of the axial-vector coupling constant (g_A) is quenched by $\sim 20\% - 30\%$ [39, 40]. A major limitation of this model, however, is the restricted configuration space, which may further affect the pair-

ing correlations that are important in $0\nu\beta\beta$ decays [18]. As seen in Fig. 1.4, the $M^{0\nu}$'s calculated using the shell model are lower compared to most other methods.

Quasiparticle Random Phase Approximation (QRPA)

QRPA calculations consider only a limited number of correlations between the valence nucleons and so can use a much larger configuration space compared to the shell model [18, 27, 30]. In fact, QRPA calculations are performed using at least two major oscillator shells around the Fermi surface. In QRPA calculations, pairing correlations are performed in the BCS approximation [41]. However, the strengths of the interaction has to be adjusted to correctly reproduce the neutron and proton pairing gaps in both the initial and final nuclei. Additionally, the decay rate for β and $\beta\beta$ are found to be very sensitive to the strength of particle-particle interaction (g_{pp}) [42–44]. This constraint is overcome by fixing g_{pp} so it correctly reproduces the $\beta\beta$ decay strength. The same value of g_{pp} is then used for the $0\nu\beta\beta$ decay calculations. As the QRPA calculations do not account for all the correlations, they tend to overestimate the $0\nu\beta\beta$ decay matrix elements. This is evident in Fig. 1.4. The parameters in both the ISM and QRPA are adjusted to match experimental data. Therefore, the availability of precise experimental data is highly important for both calculations.



1.5 Reducing the uncertainty on NME's

To evaluate a NME, the $M^{0\nu}$ is expressed as a sum of the Gamow-Teller (M_{GT}), Fermi (M_F) and tensor matrix (M_T) elements [15]

$$M^{0\nu} = M_{GT}^{0\nu} - \left(\frac{g_V}{g_A}\right)^2 M_F^{0\nu} - M_T^{0\nu} . \quad (1.51)$$

The contribution from the tensor matrix element is negligibly small and is usually ignored [19]. In the case that the decay goes from the 0^+ ground state of the (A, Z) nucleus to the 0^+ ground state of the $(A, Z + 2)$ nucleus, the Fermi and Gamow-Teller matrix

elements is approximated as [15]

$$M_{GT} \sim \langle 0_f^+ \| \frac{1}{2} \sum_{ij} \vec{\sigma}(i) \cdot \vec{\sigma}(j) \tau_{\pm}(i) \tau_{\pm}(j) \| 0_i^+ \rangle \quad (1.52)$$

and

$$M_F = \langle 0_f^+ \| \frac{1}{2} \sum_{ij} \tau_{\pm}(i) \tau_{\pm}(j) \| 0_i^+ \rangle, \quad (1.53)$$

where

$$\sum_{ij} \tau_{\pm}(i) \tau_{\pm}(j) = \left(\sum_i \tau_{\pm}(i) \right)^2 = (T_{\pm})^2. \quad (1.54)$$

The T_{\pm} isospin raising/lowering operators in the Fermi matrix element connect the isobaric analog states (IAS) in the two nuclei. Thus, in Eq. (1.53) M_F is nonzero only if the Coulomb interaction mixes the IAS in the $(A, Z + 2)$ nucleus with its ground state. As a consequence, the contribution to $M^{0\nu}$ from M_F is small and the $M^{0\nu}$ is dominated by the Gamow-Teller part, M_{GT} .

As is evident in Fig. 1.4, the matrix elements calculated using different theoretical approaches could differ up to a factor of 3. The discrepancies in the NMEs arises primarily from the different approximations made to arrive at the solution of the nuclear many-body problem. The use of the mean field in different ways generates single particle occupancies of individual orbits that could differ significantly between different models. As mentioned earlier, the use of different valence shells either underestimates or overestimates the NMEs.

Since the closest experimentally observable phenomenon that is similar to a $0\nu\beta\beta$ decay is the $2\nu\beta\beta$ decay, which has already been observed in several nuclei, these data are useful to set constraints on the nuclear structure calculations of the NMEs. The rate of a $2\nu\beta\beta$ decay is [18]

$$[T_{1/2}^{2\nu}]^{-1} = G^{2\nu}(Q, Z) |M^{2\nu}|^2, \quad (1.55)$$

with

$$M^{2\nu} = M_{GT}^{2\nu} - \left(\frac{g_V}{g_A} \right)^2 M_F^{2\nu}. \quad (1.56)$$

The Gamow-Teller and Fermi matrix elements for this decay mode are similar to $0\nu\beta\beta$ decay

$$M_F^{2\nu} = \langle f | \sum_a \tau_a^+ | n \rangle \langle n | \sum_b \tau_b^+ | i \rangle \quad (1.57)$$

$$M_{GT}^{2\nu} = \langle f | \sum_a \sigma_a \tau_a^+ | n \rangle \langle n | \sum_b \sigma_b \tau_b^+ | i \rangle . \quad (1.58)$$

As in the case of $M_F^{0\nu}$, isospin symmetry breaking leads to negligible contribution of $M_F^{2\nu}$, concentrating all the strength of $M^{2\nu}$ in the $M_{GT}^{2\nu}$ component. The Gamow-Teller matrix element $M_{GT}^{2\nu}$ is expressed as a sum of two Gamow-Teller transition matrix elements M_{GT}^\pm [17, 45, 46]. Therefore, the $M_{GT^\pm}^{2\nu}$ NME is calculated as a sum over all virtual 1^+ states in the intermediate nucleus

$$M_{GT}^{2\nu} = \sum_m \frac{M_{GT}^+(m) M_{GT}^-(m)}{Q_{\beta\beta}/2 + m_e + E_x(1_m^+) - E_0} , \quad (1.59)$$

where $E_x(1_m^+) - E_0$ is the difference in energy between the intermediate 1^+ state and the ground state of the parent nucleus. Furthermore, deformed-QRPA calculations for $2\nu\beta\beta$ decay $^{76}\text{Ge} \rightarrow ^{76}\text{Se}$ have shown that excited states in intermediate nucleus lying in the region of the Gamow-Teller resonance contribute significantly to the matrix element of the decay [47]. The GT^\pm matrix elements have been extracted via charge-exchange reactions such as $(^3\text{He}, t)$, $(d, ^2\text{He})$ in most of the $2\nu\beta\beta$ decay candidates [17, 48–53] and are well reproduced by the sum of the matrix elements through all the low-lying 1^+ states in the intermediate nucleus [17]. Therefore, to test the $2\nu\beta\beta$ decay matrix element calculations, experimental information of the 1^+ states in the intermediate nucleus is crucial. Below I discuss some of the nuclear structure related considerations that are also important for the NME calculations.

The closure approximation

Within the framework of perturbation theory, $0\nu\beta\beta$ decay NME's are calculated assuming that the decays proceed from the initial nucleus to the final nucleus via the intermediate nucleus. This implies that wave functions of all the intermediate states (allowed by the

nuclear structure model) are required in addition to the initial and final states. This exact treatment (also referred to as non-closure methods) for the NME calculation is a computationally expensive task, especially for heavy nuclei. For instance, for the $0\nu\beta\beta$ decay of ^{76}Ge , about 1.5×10^8 states in ^{76}As have to be considered in the ISM calculations [54]. To by pass this, most calculations except QRPA [55] calculate the $0\nu\beta\beta$ decay matrix elements in the closure approximation [56, 57]. In this method the energies of the individual intermediate states are replaced by an average energy $\langle E \rangle$. The closure approximation correctly assumes that the momentum transfer due to the virtual neutrinos in the $0\nu\beta\beta$ decay is much larger (~ 100 MeV) than the difference in energy between the ground state of the parent and the excitation energies in the intermediate nucleus. Therefore structural details of the odd-odd intermediate nucleus can be ignored. Comparative studies performed for $0\nu\beta\beta$ of ^{48}Ca in the shell model have shown that the matrix elements calculated using the closure methods reproduce the non-closure $0\nu\beta\beta$ matrix elements to within 10% [26, 58].

The dominant contribution to the NMEs calculated using non-closure methods originates from low-lying intermediate states [58]. Taking advantage of this, calculations that go beyond the closure approximation use a combination of both closure and non-closure methods [54, 58]. In this approach, all excited states in the intermediate nucleus that lie below a cut-off energy E are treated in the non-closure regime while the closure approximation is used for the higher lying excited states. An alternative approach is to set the cut-off parameter N on the number of states of each J^π in the intermediate nucleus. The success of this method has been demonstrated for the $0\nu\beta\beta$ decay of ^{48}Ca , ^{76}Ge and ^{82}Se [54, 59] wherein, the matrix elements could be calculated to within $\sim 1\%$ the non-closure values.

Effect of deformation

Most of the nuclei involved in double beta decay are either spherical or weakly deformed, except for the strongly deformed ^{150}Nd . Differences in deformation between the two nuclei involved would require a significant rearrangement in the configuration of the valence

nucleons, which would further suppress the transition matrix elements for the decay [60]. It is well-known that the $2\nu\beta\beta$ matrix elements are comparatively larger when the parent and the grand-daughter nuclei have a similar deformation but decrease rapidly as the difference in deformation between the two nuclei increases. This for instance, has been demonstrated in the deformed-QRPA formalism for nearly all the $\beta\beta$ decay partners ($A = 48, 76, 82, 96, 100, 116, 128, 130, 136$ and 150) [47,61] and in the ISM calculations for a fictitious case of ^{48}Ti - ^{48}Cr [62]. The rate of the $2\nu\beta\beta$ decay is also used to constrain the variables (for e.g. particle-particle interaction strength) in QRPA calculations before calculating the $0\nu\beta\beta$ decay matrix element. Additionally, in the QRPA regime the ground state wavefunctions of the parent and daughter nuclei are assumed to be BCS correlated states [41]. A deformed nucleus cannot be described in the BCS approximation. Nuclear deformations can be studied for example by investigating nuclear shapes via Coulomb excitation experiments or by studying the strength of 0^+ states excited in pair-transfer reactions.

Occupancies of valence orbits

Experimental information on occupancies (or vacancies) of the valence orbits can establish important constraints on the nuclear models used in the various approaches. In particular, single or two nucleon transfer reactions can provide important spectroscopic information in this regard. For example, on tuning the ISM [63] and QRPA [64, 65] calculations to reproduce experimental data in the $A = 76$ nuclei have led to a significant change in ^{76}Ge $0\nu\beta\beta$ decay NME both calculations. This reduced the discrepancy between the calculated ISM and QRPA matrix elements.

In summary, improving the calculation of $0\nu\beta\beta$ decay matrix elements is a challenging but necessary task. Experimental information from charge-exchange and particle transfer reactions are vital and can be used to improve the quality of wavefunctions used to calculate the transition matrix elements.

1.6 Status of $^{136}\text{Xe} \rightarrow ^{136}\text{Ba}$ $\beta\beta$ decay experiments

In recent years, the search for neutrinoless double beta decay has accelerated as large scale state-of-art experiments have become operational and several others are in an advanced stage of development or construction. Some of the experiments that are currently collecting data are KamLAND-ZEN [66–68], EXO-200 [69, 70], CUORE [71], Majorana Demonstrator [72], GERDA [73] and CUPID-0 [74]. The first two experiments study the $0\nu\beta\beta$ decay of ^{136}Xe , CUORE (and its predecessors [75]) study ^{130}Te , the Majorana Demonstrator and GERDA looks for the decay of ^{76}Ge and ^{82}Se is the isotope of interest in CUPID-0. In addition to these, the NEMO-3 detector [76, 77] that operated from 2003-2011 simultaneously looked for the $0\nu\beta\beta$ of 7 isotopes, ^{48}Ca , ^{82}Se , ^{96}Zr , ^{100}Mo , ^{116}Cd , ^{130}Te and ^{150}Nd . The NEMO-3 project is currently being upgraded to SuperNEMO [78]. While all the current $\beta\beta$ decay experiments have their own set of advantages, as this thesis work is motivated towards the $0\nu\beta\beta$ of $^{136}\text{Xe} \rightarrow ^{136}\text{Ba}$, in this section we shall focus our discussion to only this particular case, which offers certain advantages that makes it an attractive candidate for double beta decay experiments. In fact, the most stringent limit on the mass of light Majorana neutrinos is currently set by the KamLAND-ZEN experiment [66] that uses enriched liquid xenon. Some of the advantages that this isotope offers are listed below.

1. ^{136}Xe relatively abundant (8.9%), affordable and easy to purify and enrich.
2. There are no long-lived xenon isotopes thus eliminating any internal contamination.
3. Xenon can be used as a gaseous detector or in the form of a liquid scintillator. High density of liquid xenon acts as a shield against external gamma backgrounds. It also allows to reconstruct the event topologies.
4. One can achieve an improved energy resolution through the collection of both ionization electrons as well as scintillation light from the xenon.
5. The liquid xenon potentially allows for complete background rejection through tagging of the daughter barium ion in this method. This is unique amongst all the

$0\nu\beta\beta$ decay experiments.

6. The detectors can be made compact by using condensed liquid xenon. This will reduce the need for underground space as well as the shielding material.
7. The measured $2\nu\beta\beta$ decay half-life [79,80] yields the smallest $2\nu\beta\beta$ matrix element amongst all cases, with $|M^{2\nu}| = 0.019 \text{ MeV}^{-1}$. This leads to maximal suppression of the standard model background.
8. The parent nucleus (82 neutrons, 54 protons) is singly closed shell and mostly spherical, which should make matrix element calculations relatively simpler.

In light of the above, searches for $0\nu\beta\beta$ decays of ^{136}Xe has been the focus of state-of-art experiments such as KamLAND-ZEN [66] and EXO [69]. Some results from these experiments are summarized below.

EXO-200

EXO-200 is a liquid xenon time projection chamber that uses $\sim 81\%$ enriched ^{136}Xe simultaneously as source and detector [70]. This 200 kg detector is installed at the Waste Isolation Pilot Plant (WIPP) near Carlsbad, New Mexico. The experiment was designed to attain sensitivity to Majorana neutrino masses of $\sim 100 \text{ meV}$. Additionally, it was meant to serve as a prototype for designing a ton-scale detector that would be sensitive to Majorana neutrino masses of $\sim 10 \text{ meV}$. Phase I of EXO-200 consisted of 150 kg enriched LXe and it was the first to observe the $2\nu\beta\beta$ decay of ^{136}Xe [79]. Data collected during this phase was equivalent to 100 kg.yr exposure establishing a limit on the $0\nu\beta\beta$ half life of ^{136}Xe to be $< 1.1 \times 10^{25} \text{ yr}$ at 90% CL corresponding to a limit on the neutrino mass of 0.2-0.4 eV [69,81]. As part of Phase II, EXO-200 has improved its resolution and aims to run for 3 years to attain a sensitivity of $T_{1/2}^{0\nu} > 5.7 \times 10^{26} \text{ yr}$ at 90% C.L. or the equivalent of $\langle m_{\beta\beta} \rangle < 0.09 \text{ eV}$. Extensive R&D is being conducted currently to implement barium tagging in nEXO [82,83], which is the upgrade to EXO-200.

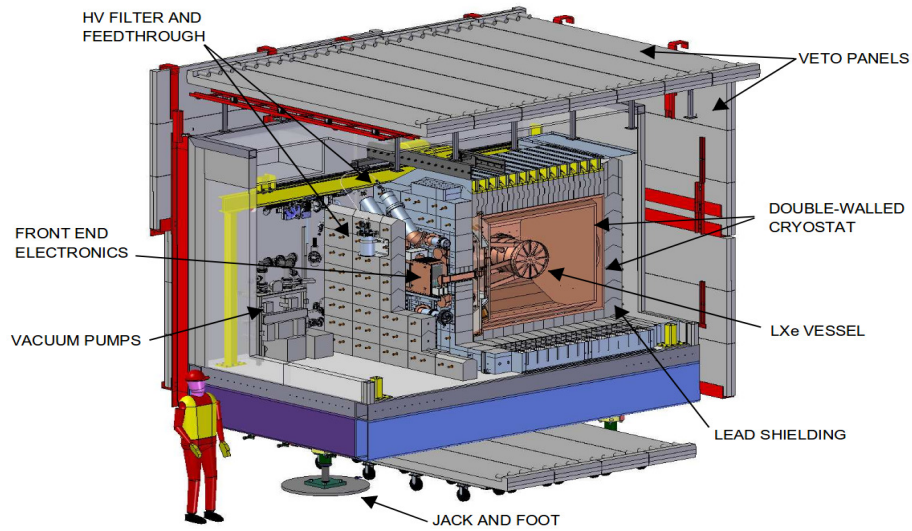


Figure 1.5: Cutaway view of the EXO-200 setup [70]

KamLAND-ZEN

KamLAND-ZEN [66] is an upgrade of the Kamioka Liquid Scintillator Antineutrino Detector (KamLAND) [84] that was originally designed to study the reactor antineutrino flux. KamLAND-ZEN, world's largest liquid scintillator detector is located in the Kamioka mine in Japan. As shown in Fig. 1.6, enriched xenon ($\sim 91\%$ ^{136}Xe) dissolved in a liquid scintillator (composed of 1000 metric tons of mineral oil, benzene, and fluorescent chemicals) is filled inside a 3.08 m balloon placed at the center of the original KamLAND detector [67]. The inner balloon is surrounded by 1000 ton ultra pure liquid scintillator that acts as a shield. KamLAND-ZEN recently completed Phase II of data taking corresponding to an exposure of 504 kg.yr of ^{136}Xe . They report a limit on the half life ^{136}Xe $0\nu\beta\beta$ decay of $T_{1/2}^{0\nu\beta\beta}(^{136}\text{Xe}) > 1.07 \times 10^{26}$ yr at 90% CL that translates to $m_{\beta\beta} < (61 - 165)$ meV for light Majorana neutrinos [66]. To date, this is the most stringent limit on light Majorana neutrino masses. KamLAND-ZEN is now in the process of upgrading to 800 kg of enriched Xe. This will increase the sensitivity of the experiment to the region $\langle m_{\beta\beta} \rangle < 50$ meV. KamLAND-ZEN would thus be the first $0\nu\beta\beta$ experiment that probes the inverted mass hierarchy region [66,67] as shown in Fig. 1.7.

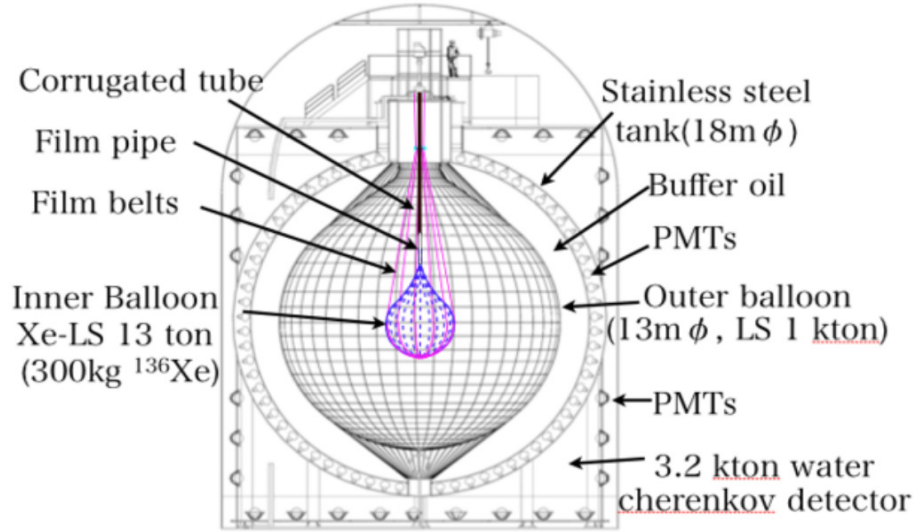


Figure 1.6: Schematic representation of the KamLAND-ZEN detector. At the center of the detector is the 3.08 m balloon filled with enriched ^{136}Xe [68].

1.6.1 Information on ^{136}Cs intermediate states

As shown in Fig. 1.2, the intermediate nucleus in the $\beta\beta$ decay of $^{136}\text{Xe} \rightarrow ^{136}\text{Ba}$ is the odd-odd ^{136}Cs nucleus. Until 2002, the only excited state known in ^{136}Cs was the 8^- isomeric state [85]. It was only in 2011, that the $^{136}\text{Xe}(^3\text{He}, t)$ charge exchange reaction was used to produce a large number of 1^+ states in ^{136}Cs [48, 86] and further obtain the integrated $B(GT)$ value from the reaction. This measurement was done using the Grand Raiden Spectrometer at the Research Center for Nuclear Physics (RCNP) in Japan. The tritons were measured close to 0° and a multipole decomposition method was used to identify the 1^+ states in ^{136}Cs . The spectrum from this experiment (shown in Fig. 1.8) was limited by an energy resolution of ~ 40 keV. Moreover, the charge exchange reaction is highly selective producing mostly 1^+ states. Nevertheless, this experiment provided the only available information of the energy spectrum in ^{136}Cs until a recent experiment studied other higher spin states [86, 87].

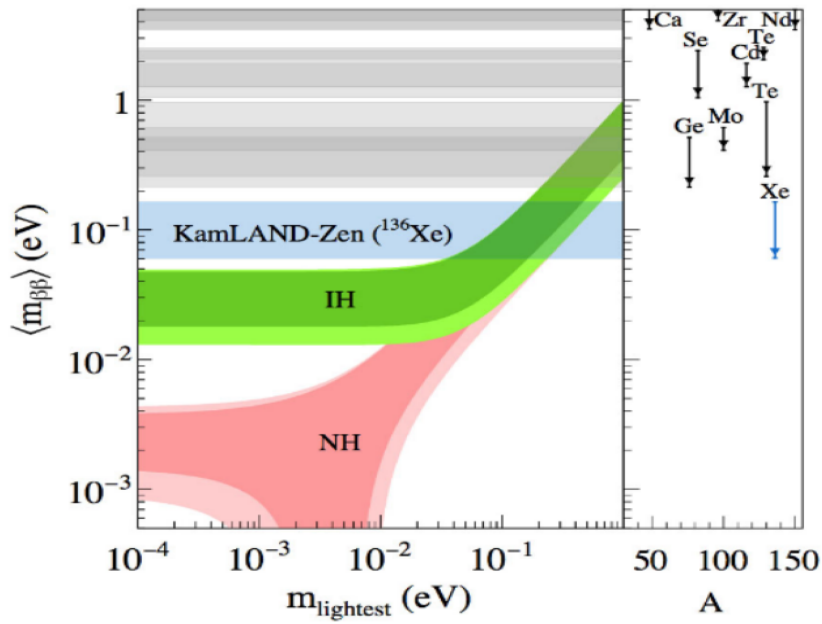


Figure 1.7: $\langle m_{\beta\beta} \rangle$ as a function of the lightest neutrino mass. The shaded regions for the normal hierarchy (NH) and the inverted hierarchy (IH) are the current limits set by neutrino oscillation experiments. The horizontal blue band is the current 90% C.L. limits on $\langle m_{\beta\beta} \rangle$ set by the KamLAND-Zen experiment [66]. Currently, KamLAND-ZEN provides the most stringent limit on the masses of light Majorana neutrinos.

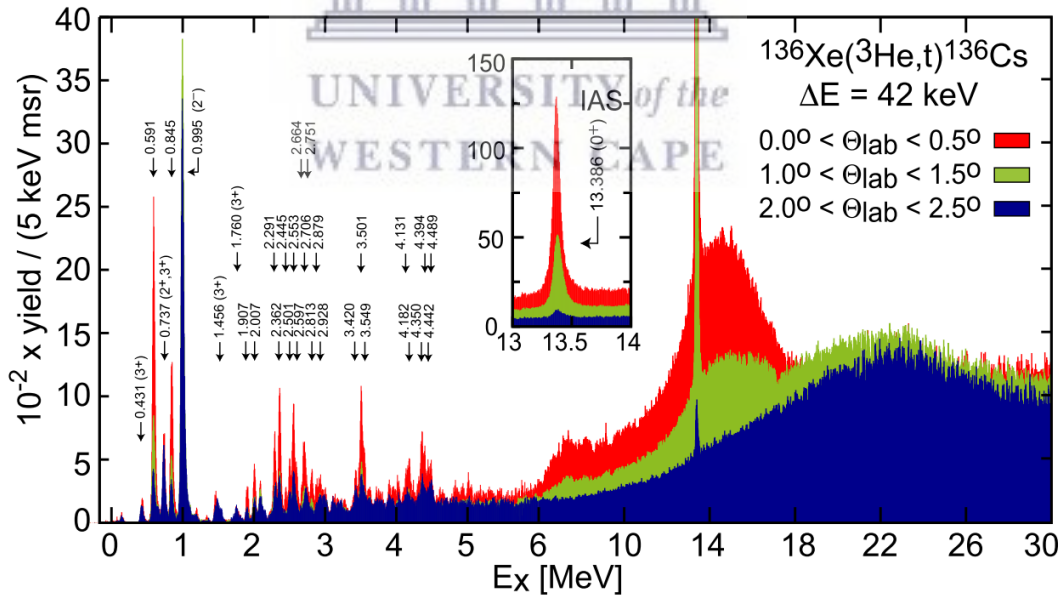


Figure 1.8: Triton spectrum from the $^{136}\text{Xe}(^3\text{He}, t)^{136}\text{Cs}$ reaction, observed with the the Grand Raiden Spectrometer at RCNP. Figure extracted from Ref. [48].

Recent pnQRPA calculations have suggested that the 1^- , 2^\pm , 3^+ , 4^+ states in ^{136}Cs could contribute significantly to the ground state to ground state transition and 0^+ , 1^+ , 2^\pm to the ground state to first excited state transition [88].

In light of the above, a high resolution measurement of states in ^{136}Cs is a timely requirement.



2 | Direct Nuclear Reactions as a Probe of Nuclear Structure

I am now convinced that theoretical physics is actually philosophy

Max Born

Since this work aims to study the structure of ^{136}Ba and ^{136}Cs nuclei using the $^{138}\text{Ba}(p, t)$ and $^{138}\text{Ba}(d, \alpha)$ two-nucleon transfer reactions, I begin this chapter with a brief description of general scattering theory. This is followed by an explanation of the distorted wave method used in the analysis of nuclear reactions. The chapter concludes with a discussion on the use of direct two-nucleon transfer reactions to study nuclear structure, particularly in the context of pairing correlations.

In a standard nuclear reaction, a beam of accelerated particles (a) strikes the target (A) at rest resulting in a number of different possible nuclei. This can be denoted as,



Depending on the energy in the center of mass frame and impact parameter of the incident particle, different types of nuclear reactions can occur. Simplest of these is the *elastic scattering* of the projectile a by the target A with no change in the internal configuration of the target and projectile ($b = a$ and $B = A$). A slight variation of elastic scattering process is the *inelastic scattering*, where the projectile or target is excited ($b = a^*$ or $B = A^*$). A nuclear reaction occurs when $A \neq B$. When the projectile makes glancing collisions with the target nuclei, energy is exchanged between few nucleons of the interacting nuclei.

In such *direct* reactions, the initial and final states of the nuclei are very similar and the reaction usually occurs on a very short time-scale (approximately the time required for the projectile to pass through the target nucleus). A *compound* nuclear reaction on the other hand occurs at relatively longer time scale. In this case, the projectile interacts with a larger number of nucleons within the target nucleus resulting in the energy being shared between many nucleons. The reaction products are independent of the initial states and depend only on the energy of the compound nucleus formed in the process.

2.1 General non-relativistic scattering theory

For a general nuclear reaction the wavefunction $\Psi_{initial}$ describing the initial state of the system [89] is given by

$$\Psi_{initial} = A_0 e^{i(\vec{k}_\alpha \cdot \vec{r}_\alpha)} \psi_a \psi_A, \quad (2.2)$$

where ψ_a and ψ_A are the wavefunctions of the projectile and target, r_α is relative separation between the centers of mass of a and A , k_α is the wave number and A_0 is the amplitude of the incident wave, which is related to the flux of the beam. At large distances from the target ($kr \gg 1$), the final state wavefunction contains the summed scattered waves for each reaction channel β , as well as the incident wave

$$\Psi_{final} \stackrel{kr \gg 1}{\approx} A_0 \left[e^{i(\vec{k}_\alpha \cdot \vec{r}_\alpha)} \psi_a \psi_A + \sum_{\beta} \frac{e^{i(\vec{k}_\beta \cdot \vec{r}_\beta)}}{r_\beta} f_\beta(\theta, \phi) \psi_b \psi_B \right]. \quad (2.3)$$

In the above, the scattered wave in each channel is a spherical wave [89]. Fig. 2.1 shows a schematic representation of this situation. Of particular interest in a nuclear reaction is the differential scattering cross section $\frac{d\sigma}{d\Omega}$, measured by a detector subtending a small solid angle $\Delta\Omega$ as shown in the figure. It is defined as

$$\left(\frac{d\sigma}{d\Omega} \right)_\beta = \frac{|\vec{j}_\beta|}{|\vec{j}_\alpha|} = \frac{v_\beta}{v_\alpha} |f_\beta(\theta, \phi)|^2, \quad (2.4)$$

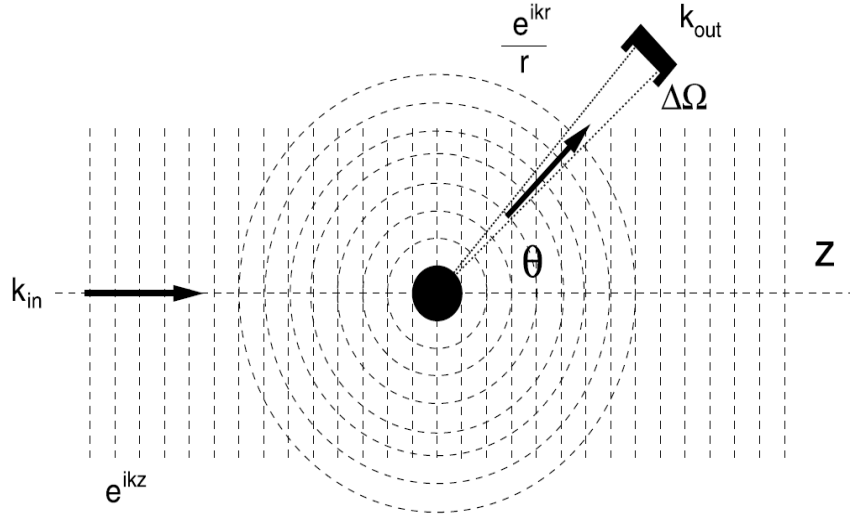


Figure 2.1: Quantum mechanical description of scattering. An incident plane wave results in a spherical scattered wave due to the scattering potential. For a detector placed at an angle θ with respect to the direction of the incident particles, $k_{out} = k_{\beta}$ is the momentum of the scattered wave in the reaction channel β while $k_{in} = k_{\alpha}$ is the incident momentum of $\Psi_{initial}$. Picture taken from Ref. [90].

where v_{β} is the relative velocity of the scattered particles from the residual nucleus and v_{α} is the velocity of the incident beam.

In the calculation of scattering cross sections from a spherically symmetric potential $V(r)$, the central force Hamiltonian commutes with the orbital angular momentum of the reaction, L^2 and L_z . In such a scenario L^2 , L_z and H must have a set of common eigenstates whose radial and angular parts can be separated as

$$\Psi(r, \theta) = \sum_{\ell=0}^{\infty} \sum_{m=-\ell}^{\ell} C_{\ell m} R_{\ell m}(kr) P_{\ell}(\cos \theta). \quad (2.5)$$

These wavefunctions must satisfy the boundary conditions that $V(r) \rightarrow 0$ as $r \rightarrow \infty$ and $\Psi \rightarrow 0$ as $r \rightarrow 0$. This reduces the radial part of the Schrödinger equation to a spherical Bessel differential equation whose solutions are of the form [90]

$$R_{\ell m}(k, r) \xrightarrow{r \rightarrow \infty} \frac{\sin(kr - \ell\pi/2)}{kr}, \quad (2.6)$$

for a fixed k , with different ℓ values. Additionally, the azimuthal symmetry eliminates all $m \neq 0$ combinations in Eq. (2.5). Due to this decomposition of the incoming plane waves (with fixed momentum $\hbar k$) into a set of infinite partial waves with different values of orbital angular momentum ℓ , the scattering amplitude $f(\theta)$ takes the form [90]

$$f(\theta) \sim \frac{1}{k} \sum_{\ell=0}^{\infty} (2\ell + 1) \sin \delta_{\ell} e^{i\delta_{\ell}} P_{\ell}(\cos \theta). \quad (2.7)$$

The quantity δ_{ℓ} is the phase shift of the scattered wave due its passage through a region of potential $V(r)$. Even though ℓ can take values up to infinity, depending on the energy of the incident beam and the range of the scattering potential only a few partial waves contribute significantly towards the cross sections [91].

It must be noted that Eq. (2.7) is the scattering amplitude for the special case of elastic scattering. For a general scattering process, the amplitude takes the form [89]

$$f(\theta, \phi)_{\beta} = \frac{1}{2ik_{\alpha}} \left(\frac{v_{\alpha}}{v_{\beta}} \right)^{1/2} \sum_{\ell=0}^{\infty} (2\ell + 1) [\eta_{\ell, \beta} - \delta_{\alpha, \beta}] P_{\ell}(\cos \theta), \quad (2.8)$$

where $\delta_{\alpha, \beta} = 0$ for non-elastic processes and $\eta_{\ell, \beta}$ are set of amplitudes that form the scattering S matrix $S_{\beta, \alpha}^{\ell}$. For complex nuclear systems the Hamiltonian that solves the Schrödinger equation for the scattering process can be separated into different parts that describe the internal degrees of freedom and the relative motion of the nuclei, so that

$$H_{tot} = H_a + H_A - \frac{\hbar^2}{2\mu_{\alpha}} \nabla_{\alpha}^2 + V_{\alpha}. \quad (2.9)$$

Here, V_{α} is the interaction potential between the two nuclei a and A leading to the final states in a particular exit channel. The internal wavefunctions ψ_a, ψ_A are solutions to their corresponding Schrödinger equations

$$\begin{aligned} H_a \psi_a &= E_a \psi_a \\ H_A \psi_A &= E_A \psi_A. \end{aligned} \quad (2.10)$$

The exact solutions to the full Schrödinger equation

$$H_{tot}\Psi_{tot} = E_{tot}\Psi_{tot} \quad (2.11)$$

need complete information about the internal structure of the nuclei, for which one has to solve the many-body Schrödinger equation. This is a nearly impossible task even with modern computing systems. However, approximation methods work really well in describing the nuclear wave functions accurately. Furthermore, if the interaction potential V_α is weak, the amplitude of the scattered waves in Eq. (2.3) are small.

To better understand the power of approximation methods we revert back to the Schrödinger equations for the scattering of a single particle by a general potential. It is written as

$$-\frac{\hbar}{2m}\nabla^2\chi(\vec{r}) + \lambda V(\vec{r})\chi(\vec{r}) = E\chi(\vec{r}), \quad (2.12)$$

which produces a continuous spectra of states. In the above equation, λ is a parameter that gives a measure of the strength of the potential $V(\vec{r})$, so that for $\lambda \rightarrow 0$ only free particle solutions exist. Eq. (2.12) reduces to the Helmholtz equation

$$(\nabla^2 + k^2)\chi(\vec{r}) = \lambda U(\vec{r})\chi(\vec{r}) \quad (2.13)$$

where

$$U(\vec{r}) = \frac{2m}{\hbar^2}V(\vec{r}). \quad (2.14)$$

This equation can be solved using the familiar Green's function techniques and other approximations even if the exact form of $U(\vec{r})$ is not known. The solution for outgoing waves is an integral equation for $\chi(\vec{r})$

$$\chi(\vec{r}) = e^{i\vec{k}\cdot\vec{r}} + \lambda \int d^3r' G(\vec{r}, \vec{r}') U(\vec{r}') \chi(\vec{r}'), \quad (2.15)$$

such that the boundary condition in Eq. (2.3) is still valid, i.e. as $r \rightarrow \infty$

$$\chi(\vec{r}) = e^{i\vec{k}\cdot\vec{r}} + f(\theta, \phi) \frac{e^{ikr}}{r}. \quad (2.16)$$

At large r Eq. (2.15) reduces to

$$\chi(\vec{r}) \approx e^{i\vec{k}\cdot\vec{r}} - \frac{\lambda}{4\pi} \frac{e^{ikr}}{r} \int d^3r' e^{-i\vec{k}'\cdot\vec{r}'} U(\vec{r}') \chi(\vec{r}'), \quad (2.17)$$

which in comparison to Eq. (2.16) results in [89]

$$f(\theta, \phi) = -\frac{\lambda}{4\pi} \int d^3r' e^{-i\vec{k}'\cdot\vec{r}'} U(\vec{r}') \chi(\vec{r}'), \quad (2.18)$$

where $\hbar\vec{k}$ is the momentum of the scattered particle in the direction of a detector placed at (θ, ϕ) . The above equation can be solved iteratively by a series expansion in terms of λ (assuming that λ is small). This series is called the Born Series, whose leading order correction is the first Born Approximation. The scattering amplitude in the first Born approximation is obtained by assuming $\chi(\vec{r}') = e^{i\vec{k}\cdot\vec{r}'}$, such that

$$f_{BA}(\theta, \phi) = -\frac{\lambda}{4\pi} \int d^3r' e^{-i\vec{k}'\cdot\vec{r}'} U(\vec{r}') e^{i\vec{k}\cdot\vec{r}'} \quad (2.19)$$

The next terms in the series, arise from the second part of

$$\chi(\vec{r}') = e^{i\vec{k}\cdot\vec{r}'} + \left[-\frac{\lambda}{4\pi} \int d^3r'' e^{-i\vec{k}'\cdot\vec{r}''} U(\vec{r}'') \chi(\vec{r}'') \right] \dots \quad (2.20)$$

shown in the parenthesis and so on, which converges for sufficiently small λ .

A more sophisticated version of the plane wave Born approximation is the distorted wave Born approximation (DWBA), which takes into account the distortion of the plane wave due to the potential. This is usually when the scattering field is large and cannot be used as a perturbation anymore. In such a case, it is possible to solve the scattering problem in a neighboring potential, which has the required weak effect on the scattering process.

Thus, the potential U can be written as the sum of two parts [89],

$$U = U_1 + U_2 \quad (2.21)$$

with U_2 being the small perturbation to the much stronger potential U_1 . Then in the DWBA, the scattering state solutions can be determined by the Born approximation

$$\chi(\vec{r}) = \chi_1(\vec{r}) - \frac{\lambda}{4\pi} \frac{e^{ikr}}{r} \int d^3r' e^{-i\vec{k}' \cdot \vec{r}'} U_2(\vec{r}') \chi_1(\vec{r}') \quad (2.22)$$

to describe the scattering of the incident ‘distorted’ wave $\chi_1(\vec{r})$. The latter is the outgoing solution of the Helmholtz equation for U_1

$$[\nabla^2 + k^2 - U_1(\vec{r})] \chi_1(\vec{r}) = 0 . \quad (2.23)$$

The total scattering amplitude for the two potentials U_1 and U_2 is [89]

$$f_{DWBA}(\theta, \phi) = -\frac{\lambda}{4\pi} \int d^3r' e^{-i\vec{k}' \cdot \vec{r}'} U_1(\vec{r}') \chi_1(\vec{r}') - \frac{\lambda}{4\pi} \int d^3r' \chi_1^-(\vec{r}')^* U_2(\vec{r}') \chi(\vec{r}') \quad (2.24)$$

where we assume $\chi(\vec{r}) \approx \chi_1(\vec{r})$ for a small perturbation. In the above equation, the wavefunction $\chi_1^-(\vec{r}')^*$ represents an incoming scattered wave. This should be apparent from observing the first term in the amplitude, where $e^{-i\vec{k}' \cdot \vec{r}'}$ represents an incoming plane wave.

Optical Model Potential

The distorting potential widely used in the DWBA analysis for single step direct reactions is the optical model potential. The underlying principle of the optical model is that when a light projectile is incident on a target nucleus the dominant mode of interaction is elastic scattering. Any inelastic scattering or nuclear reaction is treated as a perturbation to elastic scattering [89, 92]. For a given reaction channel α , the interaction potential is

written as

$$U(r) = V(r) + iW(r) , \quad (2.25)$$

with, a real part (V) for the elastic scattering amplitude and an imaginary part (W), which is the perturbation accounting for the non-elastic channels. The optical model potential is further divided into volume, surface, spin-orbit and Coulomb potential

$$U(r) = U_{volume}(r) + U_{surface}(r) + U_{spin-orbit}(r) + U_{Coulomb}(r) . \quad (2.26)$$

The first term in the optical model potential, $U_{volume}(r)$ is the volume Wood-Saxon (WS) term, that describes the interaction between the projectile and the nuclear-core of the target nucleus. The volume potential dominates when the energy of the projectile is large enough that it can probe through the target nucleus. It is defined by V_R and W_V , the real and imaginary well-depths respectively, $R_R = r_R A^{1/3}$ and $R_V = r_V A^{1/3}$, the geometrical radius defined in terms of A the target mass and a_R , a_V the diffuseness parameters

$$U_{volume}(r) = -V_R f(r, R_R, a_R) - iW_V f(r, R_V, a_V) , \quad (2.27)$$

where

$$f(r, R_i, a_i) = \frac{1}{1 + e^{(r-R_i)/a_i}} , \quad i = R, V \quad (2.28)$$

To account for the absorption due to the valence nucleons, the surface potential is defined in terms of a derivative Wood-Saxon. This potential peaks at the surface and is important at lower energies when the projectile does not probe much of the nuclear interior. This potential is generally defined by only the imaginary term

$$U_{surface}(r) = i4a_s W_s \frac{d}{dr} f(r, R_s, a_s) . \quad (2.29)$$

In the above, $R_s = r_s A^{1/3}$, a_s are the radii and diffuseness parameters of the potential and $f(r, R_s, a_s)$ has the same form as Eq. (2.28) except that $i = s$.

The spin-orbit interaction, $U_{spin-orbit}(r)$ is weaker compared to the volume and surface potential but becomes significant when polarization studies are performed. This potential

is also surface peaked since the nuclear core is assumed to be coupled to spin 0. Thus only the valence nucleons interact via the spin-orbit potential.

$$U_{spin-orbit}(r) = (V_{so} + iW_{so}) \left(\frac{\hbar}{m_{\pi}c} \right)^2 \frac{1}{r} \frac{d}{dr} f(r, R_{so}, a_{so}) (2\vec{L} \cdot \vec{s}) . \quad (2.30)$$

The factor $(\hbar/m_{\pi}c)^2 \approx 2.0$ is the square of the reduced Compton wavelength of the pion. As in the previous two cases, $R_{so} = r_{so}A^{1/3}$ is the radius and a_{so} is the diffuseness of the spin-orbit potential. Additionally, for charged particles the optical model potential also includes the Coulomb term that can be approximated as the potential of a uniformly charged sphere with radius $R_c = r_cA^{1/3}$,

$$U_{Coulomb}(r) = V_C(r) = \begin{cases} \frac{Z_1 Z_2 e^2}{2R_c} \left[3 - \left(\frac{r}{R_c} \right)^2 \right] & r \leq R_c \\ \frac{Z_1 Z_2 e^2}{r} & r > R_c \end{cases} \quad (2.31)$$

where Z_1 , Z_2 are the atomic numbers of the projectile and target and e is the elementary charge. Combining Eqs. (2.27), (2.29), (2.30) and (2.31) the optical model potential is written as

$$U(r) = -V_R f(r, R_R, a_R) - iW_v f(r, R_V, a_V) + i4a_s W_s \frac{d}{dr} f(r, R_s, a_s) + (V_{so} + iW_{so}) \left(\frac{\hbar}{m_{\pi}c} \right)^2 \frac{1}{r} \frac{d}{dr} f(r, R_{so}, a_{so}) (2\vec{L} \cdot \vec{s}) + V_C(r) . \quad (2.32)$$

In the above equations the well-depths (V_i , W_i) are specified in MeV and the radii (R_i) and diffuseness (a_i) parameters are defined in femtometers (fm). To obtain the parameters of the potential (V_i , W_i , r_i , a_i where $i = R, V, s, so$ and C) the phenomenological form in Eq. (2.32) is fit to experimental elastic scattering data for a large number of different targets and incident projectile energies. The result is a ‘global’ set of optical model potential parameters that are applicable for a wide range of nuclei and beam energies.

2.2 Two Nucleon Transfer Reactions

Information about the reaction mechanism and nuclear structure is embedded in the transition matrix element $T_{\beta\alpha}$ which in the DWBA formalism can be written as [93,94]

$$T_{\beta\alpha} = \int d^3r_\beta \int d^3r_\alpha \chi^{(-)*}(\vec{k}_\beta, \vec{r}_\beta) \langle \psi_b \psi_B | V | \psi_a \psi_A \rangle \chi^{(+)}(\vec{k}_\alpha, \vec{r}_\alpha) . \quad (2.33)$$

In the above equation, α and β represent the incoming and outgoing channels, r_α and r_β are the relative coordinates, $\chi^{(+)}, \chi^{(-)}$ are the incoming and outgoing distorted waves (described by the notations χ_1^-, χ_1^+ in Sect. 2.1) generated by the optical potential. In the asymptotic limit these distorted waves reduce to Eq. (2.16). When the initial or final projectiles have spin, the distorted waves become matrices in spin space

$$\chi^{(\pm)}(\vec{k}, \vec{r}) \eta_{s,m} = \sum_{m'} \chi_{m,m'}^{(\pm)}(\vec{k}, \vec{r}) \eta_{s,m'} , \quad (2.34)$$

where $\eta_{s,m}$ are spin functions and the partial wave expansion for $\chi_{m,m'}^{(\pm)}(\vec{k}, \vec{r})$ is

$$\chi_{m,m'}^{(\pm)}(\vec{k}, \vec{r}) = \frac{\sqrt{4\pi}}{kr} \sum_{J,L} i^L \sqrt{2L+1} \chi_{JLs}(k,r) (LsMm | JM') \begin{matrix} (LsM' - m' m' | JM') Y_L^{M'-m}(\vec{r}) d_{0,M'-m'}^L(\vec{k}) . \end{matrix} \quad (2.35)$$

In the above equation, $d_{0,M'-m'}^L$ are rotation functions for integer spin [93, 95] and the symbol $(...|...)$ represent the Clebsch-Gordan coefficients. The radial part of the distorted waves satisfy the Schrödinger equation

$$\left(\frac{d^2}{dr^2} + k^2 - \frac{L(L+1)}{r^2} - \frac{2\mu}{\hbar^2} U(r) \right) \chi_{JLs}(k,r) = 0 , \quad (2.36)$$

where $U(r)$ is the optical potential described in the previous section. The quantity $\langle \psi_b \psi_B | V | \psi_a \psi_A \rangle$ in Eq. (2.33) contains the nuclear structure information and can be writ-

ten as [93, 96]

$$\begin{aligned}
\langle \psi_b \psi_B | V | \psi_a \psi_A \rangle &\equiv \langle J_B M_B s_b m_b | V | J_A M_A s_a m_a \rangle \\
&= \sum_{lsj} i^{-l} B_{lsj} (J_A j M_A M_B - M_A | J_B M_B) (s_a s_b m_a - m_b | s_a m_a) \\
&\times (l s m m_a - m_b | j M_A - M_B) f_{lsj}(r) \delta \left(r_b - \frac{A}{B} r_a \right) Y_l^m(\vec{r})^* ,
\end{aligned} \tag{2.37}$$

In Eq. (2.37), B_{lsj} is a measure of the interaction strength and f_{lsj} contains details of the reaction model. For the case of two-nucleon pick-up reaction (e.g (d, α) , (p, t)) for unpolarized projectile and target, the differential cross section in terms of the $T_{\beta\alpha}$ is [97]

$$\left(\frac{d\sigma}{d\Omega} \right) = \frac{\mu_\alpha \mu_\beta}{(2\pi\hbar^2)^2} \frac{k_\beta}{k_\alpha} \frac{1}{(2J_A + 1)(2s_a + 1)} \sum_{M_A M_B m_a m_b} |T_{\beta\alpha}|^2, \tag{2.38}$$

where μ_α , μ_β are the reduced masses in the incoming and outgoing channel. Combining Eq. (2.33), (2.37) and (2.38) and following the procedure outlined in Ref. [91] and [94], the cross section can be expressed as

$$\left(\frac{d\sigma}{d\Omega} \right) \propto \sum_{LSJT} C_{ST}^2 \sum_M \left| \sum_N G_{NLSJT} B_{NL}^M \right|^2, \tag{2.39}$$

where

$$C_{ST} = (T_a T_{z_a} T T_Z | T_b T_{z_b}) b_{ST}, \tag{2.40}$$

is specific to the reaction type. The L, S, J and T quantum numbers represent the orbital, spin, total angular momentum and the isospin of the transferred pair. The b_{ST} factor gives the weight by which the spin-singlet ($S = 0$) and spin-triplet ($S = 1$) states of the transferred nucleon pair contribute towards the transfer cross section [94].

As evident in Eq. (2.39), the two-nucleon transfer cross sections cannot be factorized independently into a nuclear structure part (G_{NLSJT}) and a reaction kinematics part (B_{NL}^M), which is otherwise possible for a single-nucleon transfer reaction. This happens because different two-nucleon configurations (characterized by the principal quantum number N and weighted by the structure factor G_{NLSJT}) contribute coherently to the transfer cross

section. This makes the cross sections sensitive to pair correlations in the nuclear wavefunctions and are therefore used to study the pairing properties of nuclei, something that cannot be achieved using single-nucleon transfer reactions.

In Eq. (2.39), B_{NL}^M contains information on all aspects of the reaction, i.e. mechanism and kinematics. Since no nuclear structure information is embedded in B_{NL}^M , it represents the probability of transferring a structureless nucleon pair between the target and projectile [91]. The second term G_{NLSJT} is called the structure amplitude and is analogous to the spectroscopic factor of a single-nucleon transfer reaction. It contains all the nuclear structure information of the transferred particle as well as the initial and final nuclei with mass numbers A and $A+2$. G_{NLSJT} can further be expressed as a product of three overlap integrals [91],

$$G_{NLSJT} = g \sum_{\gamma} \beta_{\gamma LSJT} \langle n\lambda, N\Lambda; L | n_1 l_1, n_2 l_2; L \rangle \Omega_n, \quad (2.41)$$

where $\gamma \equiv (n_1, l_1, j_1; n_2, l_2, j_2)$ represents the internal quantum numbers for the individual nucleons and the factor g depends on the symmetry of the nuclear wavefunction

$$g = \begin{cases} 1, & \text{if } n_1 l_1 j_1 = n_2 l_2 j_2 \\ \sqrt{2}, & \text{otherwise} \end{cases} \quad (2.42)$$

The first overlap integral $\beta_{\gamma LSJT}$ in Eq. (2.41) is called the parentage factor. For the (d, α) or (p, t) pick up reactions, it describes the degree to which the ground state of the $(A+2)$ nucleus (^{138}Ba in this case) can be described as the state in the ^{136}Cs (^{136}Ba) formed in the reaction plus a deuteron (neutron pair). More precisely [91]

$$\beta_{\gamma LSJT}(J_A J_B) \propto \int [\psi_{J_A, T_A}^*(A') \times \phi_{\gamma LSJT}^*(r_1, r_2)]_{J_B T_B} \psi_{J_B T_B}(A', r_1, r_2) dA' dr_1 dr_2, \quad (2.43)$$

where A' denotes the number of nucleons in the target, ψ_{J_A, T_A} , ψ_{J_B, T_B} are the wavefunctions of the target and residual nuclei, $\phi_{\gamma LSJT}(r_1, r_2)$ characterizes the wavefunction of the transferred pair and the square bracket denotes vector coupling. β can be calculated exactly if the wavefunctions ψ_A, ψ_B for the target and residual nucleus are known.

The $\langle n\lambda, N\Lambda; L | n_1 l_1, n_2 l_2; L \rangle$ term, is the overlap between the spatial parts of the wave-

function of the two nucleon treated individually (with quantum numbers n_1l_1, n_2l_2) with wavefunction of the two nucleons treated as a cluster. The quantities λ, Λ are the orbital angular momenta of the relative and center-of-mass motions of the cluster and n, N their principal quantum numbers. A general assumption of two-nucleon transfer reactions is that the nucleon pair within the cluster has no relative angular momentum, i.e. $\lambda = 0$ and the pair is said to be in a relative ‘s-state’ motion [91]. Therefore, in a direct, single-step two-nucleon transfer reaction $\Lambda = L$ and the differential cross sections are sensitive to the transferred orbital angular momentum L [94].

The final Ω_n term is the overlap between the relative motion of the two nucleons in the cluster $\phi_{n\lambda}$ with the relative motion of the pair in the ejectile (alpha or triton) that picks up the two nucleons. Consequently, the only configurations that will contribute significantly towards two-nucleon transfer cross sections are the ones that are similarly correlated as the transferred pair. Thus two-nucleon transfer reactions can provide a critical test of nuclear structure wavefunctions.

2.2.1 Two nucleon transfer reaction as a probe to study nuclear structure

Two-nucleon transfer reactions are classified into two distinct categories based on whether the transferred nucleons are identical or not. When identical, the two nucleons couple to total spin $S = 0$ and isospin $T = 1$. For example, (p, t) reactions that transfer a pair of neutrons between the projectile and target belong to this category. In the second kind, the neutron-proton pair can couple to either $S = 0, T = 1$ or $S = 1, T = 0$. As the deuteron is found predominantly in the $S = 1$ (spin-triplet) state, in the (d, α) reaction the transferred ‘deuteron’ pair couples to $S = 1, T = 0$. The (p, t) and (d, α) reactions have different qualitative properties which allows to study different aspects of the nuclear structure. Thus the two reactions are discussed below.

2.2.2 The (d, α) reaction

Spectroscopic information on odd-odd nuclei such as ^{136}Cs are quite scarce due to the experimental challenges posed by the need of suitable targets to excite these nuclei using single-nucleon transfer reactions and the large density of states in such odd-odd nuclei. Direct, single-step (d, α) reactions excite proton-neutron hole $(\pi^{-1}\nu^{-1})$ states and are particularly useful on closed shell nuclei. As mentioned above, the (d, α) reaction can be modeled as a deuteron transfer between the target and projectile in a relative $\ell = 0$, $S = 1$ and $T = 0$ state. Thus the final states populated in $^{138}\text{Ba}(d, \alpha)^{136}\text{Cs}$ would follow the selection rule

$$|J_i - J| \leq J_f \leq |J_i + J| , \quad (2.44)$$

where $J = L + S$ is the total angular momentum transferred by the deuteron and J_i is the total angular momentum of the target. The above selection rules for a $J^\pi = 0^+$ target further reduces to,

$$|L - 1| \leq J_f \leq |L + 1| . \quad (2.45)$$

Owing to the additional rule of parity conservation

$$(\pi_i)(\pi_f) = (-1)^L , \quad (2.46)$$

the natural parity states are populated via

$$J_f = L \quad (2.47)$$

and unnatural parity states can be populated by two different orbital angular momenta transfers

$$J_f = L \pm 1 . \quad (2.48)$$

In addition to the above selection rules the (d, α) reaction requires that $J + S = \text{even}$ if the neutron and proton are transferred from (or to) the same state [91]. Thus the (d, α) cross section to these states would provide a measure of the configuration mixing in the

initial and final wavefunctions.

2.2.3 The (p, t) reaction

This two-neutron transfer reaction is ideal for measuring the spin-singlet ($S = 0$) correlations in the nuclear wavefunctions. Direct (p, t) reactions are ideally suited to study nuclear states with excited 2-neutron hole configurations. As in the case of the (d, α) reaction, the (p, t) reaction too follows the $|J_i - J| \leq J_f \leq |J_i + J|$ selection rule. For a 0^+ target, coupled with the $S = 0$ criterion, the states populated in this reaction follow the simplified selection rules,

$$\begin{aligned} J_f &= L \\ (\pi_i)(\pi_f) &= (-1)^L \end{aligned} \tag{2.49}$$

thereby restricting the direct single-step mechanism to populating only natural parity states. Of all the states populated in the (p, t) reaction, the $L = 0$ transfer is a very specific probe of nuclear collectivity. As evident from Eq. (2.49), the $L = 0$ transfer populates the $J^\pi = 0^+$ states in the residual nucleus. In even-even nuclei, these states are the result of coupling two identical nucleons to spin $J = 0$ and isospin $T = 1$. These 0^+ states contain a large number of two-particle configurations brought about by the pairing interaction. This effect is pronounced in spherical and deformed nuclei far from the shell closures and manifests in (p, t) reactions as a strong $L = 0$ transition to the ground state, while populating the excited 0^+ states much more weakly [98, 99].

In some situations the (p, t) reaction populates excited 0^+ states with a significant strength compared to the $L = 0$ transfer to the ground state. This splitting of strength occurs typically in nuclei in the vicinity of the closed shells where the pairing interactions is weaker than the shell gap as a result of which, the orbitals above and below the shell gap mix separately resulting in two different correlated 0^+ states. A large strength to excited 0^+ states would also be observed in cases where there is a sudden change in deformation between the target and residual nuclei. In this situation the strong population of the excited 0^+ state results from the large overlap in the wavefunctions of the excited state

in the residual nucleus with the ground state of the target nucleus. This for instance has been observed in (p, t) and (t, p) reactions on samarium isotopes, where a change from spherical to deformed shape occurs around the neutron number $N = 88$ [98, 100, 101]. A systematic study of the $L = 0$ transitions in two-neutron transfer reactions on neighboring isotopes can shed light on the nature of excited 0^+ states [99].

2.3 Pairing interactions and two-neutron transfer reactions

Strong signatures of nuclear pairing are evident along the nuclear landscape, for instance, in the odd-even staggering of nuclear binding energies and single nucleon separation energies or in the relatively high excitation energy of the first excited state in even-even nuclei compared to the neighboring odd-odd and odd-even nuclei. Theoretical understanding of the pairing interactions were initiated in the early 1960's by the work of Bohr, Mottelson and Pines [102] following the BCS theory of superconductivity in metals [103]. Similar to the mechanism that generates the Cooper pairs in superconductors, the short-ranged, strong and attractive nuclear pairing interaction couples the valence nucleons in time-reversed orbits to integral spins $S = 0, 1$ depending on the isospin ($T = 1, 0$) of the coupled pair. As the nuclear force does not distinguish between the neutrons and protons, the isospin symmetry of the pairing Hamiltonian leads to two kinds of pairing interactions, the isoscalar and isovector interaction. The isovector interaction couples the nucleons into states with $S = 0$, $T = 1$ and isospin projections $T_z = 1, 0, -1$ corresponding to a neutron-neutron, neutron-proton and proton-proton pair, while the isoscalar interaction leads to a $S = 1, T = 0$ proton-neutron pair. Pairing correlations in nuclei manifest largely via the isovector interaction, as the isoscalar proton-neutron interaction is plagued by the requirement that both the valence neutron and proton should be in the same shell-model orbits [104, 105].

Even though the pairing energy is small compared to the binding energy of the nucleus, the pairing interaction contributes significantly towards nuclear collectivity. In nuclei far

from closed shells, the pairing interaction mixes the single particle orbits, resulting in the ground state of an even-even nucleus being a BCS (superfluid) condensate of a large number of nucleon pairs coupled to $J^\pi = 0^+$. A remarkable feature of this pairing mode is observed with systematic studies along an isotopic (isotonic) chain, revealing a nearly constant energy difference between the ground state and the first 2^+ state [106,107]. Deformed nuclei with open proton or neutron shells are also known to exhibit properties of pairing condensates [106]. In nuclei around closed shells, the energy gap between single particle states at shell closures is much larger than the pairing energy. This causes the single particle states above and below the shell gap to mix separately and thus form different correlated 0^+ states above and below the shell gaps.

These BCS correlated states can be probed by two-particle transfer reactions where the spatial correlation of the transferred pair matches that of the nucleus being probed. For instance the (p, t) and (t, p) reactions that transfer two neutrons between the projectile and target, can probe the $T_z = 1$ component of the isovector pairing interaction and the $({}^3\text{He}, n)$ reaction as it transfers a proton pair will be sensitive to the $T_z = -1$ component. The $({}^3\text{He}, p)$, $(p, {}^3\text{He})$ reactions on the other hand, can transfer the $n - p$ pair in a $S = 0, T = 1$ or $S = 1, T = 0$ state and is sensitive to the $T_z = 0$ component of both, the isovector and isoscalar interaction. BCS correlations in these reactions are identified by a strong $L = 0$ transition to the ground state, with the excited 0^+ states being populated rather weakly. The enhanced cross-section to the ground 0^+ state in two-particle transfer reactions is a direct manifestation of the pairing correlations in this state. The reaction mechanism favors not only the direct transfer of a single spatially correlated pair but also the successive addition or removal of two single uncorrelated nucleons [106]. Thus in the case that the ground state had strong correlations the dominant contribution would be from the single-step mechanism. Conversely, if the nucleons were not correlated, the sequential two-step mechanism would dominate. Classic examples of nuclei exhibiting this superfluidity are the Sn isotopes.

2.4 Implication of pairing correlations on neutrinoless double beta decay matrix elements

Assumptions in the pairing structure of the initial and final nuclei play a significant role in the magnitude of calculated neutrinoless double beta decay matrix elements. These calculations involve a sum of pair creation ($\hat{P}_{J^\pi}^\dagger$) and annihilation operators (\hat{P}_{J^π}) that converts a neutron pair coupled to J^π in the parent nucleus into a proton pair in the final nucleus [32, 98]

$$M^{0\nu} \sim \sum_{J^\pi} \hat{P}_{J^\pi}^\dagger \hat{P}_{J^\pi}. \quad (2.50)$$

The overlap of the resulting state obtained from this operator and the ground state of the final $0\nu\beta\beta$ nucleus gives the magnitude of J^π contribution to the NME [108]. Thus precise information about the pairing correlations and ground state properties of these $\beta\beta$ -decay nuclei are crucial for testing the matrix element calculations.

Furthermore, the dominant contribution to the Gamow-Teller part of the NME in both the QRPA and ISM calculations result from the nucleon pairs coupled to $J = 0$, while the contributions from the $J > 0$ pairs is either negligible or have an opposite sign which will result in a reduction of the NME [32, 109]. Thus, if the decay occurs between two superfluid states, the contribution from the $J^\pi = 0^+$ states will dominate, resulting in a relatively larger value of $M^{0\nu}$ for the decay. However, in reality, there are no $\beta\beta$ pairs where the parent as well as grand-daughter are superfluid nuclei and thus the contributions arising from the decaying pair coupled to $J > 0$ needs to be considered as well. In the remainder of this section I discuss the effect of the pairing interactions on the NME in the generalized seniority regime. In the seniority structure, s defines the number of unpaired nucleons in the nucleus. Thus for $J = 0$, where there are no unpaired nucleons, $s = 0$. The existence of 2 unpaired nucleons ($s = 2$) can couple to form states with angular momenta $J = 2, 4, 6$ etc [110]. When the NME calculations are performed in a low seniority approximation ($s \leq 4$), only partial correlations in the nuclear wavefunctions are considered. This leads to an overestimation of the NME [32, 109] and

can cause a significant error, especially when the initial and final states have different deformation. For instance, it has been illustrated in Ref. [98] for a hypothetical case of $A = 66$ mirror nuclei, that for a difference in deformation of ~ 0.06 between the initial and final nuclei, the NME reduces by a factor of ~ 3 . In highly deformed nuclei, the ground state wavefunction is dominated by high seniority components which leads to a seniority mismatch between the two nuclei and consequently a reduction in the matrix element. Thus experimental study of pair correlations in the double beta nuclei can also help in constraining the matrix element calculations, while simultaneously testing the nuclear models used [63]. One of the most significant example in this respect has been the (p, t) reactions on ^{76}Ge and ^{76}Se , where incorporating the results lead to a significant change in the calculated NME for the decay [63–65]. A series of experiments were followed to study the occupancies, vacancies and pairing properties of other $\beta\beta$ decay candidates, particularly in the $A = 76, 100, 130$ and 136 systems [111–119]. A short summary of the current status on pairing correlations in some of most relevant $0\nu\beta\beta$ decay candidates is discussed in the next section.

Status of pairing correlations in the $\beta\beta$ decay nuclei

As mentioned in Section 1.6, some of the most interesting neutrinoless double beta decay pairs are $^{48}\text{Ca} \rightarrow ^{48}\text{Ti}$, $^{76}\text{Ge} \rightarrow ^{76}\text{Se}$, $^{82}\text{Se} \rightarrow ^{82}\text{Kr}$, $^{100}\text{Mo} \rightarrow ^{100}\text{Ru}$, $^{130}\text{Te} \rightarrow ^{130}\text{Xe}$, $^{136}\text{Xe} \rightarrow ^{136}\text{Ba}$ and $^{150}\text{Nd} \rightarrow ^{150}\text{Sm}$. Pair transfer experiments performed on ^{76}Ge and ^{76}Se have shown that both, neutron and proton pairing correlations are similar in the initial and final nuclei and thus validating the BCS approximation in this $0\nu\beta\beta$ decay pair [116, 120]. In the $^{130}\text{Te} - ^{130}\text{Xe}$ pair the $(^3\text{He}, n)$ proton-pair adding reaction on $^{122-130}\text{Te}$ targets showed a significant strength ($\sim 20-40\%$) populating at least one excited 0^+ state. This breakdown is attributed to the shell closure at $Z = 64$ in these nuclei [121]. Further, a fragmentation of the neutron pair transfer strength is observed in the $^{100}\text{Mo}(p, t)$ as well as the $^{100}\text{Mo}(t, p)$ reactions [114, 122, 123], while $\sim 95\%$ of the (p, t) transfer strength leading to and from ^{100}Ru was observed in the ground state $L = 0$ transition [114]. There was no evidence of a similar fragmentation in the proton pair transfer strength [124]. This should not be

surprising since ^{100}Mo lies in a region of gradual shape change, while the ^{100}Ru nucleus is nearly spherical. Extensive literature on (p, t) and (t, p) reactions on the neodymium and samarium isotopes [125–128] show indications of breakdown in the BCS approximation for ^{150}Sm and ^{150}Nd owing to the onset of deformation at $N \sim 90$. Pair transfer reaction in these nuclei have resulted in strong population of excited 0^+ states, that are similarly deformed as ground state of the target nucleus.

For one of the most promising $\beta\beta$ candidates, $^{136}\text{Xe} \rightarrow ^{136}\text{Ba}$, no neutron-pairing correlations studies have been performed on either ^{136}Xe or ^{136}Ba [129] even though the xenon and barium nuclei are known to lie within a typical transitional region of the nuclear landscape [130–133]. However, (p, t) reactions leading to the lighter barium isotopes ($^{128}\text{--}^{134}\text{Ba}$) have observed strong population of at least one excited 0^+ state [134–138]. The only previous $^{138}\text{Ba}(p, t)^{136}\text{Ba}$ measurement that was performed was at $E_p = 52$ MeV [131] and not particularly sensitive to the $L = 0$ transfers due to the higher incident energy of the protons. In fact, the authors report strong excitations of the first 5^- and 7^- state in ^{136}Ba and the only 0^+ state reported in this work was the ground state. In contrast, the $^{136}\text{Ba}(t, p)$ reaction was performed at $E_t = 17$ MeV [139]. This experiment observed a strong excitation of the 3.61 MeV 0^+ state in ^{138}Ba . Additionally, a $(^3\text{He}, n)$ reaction on a ^{136}Xe and ^{138}Ba targets observed considerable ($\sim 10\%$) $L = 0$ strength to excited 0^+ states [140]. In light of the above, it is important to study the pairing properties of ^{136}Ba and ^{136}Xe . This thesis aims to address this issue by studying neutron pairing correlations in ^{136}Ba via the $^{138}\text{Ba}(p, t)$ reaction.

3 | Experimental Setup

Science walks forward on two feet, theory and experiment, but continuous progress is only made by the use of both.

Robert A Millikan

3.1 Overview of the Experiments

The data discussed in this thesis were obtained at the Maier-Leibnitz Laboratory (MLL) in Garching, Germany. The first run was performed in October 2014 when several new states in ^{136}Cs were observed for the first time using the $^{138}\text{Ba}(d, \alpha)$ reaction. We performed the second experiment in April 2016, to study pairing properties in ^{136}Ba via the $^{138}\text{Ba}(p, t)$ reaction. This chapter briefly summarizes the experimental facility and apparatus used to perform the measurements. An in-depth discussion on the data analysis follows in the next chapter.

3.2 Experimental Facility

The Maier-Leibnitz Laboratory (MLL) is situated on the joint campuses of Ludwig - Maximillians Universität (LMU) and the Technische Universität München (TUM) in Garching, Germany. At the heart of MLL is the 14 MV MP tandem Van de Graff accelerator, shown in Fig. 3.1, that can produce both polarized and unpolarized accelerated beams. The ions for acceleration are provided by a conventional Stern-Gerlach ion source [141]. The major components are the atomic beam source (ABS), an electron

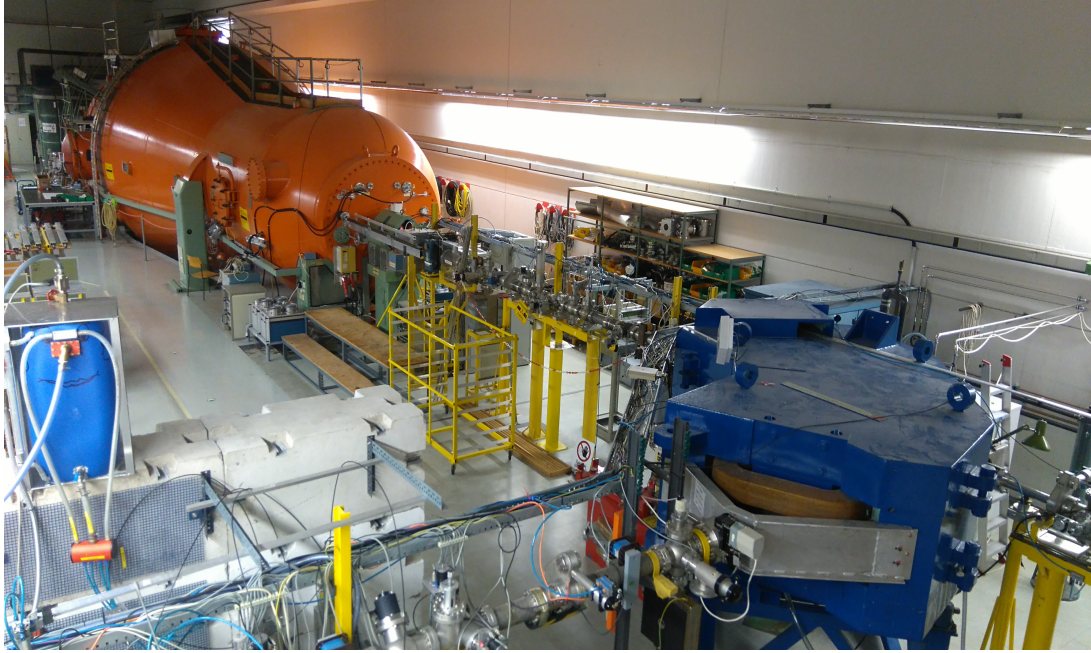


Figure 3.1: The tandem Van de Graaff accelerator hall at MLL. The tandem is shown in orange and the analyzing magnet is painted blue.

cyclotron resonance (ECR) chamber and a cesium vapor jet target. A vertical section of the ion source is shown in Fig. 3.2. Molecular hydrogen or deuterium gas injected into the ABS chamber is split into atomic hydrogen or deuterium by electron scattering inside a cold plasma. An atomic jet is created by allowing the gas to expand adiabatically into a vacuum chamber from an aluminum nozzle cooled to 80 K. From here the jet can be directed into the sextupole magnet system comprising of four Stern-Gerlach FeNdB permanent magnets for polarization or directly into the ECR unit for ionization. At this stage the ABS can provide beam intensities of 6.4×10^{16} atoms/s for hydrogen and 5×10^{16} atoms/s for deuterium [141]. The ionization is achieved in a two-step charge-exchange procedure. In the first step, the atomic beam of hydrogen or deuterium is singly ionized within an ECR-plasma with a few percent efficiency resulting in H^+ or D^+ ions. The positive beam is then transported to the cesium vapor jet target by two deceleration electrodes. Here the H^+ or D^+ ions pick up two electrons with an efficiency $> 30\%$, resulting in negatively charged H^- or D^- ions which are then directed into the tandem accelerator. A tandem accelerator is a two-stage Van de Graaff accelerator, which uses the same electrostatic field twice to accelerate the charged particles. Negative ions (H^- , D^-) from the

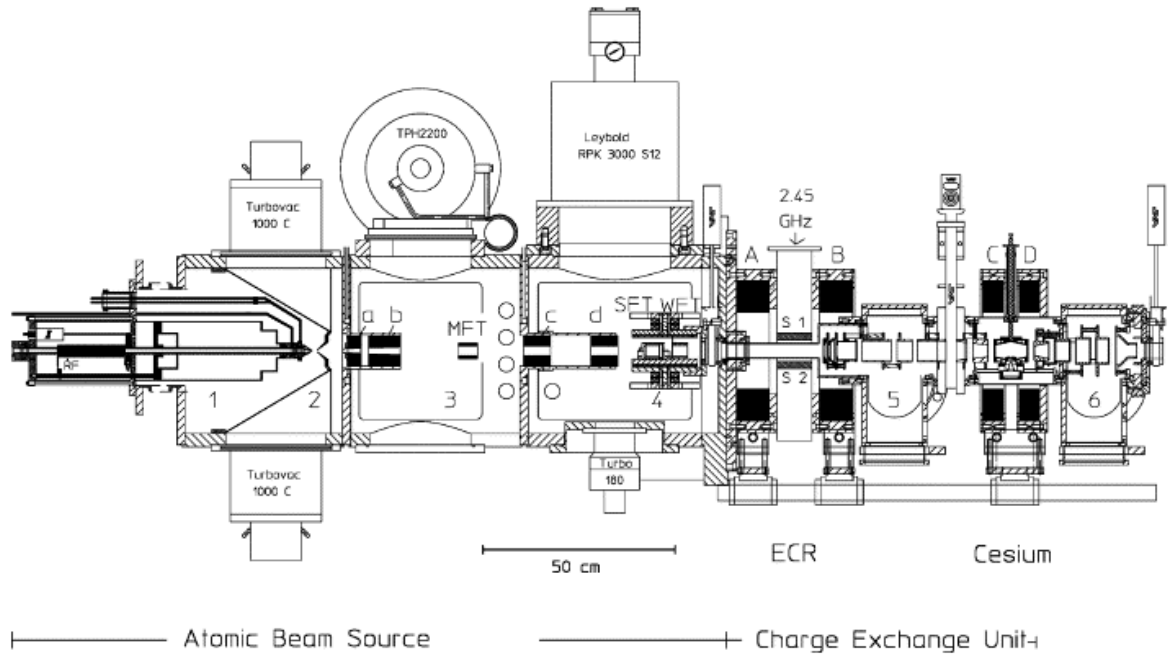


Figure 3.2: Schematic representation of the Stern-Gerlach ion source at the MLL. Adapted from Ref [141].

ion source entering the tandem are accelerated from the ground potential to a positive terminal voltage at center of the tank. At the center, these negatively charged particles encounter a carbon foil that strips off the electrons making them positively charged (H^+ , D^+). These positively charged ions are then repelled away from the central positive potential thereby causing the second acceleration. The MLL tandem can (theoretically) be set to a maximum terminal voltage of 14 MV, but for the purpose of our experiments, the terminal voltages 11 and 11.5 MV were used to accelerate the deuterons and protons to 22 and 23 MeV respectively.

The accelerated protons or deuterons are then sent to the Q3D experimental hall through the 90° analyzing magnet (seen in blue in Fig. 3.1). The analyzing magnet selects and maintains the energy of the beam within a precision of $\Delta E/E \leq 10^{-4}$ with the help of a feedback loop placed downstream of the magnet. The feedback loop consists of a pair of slits that measures the beam current on either side. If the current on the left slit is greater than on the right, it means that the energy of the particles is less than the desired value. The terminal voltage on the tandem is then automatically increased to increase the acceleration and vice versa.

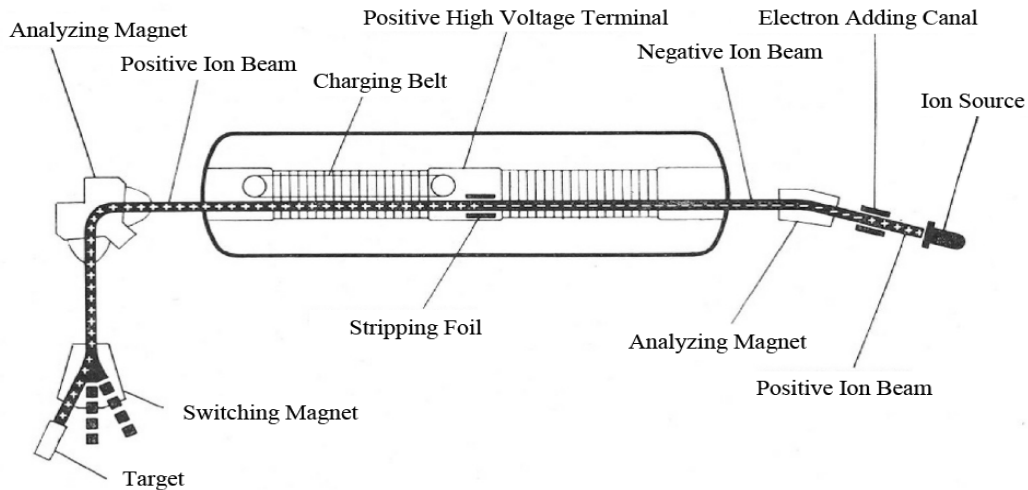


Figure 3.3: A schematic representation of the MP tandem accelerator used at MLL.

3.3 Q3D Magnetic Spectrometer

For our experiments, the reaction products were analyzed with a high-resolution magnetic spectrometer called the Q3D (Fig. 3.4). The principle working criterion of a magnetic spectrometer is the separation of the reaction products based on the differences in the curvature of the trajectory of charged ejectiles based on their momenta. The Q3D spectrometer has one quadrupole and 3 dipole magnets [142]. The quadrupole magnet focuses the reaction products onto the focal plane, while the three dipole magnets separate the trajectories depending on their magnetic rigidity (momentum-to-charge ratio). The position of these particles on the focal plane therefore is a function of their kinetic energy and as a consequence is directly related to the excitation energy of the residual nucleus. The length of the focal plane detector limits the accessible range in excitation energies per magnetic setting. For the Q3D this range is $\sim 8\%$ of the maximum ejectile kinetic energy. The fields set on the spectrometer can be varied to project different ranges of excitation energies (momentum bite) on the focal plane. The magnetic fields are set using a computer code that accounts for the radius of the Q3D, the momentum bite, the Q3D angle for detecting the ejectiles, and the charge and masses of the four nuclei. The spectrometer can be rotated along a circular track that is controlled by an electric motor, to perform angular distribution measurements. The angular range varies from 5° to $\sim 150^\circ$

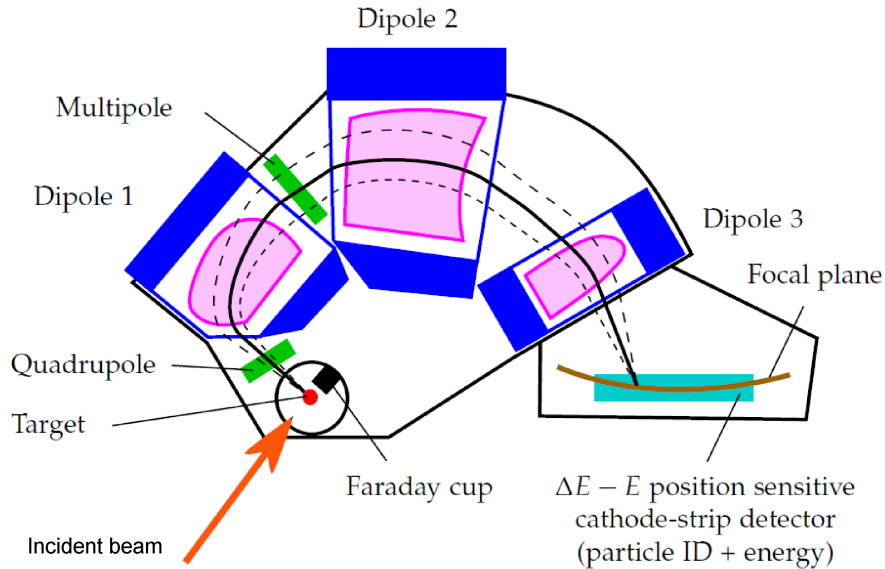


Figure 3.4: Schematic of the Q3D spectrometer

with respect to the incident beam direction. Figure 3.4 shows a schematic of the Q3D spectrometer.

3.4 Focal-Plane Detector

Ejectiles arriving at the focal plane [143, 144] are first incident on 25 μm kapton window at angle of $40^\circ - 50^\circ$, following which they pass through two proportional counters where they deposit a part of their energy. These proportional counters are filled with ~ 500 mbar of isobutane gas. As the ejectiles transit through the two proportional counters, they ionize the gas, creating an avalanche of free electrons. These electrons drift towards the anode wires, where they generate a signal ΔE_1 proportional to the energy loss. Simultaneously, the positive ions are deposited on a cathode foil. Unlike the first proportional counter, the second has two anode wires, ‘upper’ and ‘lower’ that record a summed ΔE signal. Comparing the partial energy losses ΔE_1 and ΔE between the two proportional counters provides an effective method for identifying the ejectiles.

Another difference in the second proportional counter is that instead of the cathode foil there is a strip foil, with 272 strips each separated by 0.5 mm spacing. These strips are

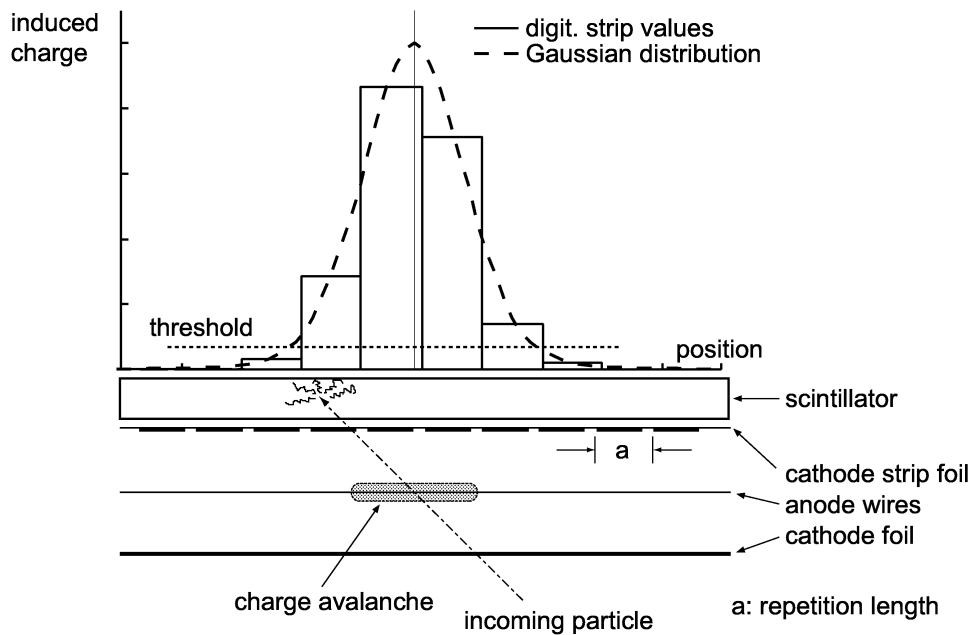


Figure 3.5: Cartoon depicting the response of the cathode-strip detector to a charged particle interaction. Figure obtained from Ref. [145].

3 mm long and electrically isolated. Each strip is connected to separate pre-amplifiers and shape amplifiers. This gives the position of the ejectiles along the focal plane. To consider a random ionization as a valid event, a signal has to be registered on 3-7 consecutive strips. Figure 3.5 shows the response of the cathode strips to an incoming charged particle. Finally, on exiting the proportional counters, the ejectiles are incident on a 7-mm-thick plastic scintillator that stops most of the light ions. This plastic scintillator is coupled to four photomultiplier tubes (PMT) that collect and amplify the scintillation light. The resulting PMT signal is proportional to the total energy (E) of the particles. This information (E) is used along with the energy losses ($\Delta E_1, \Delta E$) to set additional particle identification gates.

The signals from the upper and lower anode wires described earlier, are also recorded individually to check for the vertical alignment of the proportional counters with the plastic scintillator. The misalignment is easily detected by a surplus of events on one of the anode wires compared to the other. In order to correct that, the entire detector can be manually raised or lowered. A schematic view of the focal plane detector is shown in Fig. 3.6.

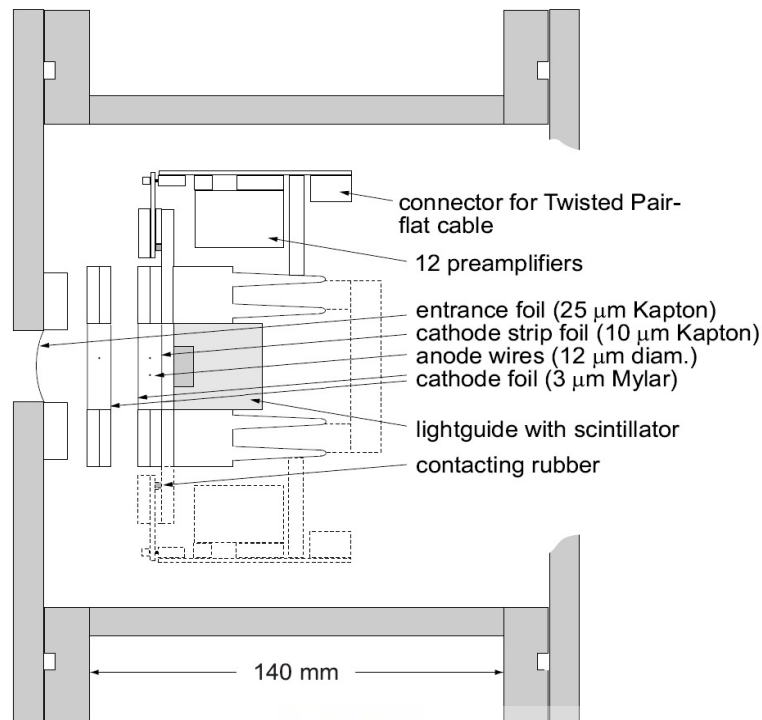


Figure 3.6: Cross sectional schematic view of the focal plane detector taken from Ref. [145]

3.5 Experimental details

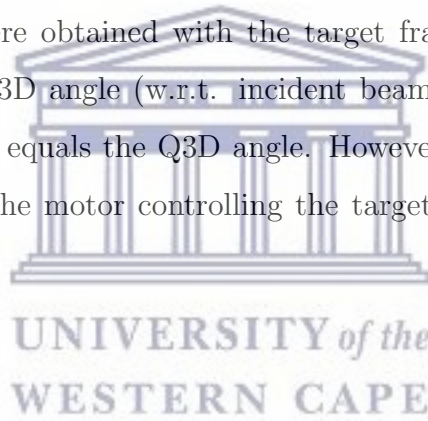
3.5.1 $^{138}\text{Ba}(p, t)^{136}\text{Ba}$

States in ^{136}Ba were produced using an $\sim 1.5 \mu\text{A}$, 23 MeV proton beam which was incident on a $40 \mu\text{g}/\text{cm}^2$ thick, $^{138}\text{BaCO}_3$ target that was isotopically enriched to 99.9% ^{138}Ba . The triton focal plane spectra were collected at ten laboratory angles from $5^\circ - 50^\circ$ over four sets of excitation energy ranges, up to 4.6 MeV. Energy calibrations were done using the well-known states in ^{136}Ba up to an excitation energy of 2.5 MeV, and beyond that using known states in ^{134}Ba that were produced via the $^{136}\text{Ba}(p, t)$ reaction. Elastic scattering angular distribution measurements were done from $15^\circ - 115^\circ$, to determine the optimum proton optical model parameters and to accurately measure the ^{138}Ba target thickness.

3.5.2 $^{138}\text{Ba}(d, \alpha)^{136}\text{Cs}$

Using this reaction we populated states in ^{136}Cs up to ~ 2.6 MeV in excitation energy. For this experiment ~ 600 nA of 22 MeV deuterons were incident on the ^{138}Ba target. For energy calibration we used the $^{94}\text{Mo}(d, \alpha)^{92}\text{Nb}$ and $^{92}\text{Zr}(d, \alpha)^{90}\text{Y}$ reactions, with enriched $^{94}\text{MoO}_3$ and ^{92}Zr targets that had approximate thickness of $100 \mu\text{g}/\text{cm}^2$ and $50 \mu\text{g}/\text{cm}^2$ respectively. The (d, α) spectra were collected at laboratory angles of $5^\circ - 45^\circ$ with increments of 5° . To determine the target thickness and optimal deuteron optical model parameters, elastic scattering angular distribution measurements were done for $\theta_{\text{lab}} = 15^\circ - 115^\circ$.

All reactions were performed with the carbon-backing side facing the beam to minimize additional straggling effects on the ejectiles due to the carbon backing. Additionally, the elastic scattering data were obtained with the target frame rotated so that the target angle is set to half the Q3D angle (w.r.t. incident beam direction) while for the (d, α) reactions the target angle equals the Q3D angle. However, for the (p, t) and (p, p) runs, due to a malfunction of the motor controlling the target frame, the angle was set at a fixed value of 19.6° .



4 | Data Analysis

We have to remember that what we observe is not nature herself,
but nature exposed to our method of questioning.

Werner Heisenberg

In this chapter I discuss details of various analysis procedures employed to determine differential scattering cross sections, excitation energies and spin-parities of states in ^{136}Ba and ^{136}Cs nuclei, from the (p, t) and (d, α) reactions. The procedure to calibrate the focal plane spectra is outlined in detail, while results are discussed in the following chapters.

4.1 Particle Identification

Since a given nuclear reaction can have several exit channels, different ejectiles will be detected at the focal plane of the spectrometer. To ensure that the data collected correspond only to (d, α) and (p, t) reactions, appropriate particle identification gates need to be set on the ejectiles. In the data acquisition software, this is accomplished by setting two different gates. The first gate is set by comparing the partial energy loss in the two proportional counters (ΔE_1 with ΔE) and the second one by comparing the energy loss in the second counter with the total energy (E) deposited in the plastic scintillator. This was done by plotting 2-dimensional (2D) histograms of ΔE_{anode} vs ΔE_{anode1} and ΔE_{anode} vs E_{residual} . Fig. 4.1 shows the alpha gates set using these 2D plots for the $^{138}\text{Ba}(d, \alpha)$ reaction.

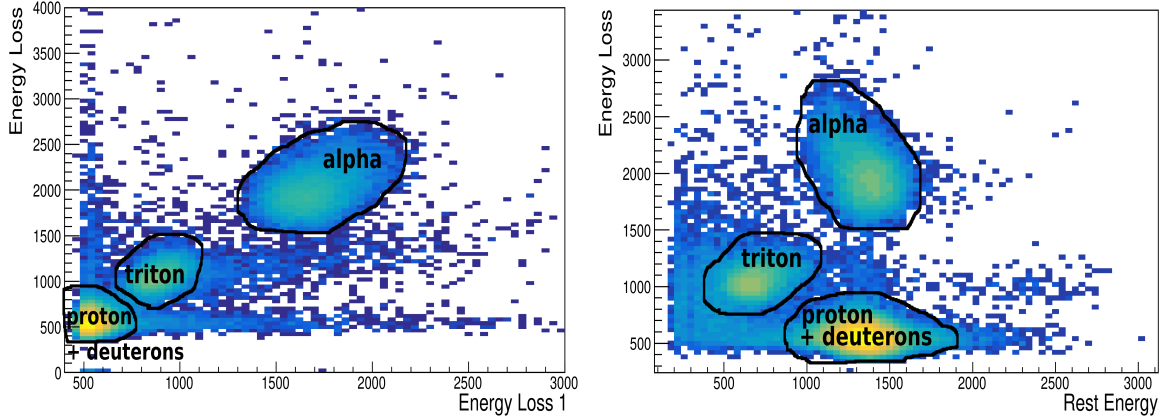


Figure 4.1: Particle identification spectra - left panel: $\Delta E - \Delta E_1$, partial energy loss of the ejectiles in the two proportional counters. Right panel: $\Delta E - E$ spectrum from the second proportional counter and the plastic scintillator. In the $\Delta E - E$ spectra it is difficult to distinguish between the protons from $^{138}\text{Ba}(d, p)$ and deuterons from $^{138}\text{Ba}(d, d)$ as the energy deposited by these two ejectiles is very similar. However the tritons from $^{138}\text{Ba}(d, t)$ have comparatively less energy and thus higher energy loss (compared to the deuterons and protons) and thus the left blob in the right figure. The energy loss information from the $\Delta E - E$ spectra can then be easily used to deduce the position of the tritons in the $\Delta E - \Delta E_1$ spectrum.

4.2 Peak fitting

Once the correct reaction was selected, the peaks at the focal plane were fit using a Levenberg-Marquardt χ^2 minimization [146] procedure to obtain peak centroids and areas. The lineshape function used is the convolution of a Gaussian with a low energy exponential tail on a flat background [147]. The low energy exponential tail accounts for the energy straggling of the ejectiles through the target material and the focal plane detector. An example is shown in Fig. 4.2.

4.3 Energy calibration

While states in ^{136}Ba have been extensively studied in the past, information on excited states above ~ 4 MeV in this nucleus was limited [129]. Additionally, as mentioned previously, very few excited states in ^{136}Cs were known prior to this work [129]. Therefore, to calibrate the $^{138}\text{Ba}(p, t)$ spectra above 2.5 MeV we used the $^{136}\text{Ba}(p, t)$ reaction and for

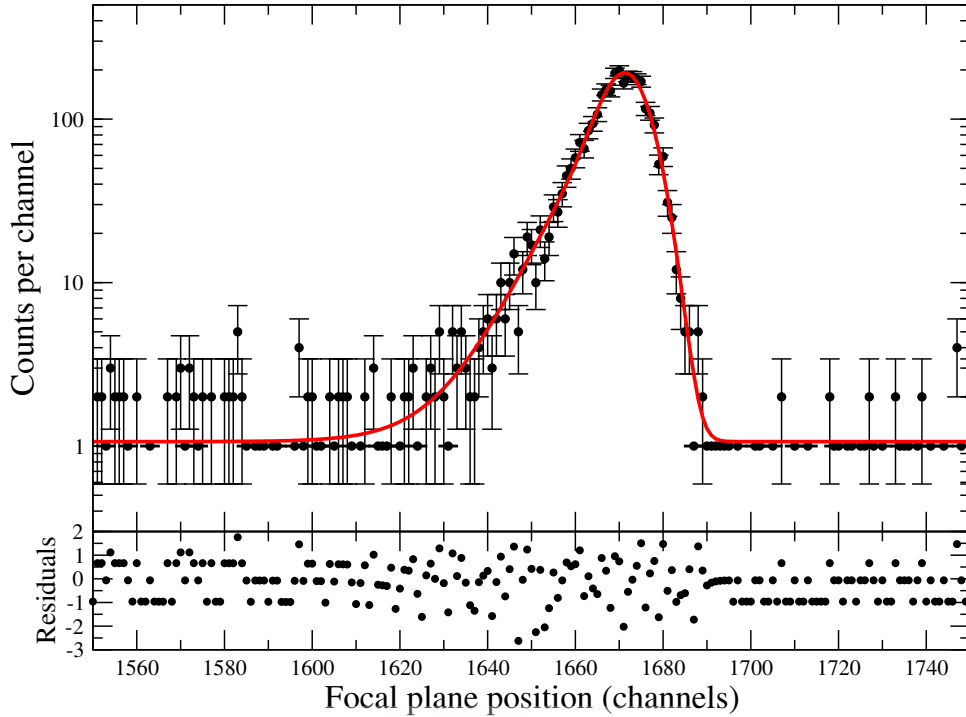


Figure 4.2: A sample fit to the uncalibrated 1866 keV peak in ^{136}Ba . The lineshape function is the convolution of a Gaussian with a low energy exponential tail on a flat background.

the $^{138}\text{Ba}(d, \alpha)$ we used the $^{94}\text{Mo}(d, \alpha)$ and $^{92}\text{Zr}(d, \alpha)$ calibration reactions. To perform these calibrations, we converted the excitation energies of ^{134}Ba (^{92}Nb and ^{90}Y) [148–150] to ‘effective’ excitation energies of ^{136}Ba (^{136}Cs) by using relativistic kinematics discussed in Appendix A after taking into account energy loss corrections. The detailed procedure is described below.

4.3.1 Effective excitation energy transformations

To describe this procedure in the most general way possible I use two notations. Reaction $P(a, b)Q$ represents $^{138}\text{Ba}(p, t)$ and $^{138}\text{Ba}(d, \alpha)$ reactions, while $X(a, b)Y$ represents the $^{136}\text{Ba}(p, t)^{134}\text{Ba}$, $^{92}\text{Zr}(d, \alpha)^{90}\text{Y}$ and $^{94}\text{Mo}(d, \alpha)^{92}\text{Nb}$ calibration reactions. For the generic transfer reaction

$$a + X \rightarrow b + Y, \quad (4.1)$$

the projectile a bombards the target X resulting in the excitation of the nucleus Y and the emission of the ejectile b , that is detected at an angle θ_{lab} with respect to the direction

of incident beam. Following the laws of 4-momentum conservation, one can obtain the relativistic momentum (p_b) and kinetic energy (E_b) of the ejectile in the laboratory frame. These can be used to extract relevant excitation energies of the nucleus Y. These kinematic relations are briefly discussed in Appendix A and the procedure to convert a focal plane centroid from the X(a, b)Y reaction to an effective excitation energy for P(a, b)Q is described below.

1. Assuming the reaction happens at the center of the target, calculate the energy loss of the beam in the target

$$E'_a = E_a - \int_0^{\frac{T_x}{2}} dx \left(\frac{dE}{dx} \right)_{E_a}, \quad (4.2)$$

here E_a is the kinetic energy of the incident beam, dE/dx is the energy loss of the projectile per unit length of the target material and T_x is the full thickness of the target X.

2. Using the reduced beam energy E'_a and Eq. (A.14), obtain the momentum p_b corresponding to the calibration reaction X(a, b)Y. This momentum p_b is the 'effective' momentum for the P(a, b)Q reaction.
3. Convert the effective momentum p_b to kinetic energy of the ejectile (E_b) using the relativistic mass-energy relation

$$E_b = \sqrt{p_b^2 + m_b^2} - m_b. \quad (4.3)$$

The ejectile b in this step corresponds to the P(a, b)Q reaction.

4. In an actual experiment performed in the laboratory, this ejectile loses energy in half of the target material P. In order to account for this energy loss, we add back the energy lost by the ejectile

$$E'_b = E_b + \int_0^{\frac{T_P}{2}} dx \left(\frac{dE}{dx} \right)_{E_b}. \quad (4.4)$$

Here, dE/dx is the stopping power of the ejectile b in the target material P and T_P is the full thickness of the target.

- Convert the kinetic energy E'_b for the ejectile to a new momentum p'_b .

$$p'_b = \sqrt{(E'_b + m_b)^2 - m_b^2} \quad (4.5)$$

- Calculate the effective excitation energy of Q using momentum p'_b and variables of the $P(a, b)Q$ reaction in Eq. (A.17). This converts the excitation energies of the nucleus Y into effective excitation energies of Q while implicitly correcting for the Q -value difference between the two reactions. As the energy loss of the beam is different in the targets P and X , to obtain the effective excitation energy from Eq. (A.17), E'_a in this step should correspond to the energy loss of the beam in target P .

- Use a quadratic regression together with a modified Gaussian χ^2 statistics. Fit the focal plane centroids of the $X(a, b)Y$ reaction to the effective excitation energies calculated in the previous step. To perform the modified χ^2 minimization, uncertainties in both the effective excitation energy and the focal plane centroids are used, so that

$$\chi^2 = \sum_i \frac{[y_i - y_{\text{fit}}(x_i)]^2}{\left(\sigma_{y_i}^2 + \sigma_{x_i}^2 \frac{dy_{\text{fit}}(x_i)^2}{dx}\right)}. \quad (4.6)$$

The sum is over all the excited states in the nucleus Y that are used for the calibration. The coordinates (x, y) and their uncertainties (σ_x, σ_y) in the above equation correspond to the focal plane centroids and effective excitation energies respectively. A ROOT program using the MINUIT library was written to perform this minimization and obtain fit coefficients for the polynomial

$$E(x_i) = A_0 + A_1 x_i + A_2 x_i^2. \quad (4.7)$$

This was because the curvature of the focal plane detector implies that the relation

between the focal plane position and momentum (and consequently the effective excitation energy) of the ejectiles do not have a linear relationship.

8. Use the coefficients A_0 , A_1 and A_2 to convert the focal plane positions of the $P(a, b)Q$ reaction to excitation energies of the nucleus Q .

To validate the above procedure, we calibrated the $^{94}\text{Mo}(d, \alpha)^{92}\text{Nb}$ focal plane spectrum using $^{92}\text{Zr}(d, \alpha)^{90}\text{Y}$ as the calibration reaction. Based on the success of the method, the $^{138}\text{Ba}(d, \alpha)$ and $^{138}\text{Ba}(p, t)$ reactions were calibrated using a set of C++ programs and shell scripts. The calibrated spectra are shown in Sections 5.1 and 6.1.

4.3.2 Corrections due to energy loss in targets

If energy losses of the triton or alpha particles through the target materials are not corrected for, they would affect the final determination of effective excitation energies. This would be most significant for alpha particles passing through the molybdenum target. This is clearly evident in Table 4.1, where the difference in energy loss for the alphas between the molybdenum and barium targets is ~ 5 keV. For the $^{138}\text{Ba}(d, \alpha)$ measurement our aim was to provide information about excited states in ^{136}Cs with uncertainties much less than 5 keV. Hence, it was imperative that we correct for the alpha energy losses between the barium, molybdenum and zirconium targets.

Table 4.1: Energy losses for 22 MeV deuterons, 30 MeV alphas, 23 MeV protons and 15 MeV tritons. The total energy loss for the projectiles (deuterons and protons) are calculated assuming that they pass through the full backing material and half the target material. While the ejectiles (alphas and tritons) are assumed to traverse through the other half of target material.

Target (nominal thickness)	Backing (nominal thickness)	Energy loss (keV)			
		p	t	d	α
$^{138}\text{BaCO}_3$ (40 $\mu\text{g}/\text{cm}^2$)	^{12}C (30 $\mu\text{g}/\text{cm}^2$)	0.905	0.889	1.681	2.716
$^{136}\text{BaCO}_3$ (40 $\mu\text{g}/\text{cm}^2$)	^{12}C (30 $\mu\text{g}/\text{cm}^2$)	0.902	0.881	–	–
^{92}Zr (50 $\mu\text{g}/\text{cm}^2$)	^{12}C (12 $\mu\text{g}/\text{cm}^2$)	–	–	1.042	0.458
$^{94}\text{MoO}_3$ (100 $\mu\text{g}/\text{cm}^2$)	^{12}C (40 $\mu\text{g}/\text{cm}^2$)	–	–	2.834	7.332

The energy losses for the protons, tritons, deuterons and alpha particles were estimated using the Stopping and Range of Ions in Matter (SRIM) program [151]. SRIM requires

information about the type of charged particle, target material composition and target material density. It then outputs the energy loss per unit length ($\frac{dE}{dX}$) as a function of kinetic energies. We adopt a conservative 10% relative uncertainty in the extracted ($\frac{dE}{dX}$) values. These values are then fit to a suitable N^{th} order polynomial using a least squared minimization routine,

$$\frac{dE}{dX} = \sum_{i=0}^N A_i E^i. \quad (4.8)$$

For both (d, α) and (p, t) reactions we found that an order 4 polynomial gave a good fit to the SRIM data. These coefficients are then used to calculate ($\frac{dE}{dX}$) at desired interpolated energies as the beam and ejectiles traverse the target material. This interpolation was

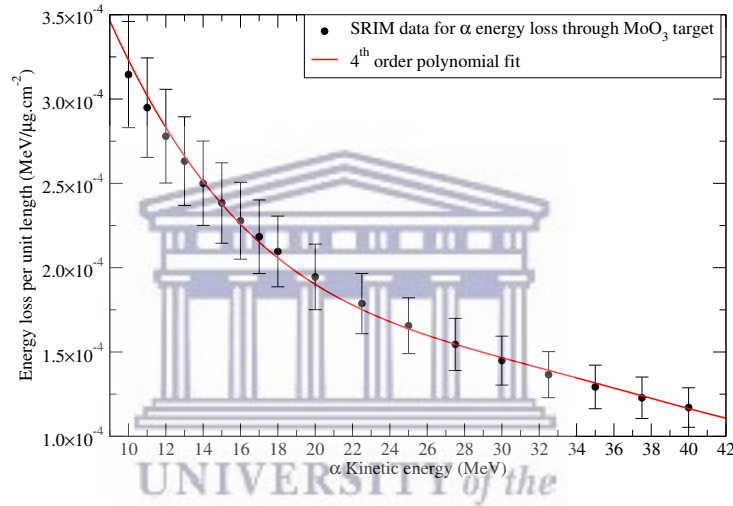


Figure 4.3: Least squared fit to energy loss values obtained from SRIM [151] for α particles passing through a $^{94}\text{MoO}_3$ target. The lowest order polynomial that adequately describe the SRIM output values within the required energy range was found to be 4. This procedure was repeated for all the charged particle-target combinations encountered in this analysis.

used to calculate the energy loss of the beam and ejectiles described in Eq. (4.2) and (4.4). The path of the beam and ejectiles as they traverse the target material and loose energy is depicted pictorially in Fig. 4.4.

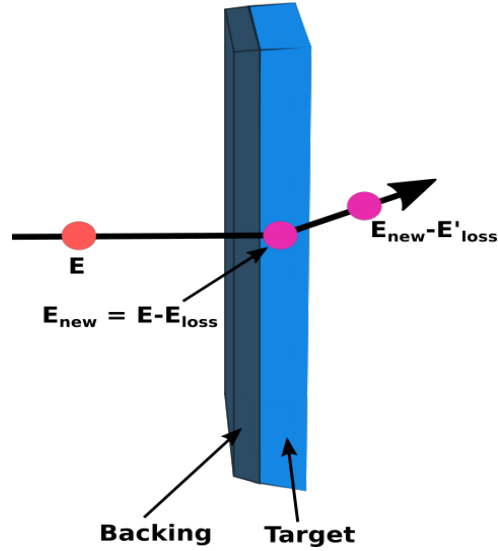


Figure 4.4: A schematic representation depicting the path of the charged particles through the target material. Assuming the reaction occurs at the center of the target, the projectile with energy E passes through the backing and half the target material where it loses energy $E - E_{loss}$. The resulting ejectile with energy E_{new} then passes through the other half of the target where it additionally loses energy ($E_{new} - E'_{loss}$) before it is detected at the focal plane.

4.3.3 Uncertainties on effective excitation energy

Below I discuss various uncertainty contributions in this analysis.

1. **Reaction kinematics** requires information of the beam energy, masses of the nuclei and the Q3D calibration angle. Thus uncertainties in the beam energy and masses of the nuclei involved contribute. The uncertainty in the angle arises due to the angular acceptance of the Q3D and depends on the x-slit width (Δx) and the distance (D) between aperture and target and is given by

$$\Delta\theta = \tan^{-1} \left(\frac{\Delta x}{2D} \right). \quad (4.9)$$

2. **Energy loss corrections** depends on the target thickness, energy loss parameters obtained using SRIM and the target thickness where the reaction occurs. In this thesis, we assume that the reaction happens at the target center. This is based on the assumption that thickness of the target is uniform, which in turn, results in a uniform distribution of the charged particle's momentum (and kinetic energy)

along the target [152, 153]. The 1σ variation due the ‘reaction location thickness’ ($T_{loc} = T_{max}/2$) is

$$\sigma = \sqrt{\frac{1}{12}(T_{max} - T_{min})^2}, \quad (4.10)$$

where $T_{min} = 0$ and T_{max} is the full target thickness. The reaction location uncertainty is calculated for the $^{138}\text{BaCO}_3$ target as well as the calibration targets, $^{136}\text{BaCO}_3$, $^{94}\text{MoO}_3$ and ^{92}Zr .

4.4 Cross Section Calculation

To determine the spin and parity of the states excited in ^{136}Ba and ^{136}Cs , we need to calculate differential scattering cross sections for these states at different angles. These experimental cross sections are proportional to the ratio of the total counts under the peak (N_c) with respect to the number of reaction centers (N_t) per unit area in the target and the number of incident beam particles (N_b) over the duration of the experimental run. Thus the cross section in the laboratory frame are calculated as

$$\left(\frac{d\sigma}{d\Omega}\right)_{\text{lab}} = \frac{N_c}{N_t N_b LT_{\text{Det}} LT_{\text{ASIC}} \Omega} 10^{34} \text{ (mb/sr)}. \quad (4.11)$$

These cross-sections are corrected for the live time of the detector (LT_{det}) and the data acquisition system (LT_{ASIC}) and take into consideration the angular acceptance of the Q3D, denoted by Ω . The determination of the parameters in the above formula are described in Sections 4.4.2, 4.4.3 and 4.4.5. Finally, for comparison of the experimental angular distributions with DWBA calculations, the laboratory angles and cross-sections need to be transformed to their equivalent values in the center-of-mass frame. For this purpose, the following formulae are employed [89]

$$\theta_{\text{cm}} = \sin^{-1}(\gamma \sin\theta_{\text{lab}}) + \theta_{\text{lab}}, \quad (4.12)$$

$$\left(\frac{d\sigma}{d\Omega}\right)_{\text{cm}} = \left(\frac{d\sigma}{d\Omega}\right)_{\text{lab}} \left(\frac{1 + \gamma \cos\theta_{\text{cm}}}{(1 + 2\gamma \cos\theta_{\text{cm}} + \gamma^2)^{3/2}}\right), \quad (4.13)$$

where the scaling factor γ is,

$$\gamma = \sqrt{\frac{m_1 m_3}{M_2 M_4} \left(\frac{1}{1 + \left(1 + \frac{m_1}{M_2}\right) \frac{Q}{E}} \right)}. \quad (4.14)$$

Here, m_1, m_3, M_2, M_4 are the masses of the projectile, ejectile, target and recoil nuclei, Q the reaction Q value for the excited state and E the beam energy.

4.4.1 Elastic scattering

The purpose of performing elastic scattering cross section measurements is two-fold. Firstly, they determine a suitable set of optical model parameters to analyze the data. Secondly, they help to determine the target thicknesses accurately. These are discussed in further details below.

Choosing the optical model parameters

To perform DWBA calculations we need to use suitable optical model parameter (OMP) sets for the entrance and exit channels of the (p, t) and (d, α) reactions. To do this, we compare the ratio of elastic scattering cross sections to Rutherford cross sections with DWBA predictions from several different global OMPs. We choose the ratio to Rutherford instead of the absolute elastic scattering cross section because the difference in the optical model parameters arise from the nuclear component of the interaction rather than the Coulomb part. Thus one can reliably select the correct optical model parameters by comparing experimental ratio-to-Rutherford cross section with DWBA predictions. The experimental elastic cross section $\left(\frac{d\sigma}{d\Omega}\right)_{elastic}$ is calculated using Eq. (4.11)-(4.14), while the Rutherford cross sections is

$$\left(\frac{d\sigma}{d\Omega}\right)_{Rutherford} = 10 \left[\frac{z_1 z_2 \alpha (\hbar c)}{4 E_{cm} \sin^2 \left(\frac{\theta_{cm}}{2}\right)} \right]^2 \text{ mb/sr}. \quad (4.15)$$

Here, $\alpha = 1/137$ is the fine structure constant, $\hbar c = 197 \text{ MeV}\cdot\text{fm}$, z_1, z_2 are the atomic numbers of the projectile and target and E_{cm}, θ_{cm} are the projectile energy and ejectile

detection angle in the center-of-mass frame. The factor of 10 converts the cross section from fm² to mb. We then chose the OMP that gave the least χ^2 , defined by

$$\chi^2 = \sum_i \frac{[Y_{DWBA}(\theta_i) - Y_{Expt}(\theta_i)]^2}{\sigma_{Expt}^2(\theta_i)}. \quad (4.16)$$

Here $Y_{DWBA}(\theta_i)$ and $Y_{Expt}(\theta_i)$ are DWBA predicted and experimentally measured ratio-to-Rutherford cross sections, θ_i is the center-of-mass angle and $\sigma_{Expt}^2(\theta_i)$ is the total uncertainty (statistical and systematic) in $Y_{Expt}(\theta_i)$. A similar procedure can be implemented for the exit channels as well if experimental data are available.

Estimating the correct target thickness

Once the correct OMPs are chosen, the elastic scattering cross sections also determine the correct target thicknesses. This is possible because Rutherford scattering dominates at low angles. As a result, the measured cross sections are largely independent of the choice OMP parameters used. This is evident in Figs. 5.3 and 6.3 where the elastic scattering cross sections computed using different proton and deuteron optical models start diverging at $\theta > 15^\circ$. In principle the nominal number of target atoms (based on the nominal areal density ρt) is given by

$$N_t = \frac{\rho t N_A}{M_t \cos\theta_t}. \quad (4.17)$$

In the above, M_t is the molar mass of the target (¹³⁸BaCO₃), N_A the Avogadro number and θ_t is target angle for the frame. The $\cos\theta_t$ factor arises due to the fact that the target frame is rotated for each angle. The calculated scattering cross sections using the N_t values from Eq. (4.17) is then normalized to DWBA predictions for $\theta \leq 15^\circ$, such that the actual ‘measured’ number of target atoms are

$$N'_t = N_t \beta, \quad (4.18)$$

where β is the normalization factor. The cross sections in Eq. (4.11) for the (d, α) and (p, t) reactions are then calculated using Eq. (4.17) and Eq. (4.18).

4.4.2 Beam particle normalization

To calculate the absolute cross-section of an excited state using Eq. (4.11) we need to know the total number of particles (N_b) that are incident on the target over the experiment. This information is provided by a Brookhaven Instruments Corporation (BIC) current integrator. BIC was connected to the Faraday cup placed behind the target at 0° to the beam axis. As most of the beam goes undeflected, the integrated current on the Faraday cup is proportional to N_b . The total current recorded on the Faraday cup is converted into digital pulses and stored in the data acquisition (DAQ) system using a scaler module (named *Scaler1*). Since the digitizing rate for the BIC is set at a fixed value of 1 kHz full scale from the manufacturer, the integrated N_b value can be determined as

$$N_b = Scaler1 \frac{\text{full scale}}{1000 N_e}, \quad (4.19)$$

where, N_e is the total charge state of the projectile in units of the elementary charge and the full scale setting for our experiment was 2×10^{-6} .

4.4.3 Dead time corrections

The absolute measured cross-sections are affected by the dead times of the detector and the data acquisition system. When the incoming event rates are higher than the event processing time, the detector goes ‘dead’ and any event that is received in this time interval will be not be processed. In such a situation, if the DAQ is processing an event, a ‘busy’ signal is generated and the current integrator increments the quantity called *Scaler3*. Thus the ratio of *Scaler3* to *Scaler1* gives the DAQ dead time, which can be related to the live time (LT) by the relation

$$LT_{DAQ} = 1 - \left(\frac{Scaler3}{Scaler1} \right) \quad (4.20)$$

The dead time associated with the detector is due to the application-specific integrated circuits (ASICs) that digitize the signals from the cathode strips. If the ASIC is busy

processing a signal, it increments the quantity in channel 0 of the analog-to-digital converter (ADC) unit. A good ADC signal is typically stored between ADC channels 1 and 2550. Thus to get the total ASIC livetime we need to take the ratio of counts in channel 0 to the total integrated counts in the spectrum

$$LT_{ASIC} = 1 - \left(\frac{\text{channel}(i = 0)}{\sum_{i=0}^{2550} \text{channel}(i)} \right). \quad (4.21)$$

4.4.4 Dark current correction

Noise in the current integrator circuit will lead to an over-estimation in N_b and an incorrect determination of the DAQ live time. In order to estimate this we recorded *Scaler1* and *Scaler3* over an extended interval of time with no beam on target. The small corrections due to the ‘dark current’ were performed using the relations

$$Scaler1_{corrected} = Scaler1_{with\ beam} - \left(\frac{Scaler1_{no\ beam}}{Run\ time_{no\ beam}} \right) Run\ time_{with\ beam} \quad (4.22)$$

$$Scaler3_{corrected} = Scaler3_{with\ beam} - \left(\frac{Scaler3_{no\ beam}}{Run\ time_{no\ beam}} \right) Run\ time_{with\ beam}. \quad (4.23)$$

4.4.5 Solid Angle Estimation

The ejectiles from the scattering chamber enter the detector via a diamond shaped aperture with height $2B$ and width $2A$ shown in Fig. 4.5. The solid angle is controlled by changing the distance between the horizontal and vertical slits, while the height and width of the diamond-shaped opening is fixed at 63 mm and 73.5 mm respectively. The distance D between the aperture and the target is fixed at 354.8 mm. The solid angle Ω for this setup is calculated as,

$$\Omega = \frac{1}{D^2} \left[4\Delta x \Delta y - 2 \left(\Delta x - A + \frac{A\Delta y}{B} \right) \left(\Delta y - B + \frac{B\Delta x}{A} \right) \right]. \quad (4.24)$$

Here $\Delta x = x - x_{off}$ and $\Delta y = y - y_{off}$ is distance between the x and y-slits and x_{off} , y_{off} are their systematic offsets and are further discussed in Section 4.4.6. The y-slits are

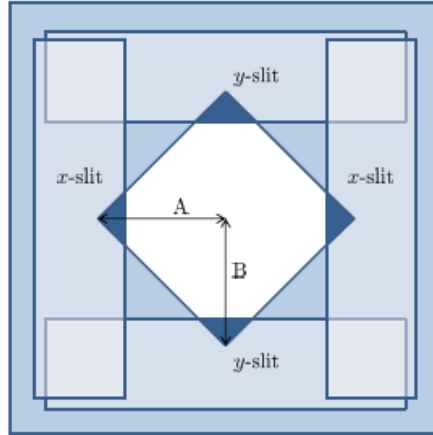


Figure 4.5: Schematic representation of the Q3D opening with the slits.

set at a constant opening of 24.5 mm for the entire duration of the experiment while the x-slits are altered to change the solid angle opening. When the distance between the slits is too small, the second term in Eq. (4.24) does not contribute. However, when the distance between the slits is large enough, the corners of the square are obscured by the diamond-like shape of the aperture. This happens when the criterion, $\frac{x}{A} + \frac{y}{B} > 1$ is satisfied.

4.4.6 Slit offset calibration

Due to the wear and tear of the micrometer screw gauges that control the opening of the slits, there is a systematic offset at the read out. As evident in Eq. (4.24), to accurately calculate the solid angle, one needs to determine the x and y offsets (x_{off} , y_{off}). To calculate these offsets, a linear regression is performed between the ratio of dead-time corrected elastic peak area to *Scaler1*, $(\frac{N_c}{LT \text{ Scaler1}})$ and the x-slit width. This is illustrated in Fig. 4.6 for $^{138}\text{Ba}(p,p)$ elastic data. All other experimental conditions including the y-slits are left unchanged. The x-intercept of the fit then gives the x-slit offset. The slit settings and the resulting solid angle for all the runs in this thesis are given in Table 4.2. The solid angle is significantly reduced for the forward angles especially in the elastic runs to prevent damage to the focal plane detector due to the high event rates.

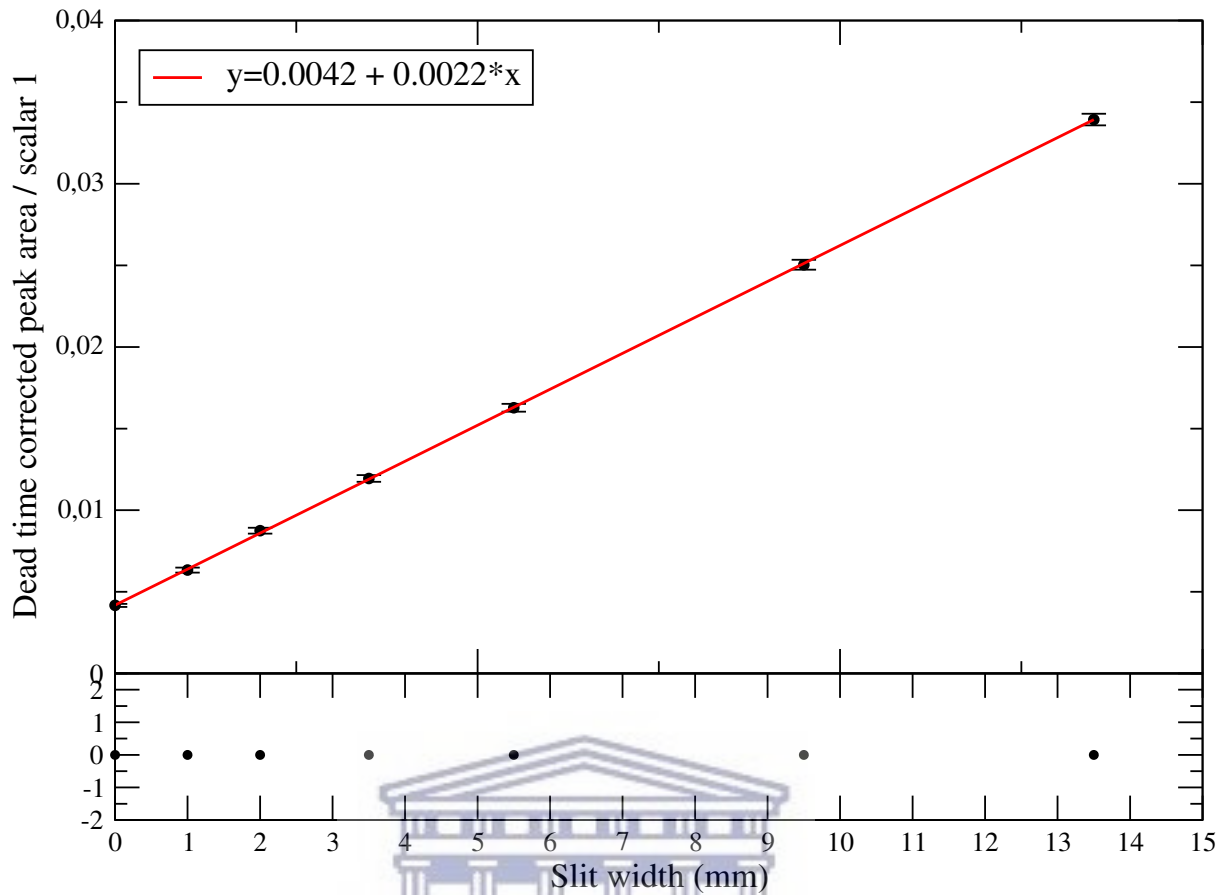


Figure 4.6: Linear fit to the ratio of dead-time corrected elastic peak area over *Scaler1* as a function of different x-slit width.

Table 4.2: Slit settings used for the different experiment runs.

Reaction	Lab angle	x × y (mm)	x-offset (mm)	Solid angle (msr)
$^{138}\text{Ba}(p, t)$	5°	10 × 24.5	-1.90 (4)	9.3 (14)
	10° – 50°	20 × 24.5		14.6 (7)
$^{138}\text{Ba}(p, p)$	15° – 25°	1 × 24.5	-1.90 (4)	2.3 (15)
	30°	5 × 24.5		5.4 (15)
	35° – 115°	20 × 24.5		14.6 (7)
$^{138}\text{Ba}(d, \alpha)$	5° – 10°	8 × 24.5	0.618 (3)	5.7 (5)
	15° – 45°	21 × 24.5		14.1 (2)
$^{138}\text{Ba}(d, d)$	10° – 20°	2 × 24.5	0.618 (3)	1.1 (5)
	20° – 60°	8 × 24.5		5.7 (5)
$^{138}\text{Ba}(d, d)$ Dec 2016	10° – 35°	2 × 24.5	0.623 (8)	1.1 (5)
	40° – 115°	21 × 24.5		14.1 (2)

4.4.7 Uncertainties in Cross-Section

In addition to the statistical uncertainties on the differential cross sections, several systematic uncertainties contribute to our measurements. For example, to estimate the uncertainty contribution from the target thickness, we rely on elastic scattering data. However, as discussed in Section 4.4.1 this method is heavily dependent upon the choice of optical model parameters. Therefore, the uncertainty in the target thickness arising from different OMPs will affect the determined experimental cross sections. Furthermore, uncertainties in the laboratory angles, masses of the nuclei, reaction Q values and the beam energy will also contribute to the final uncertainty in the measured values.

4.5 DWBA Calculation

In order to determine the J^π of the states, the experimental angular distributions are compared with the DWBA angular distributions. Based on the agreement between the shapes of the two distributions, the states is assigned a particular value of spin and parity. Several DWBA codes have been developed over time to calculate observables for elastic and inelastic scattering as well as transfer reactions. Some of the major differences between these codes are in the approximations used. For example, in the use of zero or finite-range approximations, or if the DWBA approximation is to first order (single-step transfer) or second-order (sequential transfer). In this thesis, the DWBA analysis was performed using the DWUCK4 [93] code, which is discussed in the following section.

4.5.1 DWUCK4

The DWUCK4 reaction code does zero-range, single-step DWBA calculations with an option to make finite-range corrections. However, does not perform coupled-channel or multi-step calculations. In our case finite range corrections are important for the (d, α) data. Such corrections donot have significant effect on the calculated cross sections for (p, t) reactions. DWUCK4 allows the usage of various potentials to calculate the reaction cross sections. For instance, one can use Woods-Saxon potential (WS), the WS scaled

by a r^{power} term, a Legendre polynomial expansion of the volume WS (with options for specifying the nuclear deformation), harmonic oscillator and other user-defined external potentials. The form of the potential is specified in the input file using an appropriate value for the variable ‘OPTION’. Each OPTION type defines a specific potential, with both the real and imaginary components. As the generic form of the optical model potential is a sum of volume, surface and spin-orbit Woods-Saxon potential (see Section 2.1), we used a similar form in the DWBA calculations for the data described in this thesis. In DWUCK4 terminology this potential is constructed by using OPTION = 1.0, 2.0 and 4.0 resulting in,

$$\begin{aligned}
 V(r) = & -V_R f(x_R) - iV_I f(x_I) && \text{OPTION} = 1.0 \\
 & + V_R g(x_R) + iV_I g(x_I) && \text{OPTION} = 2.0 \\
 & - \left(\frac{V_{SOR}}{r} \frac{df(x_R)}{dr} + \frac{iV_{SOI}}{r} \frac{df(x_I)}{dr} \right) \vec{L} \cdot \vec{s} && \text{OPTION} = 4.0
 \end{aligned} \tag{4.25}$$

The form factors $f(x_i)$ and $g(x_i)$ are defined as,

$$f(x_i) = \left(1 + e^{\left(\frac{r - r_{0i} A^{1/3}}{a_i} \right)} \right)^{-1}, (i = R, I) \tag{4.26}$$

$$g(x_i) = \frac{df(x_i)}{dx} \tag{4.27}$$

The strengths of real and imaginary potentials (V_R and V_I), the reduced radius of the target or recoil nucleus ($R_i = r_{0i} A^{1/3}$) and the diffuseness of the potential, (a_i) for the three forms of the Woods-Saxon potentials are taken from the global optical model parameter (OMP) sets. In these global OMP sets, the V_R 's are usually denoted by V_v or V_R for real volume Woods-Saxon and V_{so} for the real part spin-orbit potential. The real part of the surface potential is usually zero. The imaginary potentials are denoted by W_R for the volume potential, W_S or W_D for the surface Woods-Saxon and usually W_{so} for the spin-orbit potential is set to zero. In addition to the differences in notations between DWUCK4 and the global OMPs, the strength of the potentials also need to be scaled. These are mentioned below.

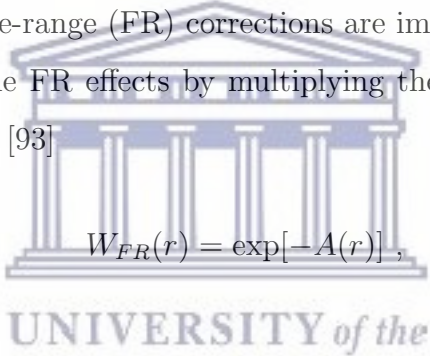
1. DWUCK4 does not include the factor of 4 in the surface Woods-Saxon potential. Hence to match the global OMP, the DWUCK input needs to be adjusted to

$$\begin{aligned} V_I(\text{DWUCK}) &= 4 \times V_I(= W_D \text{ or } W_S) \\ &= 4 \times V_I(\text{OMP}) . \end{aligned} \quad (4.28)$$

2. The spin-orbit term in DWUCK4 is defined as $\vec{L} \cdot \vec{s}$ as opposed to $\vec{L} \cdot \vec{\sigma}$ in the global optical potentials and without the factor of 2 for $(\frac{\hbar}{2\pi})^2$. V_I for the spin-orbit potential needs to be adjusted accordingly to account for this scaling between DWUCK4 and the global optical potential

$$V_{SOR}(\text{DWUCK}) = 2 \times 2 V_{so}(\text{OMP}) . \quad (4.29)$$

As mentioned earlier, finite-range (FR) corrections are important for the (d, α) reaction. DWUCK4 accounts for the FR effects by multiplying the form factor in the scattering amplitude by the function [93]

$$W_{FR}(r) = \exp[-A(r)] , \quad (4.30)$$


where

$$A(r) = \frac{2}{\hbar^2} \frac{m_b m_x}{m_a} R^2 [E_b - V_b(r_b) + E_x - V_x(r_x) - E_a + V_a(r_a)] . \quad (4.31)$$

For the reaction $A(a, b)B$, where transferred particle is labeled by x the energies (E) and potentials (V) are given w.r.t. the target nucleus A . The finite-range correction parameter is R and it's usage is discussed further in Section 6.3. Detailed description for the DWUCK4 input file is given in Appendix B.

4.6 Identification of impurities

Impurities in the targets arise from three primary sources.

1. Similar mass impurities: These impurities arise from nuclei in the target sample that

have a similar mass as the barium but are not isotopes of barium. The only stable $A = 138$ candidates are lanthanum and cerium. The presence of these impurities is highly unlikely. Furthermore, the large differences in reaction Q values immediately rules out the possibility of contaminants from the $^{138}\text{La}(d, \alpha)$ reaction. A careful analysis of the $^{138}\text{Ba}(p, t)$ and $^{138}\text{Ba}(d, \alpha)$ spectra showed no signs of contamination from the $^{138}\text{Ce}(d, \alpha)$, $^{138}\text{Ce}(p, t)$ or $^{138}\text{La}(p, t)$ reactions.

Table 4.3: Ground state reaction Q -values (in MeV) for the possible contaminants. The Q values for reactions on ^{138}Ba target are shown for comparison.

	^{138}Ba	^{138}La	^{138}Ce	^{16}O	^{12}C	^{13}C	^{14}C
(d, α)	8.787	13.070	9.177	3.110	-1.340	5.168	0.361
(p, t)	-7.035	-8.142	-8.723	-20.41	-23.36	-15.185	-4.64

2. Isotopic impurities: Possible isotopic contamination in the ^{138}Ba target could arise from $^{134-137}\text{Ba}$ as these are the only stable barium isotopes with a relative abundance $> 1\%$ in $^{\text{nat}}\text{Ba}$ (see Table. 4.4). We did not explicitly identify contributions from isotopic impurities in both the $^{138}\text{Ba}(d, \alpha)$ and $^{138}\text{Ba}(p, t)$ spectra, given the high enrichment level of the targets.

Table 4.4: Reaction Q -values in MeV for the possible isotopic contaminants. The percentages indicate relative abundance of the isotopes in natural barium.

	^{138}Ba (71.7%)	^{137}Ba (11.2%)	^{136}Ba (7.8%)	^{135}Ba (6.6%)	^{134}Ba (2.4%)
(d, α)	8.787	10.57	8.72	10.93	8.91
(p, t)	-7.035	-7.53	-7.6	-7.96	-8.18

3. Light mass impurities: These contaminants arise from moisture and other sources such as the carbon backing used for making the targets, as well as poor vacuum in the scattering chamber. Additionally, the ^{138}Ba and ^{94}Mo targets were chemical compounds that include oxygen ($^{138}\text{BaCO}_3$ and $^{94}\text{MoO}_3$). However due to the difference in reaction kinematics, light mass impurities in the spectra are easily identifiable as they appear kinematically broadened and move towards lower channels as the measurements are performed at higher angles.

All the data analysis procedure described in this chapter are use to arrive at the results of the (p, t) and (d, α) reactions which are discussed in the next two chapters.



5 | $^{138}\text{Ba}(p, t)^{136}\text{Ba}$ Results

The first principle is that you must not fool yourself and you are the easiest person to fool.

Richard Feynman

As mentioned before, the motivation for this experiment was to study neutron pairing correlations in ^{136}Ba using the $^{138}\text{Ba}(p, t)$ reaction. In this reaction, we observed a total of 110 states in ^{136}Ba up to an excitation energy of 4.6 MeV. A total of 12 0^+ states are observed, out of which 6 states are being reported for the first time. As the (p, t) reaction populates all possible natural parity states, unique J^π assignments could be made for 56 additional newly identified states.

5.1 Energy Calibration

Due to the large negative Q value of the $^{138}\text{Ba}(p, t)$ reaction, the Q3D focal plane spans ~ 1 MeV in excitation energy per momentum setting. Hence we collected the ^{136}Ba excitation spectra at 4 different momentum settings. The first three momentum bites are self calibrated using well-known states in ^{136}Ba [85, 129]. Above 2.5 MeV as the density of states in the focal plane spectrum increases, peak identification becomes increasingly challenging. Additionally, very few states were previously known in this nucleus above 4 MeV [85, 129]. Thus, tritons produced from the $^{136}\text{Ba}(p, t)$ reaction (at the same magnetic setting) are used to perform an additional calibration using well known energy levels in ^{134}Ba . To accomplish this the relevant states in ^{134}Ba were identified and then converted

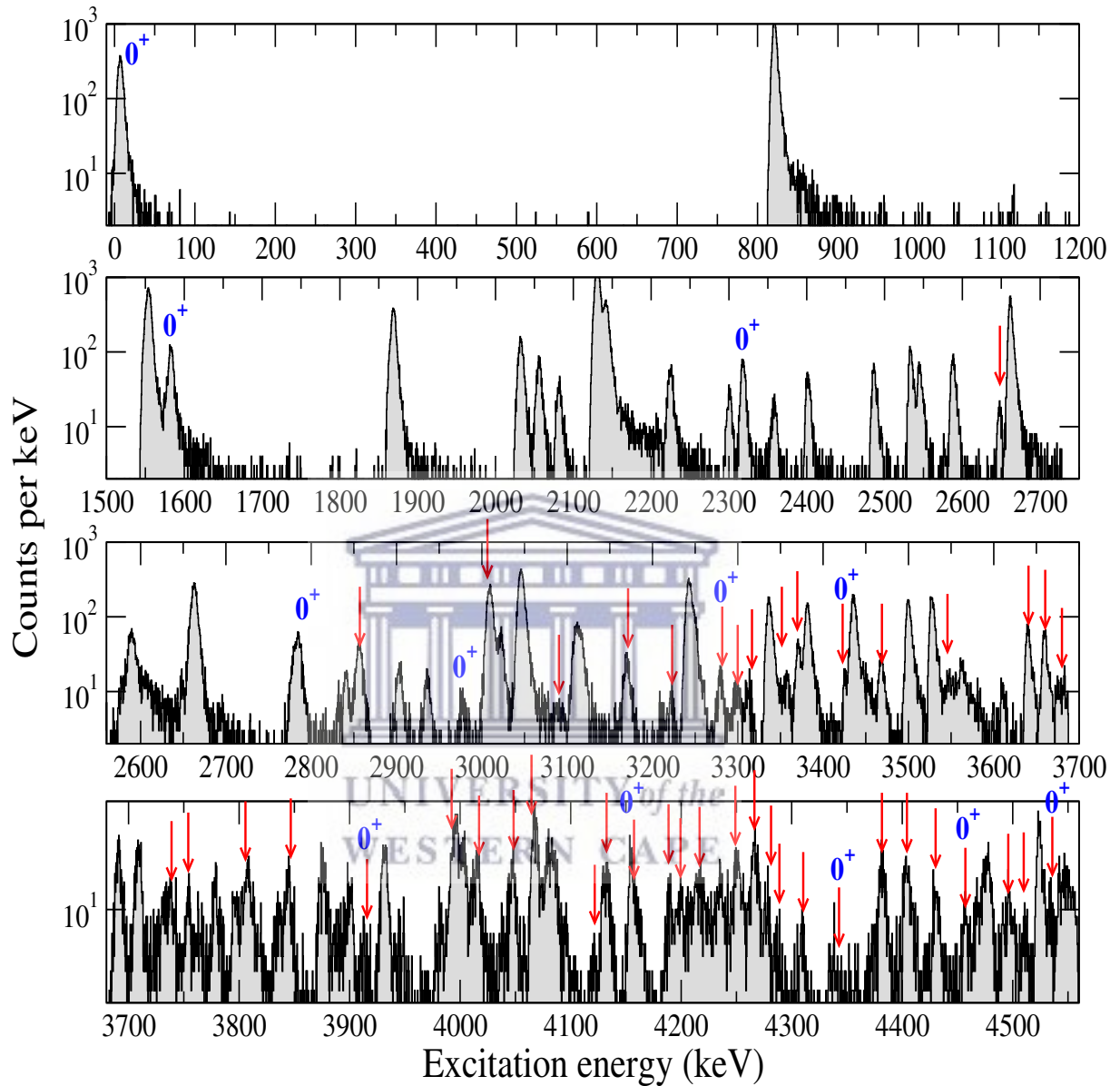


Figure 5.1: Excitation energy spectrum for ^{136}Ba at $\theta_{\text{lab}} = 15^\circ$. The triton spectra were collected at 4 different momentum settings up to 4.6 MeV. All the 0^+ states identified from this experiment are indicated. The red arrows indicate new states observed in this work.

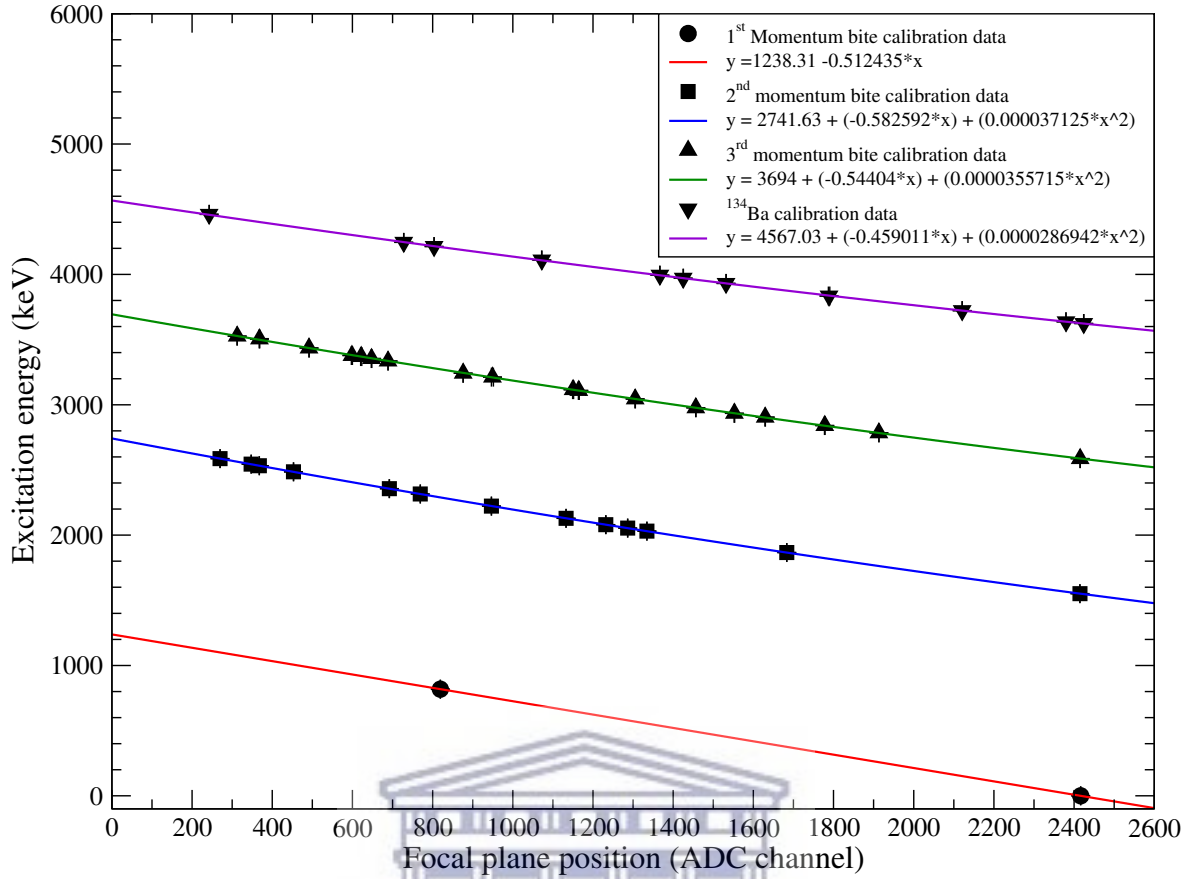


Figure 5.2: Energy calibrations for the $^{138}\text{Ba}(p, t)$ reaction at 4 different momentum bites. The small x and y uncertainties are included in the image. The first three bites were calibrated using known excitation energies in ^{136}Ba . The 4th bite is calibrated using ^{134}Ba excitation energies that were extracted using the procedure described in Section 4.3.

to effective excitation energies of ^{136}Ba following the procedure outlined in Section 4.3.

The calibrated energy spectrum for $\theta_{\text{lab}} = 15^\circ$ is shown in Fig. 5.1.

Table 5.1: Excited states in ^{136}Ba observed with the $^{138}\text{Ba}(p, t)$ reaction. The energies and spin-parities listed in the first two columns are from the nuclear data sheets for $A = 136$ [129]. Statistical and systematic (see Section 4.3.3) uncertainties are added in quadrature to give the final uncertainty in our excitation energies. The uncertainties in the last momentum bite ($E_x > 3.6$ MeV) are larger compared to the first three, due to additional contributions from the systematics of $^{136}\text{Ba}(p, t)$ calibration (target thickness, energy loss, etc).

Literature		This work	
E_x (keV)	J^π	E_x	J^π
0.0	0^+	0.0	0^+
818.522(10)	2^+	818.5(6)	2^+
1550.987(13)	2^+	1551.4(6)	2^+

Table 5.1 – continued

E_x (keV)	J^π	E_x	J^π
1578.969(13)	0 ⁺	1579.7(6)	(0 ⁺)
1866.611(18)	4 ⁺	1866.1(6)	4 ⁺
2030.535(18)	7 ⁻	2030.3(6)	7 ⁻
2053.892(18)	4 ⁺	2053.6(6)	4 ⁺
2080.13(3)	2 ⁺	2080.3(6)	2 ⁺
2128.869(25)	2 ⁺	2129.3(6)	2 ⁺
2140.237(18)	5 ⁻	2140.2(6)	5 ⁻
2222.709(19)	(2) ⁺	2223.4(6)	2 ⁺
2298.69(4)	(6 ⁻)	2299.0(6)	6 ⁺
2315.26(7)	0 ⁺	2315.5(6)	0 ⁺
2356.497(22)	4 ⁺	2356.3(7)	4 ⁺
2399.94(5)	(1) ⁺	2399.8(7)	(1 ⁻)
2485.13(5)	2 ⁺	2485.3(7)	2 ⁺
2532.653(23)	3 ⁻	2532.4(6)	3 ⁻
2544.481(24)	4 ⁺	2543.8(6)	(5 ⁻ , 6 ⁺)
2587.08(3)	(5) ⁺	2587.6(7)	4 ⁺
		2646.4(8)	7 ⁻
2661.48(5)	1, 2 ⁺	2660.4(7)	2 ⁺
2784.44(13)	0 ⁺	2783.4(7)	0 ⁺
		2829.9(8)	6 ⁺ , 7 ⁻
2840.74(10)	(4 ⁺)	2839.1(7)	4 ⁺
		2854.3(7)	5 ⁻
2905.0(5)		2902.0(7)	(4 ⁺ , 5 ⁻)
2935.1(9)	(1, 2 ⁺)	2935.1(7)	(1 ⁻ , 2 ⁺)
2977.67(18)		2977.1(7)	0 ⁺
		3007.2(8)	5 ⁻
3022.10(8)	(1, 2 ⁺)	3021(1)	2 ⁺
3044.54(5)	1 ⁽⁻⁾	3044.5(7)	(1 ⁻ , 3 ⁻)
		3089(1)	(4 ⁺ , 5 ⁻)
3109.59(9)	2 ⁺	3108.7(8)	
3116.08(6)	2 ⁺	3115.3(9)	2 ⁺
		3170.0(7)	6 ⁺
3212.0(5)	0 ⁽⁺⁾ , 1, 2, 3 ⁽⁺⁾	3210(1)	(2 ⁺ , 3 ⁻)
		3221(2)	(2 ⁺)
3241.89(17)		3244.7(7)	2 ⁺

Table 5.1 – continued

E_x (keV)	J^π	E_x	J^π
		3278.6(7)	0 ⁺
		3297.1(8)	5 ⁻
		3310(1)	(1 ⁻ , 2 ⁺)
3335.6(3)		3336.2(7)	2 ⁺
3354.5(3)		3356.7(8)	
3370.07(21)		3369(1)	(1 ⁻ , 2 ⁺)
3378.0(5)		3381(1)	2 ⁺
		3426.7(8)	0 ⁺
3435.0(1)	1 ⁻	3435.1(7)	(1 ⁻ , 2 ⁺)
		3468.2(9)	
3505.5(9)	0 ⁽⁺⁾ , 1, 2, 3 ⁺	3498.7(8)	(2 ⁺ , 4 ⁺ , 5 ⁻)
3526.7(4)	2 ⁺	3527.6(7)	2 ⁺
		3547.9(7)	4 ⁺
		3640(1)	4 ⁺
		3660(1)	2 ⁺
		3684(1)	
3691.92(13)	(1 – 3)	3691(1)	5 ⁻
3706.1(6)	(1, 2 ⁺)	3708(2)	(1 ⁻ , 2 ⁺)
		3720(1)	($J > 5$)
		3739(1)	(2 ⁺)
		3754(1)	(4 ⁺ , 5 ⁻)
3768.9(3)	1 ⁽⁻⁾ , 2, 3 ⁺	3768(1)	3 ⁻
3795.34(15)	(1, 2 ⁺)	3799(1)	(1 ⁻)
		3808(1)	(3 ⁻)
		3842(1)	2 ⁺
		3858(2)	(5 ⁻ , 6 ⁺)
3863.47(23)	(1, 2 ⁺)	3868(1)	(2 ⁺ , 6 ⁺)
		3883(2)	(7 ⁻ , 8 ⁺)
		3902(1)	2 ⁺
		3921(1)	0 ⁺
		3972(1)	2 ⁺
3979.76(20)	(1)	3980(1)	4 ⁺
3992.56(19)	0 ⁽⁺⁾ , 1, 2, 3 ⁺	3994(1)	(2 ⁺)
		4011(2)	(3 ⁻)
		4029(1)	(1 ⁻ , 2 ⁺)

Table 5.1 – continued

E_x (keV)	J^π	E_x	J^π		
4075(10)		4042(1)	(1 ⁻ , 2 ⁺)		
		4052(1)	2 ⁺		
		4064(1)	(5 ⁻ , 6 ⁺)		
		4070(2)	(2 ⁺ , 3 ⁻)		
		4079(2)			
		4107(2)	(3 ⁻)		
		4120(1)	4 ⁺		
		4127(2)	2 ⁺		
		4147(1)	(0 ⁺ , 4 ⁺)		
		4156(1)	(5 ⁻ , 6 ⁺)		
		4185(2)			
		4193(2)			
		4201(2)			
		4214.9		4213(1)	(5 ⁻)
4231.17(20)	1	4233(2)	(2 ⁺ , 3 ⁻)		
		4250(1)	2 ⁺		
		4268(1)	(1 ⁻ , 3 ⁻)		
		4279(2)	(1 ⁻ , 2 ⁺)		
		4292(2)	(2 ⁺ , 3 ⁻)		
		4312(2)	3 ⁻		
		4344(1)	0 ⁺		
		4383(2)	(4 ⁺ , 5 ⁻)		
		4394(2)	2 ⁺		
		4413.28(10)	(1)	4406(2)	
				4416(1)	(1 ⁻ , 2 ⁺)
4421(2)	(1 ⁻ , 2 ⁺)				
4444(1)	0 ⁺				
4451(2)	3 ⁻				
4475.18(10)	(1)			4475(2)	(2 ⁺ , 3 ⁻)
		4487(2)	(2 ⁺)		
		4497(1)	(2 ⁺)		
		4517(2)			
4536.4(3)	1	4534(2)	(0 ⁺ , 4 ⁺)		
		4547(1)	2 ⁺		
		4558(2)			

5.2 Elastic scattering

As discussed earlier in Sect. 4.4.1, to obtain the optimal proton optical model parameter (OMP) set, we compare our measured experimental elastic differential cross sections (as a ratio-to-Rutherford) with DWUCK4 calculations. Proton OMPs suitable for this (p, t) reaction are the ones given by Becchetti and Greenlees (BG) [154], Koning and Delaroche (KD) [155], Varner *et al.* [156], Menet *et al.* [157] and Walter and Guss (WG) [158]. To decide the OMP set that best describes the incoming $p-^{138}\text{Ba}$ channel, we normalize the DWBA cross sections to experimental data using a chi-squared minimization routine and choose the OMP set that gives the least χ^2 value. Thus we find that the OMP from Ref. [156] is the optimal choice. The reduced chi-square values given in Table 5.2 affirms this choice.

Table 5.2: Normalization factors β for experimental elastic (ratio-to-Rutherford) scattering cross corresponding to different global proton OMP sets used in DWUCK4.

Optical Model Parameter set	Normalization factor (β)	χ^2_ν
Varner <i>et al.</i> [156]	0.639	784
Becchetti & Greenlees [154]	0.647	1809
Walter & Guss [158]	0.640	2014
Menet <i>et al.</i> [157]	0.639	3268
Koning & Delaroche [155]	0.645	3873

To determine the correct target number of target nuclei (N_t) we normalize experimental ratio-to-Rutherford cross section to DWBA prediction using the OMP of Ref. [156] at $\theta_{CM} = 15.11^\circ$. This gave us a normalization factor of $\beta = 0.64 \pm 0.01$ which further translates to a measured target thickness of $\rho t' = 25 \pm 2 \mu\text{g}/\text{cm}^2$.

5.3 DWBA Calculations

To calculate the (p, t) differential cross-section in DWUCK4 [93] we assume a single step transfer of a di-neutron in a $S = 0$, (singlet) state. To describe the interactions in the entrance ($p-^{138}\text{Ba}$) and exit ($t-^{136}\text{Ba}$) channels in DWUCK4 we used the Wood-Saxon form of the optical potential [90]. As mentioned above, we chose the proton optical

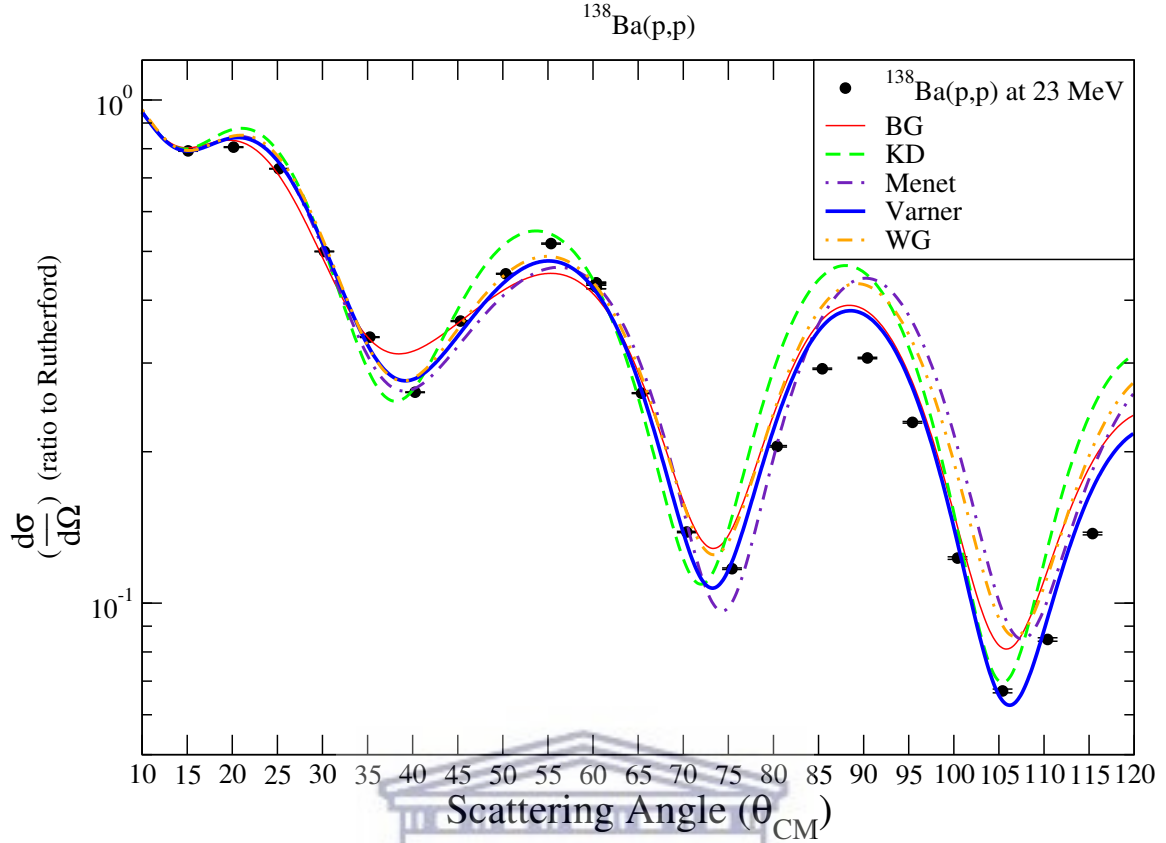


Figure 5.3: Experimental elastic scattering angular distributions for 23 MeV protons on ^{138}Ba compared with DWBA angular distribution. Global proton optical model parameters used are from Becchetti and Greenlees (BG) [154], Koning and Delaroche (KD) [155], Varner *et al.* [156], Menet *et al.* [157] and Walter and Guss (WG) [158]. The proton OMP that best reproduces the elastic scattering data is the one by Varner *et al.* [156]. This OMP is further used in the DWBA analysis.

model parameters from Ref. [156] by comparing experimental and DWBA differential cross sections for elastic scattering. As experimental triton elastic scattering data on ^{136}Ba or a similar nucleus is not available, we had to choose the triton OMP set that (in combination with the proton OMP) best reproduces the the ground state angular distribution. We found that the global triton OMP set by Li *et al.* [159] was a better fit to data compared to the one by Becchetti and Greenlees [160]. This is clearly evident in Fig. 5.4. Thus, for this analysis, we use the proton and triton global OMP sets from Ref. [156] and Ref. [159]. For each excitation energy, the triton optical model parameters are calculated as a function of the outgoing triton energy (Table 5.3), while the proton OMP values are fixed for $E_p = 23$ MeV. To calculate the two-neutron transfer form

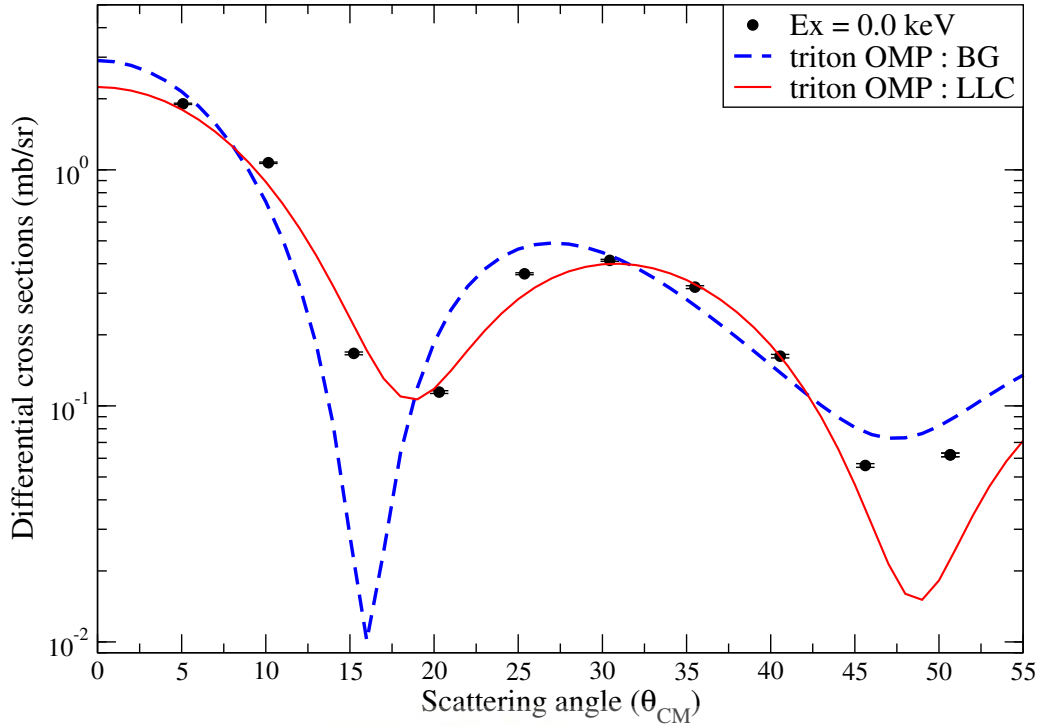


Figure 5.4: DWBA angular distributions from DWUCK4 for the ground state using different triton optical model parameters. The OMP from Li *et al.* (LLC) [159] results in a better fit to the data compared to the one recommended by Becchetti and Greenlees (BG) [160].

factor, the depth of the real volume term in the neutron OMP is varied so that each of the transferred neutron gets a binding energy of half the two-neutron separation energy and the excitation energy of the residual nucleus

$$BE = \frac{S_{2n}({}^{138}\text{Ba}) + Ex({}^{136}\text{Ba})}{2}. \quad (5.1)$$

The final optical model parameters used in the calculations are given in Table 5.3.

In DWUCK4 different orbital configurations are used to pick up the two neutrons for calculating the DWBA cross sections corresponding to different L -transfers. For $L = 0$ and $L = 2$, the neutron pair is picked up from the $(1h_{11/2})$ orbit, due to its proximity to the Fermi surface [118]. For the 1^- states, the combination $(3p_{3/2})(2d_{3/2})$ or $(3p_{3/2})(3s_{1/2})$ are the only orbital configurations that can make a 1^- state in DWUCK4. In this analysis, the first combination is used. Based on the results from Ref. [161], for $L = 3, 5$ and 7 we use the combination $(1h_{11/2})(2d_{3/2})$ and for the 4^+ and 6^+ states the pair is picked up

Table 5.3: Optical model parameters used for the proton, triton and bound state of the transferred di-neutron cluster in the DWBA analysis. The proton parameters are used from Ref. [156], tritons from Ref. [159] and neutrons from Ref. [154].

	p	t	n
V_r	52.938	$0.436E_t^2 - 0.1456E_t + 186.8304^a$	$-^b$
r_r	1.206	1.094	1.170
a_r	0.690	0.795	0.75
W_v	1.226	$-0.0097E_t^2 + 0.5025E_t + 7.383$	-
r_v	1.249	1.2898	-
a_v	0.690	1.2307	-
W_s	9.105	$-0.6451E_t + 27.8117$	-
r_s	1.249	1.1718	-
a_s	0.69	0.8791	-
V_{so}	5.90	1.9029	-
r_{so}	1.108	0.4921	-
a_{so}	0.63	0.0497	-
r_c	1.260	1.4219	-
λ			25

^a E_t is the kinetic energy of the outgoing triton calculated for the excited state.

^bWell depth adjusted to reproduce the BE for each neutron to be equal to half the two-neutron separation energy for the excited state (see Eq. (5.1)).

from the $(1g_{7/2})$ orbit. The shape of the angular distributions in (p, t) reactions does not depend on the orbital selection for the 2 neutron pick up but the magnitude changes with the choice of pick up orbital.

The assumption that the single-step (p, t) reaction mechanism is a pure $S = 0$ neutron pair transfer with no coupled channel interactions, allow the excitation of only natural parity states ($J = L, \pi = (-1)^L$). DWBA angular distributions are then calculated assuming a specific $J = L$ transfer. These angular distributions are compared with experimental data to identify the spins and parity of the states populated in this reaction. As evident from the angular distribution plots in Appendix C, the assumption of a single-step, two-neutron cluster pickup mechanism in a zero-range approximation worked sufficiently well to describe most of the states produced in this reaction. All the excited states observed in this reaction are categorized on the basis of J^π assignments and each of these are discussed in details in the following sections.

5.3.1 $J^\pi = 0^+$ states

The identification of 0^+ states in (p, t) reactions is fairly simple due to the characteristic large forward angle cross sections that falls rapidly between 0° and 20° . This is evident in comparisons made between experimental and theoretical DWBA angular distributions. Following this procedure, a total of 12 0^+ states are identified in ^{136}Ba of which 6 states are being reported for the first time and the ambiguity in J^π is resolved for two states. While we see new 0^+ states at 3278.6, 3426.7, 3921, 4147, 4344, 4444 and 4534 keV, the 2141.38 keV state listed in Ref. [129] is not populated in this reaction. We also rule out the possibility of a doublet at this focal plane position.

- **Ex = 1579.7 keV** Julian and Fessler [162] first proposed the 1578.9 keV state based on the β decay of ^{136}La to the 1578.9 keV level of ^{136}Ba . The authors suggested the state could be $J^\pi = 0^+, 1^+, \text{ or } 2^+$. They assigned a spin and parity of 2^+ to this level based on the systematics of the 2^+ states in similar nuclei and due to the non observation of a 1578 keV gamma to the ground state of ^{136}Ba . However, in later work conducted by two separate groups [161, 163, 164], the observation of the 1579.8 keV γ transition, the systematics of even-even nuclei [165] and the observation of the isotropically distributed 760.5 keV γ -transition to the 818 keV level [166] from the level at 1578 keV, established the $J^\pi = 0^+$ assignment of this state. While the authors of Ref. [161] did not rule out the possibility of spins 1, 2 and 3, subsequent work in ^{136}Ba has been carried out assuming this state is a 0^+ .

In this (p, t) measurement, the shape of the angular distributions for all the $J^\pi = 0^+$ transitions are well reproduced by the DWBA calculations except for this excited state. To understand this deviation we investigated various scenarios. We first explored the possibility of a contaminant and an unresolved doublet in the vicinity of the 1578 keV state. We also investigated the possibility of non-zero L transfers ($L = 1, 2, 3, 4$) as well as coupled-channel and multi-step effects using CHUCK3 [167]. None of these gave a suitable explanation and the discrepancy in the angular distribution of this state remains unresolved.

- **Ex = 2783.4 keV** The nuclear data sheets for ^{136}Ba [85] reports a level at 2784.41 keV with J^π assignment of (0^+) . This state has been identified in $^{135}\text{Ba}(n, \gamma)$ [161, 168] and $^{136}\text{Ba}(n, n'\gamma)$ [166] studies. The angular distribution for this state in our (p, t) measurement is reproduced by the $L = 0$ transfer, confirming $J^\pi = 0^+$ assignment for this state in agreement with the latest update of the nuclear data sheets (NDS) [129].
- **Ex = 2977.1 keV** The NDS [85] reports a level at 2976.87 keV with $J^\pi = (2^+, 3^+, 4^+)$. This level was first reported in (n, γ) studies in Ref. [168] with no spin-parity assignment. In a later work on $(n, n'\gamma)$ by Al-Hamidi *et al.* [169] this state is reported as $2^+, 3^+, (4^+)$. The angular distribution for this state matches a $L = 0$ transfer, ruling out the tentative assignments.
- **Ex = 3278.6, 3921, 4344, 4444 keV** No levels are reported in the NDS [85] at these excitation energy. The angular distribution for these 4 states is consistent with a $L = 0$ transfer. Thus these states are assigned $J^\pi = 0^+$.
- **Ex = 3426.7 keV** Based on the large forward angle cross sections and the appearance of the first minimum at $\sim 15^\circ$ as from the DWBA calculations, this state is assigned $J^\pi = 0^+$. No state is reported in the NDS [85] at this energy.
- **Ex = 4147 keV** The unevaluated dataset reports a level at 4137 keV with $J^\pi = 1$ observed in $^{136}\text{Ba}(\gamma, \gamma')$ studies [170]. This state is weakly populated in this work. The angular distribution for this state follows the characteristic shape of a $L = 0$ transfer at the forward angles but the second maximum is damped, giving it the shape of a $L = 4$ angular distribution between 20° and 45° . As this states is weakly excited and multi-step processes could alter the shape of the angular distribution the state is tentatively assigned as $(0^+, 4^+)$.
- **Ex = 4534 keV** A broad background from a contaminant on the focal plane at 5° and 10° sits in the region of the 4531 keV peak. As a result no cross sections could be extracted for this peak at these angles. While the uncertainty on the cross

sections for this state is large, from the limited information available, the angular distribution best matches a $L = 0$ transfer. The DWBA prediction for $L = 4$ is also shown in the figure (in Appendix C) to clarify any ambiguities. No information is currently available in the NDS [85] for this state. The only available information is through the most recent $^{136}\text{Ba}(\gamma, \gamma')$ studies [170] where a state at 4536.4 keV is reported as $J = 1$.

5.3.2 $J^\pi = 1^-$ states

- **Ex = 2399.8 keV** Three levels are reported in the NDS [85] around this excitation energy. The first level at 2390.79 keV with $J^\pi = 3^-$ was observed in the $^{135}\text{Ba}(n, \gamma)$ and $^{136}\text{Ba}(n, n'\gamma)$ reactions [161, 166, 169]. However, recent work in $(n, n'\gamma)$ [171] determines the spin and parity of this state to be 3^+ , which being an unnatural parity state is not likely to be populated strongly in this reaction. The other two levels are at 2392.1 and 2399.87 keV, both with $J^\pi = (1^+, 2^+)$ [85]. The 2392.1 keV level was observed only in (n, γ) studies [168]. The 2399.87 keV has been observed in (n, γ) [161, 169], (d, p) and $(n, n'\gamma)$ studies. The most recent $(n, n'\gamma)$ work [171] report the $J^\pi = (1)^+$ for this state. In this work, the general shape of the angular distribution agrees with a $L = 1$ transfer and thus we assign the state as (1^-) .
- **Ex = 2935.1 keV** The nuclear data sheets report two levels [85, 129] in the vicinity of 2934 keV, one at 2934.40 keV and the other at 2946 keV. The 2934 keV level was observed in $^{135}\text{Ba}(n, \gamma)$ reaction [168] but no spin parity assignment was reported. However later work using the $(n, n'\gamma)$ reaction [169] report $J^\pi = (1, 2^+)$ for this state. The 2946 keV state was observed in the (n, γ) studies [168] and reported as $J^\pi = 0^{(+)}, 1, 2, 3^+$. In this work we could not make a definite spin-parity assignment but the experimental data seems to follow an angular distribution for a $L = 1$ as well as a $L = 2$ transfer. Thus we tentatively assign this state as $J^\pi = (1^-, 2^+)$.
- **Ex = 3044.5 keV** This state is reported in the NDS [85] at an excitation energy of 3044.58 keV as a $1^{(-)}$ state. This level has been observed in (n, γ) [161, 168]

(γ, γ') [172, 173] and $(n, n'\gamma)$ [169] studies. The negative parity of the state was confirmed in Ref. [169]. In our work, the angular distribution for this state is reproduced by assuming an unresolved doublet with $L = 1$ (32%) and $L = 3$ (68%).

- **Ex = 3369 keV** This state is reported in the NDS [85] at an excitation energy of 3370.07 keV as observed in (n, γ) [161, 168, 174], (γ, γ') [172, 173] and $(n, n'\gamma)$ [169] experiments with spin 1. The authors of Ref. [169] however quote $J^\pi = 1^+$. In our work, the angular distribution for this state resembles a $L = 2$ transfer better than $L = 1$. Hence we assign $J^\pi = (1^-, 2^+)$ to this state.
- **Ex = 3435.1 keV** A level close to this energy was first reported by Becvar *et al.* [163] and later by Gelletly *et al.* [161] from (n, γ) experiments, but no spin-parity assignments were made for this state. A nuclear resonance fluorescence experiment performed later by Metzger [172] led to the 1^- assignment for this state. Experimental angular distribution for this state resembles a $L = 2$ transfer better than $L = 1$. Hence we assign $J^\pi = (1^-, 2^+)$.
- **Ex = 3799 keV** This state was first observed in the (n, γ) studies of Gelletly *et al.* [161], where they suggested the spin of this state as $J \leq 3$. In the $(n, n'\gamma)$ work by Al-Hamidi *et al.* [169] this state was assigned $J^\pi = 1^-$. The state being weakly populated, does not distinctly resemble a 1^- angular distribution. We thus tentatively assign this state $J^\pi = (1^-)$.

We found discrepancies between the experimental angular distributions and DWBA predictions for even well-known, strongly populated 1^- states. Thus we recommend that states with 1^- assignments be used with caution for any future work.

5.3.3 $J^\pi = 2^+$ states

In this work we identify 12 new 2^+ states at 3221, 3660, 3739, 3842, 3902, 4052, 4127, 4250, 4394, 4487, 4497 and 4547 keV. The ambiguities in 6 energy levels at 2660.4, 3021.1, 3209.7, 3244.7, 3336.2 and 3971 keV could be resolved based on our angular distribution measurements. These states are discussed below.

- **Ex = 2660.4 keV** Two levels are reported in the adopted NDS [85] at 2659.72 keV, $J^\pi = 3$ to 5 and 2661.41 keV, $J^\pi = 1^+, 2^+$. The authors of Ref. [171] have placed tentative assignment of $J^\pi = 5^{(-)}$ for 2659.72 keV and $J^\pi = (2)^+, (4)^+$ for 2661.41 keV from $^{136}\text{Ba}(n, n'\gamma)$. The angular distributions for this level in our work is consistent with a $L = 2$ transfer.
- **Ex = 3021.1 keV** Two states are reported in the adopted NDS at 3019.8 and 3021.92 keV, both with the J^π assignments of $(1, 2^+)$. The authors of Ref. [161] report the level at 3019.9 keV based on $^{135}\text{Ba}(n, \gamma)$ reaction. The level was deduced from observation of a γ transition between the capture state and a level at 3019.9 keV followed by γ transitions to spin 0 (1579.2 keV) and spin 2 (818.6, 1550.5 keV) states. The spin $(1, 2)$ assignment is made based on the condition that the 1579 keV state is 0^+ in nature. The authors of Ref. [171] in their $^{136}\text{Ba}(n, n'\gamma)$ work do not report the state at 3019.8 keV but do report 3022.19 keV with $J^\pi = (1, 2^+)$ following the de-excitation of a 2203.63 keV γ to the 818.5 keV first excited 2^+ state of ^{136}Ba . The angular distributions for the 3021.1 keV level in this work is well reproduced by a $L = 2$ transfer. We thus assign it $J^\pi = 2^+$.
- **Ex = 3209.7 keV** In Ref. [168] a level at 3213.5 keV populated via $^{135}\text{Ba}(n, \gamma)$ reaction is reported with tentative J^π assignments of $0^{(+)}, 1, 2, 3^+$. The angular distribution for this excited state is consistent with $L = 2$. We thus assign it $J^\pi = 2^+$, thereby resolving the ambiguity in this state.
- **Ex = 3244.7 keV** A level at 3242.12 keV with J^π assignment of $(2, 3^+, 4^+)$ is reported in the NDS [85]. This state is reported only in $^{136}\text{Ba}(n, n'\gamma)$ measurements, first in 1994 [169] and later in 2008 [171]. In our case, this level follows the angular distribution for a $L = 2$ transfer. Thus our assignment of $J^\pi = 2^+$ resolves the ambiguity in this state.
- **Ex = 3336.2 keV** This level is only reported in the $^{136}\text{Ba}(n, n'\gamma)$ work of Ref. [169] with $J = 1 - 3$. The angular distribution from this work is reproduced by $L = 2$ transfer, thus our assignment is $J^\pi = 2^+$.

- **Ex = 3972 keV** The only excited states reported in NDS [85, 129] in the vicinity of this state are 3965.51 keV with $J^\pi = (1, 2^+)$ and 3979.76 keV as $J^\pi = (1)$. From our analysis this state is a 2^+ and is possibly reported for the first time.
- **Ex = 3221.3, 3660, 3739, 3842, 3902, 4052, 4127, 4250, 4394, 4487, 4497, 4547 keV** All these levels are being reported for the first time for ^{136}Ba . The angular distributions all of these levels exhibit a $L = 2$ behavior. We thus assign $J^\pi = 2^+$ for all these excited states.

5.3.4 $J^\pi = 3^-$ states

In addition to the 3^- state in ^{136}Ba at 2532.57 keV, three additional 3^- states are observed where a definite assignment could be made. However the first 3^- state at 2390.79 keV is not observed in this (p, t) measurement.

- **Ex = 3768 keV** In the NDS [85, 129] a level is identified at 3767.1 keV with $J^\pi = 1^{(-)}, 2, 3^+$ deduced from (n, γ) studies [161]. In this work, the angular distributions is reproduced by assuming a $L = 3$ transfer. We assign this state $J^\pi = 3^-$.
- **Ex = 4312, 4451 keV** Angular distributions for both these states are consistent with a $L = 3$ transfer. No level is reported in the NDS at these excitation energies. Our assignment for these two levels is $J^\pi = 3^-$.

5.3.5 $J^\pi = 4^+$ states

The difference in angular distribution for $L = 4$ and $L = 5$ is subtle. While the maximum of the distribution for the 4^+ states is approximately between $25^\circ - 35^\circ$, the 5^- distribution peaks between $30^\circ - 40^\circ$. For both these L -transfers, the maximum of the distribution varies within an order of magnitude, as opposed to the 0^+ or 2^+ states. While the 4^+ DWBA distribution has its first minimum at $\sim 15^\circ$, experimental angular distributions do not always follow this pattern. As such, one needs to compare experimental cross sections with DWBA for both 4^+ and 5^- . By carefully following this prescription, we identify

total of 7 states including the well known ones at 1866.5 and 2053.8 keV, in addition to several other states with a tentative assignment of $J^\pi = 4^+$.

- **Ex = 2839.1 keV** In the NDS [129] this level is reported at 2840.74 keV with spin-parity (4^+). This level was observed for the first time in $^{136}\text{Ba}(n, n'\gamma)$ measurement [166] but the authors did not include it in their level scheme for ^{136}Ba . The authors did not report the J^π for this state either. In later work by Al-Hamidi *et al.* [169], γ transitions corresponding to this level were observed. The authors report $J^\pi = 4^+$ for this level. Our differential cross angular distributions for this level are consistent with $J^\pi = 4^+$.
- **Ex = 3547.9 keV** An excited state at 3550.70 keV with $J^\pi = 0$ to 4 is reported in NDS [129]. This state is only observed in $^{136}\text{Ba}(n, n'\gamma)$ in Ref. [169] and assigned spin and parity of $2^+, 3^+, 4^+$. We find the χ^2 minimum value for the angular distribution consistent with $L = 4$ transfer.
- **Ex = 3640 keV** No excited state is reported for this energy in the evaluated or unevaluated nuclear datasets [85, 129]. Our analysis favors the angular distribution for $J^\pi = 4^+$.
- **Ex = 3980 keV** The NDS [129] lists the spin for a level at 3979.76 keV as (1), based on $^{136}\text{Ba}(\gamma, \gamma')$ data [172, 173]. In our work a $L = 4$ transfer represents the data better than $L = 1$.
- **Ex = 4120 keV** No level is reported at this energy for ^{136}Ba . Our measured differential cross section is well reproduced assuming the state is 4^+ . This assignment gives minimum value of χ^2 , when different L transfers are compared with experimental data.

5.3.6 $J^\pi = 5^-$ states

The adopted level scheme for ^{136}Ba reports a single 5^- state at 2140.2 keV [129]. In this section we discuss previously unreported states where definitive $J^\pi = 5^-$ could be made. States with tentative 5^- assignments are discussed later.

- **Ex = 2854.3, 3007.2, 3297.1 keV** The angular distribution for these states agree with DWBA predictions for a $L = 5$ transfer. No states are reported in the NDS [85] at this excitation energy. We assign these three states with $J^\pi = 5^-$.
- **Ex = 3691 keV** A level is reported in the NDS at 3691.92 keV [129] with a tentative spin assignment of 1 to 3. This level is adopted from $^{135}\text{Ba}(n, \gamma)$ studies [161], where the authors suggests the spin of this level to be 2 or 3. The angular distribution for this state is well reproduced by a $L = 5$ transfer. Therefore this might not correspond to the 3691.89 keV state reported in Ref. [129].

5.3.7 $J^\pi = 6^+$ states

The first excited 6^+ at 2207.1 keV [129] is not observed in this work. For the next possible 6^+ state at 2298.69 keV, the NDS reports a tentative (6^-) assignment [85, 129]. Our measured angular distribution for the state at 2299.0 keV is consistent with a 6^+ assignment. A new 6^+ state at 3170.0 keV is also observed for the first time in this measurement. Other possible 6^+ states are discussed in Section 5.3.9.

5.3.8 $J^\pi = 7^-$ states

In addition to the first 7^- state at 2030.5 keV [129], we observe a new 7^- state at 2646.4 keV. This level has not been reported in the adopted level scheme [129]. Another state at 3883 keV that is tentatively assigned a 7^- is discussed in detail in Section 5.3.9.

5.3.9 Tentative assignments

About 26 states are discussed in this section, where J^π assignments could not be made with certainty. For some of these states, due to low statistics, a definitive L cannot be accepted solely on the basis of χ^2 minimization. On the contrary, for some of the strongly populated states, the DWBA distributions do not reproduce the experimental data (as well as it does for most other states). Consequently, the J^π assignment for these states are tentative.

- **Ex = 2543.8 keV** The nuclear data sheets report a level at 2544.51 keV [85] with tentative spin and parity assignment 0 to 4. In a $(n, n'\gamma)$ [169] study, this level is assigned $J^\pi = 4^+$. In our work the angular distribution is compatible with $J^\pi = 5^-$ and $J^\pi = 6^+$, hence we tentatively assign this state to be $(5^-, 6^+)$.
- **Ex = 2587.6 keV** The NDS [85] report a level at 2587.05 keV with spin parity 3 to 5. This level is reported from $^{136}\text{Ba}(n, n'\gamma)$ measurements in Refs. [169] and [171]. The authors of Ref. [171] suggest spins of 5 or 6^+ . In our case, this level follows the angular distribution for a $L = 4$ transfer at larger angles but is better reproduced by a $L = 5$ transfer at the smaller angles. The chi-squared for both these distributions are very similar ($\chi_{4^+}^2 = 100$, $\chi_{5^-}^2 = 108$). We therefore tentatively assign a $J^\pi = 4^+, 5^-$ to this state.
- **Ex = 2829.9 keV** No level is reported for this excitation energy in the NDS [85]. From our analysis, the χ^2 minimum corresponds to $L = 7$. Due to the low statistics in this peak, the $L = 6$ transfer cannot be ignored, hence we tentatively assign $J^\pi = (6^+, 7^-)$ for this state.
- **Ex = 2902.0 keV** The adopted level scheme has a level at 2905.0 keV that was identified in the $^{135}\text{Ba}(n, \gamma)$ reaction [168]. No spin and parity assignment is reported for this state. Our angular distribution indicates both $L = 4$ as well as $L = 5$ transfer, making it difficult for us to assign a spin and parity for this state. The χ^2 minimum however favors a $L = 5$ angular distribution. We thus tentatively assign this state $J^\pi = (4^+, 5^-)$.
- **Ex = 3088.7 keV** As this state is populated quite weakly, the angular distribution lacks the required statistics for a conclusive measurement. The magnitude and shape for the cross sections available indicate a $L = 4$ or $L = 5$ transfer. We thus tentatively assign this state $J^\pi = (4^+, 5^-)$.
- **Ex = 3221.3 keV** Based on the agreement between DWBA and experimental angular distribution up to $\sim 35^\circ$ this state is tentatively assigned $J^\pi = (2^+)$. This level is not reported in the NDS [129].

- **Ex = 3310 keV** No excited state is reported at this energy in the NDS [85, 129]. The angular distribution in this work is reproduced by a $L = 1$ as well as a $L = 2$ transfer. Our chi-squared analysis yields a minimum for $L = 2$ transfer. We thus tentatively assign this state $J^\pi = (1^-, 2^+)$.
- **Ex = 3498.7 keV** The NDS report two levels in the vicinity of 3498 keV, one at 3505.5 keV and the other at 3508.7 keV [129]. The 3505.5 keV level was observed in a $^{135}\text{Ba}(n, \gamma)$ reaction [168] with $J^\pi = 0^{(+)}, 1, 2, 3^+$. The 3508.7 keV state with $J^\pi = 2, 3^+, (4^+)$ was observed in the $(n, n'\gamma)$ studies [169]. This is a strongly populated state and the angular distribution is reproduced reasonably well by assuming an unresolved triplet with $J^\pi = 2^+$ (38%), $J^\pi = 4^+$ (30%) and $J^\pi = 5^-$ (32%).
- **Ex = 3708 keV** The NDS report two levels at 3706.1 and 3706.4 keV with spin-parity assigned as $(1, 2^+)$ for the former and none for the later [129]. The first state was observed in $(n, n'\gamma)$ reactions [166, 169] and the second in $^{139}\text{La}(^{82}\text{Se}, X\gamma)$ [175] and $^{198}\text{Pt}(^{136}\text{Xe}, X\gamma)$ reactions [176]. While no spin-parity assignment is made in Ref. [175] and [176], Al-Hamidi *et al.* [169] reported this state as spin 1. The large uncertainty on the cross sections in the current work does not allow to distinguish between a $J^\pi = 1^-$ or 2^+ assignment. On the basis of a χ^2 analysis, the 2^+ assignment is favored. Thus we tentatively assign this state $J^\pi = (1^-, 2^+)$.
- **Ex = 3720 keV** The angular distribution of this state is typical of large L transfers i.e. increased cross sections with larger scattering angles. As the state is weakly populated, a definite J^π assignment cannot be made. Our analysis indicates that this state is populated by a $L > 5$ transfer.
- **Ex = 3739 keV** No state is reported at this excitation energy in the NDS [85]. Our measured angular distributions resembles a $L = 2$ transfer but since the cross sections have large uncertainties, a definitive assignment could not be made. We thus make a tentative assignment of $J^\pi = (2^+)$.
- **Ex = 3754 keV** No information is available in the NDS [85] for this excitation energy. Our least squared minimization procedure indicates both the $L = 4$ and

$L = 5$ transfers. We thus tentatively assign this state $J^\pi = (4^+, 5^-)$.

- **Ex = 3808 keV** No level is reported at this excitation energy in the NDS [85]. Due to the low statistics in the peaks and large uncertainties on the cross sections a definitive spin parity assignment cannot be made for this state. The χ^2 minimum however corresponds to a $L = 3$ transfer. Thus the tentative assignment for this state is (3^-) .
- **Ex = 3858 keV** Two levels are reported in the NDS [85] in the vicinity of 3858 keV, one at 3852.7 keV with $J^\pi = (1, 2^+)$ deduced from $(n, n'\gamma)$ [169] and the other at 3863.47 keV with $J^\pi = 0^{(+)}, 1, 2^+$. The angular distribution corresponding to $L = 5$ or $L = 6$ reproduces our data better compared to $L = 0 - 4$. This state is thus tentatively assigned $J^\pi = (5^-, 6^+)$.
- **Ex = 3868 keV** The NDS [129] reports an excited state at 3863.47 keV with spin-parity assignment $(1, 2^+)$, which was observed with the (n, γ) reaction [161,174]. The angular distribution for this state does not represent pure 2^+ or 1^- . It is however well reproduced assuming a doublet with $J^\pi = 2^+$ (55%) and $J^\pi = 6^+$ (45%).
- **Ex = 3883 keV** A state at 3881.17 keV is reported in the NDS [129] from (n, γ) studies [169] with spin assignment 1 to 3. This level is also observed with the (γ, γ') reaction [170] but no definite spin parity assignments were made. However, the authors report γ transitions from this level to the 0^+ ground state, implying the state is either a spin 1 or 2. The DWBA distribution for this state is partially compatible with a $L = 1$ transfer. We thus tentatively assign this state $J^\pi = (1^-)$.
- **Ex = 3994 keV** The NDS report two levels, one at 3992.56 keV and the other at 4008.6 keV [129]. Both the levels were observed in $^{135}\text{Ba}(n, \gamma)$ reactions [168] with $J^\pi = 0^{(+)}, 1, 2, 3^+$ for the first and $1, 2^+$ for the second. The angular distribution for our identified 3994 keV state is well reproduced by assuming a doublet with $J^\pi = 2^+$ (50%) and $J^\pi = 3^-$ (50%). The 4008 keV is very weakly populated with the (p, t) reaction, with a maximum cross section of $\sim 1 \mu\text{b}/\text{sr}$.

- **Ex = 4064 keV** No information is available in the NDS [85] for this excitation energy. Our least squared minimization procedure indicates both the $L = 5$ and $L = 6$ DWBA distributions. We thus tentatively assign this state $J^\pi = (5^-, 6^+)$.
- **Ex = 4070 keV** The angular distributions for this weakly populated state is reproduced reasonably well with both $J^\pi = 2^+$ and $J^\pi = 3^-$. In the absence of any additional information, this state is tentatively assigned $J^\pi = (2^+, 3^-)$.
- **Ex = 4156 keV** No excitation energy is reported in the NDS at ~ 4150 keV. The most probable J^π assignments for this angular distribution are $4^+, 5^-, 6^+$. The χ_{min}^2 corresponds to a $L = 5$ transfer for this state.
- **Ex = 4233 keV** Recent work in $^{136}\text{Ba}(\gamma, \gamma')$ [170] reports a level at 4231.2 keV as spin 1. This level is observed via a 4231 keV γ transition to the ground state. In our (p, t) measurement, the angular distribution is compatible with $J^\pi = 2^+$ or 3^- , with the χ_{min}^2 value suggesting a $L = 2$ transfer.
- **Ex = 4279 keV** No level is reported at this energy in the NDS [85]. Our measured angular distribution indicates $J^\pi = 1^-, 2^+$. As no definitive assignments can be made, we tentatively assign this state $(1^-, 2^+)$.
- **Ex = 4383 keV** No excitation energy is reported in the NDS [129] for this weakly populated state. The most probable J^π assignments for our angular distribution could be 4^+ or 5^- . The χ_{min}^2 favors $L = 4$ transfer. Our assignment therefore $J^\pi = (4^+, 5^-)$.
- **Ex = 4416 keV** A level at 4413.3 keV was recently observed in $^{136}\text{Ba}(\gamma, \gamma')$ studies [170], where the authors tentatively assign it as spin 1. In this work the angular distribution is compatible with $J^\pi = 1^-$ and 2^+ but χ_{min}^2 favors the state to be 1^- .
- **Ex = 4421 keV** The angular distribution for this state is consistent with both $J^\pi = 1^-$ and 2^+ . However, the minimum value of χ^2 indicates $J^\pi = 1^-$. Thus we tentatively assign this state $(1^-, 2^+)$.

- **Ex = 4475 keV** A level at 4475.18 keV was recently observed in the $^{136}\text{Ba}(\gamma, \gamma')$ studies [170] where the authors tentatively assign it as spin 1. However, the angular distribution for this state is consistent with $J^\pi = 2^+$ and 3^- . The χ_{min}^2 corresponds to $J^\pi = 3^-$. Thus we tentatively assign this state $(2^+, 3^-)$.

5.3.10 Indefinite assignments

Due to large uncertainties and in some cases incomplete angular distributions, no reliable spin-parity assignment can be made for excited states at 3108.7, 3356.7, 3684, 3961, 4079, 4107, 4185, 4193, 4201, 4213 4406, 4517 and 4558 keV.

5.4 Neutron pairing correlations in ^{136}Ba

It is known from theoretical calculations that the neutrinoless double beta decay NME are enhanced if wave functions of the parent and daughter nuclei are dominated by BCS like pairing correlations [32]. The (p, t) strength populating excited 0^+ states relative to the ground state gives substantial information about the neutron pairing correlations as well other important nuclear structure related information. The relative strength (ϵ) can be calculated as

$$\epsilon = \left(\frac{\left(\frac{d\sigma}{d\Omega} \right)_{0_{\text{ex}}^+}^{\text{Expt}}}{\left(\frac{d\sigma}{d\Omega} \right)_{0_{\text{ex}}^+}^{\text{DWBA}}} \right) \left(\frac{\left(\frac{d\sigma}{d\Omega} \right)_{0_{\text{gs}}^+}^{\text{Expt}}}{\left(\frac{d\sigma}{d\Omega} \right)_{0_{\text{gs}}^+}^{\text{DWBA}}} \right)^{-1} \quad (5.2)$$

The (p, t) reaction cross section depends strongly on the reaction Q -value. Therefore relative strength is corrected for the Q -value dependency and other kinematic effects by dividing the measured cross-sections by its DWBA predicted cross-sections. The resulting relative strengths for each excited state at $\theta_{\text{com}} \sim 5^\circ$ are tabulated in Table 5.4. Also tabulated are relative normalization factors at forward angles for the DWBA predictions. As evident from the table, there is a large fragmentation in the (p, t) transfer strength to the $0_2^+ = 2315$ keV and $0_3^+ = 2784$ keV states. The combined strength to the 0_2^+ and 0_3^+ states that lie just above the pairing gap is $\sim 30\%$ the ground state strength. This is a clear indication of breakdown in neutron BCS approximation in ^{136}Ba . All 0^+ states

produced in this work are shown in Fig. 5.5.

Table 5.4: Relative strength of populating the excited 0^+ states. The relative strength is calculated as shown in Eq. (5.2). The sum in the last row is the integrated strength of all the excited 0^+ states. The excitation energy in the first column are the values from in this work.

Ex (keV)	σ (mb/sr) $ \theta_{CM}\sim 5$	ϵ (%) $ \theta_{CM}\sim 5$	N ($5^\circ - 15^\circ$)	ϵ (%)
0.0	1.90(1)	100	21392(1602)	100
1579.7(6)	0.063(1)	4.42(8)	1151(300)	5(1)
2315.5(6)	0.149(2)	16.0(2)	3259(625)	15(3)
2783.4(7)	0.130(1)	17.5(2)	3184(189)	15(1)
2977.1(7)	0.0040(3)	0.61(5)	137(13)	0.64(8)
3278.6(7)	0.0355(8)	6.4(1)	764(250)	4(1)
3426.7(8)	0.0072(4)	1.44(9)	262(17)	1.2(1)
3921(1)	0.0084(4)	2.5(1)	467(38)	2.2(2)
4147(1)	0.0160(7)	5.8(3)	1191(95)	6(1)
4344(1)	0.0048(3)	2.1(1)	430(39)	2.0(2)
4444(1)	0.0066(4)	3.2(2)	645(61)	3.0(4)
4534(2)	–	–	139(71)	0.7(3)
Σ		59.8 (5)		54 (4)

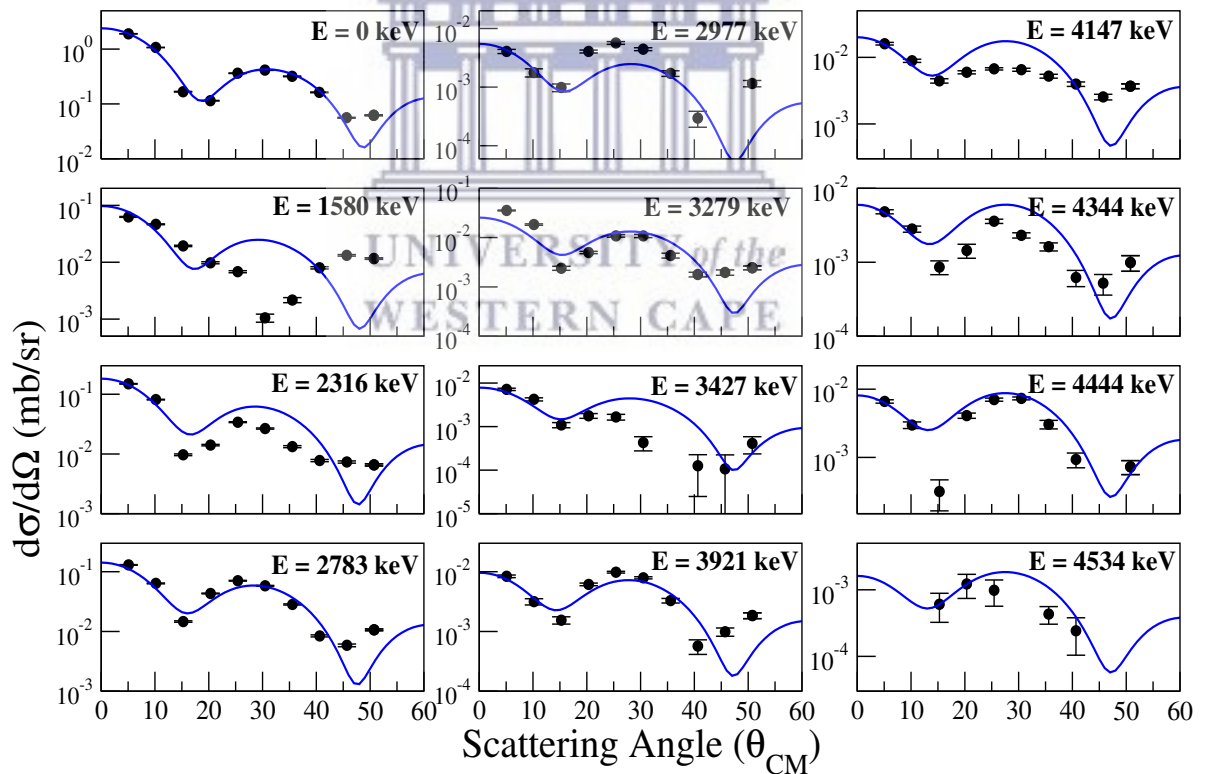


Figure 5.5: 0^+ states populated in this (p, t) reaction. The measured cross-sections are compared to normalized DWBA curves.

6 | $^{138}\text{Ba}(d, \alpha)^{136}\text{Cs}$ Results

I have not failed. I've just found 10,000 ways that won't work.

Thomas A. Edison

The motivation of this experiment was to perform a precision spectroscopy of low-lying states ^{136}Cs . From this experiment a total of 74 states were observed, up to an excitation energy of 2.6 MeV. Of these, definite spin parity assignments could be made for 35 strongly populated states. Spectroscopic factors were obtained for all the states where definite (or tentative) J^π assignments could be made.

6.1 Energy Calibration

Due to large Q value of the $^{138}\text{Ba}(d, \alpha)$ reaction, the focal plane detector of the Q3D spans ~ 2.5 MeV excitation energy in ^{136}Cs per 'momentum bite'. Beyond this energy, the density of states became quite large, given the resolution of the Q3D spectrograph. Thus, as opposed to the $^{138}\text{Ba}(p, t)$, only one momentum bite was collected per Q3D angle for this reaction. Since states in ^{136}Cs had not been studied extensively in the past, the excitation energy information on this odd-odd nucleus was sparse [129]. Thus, an external calibration is performed using $^{92}\text{Zr}(d, \alpha)^{90}\text{Y}$ and $^{94}\text{Mo}(d, \alpha)^{92}\text{Nb}$ reactions by following the procedure outlined in Section 4.3. The focal plane spectra for ^{90}Y and ^{92}Nb were obtained at the same magnetic settings and under exactly similar experimental conditions as the $^{138}\text{Ba}(d, \alpha)$ reaction. These particular calibration reactions were chosen because the Q values of these reactions are very similar to the $^{138}\text{Ba}(d, \alpha)$ reaction, thus preventing large extrapolations.

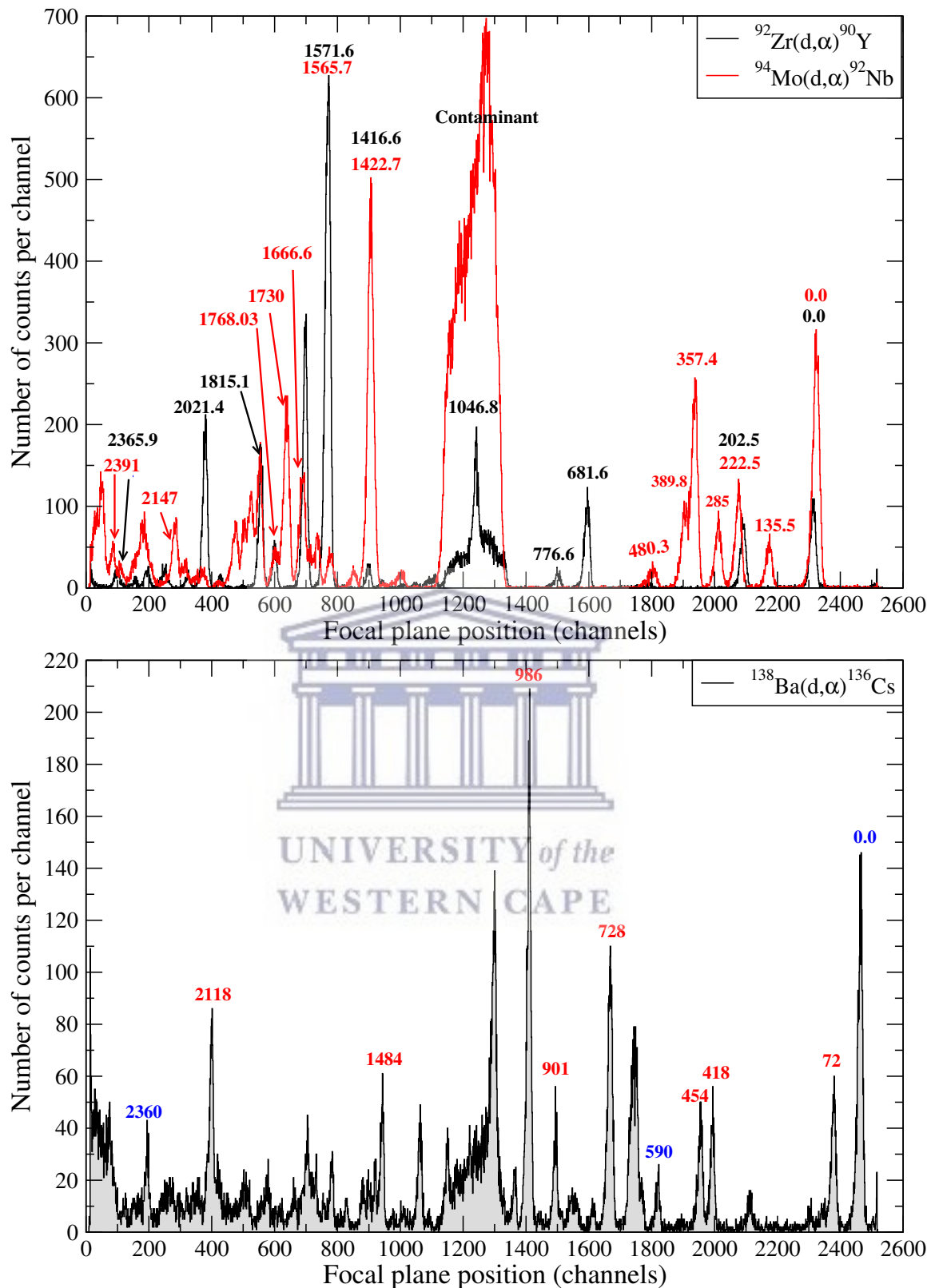


Figure 6.1: Focal plane spectra at $\theta_{\text{lab}} = 10^\circ$ for $^{138}\text{Ba}(d, \alpha)$ (bottom), $^{94}\text{Mo}(d, \alpha)$ and $^{92}\text{Zr}(d, \alpha)$ (top) reactions. The three spectra were obtained with the same field settings. The red labels (in the top panel) mark the excitation energies (in keV) of ^{92}Nb [149] while black labels mark well known ^{90}Y states [150]. In the $^{138}\text{Ba}(d, \alpha)$ spectrum, the blue labels are for the previously known states and all the other peaks are new states identified in this work. Some of the most prominent ones are labeled in red.

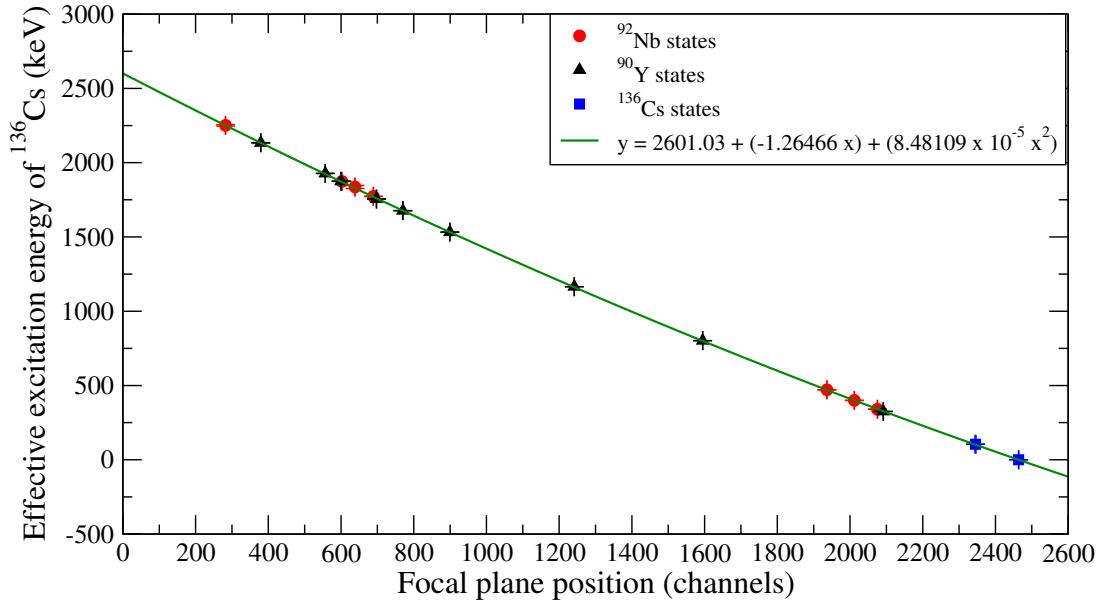


Figure 6.2: Energy calibration for $^{138}\text{Ba}(d, \alpha)^{136}\text{Cs}$ reaction using effective excitation energies from $^{92}\text{Zr}(d, \alpha)^{90}\text{Y}$ and $^{94}\text{Mo}(d, \alpha)^{92}\text{Nb}$.

Table 6.1: Q values for the $^{138}\text{Ba}(d, \alpha)$, $^{94}\text{Mo}(d, \alpha)$ and $^{92}\text{Zr}(d, \alpha)$ reaction [177].

Reaction	Q-value (keV)
$^{138}\text{Ba}(d, \alpha)^{136}\text{Cs}$	8787.87
$^{94}\text{Mo}(d, \alpha)^{92}\text{Nb}$	8750.03
$^{92}\text{Zr}(d, \alpha)^{90}\text{Y}$	8745.84

The Q values for these three reactions are compared in Table 6.1 and the focal plane spectra are shown in Fig. 6.1. Relation between the effective ^{136}Cs excitation energy and focal plane centroids of the calibration peaks is shown in Fig. 6.2.

6.2 Elastic scattering

As outlined in Section 4.4.1, we chose appropriate optical model parameters (OMPs) for deuterons and alpha particles by comparing the experimental elastic scattering cross sections with the DWBA calculations. For the $d-^{138}\text{Ba}$ incoming channel, the global deuteron OMP set of An and Cai [178] yields a minimum χ^2 with respect to our data. This comparison is shown in Fig. 6.3. In the absence of experimental $^{136}\text{Cs}(\alpha, \alpha)$ data, we used available elastic scattering cross section data on similar mass nuclei, using the

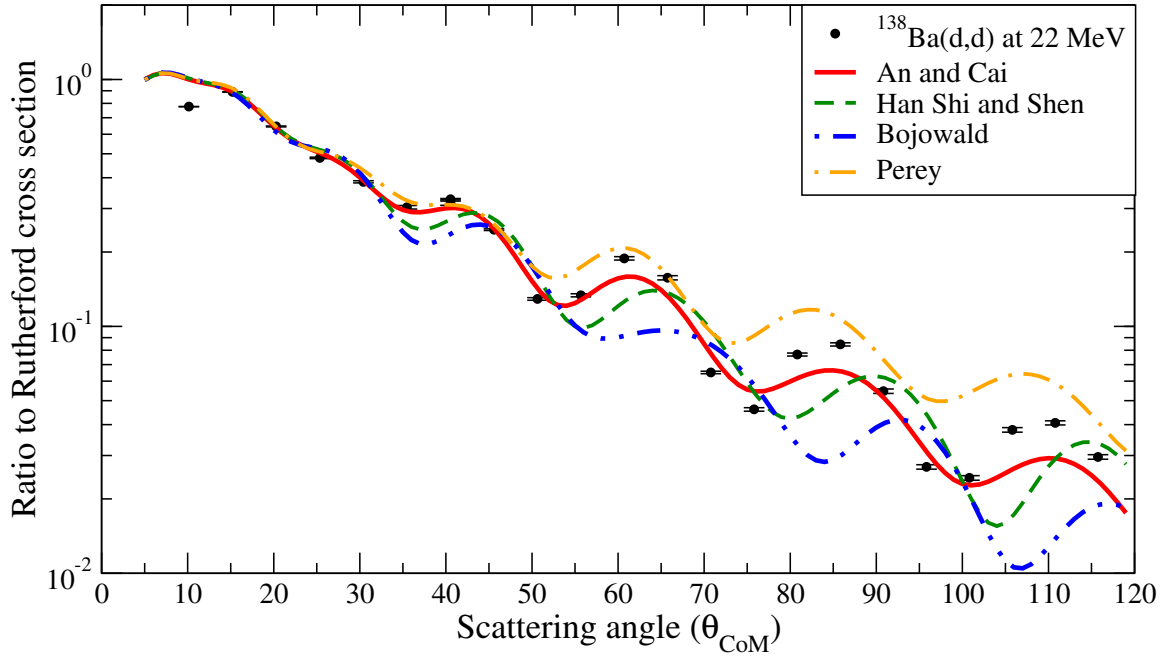


Figure 6.3: Experimental elastic scattering angular distributions for 22 MeV deuterons on ^{138}Ba , compared with DWBA cross sections. The global deuteron OMPs used for comparison are An and Cai [178], Han *et al.* [179], Bojowald *et al.* [180] and Perey *et al.* [181]. The deuteron OMP that best reproduces the data is the one provided by An and Cai [178].

following procedure. Since the highest energy of the α 's were ~ 30 MeV, we explored the Experimental Nuclear Reaction Database (EXFOR) [182] to find the available elastic scattering cross section data. At similar α energies we found α elastic scattering data on ^{136}Ba , ^{140}Ce and ^{130}Te target nuclei. For ~ 30 MeV alphas, one global OMP set by Avrigeanu *et al.* [183] and two local OMPs by Burnett *et al.* [184] and McFadden and Satchler [185] were available. As the OMP sets of Burnett *et al.* are optimized for α scattering on ^{136}Ba they expectedly reproduce our elastic scattering data better than the other two OMP sets. We additionally compare DWUCK4 angular distributions obtained using these OMPs with actual $^{140}\text{Ce}(\alpha, \alpha)$ [186] and $^{130}\text{Te}(\alpha, \alpha)$ [187] data. As evident in Figs. 6.4 and 6.5, the best choice of the α OMP in this region ($A = 130 - 140$, $E_\alpha \sim 30$ MeV) is indeed the one suggested by Burnett *et al.* [184].

Finally, the elastic scattering data were used to obtain the correct target thickness ($\rho t'$) as described previously in Section 4.4.1. We normalized the data to DWBA predictions at $\theta_{cm} = 15.2^\circ$, which yielded a normalization factor $\beta = 0.57(2)$. This translated to $\rho t' =$

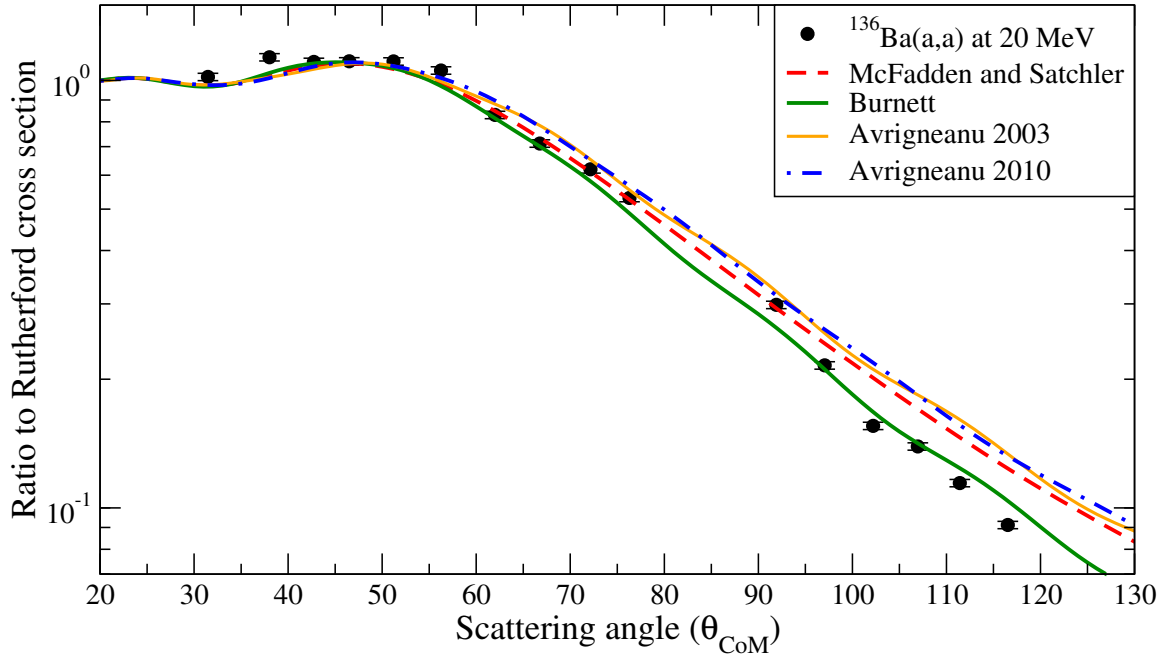


Figure 6.4: $^{136}\text{Ba}(\alpha, \alpha)$ elastic scattering data obtained from Ref. [184] compared to theoretical DWBA elastic scattering cross sections obtained using DWUCK4 that used α OMP sets from Refs. [183–185, 188]. Clearly the α OMP set recommended by Ref. [184] best reproduces the experimental data.

$22.8(1) \mu\text{g}/\text{cm}^2$, where the uncertainty includes both the contribution of the normalization as well as the differences arising from the choice of deuteron optical model parameters.

6.3 DWBA Calculations

The (d, α) DWBA cross sections were calculated assuming a single step ‘deuteron’ pickup mechanism, which implies that the transferred neutron-proton pair is in a relative $S = 1$, $T = 0$ state [91]. As determined from our deuteron and alpha elastic scattering analysis in the previous section, the optical model parameters from Refs. [178, 184] were used to build the interaction potential in the incoming $d-^{138}\text{Ba}$ and outgoing $\alpha-^{136}\text{Cs}$ channels in DWUCK4. The deuteron bound state potential was also defined using the OMP of Ref. [178]. The deuteron cluster form factor is calculated by varying the well depth of the real volume potential such that the binding energy equals the deuteron separation energy

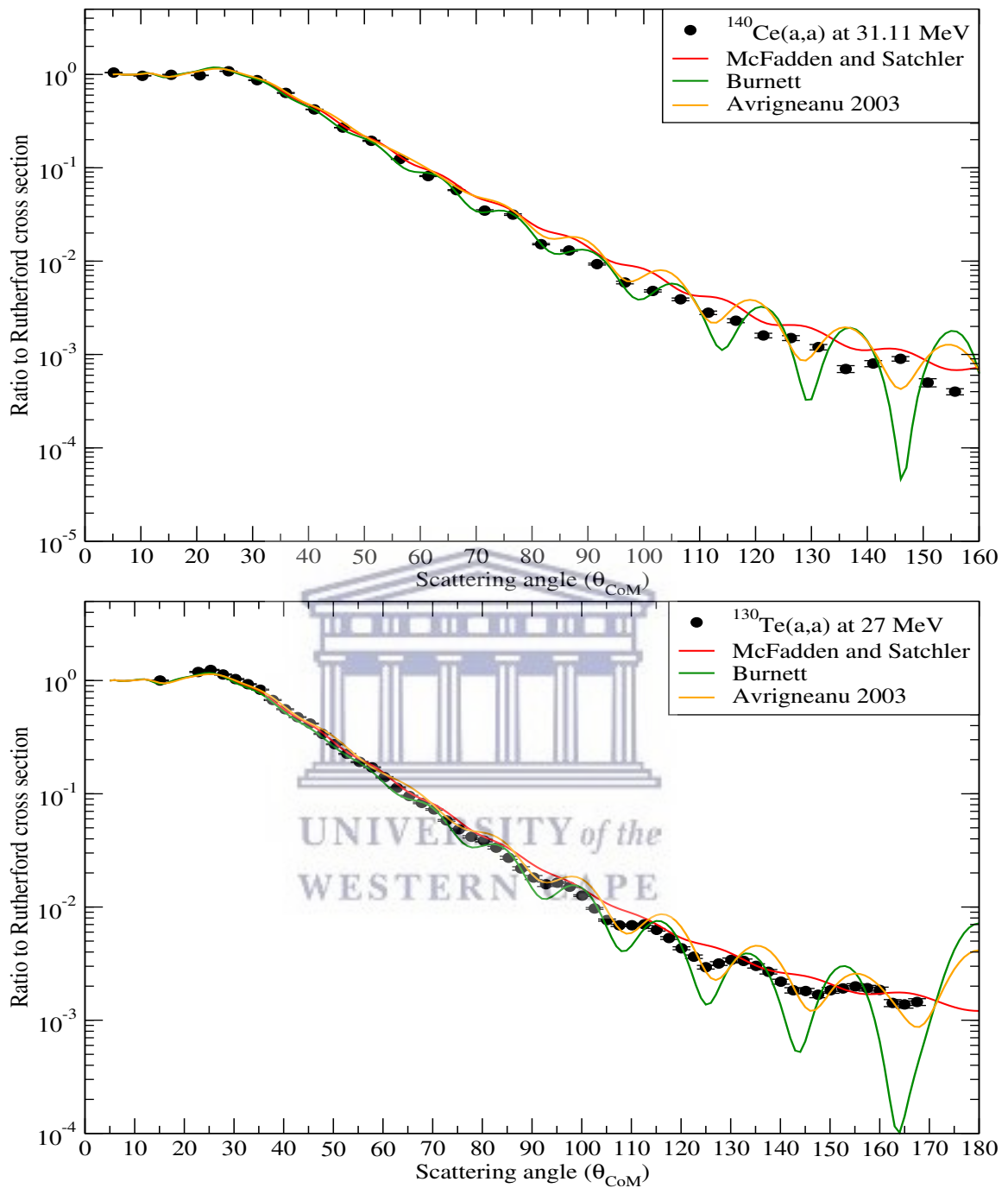


Figure 6.5: $^{140}\text{Ce}(\alpha, \alpha)$ (top) and $^{130}\text{Te}(\alpha, \alpha)$ (bottom) elastic scattering data obtained from Refs. [186,187] compared with our DWBA calculations using the optical model parameter sets of Ref [183–185].

Table 6.2: Optical model parameters for the deuteron, alpha and bound state of the transferred deuteron cluster used in our DWBA analysis. The deuteron parameters for both the incoming channel and the bound state are taken from Ref. [178] and alpha parameters are from Ref. [184].

	$d-^{138}\text{Ba}$	$\alpha-^{136}\text{Cs}$ ^a	$d-^{136}\text{Cs}$
V_r	93.385	203.0	- ^b
r_r	1.151	1.40	1.151
a_r	0.784	0.570	0.784
W_v	2.472	18.40	- ^c
r_v	1.324	1.40	1.324
a_v	0.338	0.57	0.338
W_s	10.157	-	-
r_s	1.363	-	1.363
a_s	0.851	-	0.851
V_{so}	3.557	-	-
r_{so}	0.972	-	0.972
a_{so}	1.011	-	1.011
r_c	1.303	1.40	1.303
FNRG	0.4	0.4	0.4
NLC	0.54	0.2	-

^aAs we used a local α OMP, the parameters are constant for all excited states in ^{136}Cs .

^bWell depth adjusted to reproduce the BE for deuteron as given by Eq. (6.1).

^cWell depth adjusted to reproduce the BE for deuteron as given by Eq. (6.1).

for the corresponding excited state in ^{136}Cs

$$BE = S_d(^{138}\text{Ba}) + E_x(^{136}\text{Cs}), \quad (6.1)$$

where $S_d(^{138}\text{Ba})$ is the deuteron separation energy in ^{138}Ba . Since the DWBA calculations for (d, α) reactions are highly sensitive to the radial integration cutoff limits due to the momentum mismatch between the α and deuteron, this results in significant contributions from the nuclear interior, so that, finite-range and non-locality corrections become important for the cross section calculations [189–192]. These corrections were implemented in DWUCK4 and used in the present analysis. The finite range and non-locality correction factors used for our calculations are shown in Table 6.2.

Angular momentum conservation leads to the selection rule that for each transferred orbital angular momentum value L , the final spins of the states in ^{136}Cs would be $J = |L - 1|$ to $|L + 1|$. Parity conservation restricts this to $J = L$ for natural par-

Table 6.3: Relation between allowed J^π for each L transfer in the $^{138}\text{Ba}(d, \alpha)^{136}\text{Cs}$ reaction. Natural parity states are populated by an $J = L$ transfer while for unnatural parity states both $J = L - 1$ and $J = L + 1$ transfers are allowed (See text for detailed description).

L	Notation	J^π		L	Notation	J^π		
0	S	0^+	1^+	5	H	4^-	5^-	6^-
1	P	0^-	1^-	2^-	6	I	5^+	6^+
2	D	1^+	2^+	3^+	7	J	6^-	7^-
3	F	2^-	3^-	4^-	8	K	7^+	8^+
4	G	3^+	4^+	5^+	9	L	8^-	9^-
							10^-	

ity states and $J = L \pm 1$ for unnatural parity states. A brief summary of the results of this selection for the $^{138}\text{Ba}(d, \alpha)$ reaction is listed in Table 6.3. For the purpose of book-keeping we use an L_J notation inspired from Ref. [193]. In this notation, an orbital angular momentum transfer L produces a state with total angular momentum J . For instance, a $J^\pi = 2^+$ state is designated in the L_J notation as D_2 while a 2^- state can be designated as P_2 or F_2 depending on whether the state is populated via an $L = 1$ or $L = 3$ transfer respectively. This notation is further used in Table 6.4. The spin-parity of each state observed in our measurement is determined based on a χ_{min}^2 value determined from experimental and DWBA cross sections. For the natural parity states, following the $J = L$ rule, the spectroscopic strength $G_{LJ}^{(1)}$ was determined by normalizing the DWBA calculations to experimental data,

$$\left(\frac{d\sigma}{d\Omega}\right)_{\text{expt}} \equiv G_{LJ}^{(1)} \left(\frac{d\sigma}{d\Omega}\right)_{\text{DWBA:J=L}}. \quad (6.2)$$

For unnatural parity states two L values contribute towards the total angular momentum J . Thus two spectroscopic strengths, $G_{LJ}^{(1)}$ and $G_{LJ}^{(2)}$ were extracted from a modified normalization routine

$$\left(\frac{d\sigma}{d\Omega}\right)_{\text{expt}} = G_{LJ}^{(1)} \left(\frac{d\sigma}{d\Omega}\right)_{\text{DWBA:J=L-1}} + G_{LJ}^{(2)} \left(\frac{d\sigma}{d\Omega}\right)_{\text{DWBA:J=L+1}}. \quad (6.3)$$

Not surprisingly, for states where the statistics was low, an absolute determination of the J^π value was not possible. In such cases, the two most probable spin-parity assignments based on the smallest χ^2 values are quoted in Table 6.4. In certain cases, particularly

for unnatural parities, one of the L values dominates the angular distribution. If the $J = L$ angular distribution gives a similar χ^2 value, the state was assumed to be a natural parity state ($J = L$, $\pi = (-1)^L$) [194]. The resulting DWBA angular distributions for all the excited states populated in this work are given in Appendix D and the spectroscopic strengths are listed in Table 6.4.

Table 6.4: ^{136}Cs states observed in this work. The E_x and J^π listed in the first two columns are from the ENSDF database [129]. For natural parity states, as a single L transfer contributes to J^π , the $G_{LJ}^{(1)}$ is the spectroscopic strength for the $J = L$ transfer. For unnatural parities, $G_{LJ}^{(1)}$ is the strength of the $J = L - 1$ transfer and $G_{LJ}^{(2)}$ is for the $J = L + 1$ transfer.

Literature		This work				
E_x (keV)	J^π	E_x (keV)	J^π	L_J	$G_{LJ}^{(1)}$	$G_{LJ}^{(2)}$
0.0	5^+	0	5^+	G_5I_5	1.6(6)	9.3(7)
–	–	72(1)	4^+	G_4	3.9(1)	
104.8(3)	4^+	102(1)	$(4^+, 5^-)$	G_4	0.88(3)	
				H_5	0.68(2)	
–	–	137(1)	3^-	F_3	0.96(4)	
–	–	308(1)	4^+	G_4	0.94(3)	
–	–	418(1)	4^+	G_4	0.68(2)	
–	–	454(1)	4^+	G_4	2.94(6)	
517.9(1)	8^-	510(1)	8^-	J_8L_8	0.29(3)	0.16(6)
590(5)	1^+	582(1)	1^+	S_1D_1	1.0(7)	3.1(2)
–	–	632(1)	4^+	G_4	1.15(4)	
–	–	651(1)	4^+	G_4	6.2(1)	
–	–	664(1)	3^-	F_3	6.3(2)	
–	–	728(1)	$(4^-, 5^-)$	F_4H_4	3.6(6)	5.7(5)
				H_5	6.4(1)	
–	–	782(1)	5^+	G_5I_5	0.39(8)	0.6(1)
–	–	832(1)	1^-	P_1	3.3(1)	
–	–	848(1)	5^-	H_5	0.74(3)	
–	–	884(1)	$(4^+, 5^-)$	G_4	0.70(4)	
				H_5	0.57(3)	
–	–	901(1)	5^-	H_5	2.61(6)	
–	–	986(1)	2^+	D_2	53.8(7)	

Table 6.4 – continued from previous page

E_x (keV)	J^π	E_x (keV)	J^π	L_J	$G_{LJ}^{(1)}$	$G_{LJ}^{(2)}$
–	–	1033(1)	$(3^+, 3^-)$	D_3G_3 F_3	1.2(2) 1.90(7)	0.9(1)
–	–	1063(1)	$(5^-, 6^+)$	H_5 I_6	0.45(2) 0.39(2)	
–	–	1102(1)	$(5^-, 5^+, 6^-)$	H_5 G_5I_5 H_6J_6	9.2(1) 3.2(4) 4.4(3)	7.3(5) 5.4(5)
–	–	1158(1)	2^+	D_2	2.1(1)	
–	–	1186(1)	$(2^+, 3^-)$	D_2 F_3	2.2(1) 1.03(5)	
–	–	1262(1)	$(2^+, 8^+)$	D_2 K_8	4.3(3) 2.2(1)	
–	–	1325(3)	4^+	G_4	4.15(10)	
–	–	1353(1)	–	–	–	
–	–	1412(2)	$(2^+, 3^-)$	D_2 F_3	1.9(1) 0.95(6)	
–	–	1456(1)	4^+	G_4	0.51(3)	
–	–	1484(1)	4^+	G_4	3.23(8)	
–	–	1511(1)	5^-	H_5	1.39(4)	
–	–	1530(2)	3^+	D_3G_3	0.8(2)	0.6(2)
–	–	1550(1)	$(4^-, 5^-)$	F_4H_4 H_5	0.6(2) 0.98(4)	0.8(2)
–	–	1611(1)	$(4^-, 5^-)$	F_4H_4 H_5	0.1(3) 0.84(6)	1.0(3)
–	–	1639(3)	4^+	G_4	0.35(5)	
–	–	1663(1)	$(4^+, 5^-)$	G_4 H_5	2.0(1) 1.56(8)	
–	–	1692(2)	5^-	H_5	0.60(5)	
–	–	1720(1)	4^+	G_4	1.51(9)	
–	–	1741(2)	$(3^+, 3^-)$	D_3G_3 F_3	1.7(5) 2.1(1)	0.8(3)
–	–	1751(1)	4^+	G_4	2.7(1)	
–	–	1772(2)	5^-	H_5	0.57(4)	

Table 6.4 – continued from previous page

E_x (keV)	J^π	E_x (keV)	J^π	L_J	$G_{LJ}^{(1)}$	$G_{LJ}^{(2)}$
–	–	1800(1)	4^+	G_4	1.05(6)	
–	–	1811(2)	–	–	–	–
–	–	1850(2)	4^+	G_4	0.67(6)	
–	–	1879(3)	4^+	G_4	0.55(6)	
–	–	1899(1)	3^-	F_3	2.3(1)	
–	–	1928(2)	$(3^-, 4^+)$	F_3 G_4	0.90(8) 0.56(5)	
–	–	1975(1)	$(4^-, 5^-)$	F_4H_4 H_5	0.4(2) 1.13(4)	1.1(2)
–	–	1993(1)	$(4^-, 5^-)$	F_4H_4 H_5	0.2(2) 0.99(4)	1.2(2)
–	–	2012(2)	$(5^-, 6^+)$	H_5 I_6	0.38(3) 0.36(3)	
–	–	2063(2)	–	–	–	–
–	–	2083(1)	3^-	F_3	1.55(8)	
–	–	2108(1)	$(5^-, 5^+)$	H_5 G_5I_5	5.4(1) 4.9(3)	0.4(4)
–	–	2118(2)	5^-	H_5	1.51(7)	
–	–	2155(2)	$(3^-, 4^+)$	F_3 G_4	1.21(7) 0.79(5)	
–	–	2202(2)	3^-	F_3	0.68(7)	
–	–	2218(1)	3^-	F_3	0.64(7)	
–	–	2235(1)	3^-	F_3	0.78(7)	
–	–	2256(1)	3^-	F_3	0.88(6)	
–	–	2268(2)	(3^-)	F_3	0.66(7)	
2290(5)	1^+	2290(1)	$(1^+, 2^+)$	S_1D_1 D_2	0.0 1.6(1)	2.7(2)
–	–	2300(5)	(2^+)	D_2	1.4(1)	
–	–	2312(2)	–	–	–	–
–	–	2331(5)	–	–	–	–
–	–	2356(1)	$(3^-, 3^+)$	F_3 D_3G_3	2.73(9) 1.5(3)	1.5(2)

Table 6.4 – continued from previous page

E_x (keV)	J^π	E_x (keV)	J^π	L_J	$G_{LJ}^{(1)}$	$G_{LJ}^{(2)}$
2360(5)	1 ⁺	2368(2)	(1 ⁺ , 2 ⁺)	S_1D_1 D_2	0.5(10) 1.7(1)	2.7(4)
–	–	2384(1)	–	–	–	–
–	–	2408(2)	(5 ⁺ , 5 ⁻)	G_5I_5 H_5	0.35(8) 0.47(4)	0.1(1)
–	–	2422(5)	–	–	–	–
2450(5)	1 ⁺	2451(1)	(1 ⁺ , 2 ⁻)	S_1D_1 P_2F_2	3(1) 1.2(5)	2.4(4) 0.8(2)
2500(5)	1 ⁺	2502(2)	(1 ⁻ , 1 ⁺ , 2 ⁻)	P_1 S_1D_1 P_2F_2	7.3(7) 13(1) 3(1)	0.0 0.5(5)
–	–	2511(3)	(1 ⁻ , 2 ⁺)	P_1 D_2	8.0(8) 2.6(3)	
–	–	2536(3)	(1 ⁻ , 2 ⁺)	P_1 D_2	4.3(5) 1.5(2)	
2550(5)	1 ⁺	2555(2)	(1 ⁺ , 2 ⁺)	S_1D_1 D_2	0.0 3.0(2)	5.1(2)

6.4 J^π Assignments

On comparing the experimental and DWBA angular distributions we could assign definite J^π values for 32 natural and 3 unnatural parity states in ^{136}Cs . For the other 39 states we only quote tentative J^π values. For some states where uncertainties on the cross sections are large, we make tentative assignments for even the most favorable spin-parity values. As the ^{136}Cs nucleus has not been studied extensively in the past, most of the information obtained in this work is new. Wherever previous information was available, it is mentioned in the first two columns of Table 6.4 and in the discussion of the states in the following sections.

6.4.1 Natural Parity States

$J^\pi = 1^-$ states

The angular distribution for the 832 keV state is consistent with a spin-parity assignment of 1^- . This is the only 1^- state where we could make a definite $J^\pi = 1^-$ assignment.

$J^\pi = 2^+$ states

2 states are observed at excitation energies of 986 and 1158 keV where a definite $J^\pi = 2^+$ assignment could be made. The angular distributions for these states are well reproduced by DWBA distributions for a $J = L = 2$ transfer. Both these states are newly identified in this work.

$J^\pi = 3^-$ states

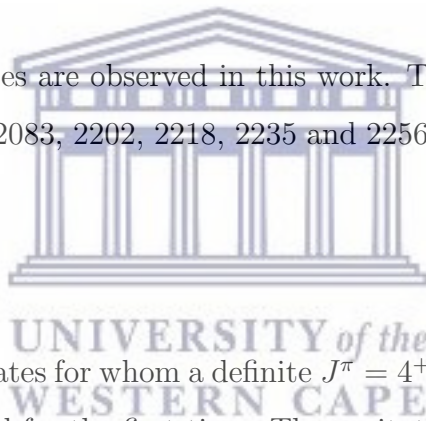
A large number of 3^- states are observed in this work. The excitation energies for these states are 137, 664, 1899, 2083, 2202, 2218, 2235 and 2256 keV. None of these states have been observed previously.

$J^\pi = 4^+$ states

We observe a total of 15 states for whom a definite $J^\pi = 4^+$ assignment could be made. All of these states are reported for the first time. The excitation energies for these states are 72, 308, 418, 454, 632, 651, 1325, 1456, 1484, 1639, 1720, 1751, 1800, 1850 and 1879 keV.

$J^\pi = 5^-$ states

A large number of 5^- states are also produced in this reaction. The definite $J^\pi = 5^-$ states are 848, 901, 1511, 1692, 1772 and 2118 keV. In addition to these 6 states, numerous other states are observed, that have been tentatively assigned $J^\pi = 5^-$. These states are discussed in Section 6.4.3.



6.4.2 Unnatural Parity Assignments

In addition to the 5^+ ground state [87, 129] and the 8^- isomeric state [87, 129], we observe three other unnatural parity states in ^{136}Cs at 582, 782 and 1530 keV. The angular distribution for 582 keV states agrees with the DWBA prediction for $J^\pi = 1^+$. A state at 590 ± 5 keV was reported in a previous $^{136}\text{Xe}(^3\text{He}, t)^{136}\text{Cs}$ charge exchange reaction as a $J^\pi = 1^+$ state [86]. The DWBA angular distribution for a $J^\pi = 5^+$ suitably reproduces the 782 keV and a $J^\pi = 3^+$ describes the 1530 keV state.

6.4.3 Tentative J^π Assignments

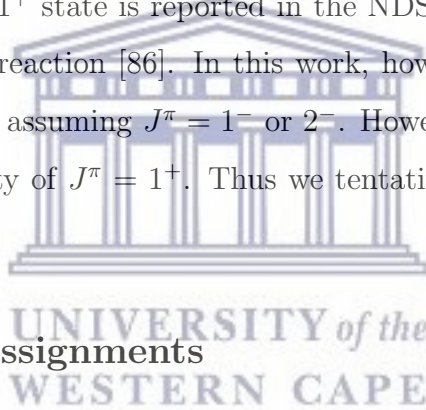
In this section we discuss all states where we could not make definite J^π assignments.

- **Ex = 102 keV** This state is reported in the adopted level scheme for ^{136}Cs at an excitation energy of 104.8 keV as a 4^+ state [87]. However, the angular distribution in this work favors a $J^\pi = 5^-$ assignment. Hence we make a tentative $(4^+, 5^-)$ assignment.
- **Ex = 884, 1663 keV** The two most probable J^π values for these states correspond to the DWBA predictions for 4^+ and 5^- . Since we cannot make a firm spin-parity assignment owing to the relatively large uncertainties on the cross sections, we tentatively assign $J^\pi = (4^+, 5^-)$ for these two states.
- **Ex = 1033, 1741, 2356 keV** For these three states our χ^2 analysis for the angular distributions indicate $J^\pi = 3^-$ and 3^+ . For 1033 and 1741 keV states, the χ^2_{min} corresponds to $J^\pi = 3^-$ and for the 2356 keV state $J^\pi = 3^+$. Therefore, we assign $J^\pi = (3^-, 3^+)$ for these three states.
- **Ex = 1063, 2012 keV** Due to the large uncertainties in cross sections for these two states, we cannot distinguish between $J^\pi = 5^-$ and 6^+ on the basis of the χ^2 values. Hence, we tentatively assign $J^\pi = (5^-, 6^+)$ for these two states.
- **Ex = 1102 keV** We tentatively assign $J^\pi = (5^-, 5^+, 6^-)$ based on the lowest χ^2 values for the angular distributions.

- **Ex = 1186, 1412 keV** None of these states are listed in the NDS for ^{136}Cs . As these states are weakly populated, clear distinction cannot be made between the $J^\pi = 2^+$ and 3^- angular distributions and hence we tentatively assign $J^\pi = (2^+, 3^-)$ for these states. For both these states, however, χ_{min}^2 corresponds to $J^\pi = 3^-$.
- **Ex = 1262 keV** We could reproduce the angular distribution for this state if we assume that it is an unresolved doublet, with 66% contribution from an excited states that is a $J^\pi = 2^+$ and 34% from $J^\pi = 8^+$.
- **Ex = 728, 1550, 1611, 1975, 1993 keV** The contribution from $L = 3$ transfer towards $J^\pi = 4^-$ is not negligible as compared to the $L = 5$ transfer for these states. Thus we cannot ignore the possibility of $J^\pi = 4^-$ for these four states. Additionally, the angular distribution for $J^\pi = 5^-$ from the $L = 5$ transfer is also a good fit to the experimental angular distribution. Hence we tentatively assign $J^\pi = (4^-, 5^-)$ for these four states.
- **Ex = 1928, 2155 keV** Due to the large uncertainties in the cross sections, a $J^\pi = 3^-$ distribution gives a similar χ^2 value as a $J^\pi = 4^+$ distribution. Thus the two state are assigned $J^\pi = (3^-, 4^+)$.
- **Ex = 2108, 2408 keV** Two of the lowest values of χ^2 are obtained for the angular distributions corresponding to $J^\pi = 5^-$ and 5^+ for these two states. Therefore both these states are tentatively assigned $J^\pi = (5^-, 5^+)$.
- **Ex = 2268, 2300 keV** While the experimental angular distribution for the 2268 keV state matches that of $J^\pi = 3^-$ due to low statistics and an incomplete angular distribution data set, this state is tentatively assigned $J^\pi = (3^-)$. For similar reasons, the state at 2300 keV is also tentatively assigned $J^\pi = (2^+)$.
- **Ex = 2290, 2555 keV** The NDS report two levels at 2290 ± 5 and 2550 ± 5 keV as $J^\pi = 1^+$ observed from $^{136}\text{Xe}(^3\text{He}, t)^{136}\text{Cs}$ data [86]. Our DWBA predictions indicate $J = 1^+$ and 2^+ for the two states. However the $L = 0$ contribution towards

the $J^\pi = 1^+$ distribution is negligible compared to the $L = 2$ transfer. Hence we assigned $J^\pi = (1^+, 2^+)$ to these two states.

- **Ex = 2368, 2451 keV** Two states are reported in the NDS in the vicinity of these states at 2360 ± 5 and 2450 ± 5 keV [129]. Both the states are reported as $J^\pi = 1^+$ observed via the $^{136}\text{Xe}(^3\text{He}, t)$ charge exchange reaction [86]. We find that the angular distributions for these states is compatible with 1^+ but the possibility of $J^\pi = 2^-$ cannot be eliminated for the 2451 keV state and 2^+ for the 2368 keV state. Thus we assign $J^\pi = (1^+, 2^+)$ for 2368 keV and $J^\pi = (1^+, 2^-)$ for 2451 keV.
- **Ex = 2511, 2536 keV** The DWBA curves assuming $J^\pi = 1^-$ and 2^+ result in similar χ^2 values when normalized to experimental angular distributions. Hence the two states were assigned $J^\pi = (1^-, 2^+)$.
- **Ex = 2502 keV** A 1^+ state is reported in the NDS [129] at 2500 ± 5 keV observed in the $^{136}\text{Xe}(^3\text{He}, t)$ reaction [86]. In this work, however, the angular distributions is reproduced better assuming $J^\pi = 1^-$ or 2^- . However the large uncertainties also lead to the possibility of $J^\pi = 1^+$. Thus we tentatively assigned $J^\pi = (1^+, 1^-, 2^-)$ for this state.



6.4.4 Indefinite Assignments

Due to large uncertainties and in some cases incomplete angular distributions, no conclusive spin-parity assignments could be made for the excited states at 1353, 1811, 2063, 2312, 2331, 2384 and 2422 keV.

One never notices what has been done; one can only see what remains to be done.

Marie Curie

In conclusion, we used the $^{138}\text{Ba}(p, t)$ and $^{138}\text{Ba}(d, \alpha)$ reactions to study properties of the $A = 136$ nuclei that are relevant for the ^{136}Xe $\beta\beta$ decays. The $^{138}\text{Ba}(p, t)$ reaction was performed to study neutron pairing correlations in ^{136}Ba , while the $^{138}\text{Ba}(d, \alpha)$ reaction was done to perform a high resolution measurement of low lying states in ^{136}Cs . These experimental information will be useful to constrain future $^{136}\text{Xe} \rightarrow ^{136}\text{Ba}$ $0\nu\beta\beta$ decay matrix element calculations. A summary of our results is below.

$^{138}\text{Ba}(p, t)^{136}\text{Ba}$

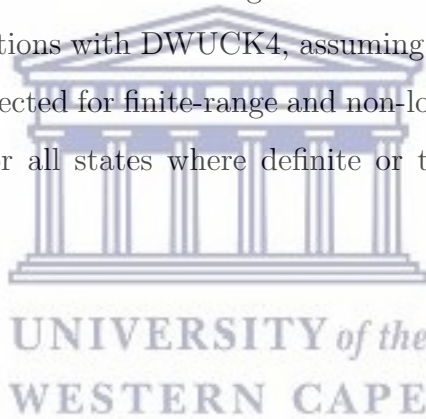
UNIVERSITY of the
WESTERN CAPE

In this experiment we identified a total of 110 states in ^{136}Ba up to an excitation energy of 4.6 MeV. A zero-range DWBA DWUCK4 analysis, assuming a di-neutron cluster pick up mechanism was carried out to generate theoretical angular distributions. These were compared with experiment to deduce the spins and parities of various states in ^{136}Ba . Using this approach we identified 8 new 0^+ states in ^{136}Ba . The angular distribution of all observed 0^+ states were well reproduced by the DWBA predictions, except for the first excited 0^+ state at 1579 keV. The discrepancy in the shape of the angular distribution still remains unresolved. Another 0^+ state at 2141.38 keV listed in the Nuclear Data Sheets was not observed in this work. In addition to the 0^+ states, we could also make definite spin and parity assignments for ~ 25 newly identified states.

We observe a large fragmentation of the (p, t) strength for the $0_2^+ = 2315$ keV and $0_3^+ = 2784$ keV states. These states are located just above the (~ 2 MeV) pairing gap in ^{136}Ba . The combined (p, t) strength to these states relative to the ground state was found to be $\sim 30\%$. This is a clear indication of a breakdown in the neutron BCS approximation for ^{136}Ba . It is interesting to note that a previous (t, p) measurement on ^{136}Ba has shown that the pairing vibrational state in ^{138}Ba lies at 3612 keV [139].

$^{138}\text{Ba}(\text{d}, \alpha)^{136}\text{Cs}$

A total of 67 new states are observed for the first time in the odd-odd ^{136}Cs nucleus, below 2.6 MeV. Definite spin and parity assignments could be made for ~ 35 states. For the remaining states we made tentative assignments. The analysis was performed using zero-range DWBA calculations with DWUCK4, assuming a single-step deuteron transfer. The calculations were corrected for finite-range and non-locality effects. We also obtained spectroscopic strengths for all states where definite or tentative spin-parities could be assigned.



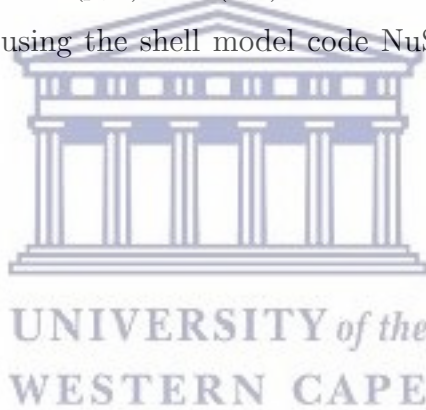
Future Work

Our results from the $^{138}\text{Ba}(p, t)$ measurement indicate a breakdown in the BCS approximation for ^{136}Ba . In the context of $0\nu\beta\beta$ decays, it is important that QRPA matrix element calculations take this experimental evidence into consideration. Since both ^{136}Ba and ^{136}Xe have open proton shells, a study of proton pairing correlations in these two nuclei can also provide useful spectroscopic information for future matrix element calculations. Additionally, reactions that probe the overlap between the ground state wavefunctions of the two nuclei would be very useful to constraining the NME calculations. One such reaction could be the double charge exchange ($^{14}\text{C}, ^{14}\text{O}$) reaction on ^{136}Ba . Indeed, similar calculations are currently being pursued by the NUMEN Collaboration [195].

In the immediate future an important first step would be to reproduce our results by tun-

ing the shell model and QRPA calculations. We are currently working with shell model theorists to reproduce our experimental results. A similar exercise is recommended for QRPA calculations as well.

In conclusion, the spectroscopic strengths for the $^{138}\text{Ba}(d, \alpha)$ reaction were extracted assuming a single-step transfer of a deuteron in a zero-range approximation with finite-range and non-locality corrections. It would be advisable to extract these factors using a theoretical framework that performs second-order DWBA calculations [196, 197], accounting for multi-step transfers and finite-range interactions. It has been shown [198, 199] that the (p, t) reaction cross sections receive a significant contribution from both, the direct single-step transfer and the two-step sequential transfer when treated under second order DWBA theory. We therefore intend to perform the sequential $^{138}\text{Ba}(d, t)^{137}\text{Ba}(t, \alpha)^{136}\text{Cs}$ and $^{138}\text{Ba}(d, ^3\text{He})^{137}\text{Cs}(^3\text{He}, \alpha)^{136}\text{Cs}$ transfer using the DWBA code FRESKO [200]. We will also do the sequential $^{138}\text{Ba}(p, d)^{137}\text{Ba}(d, t)^{136}\text{Ba}$ transfer with the two-neutron transfer amplitudes calculated using the shell model code NuShellX [201] for future publications.



A | Relativistic Kinematics

For the nuclear reaction in direct kinematics

$$a + A \rightarrow b + B \quad (\text{A.1})$$

where a is the projectile, A the target, b the light ejectile and B is the recoil nucleus. Some of the relativistic kinematic relations used in the $C++$ code, that follows from the Oak Ridge National Laboratory's relativistic kinematics code [202] are discussed below. For the projectile a with incident energy K_a ($= E_{beam}$) and mass m_a , the relativistic relations between the total energy E_a and the momentum p_a or kinetic energy K_a (in the laboratory frame) are


$$E_a = K_a + m_a c^2, \quad (\text{A.2})$$

and

$$E_a^2 = p_a^2 c^2 + m_a^2 c^4. \quad (\text{A.3})$$

Setting $c = 1$, the minimum kinetic energy required by the projectile to initiate the reaction is

$$K_{min} = \frac{-Q(m_a + m_A + m_b + m_B)}{2m_A}, \quad (\text{A.4})$$

where

$$Q = m_a + m_A - (m_b + m_B) \quad (\text{A.5})$$

is the reaction Q-value and m_A , m_b , m_B are masses of the target, ejectile and recoiling nucleus respectively. The total energy (E_T) of the system is

$$E_T = E_a + E_A = E_b + E_B. \quad (\text{A.6})$$

In the center-of-mass frame, the total momentum is zero and hence the energy and momentum relations are given by

$$E_T^{CM} = \sqrt{m_a + m_A^2 + 2m_A E_a}, \quad (\text{A.7})$$

$$p_a^{CM} = p_b^{CM} = \frac{p_a m_B}{E_T^{CM}}, \quad (\text{A.8})$$

$$E_a^{CM} = \frac{m_a^2 + m_A E_a}{E_T^{CM}}, \quad (\text{A.9})$$

and

$$E_A^{CM} = \frac{m_A^2 + m_A E_a}{E_T^{CM}}, \quad (\text{A.10})$$

In all the equation above and later, quantities without the CM superscript indicate values in the laboratory frame. For the outgoing nuclei b and B , the energies and momenta are related to the incoming channel via E_T^{CM}

$$E_T^{CM} = E_b^{CM} + E_B^{CM}, \quad (\text{A.11})$$

where

$$E_b^{CM} = \frac{(E_T^{CM})^2 + m_b^2 - m_B^2}{2E_T^{CM}} \quad (\text{A.12})$$

$$p_b^{CM} = \sqrt{(E_b^{CM})^2 - m_b^2}$$

and

$$E_B^{CM} = \frac{(E_T^{CM})^2 + m_B^2 - m_b^2}{2E_T^{CM}} \quad (\text{A.13})$$

$$p_B^{CM} = \sqrt{(E_B^{CM})^2 - m_B^2}$$

After some algebra, the energy of the ejectile b in the laboratory frame is given in terms of the masses, energies E_T and E_T^{CM} and the laboratory scattering angle θ_b of the ejectile

$$E_b = \frac{E_T}{E_T^2 - p_a^2 \cos^2 \theta_b} \left(\frac{2m_A E_a + m_a^2 + m_A^2 + m_b^3 - m_B^2}{2} \right) \pm \frac{p_a \cos \theta_b}{E_T^2 - p_a^2 \cos^2 \theta_b} \sqrt{\left(\frac{2m_A E_a + m_a^2 + m_A^2 - m_b^2 - m_B^2}{2} \right)^2 - m_b^2 m_B^2 - p_a^2 m_b^2 \sin^2 \theta_b}. \quad (\text{A.14})$$

The \pm sign in Eq. (A.14) indicates two possible solutions for E_b and the physically allowed solution(s) is decided by the quantity α

$$\alpha = \left(\frac{p_a}{E_T} \right) \left(\frac{(E_T^{CM})^2 + m_b^2 - m_B^2}{(E_T^{CM})^2} \right) \left[\left(1 - \left(\frac{m_b + m_B}{E_T^{CM}} \right)^2 \right) \left(1 - \left(\frac{m_b - m_B}{E_T^{CM}} \right)^2 \right) \right]^{-1/2}. \quad (\text{A.15})$$

If $\alpha > 1$ both the solutions of Eq.(A.14) are valid for E_b and only the positive solution of Eq. (A.14) is physical when $\alpha < 1$. The energy of the recoiling nucleus in the laboratory frame is then given by

$$E_B = E_T - E_b. \quad (\text{A.16})$$

The momenta for b and B are calculated using the usual energy momentum relation. In Eq.(A.14), E_b is calculated assuming the recoil nucleus B is in the ground state. To calculate E_b corresponding to an excited state E_x of B , all the calculations are done using $m_B = m_B + E_x$.

The code is also designed to calculate the excitation energy of the nucleus when the ejectile kinetic energy (K_b) or momentum (p_b) is known. Using the total energy relation of Eq. (A.6)

$$E_x = E_a + m_A - E_b - E_B, \quad (\text{A.17})$$

where

$$E_B = \sqrt{p_B^2 + m_B^2}, \quad (\text{A.18})$$

and

$$p_B = \sqrt{p_a^2 + p_b^2 - 2p_a p_b \cos\theta_b}. \quad (\text{A.19})$$

At this stage, p_a , p_b and θ_b are known. If instead the ejectile energy K_b is known, p_b is first calculated and then used in Eq. (A.19)

$$p_b = \sqrt{(K_b + m_b)^2 - m_b^2}. \quad (\text{A.20})$$



UNIVERSITY *of the*
WESTERN CAPE

B Description of DWUCK4 input file used for DWBA Analysis

```

INPUT BLOCK 1 | 12220000200000030   138Ba(p,t)136Ba @23.MeV, l=3
INPUT BLOCK 2 | +121.   +00.   +00.5
INPUT BLOCK 3 | +20+01+03+06
INPUT BLOCK 4 | +00.1 +00. +15. +00.
INPUT BLOCK 5 | +23.0 +1.00783+01.00 +138. +56. +01.227 +00. +00. +01.
+04. -22.523 +01.060 +00.590 +00.
+01. -53.388 +01.225 +00.657 +00.00 -01.738 +01.225 +00.657 +00.
-02. -00.000 +00.000 +00.000 +00.00 +35.075 +01.260 +00.590 +00.
INPUT BLOCK 6 | -9.57996+3.01605+01. +136. +56. +01.422 +00.00 +00.00 +01.
+04. -07.612 +00.495 +00.086
+01. -155.61 +01.091 +00.782 +00.00 -12.365 +01.286 +01.217 +00.
-02. -00.000 +00.000 +00.000 +00.00 +00.458 +01.161 +00.871 +00.
+01. +05. +01.7 +10.000 +00. +00. +00. +00.
INPUT BLOCK 7 | -09.040 +01.008 +00. +136. +56. +01.250 +00. +00. +00.
+01. -01.000 +01.170 +00.750 +25.00 +00. +00.00 +00. +00.
+00. +04. +07. +01. +10. +00. +00. +00. +00.
-08.040 +01.008 +00. +136. +56. +01.250 +00. +00. +00.
-01. -01.000 +01.170 +00.750 +25.00 +00. +00.00 +00. +00.
+00. +05. +11. +01. +10. +00. +00. +00. +00.
END OF FILE | 9
10010000300000003   138Ba(d,a)136Cs @22.MeV Ex=0.0 keV [5+ : L=4(+L=6)]
+121.   +00.   +00.5
+20+01+04+10
+00.1 +00. +10. +00. +00.4
+22.00 +02.0141+01.00 +138.00 +56.00 +01.303 +00.00 +00.54 +02.00
+01. -93.385 +01.151 +00.784 -02.472 +01.324 +00.338 +00.00
+04. -14.228 +00.972 +01.011 +00.000 +00.972 +01.011 +00.00
-02. -00.000 +01.363 +00.851 +00.00 +40.627 +01.363 +00.851 +00.00
+8.7879 +04. +02. +136. +55. +01.40 +00.00 +00.20 +00.00
-01. -203.00 +01.40 +00.570 +00.00 -18.40 +01.40 +00.57 +00.00
-15.058 -02.0141+01.00 +136. +55. +01.303 +00. +00.54 +02.00
+01. -97.012 +01.151 +00.784 -01.531 +01.324 +00.341 +00.00
+04. -14.228 +00.972 +01.011 +00.000 +00.972 +01.011 +00.00
-02. -00.000 +01.363 +00.851 +00.00 +42.48 +01.363 +00.850 +00.00
+01. +04. +10. +02. +01. +00.
9

```

Figure B.1: Sample DWUCK4 input file for $L = 3$ transfer in $^{138}\text{Ba}(p, t)^{136}\text{Ba}$ reaction and $L = 4$ in $^{138}\text{Ba}(d, \alpha)^{136}\text{Cs}$. For the purpose of illustration, the various input blocks are labeled. Description of each block is provided in the text.

The input file for DWUCK4 is divided into seven blocks with character formatting and spacing following a strict Fortran77 format that specified in the DWUCK4 manual. If this formatting is not respected, the code crashes. The first four blocks are basic initializations for the program. Blocks 5 and 6 contain information to construct the distorted waves of the incoming and outgoing channels while block 7 describe the interactions between the core nucleus and the transferred particle. A sample input for the (p, t) and (d, α) reactions is shown in Fig. B.1. The description of each input block is provided below along with the variable names given in the DWUCK4 manual.

- **Input Block 1** - This block is divided into two parts. The first part is a series of 17 ‘control flags’ referred to as ICON(i), that initializes the program and decides what outputs are to be generated or suppressed. The integer **9** at the beginning of the

input or after Input block 7 will terminate the computation. The second part is a 60 character label that is solely provided for the purpose of identifying the current calculation. It is written out *as is* to the DWUCK output file.

- **Input Block 2** - The angular range for the DWBA calculation, number of angles (N_ANGLES), minimum angle (ANGLE1) and the angular increment (D_ANGLES) are specified in this block. All angles should be specified in the center-of-mass frame.
- **Input Block 3** - In this block the maximum number of partial waves (LMAX) that are to be used for the calculation, the number of angular momentum transfers (NLTR) and corresponding to each NLTR, the orbital (LTR(i)) and total (JTR(i)) angular momentum transfer are specified. Multiple angular momentum transfers can be computed for a given reaction with the options to calculate the cross-sections as a coherent sum of amplitudes from the different L -transfers.
- **Input Block 4** - Five different parameters are specified in this section. These are, the integration step size (DR), lower (RMIN) and upper (RMAX) cut-offs for the radial integrals, Coulomb excitation scale factor (COUEX) and the finite-range correction (FNRNG) factors.
- **Input Block 5** - This is a multi-line input block that requires information about the initial conditions of the incoming channel and the optical model parameters to calculate the distorted waves. The first line reads in the energy of the incoming beam (E), the masses in amu and charges for the projectile and target (MP, ZP, MT, ZT), the charge radius of the projectile (r_{0c}) as determined from the optical model potential, a non-locality correction factor (PNLOC) and two times the spin of the projectile (2*FS). The optical potential is constructed by ‘stacking’ several individual potentials corresponding to the various forms given by the variable OPTION as specified in Eq. (4.25). The negative sign in front of OPTION (in this case, 2.0) alerts the code that the current potential is the last one for the input block. The parameters of the optical potential correspond to the global optical model parameters that are selected by following the procedure in Sect. 4.4.1.

- **Input Block 6** - This block is the same as input block 5 except that the distorted waves are constructed for the outgoing channel and instead of the beam energy the reaction Q-value for the excited state is entered.
- **Input Block 7** - This block describes interaction between the transferred particle(s) and the core nucleus. The input structure of this block varies depending on the reaction model. The underlying difference in the inputs in this block for the (d, α) and (p, t) reactions is that we calculate the two-nucleon transfer form factor for (p, t) using $\text{ICON}(2)=2$ and a single particle transfer form factor for (d, α) using $\text{ICON}(2)=0$. Specifics for the two reactions are further elaborated below.
 - The input file for (p, t) reaction is designed for an $L = 3$ transfer. To construct a negative state in a (p, t) reactions requires that the two neutrons should be picked up from two different orbitals, one with positive and other with negative parity. This is accomplished by setting $\text{CONTROL}=2$ (on line 13) which means that DWUCK4 will read different inputs for the two neutrons. This input line is not defined for the (d, α) reaction.
 - The next three (six) lines define the core-transferred particle interaction. This includes the OMP parameters for the deuteron (neutron), the binding energies and the single particle orbitals for the d and $2n$ pickup. The binding energies used here are defined in Eq. (5.1) and (6.1) for (p, t) and (d, α) respectively. For the (p, t) reaction, the single particle orbitals reflect the shell model states in ^{138}Ba for the $2n$ pick up while for the (d, α) input it reflects the state of the transferred deuteron. When $\text{FISW}=0$ (in both the inputs) DWUCK4 will vary the well-depth of the core-transferred particle potential and keep the binding energy fixed.

DWUCK4 output by default is written to screen but can be diverted into a text file with a simple terminal command,

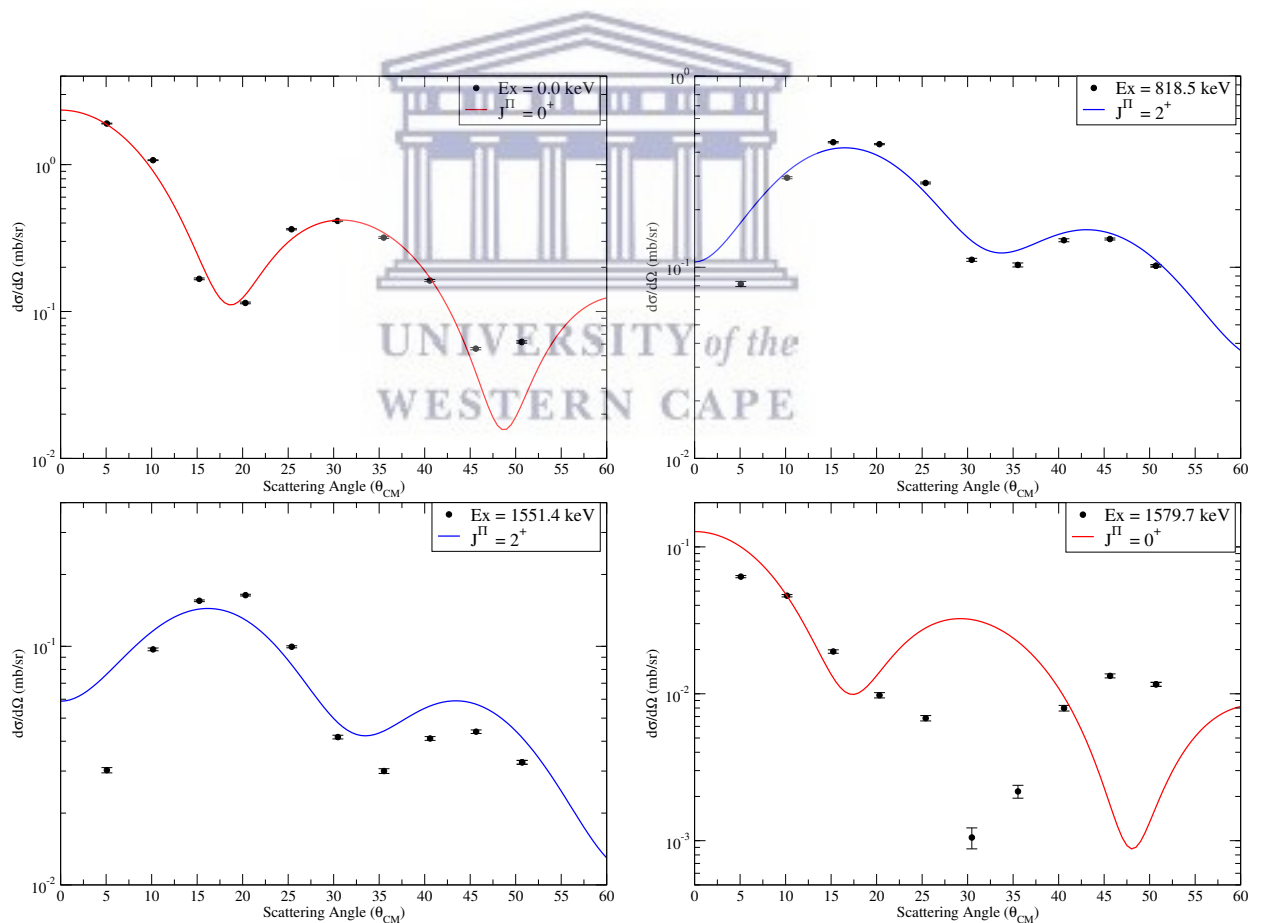
```
./dwuck4 dwuck.inp > dwuck.out
```

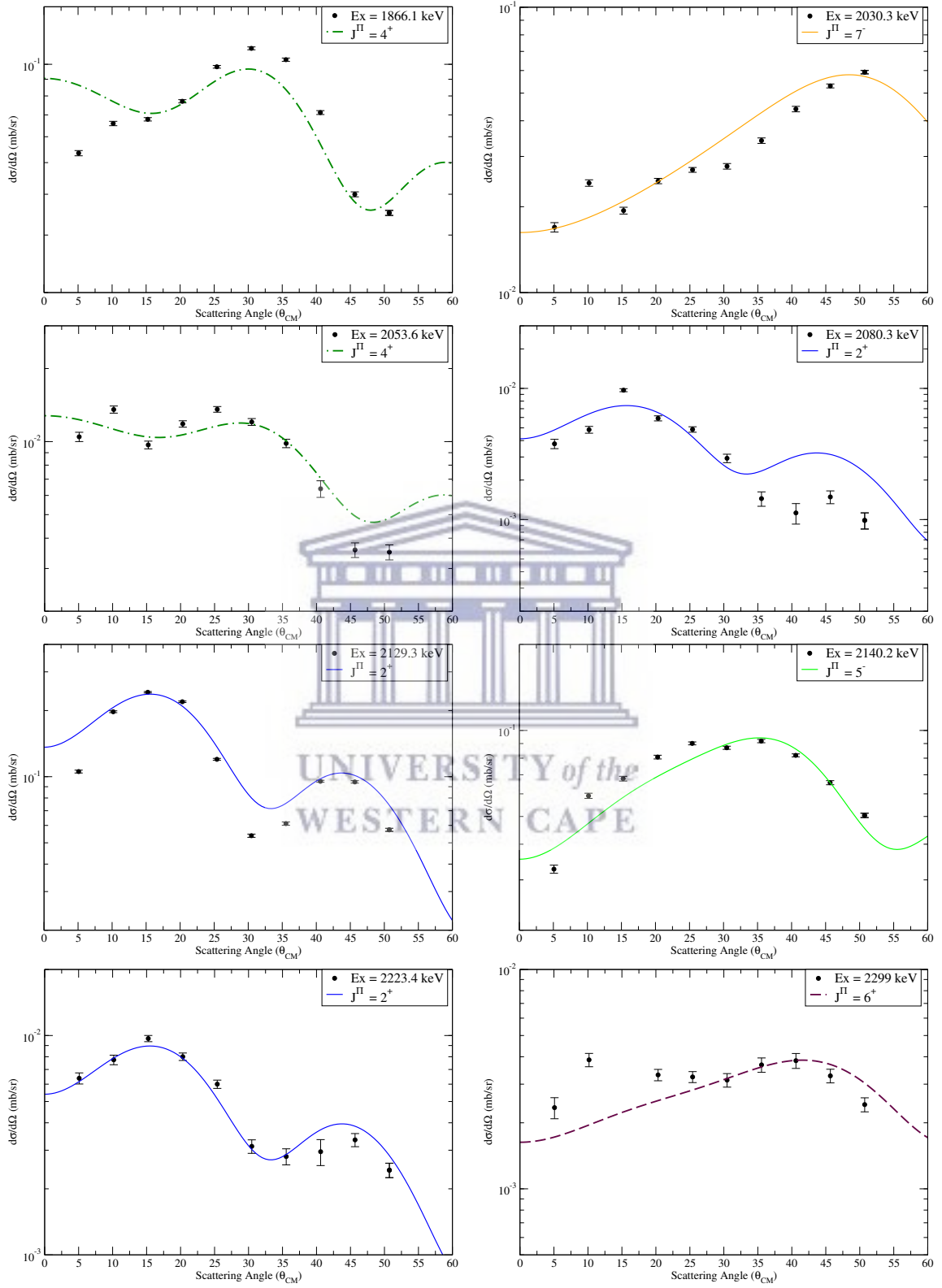
The first few lines of the output writes out the content of the input file along with the computed quantities for the distorted waves. This enables the user to perform any diagnostic tests. This is followed by the elastic scattering cross sections and a paper plot if requested by the user via the control flags. The next set of output is for the reaction channel also referred to as the inelastic channel. The cross-sections are output as a function of angle, along with the vector and tensor analyzing power. As the DWUCK4 cross sections are output in fm^2/sr , these values have to be multiplied by a factor of 10 to compare it with experimental cross-sections that are obtained in mb/sr . A paper plot for the reaction cross-sections with respect to center-of-mass angles are also output depending on the values of the control flags.

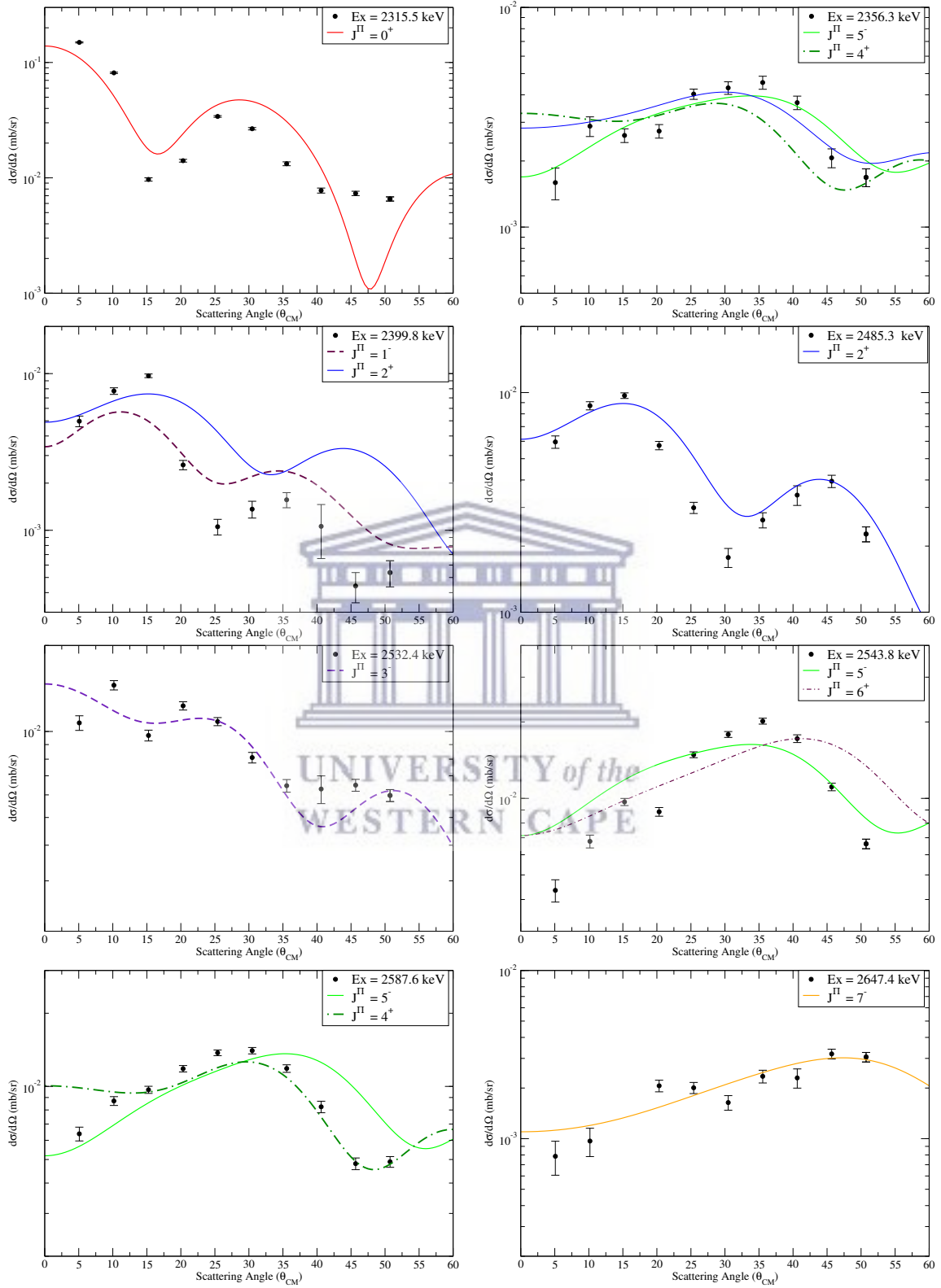


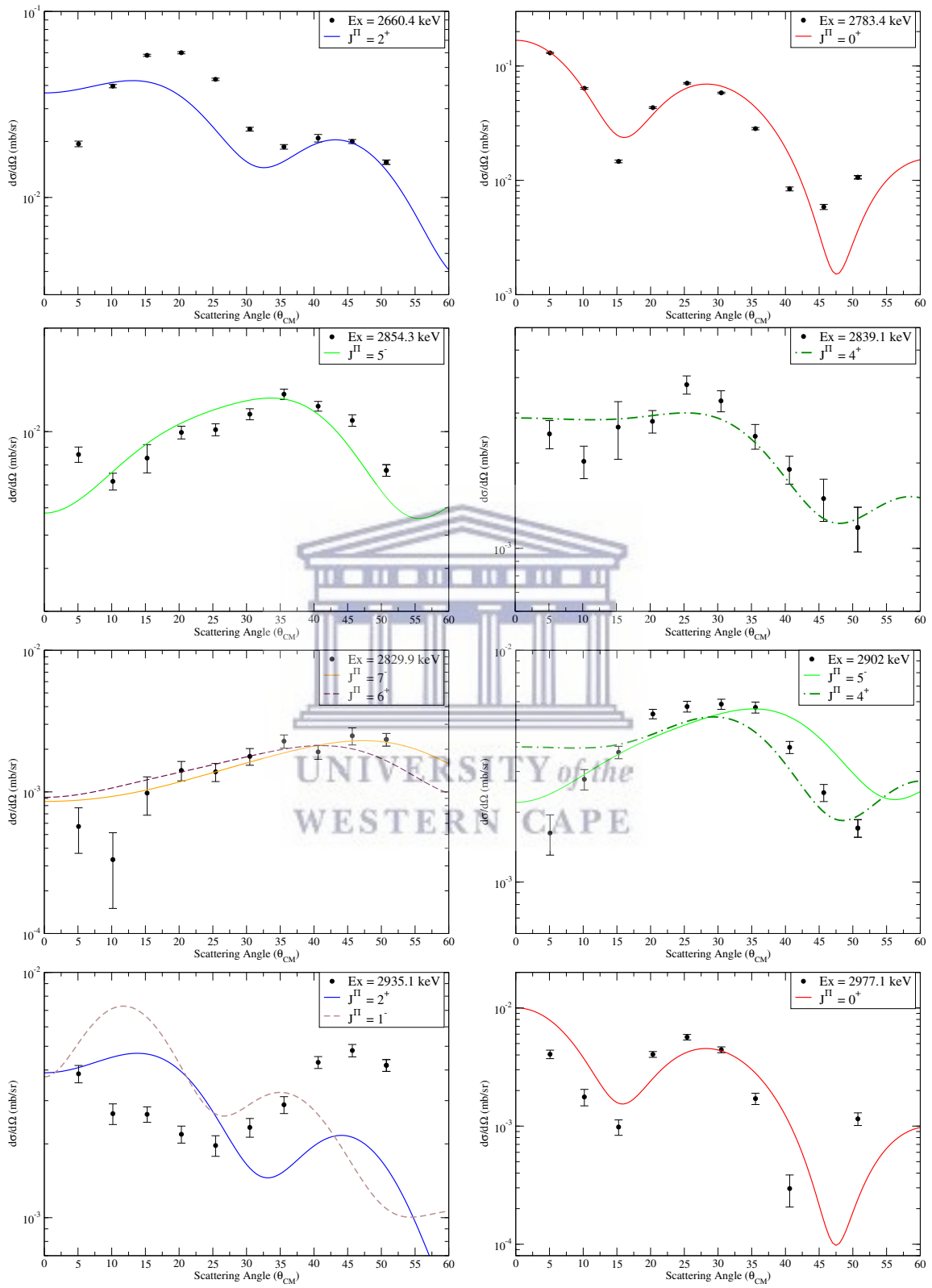
c | $^{138}\text{Ba}(p, t)^{136}\text{Ba}$ Angular distributions

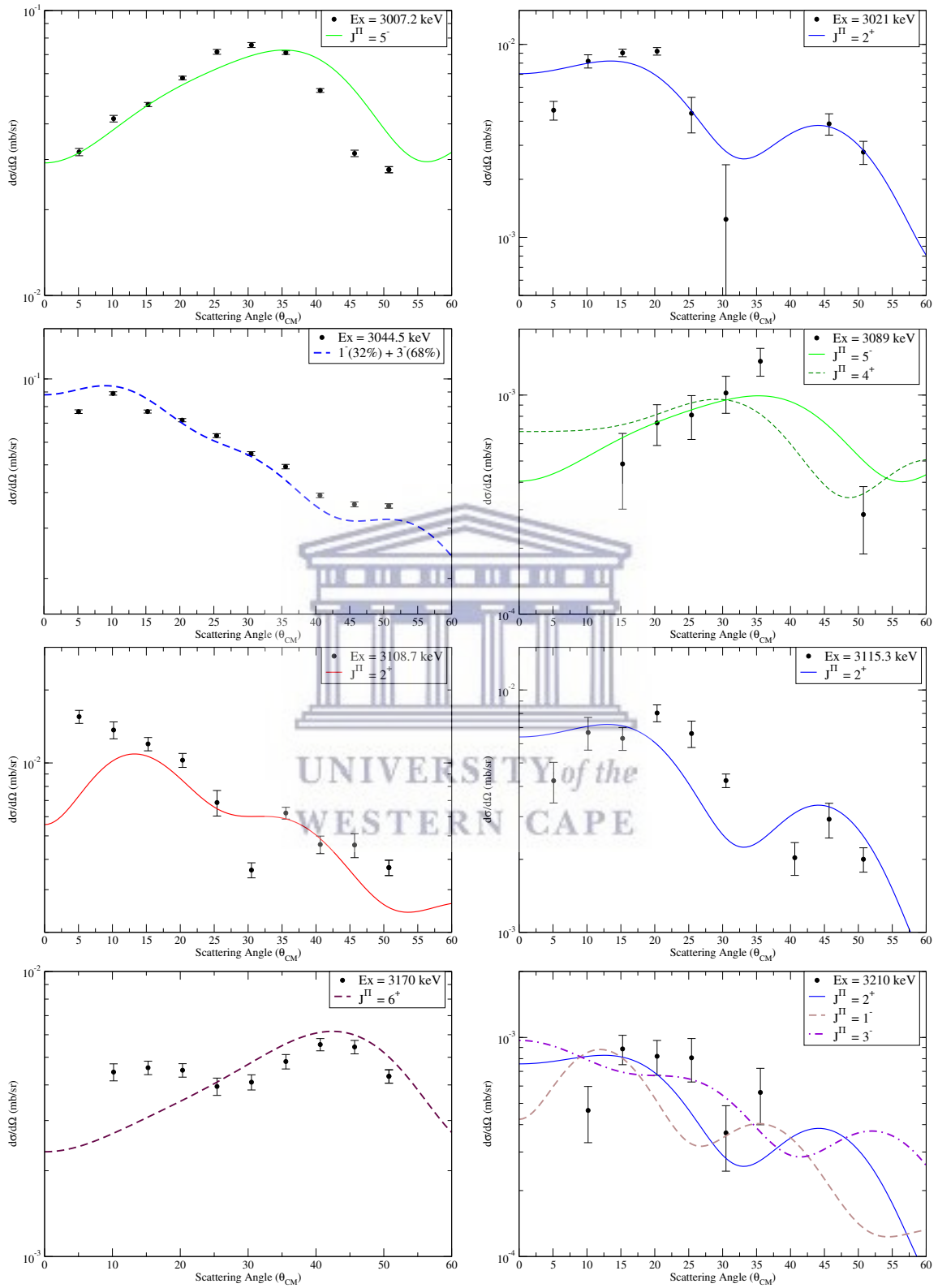
Angular distribution for the various states populated in the $^{138}\text{Ba}(p, t)^{136}\text{Ba}$ reaction are plotted along with the DWBA curves from DWUCK4 for these states. The proton optical model parameter set by Varner [156] and triton optical model parameter set by Li, Liang and Cai [159] are used for the DWBA curves. All the DWBA angular distribution are color coded and the experimental data points are plotted as solid black circles.

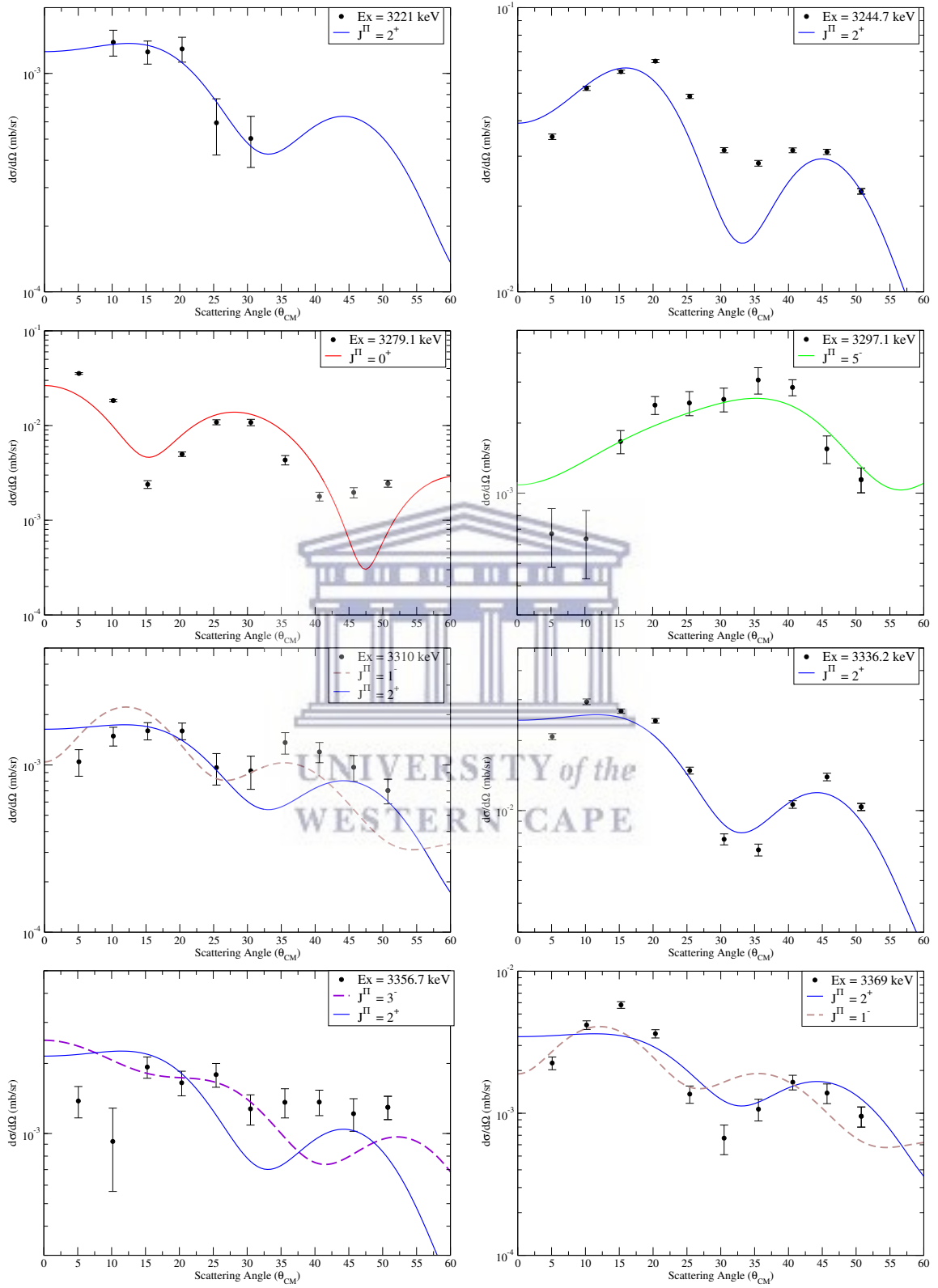


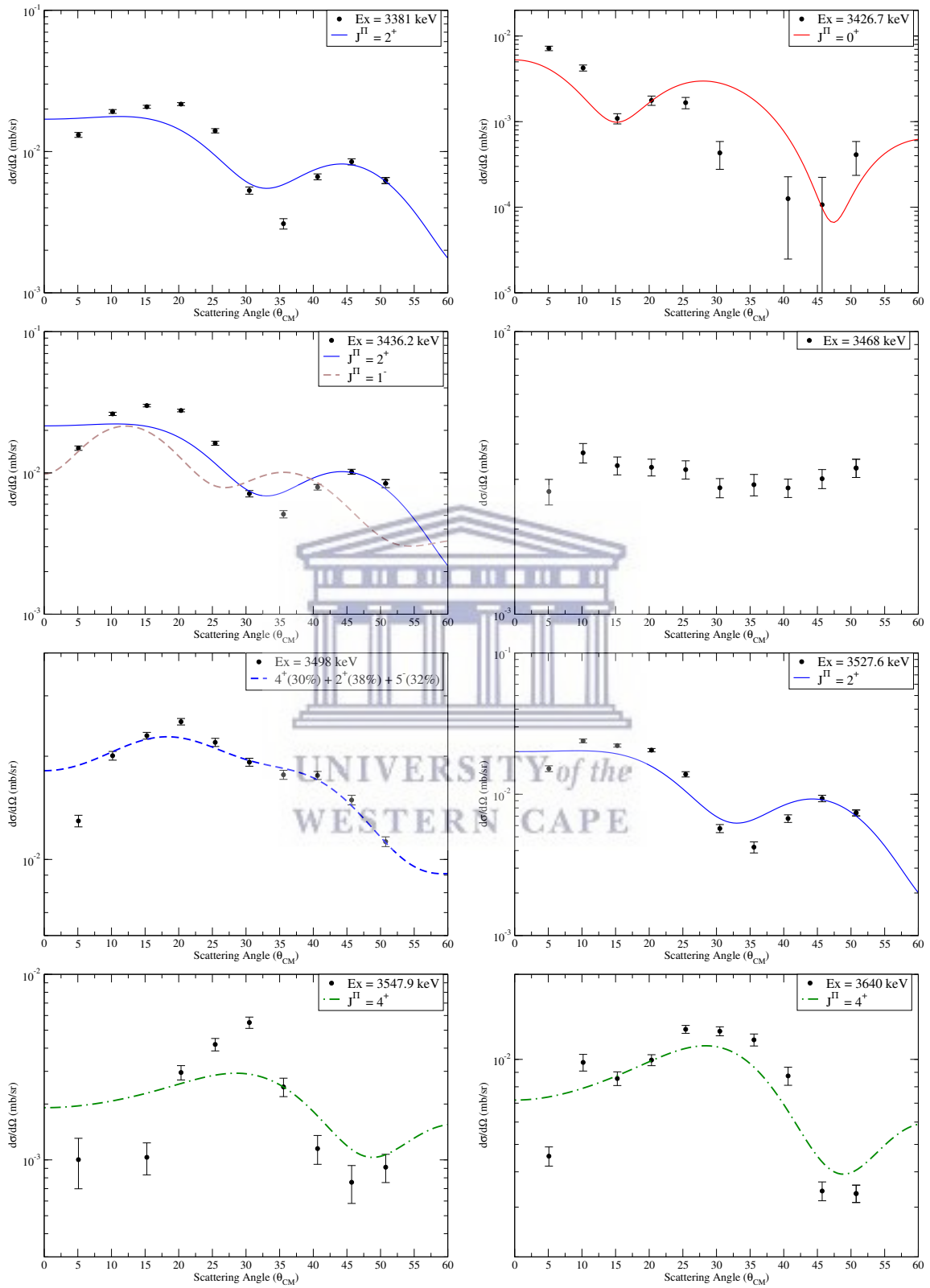


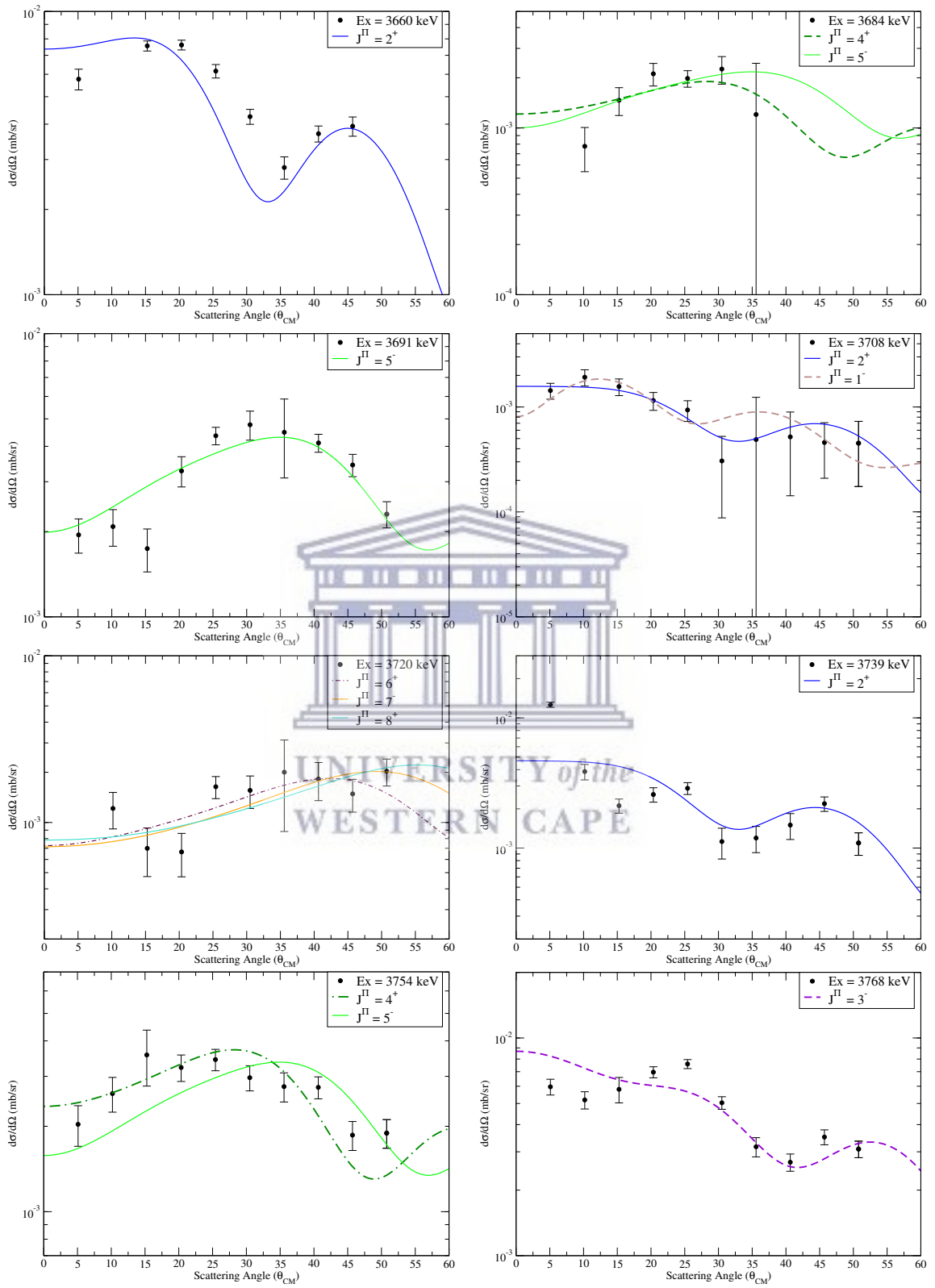


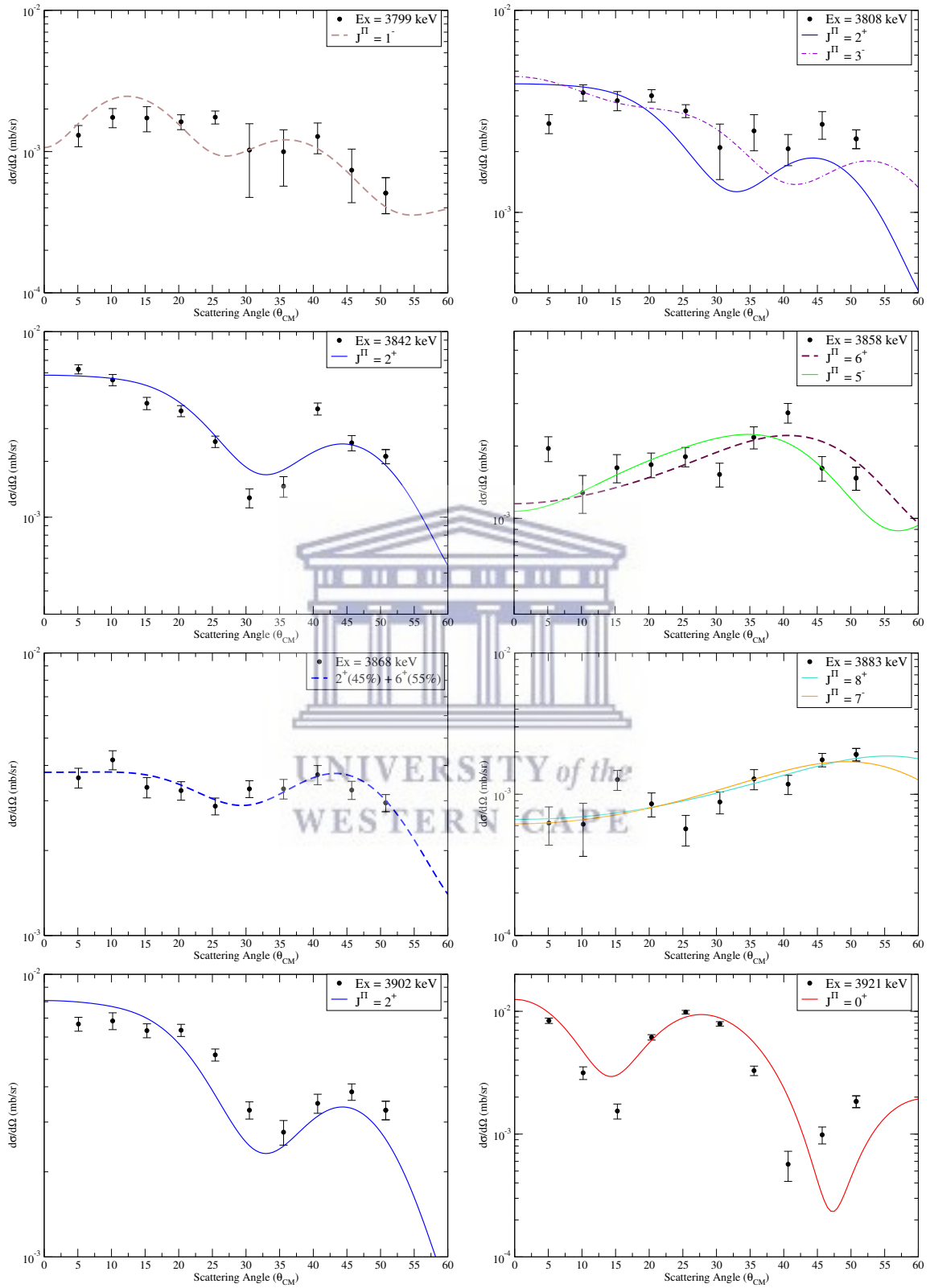


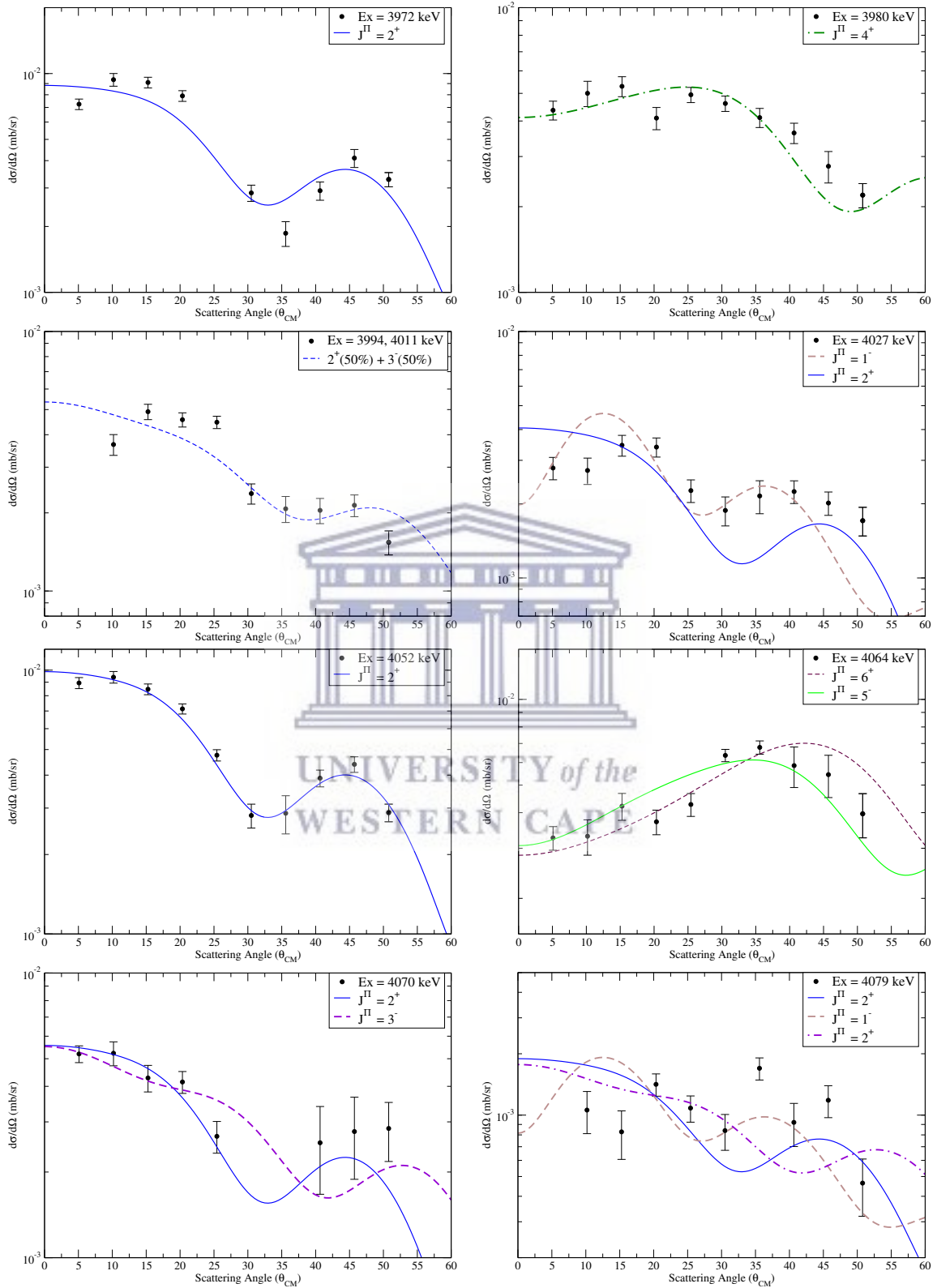


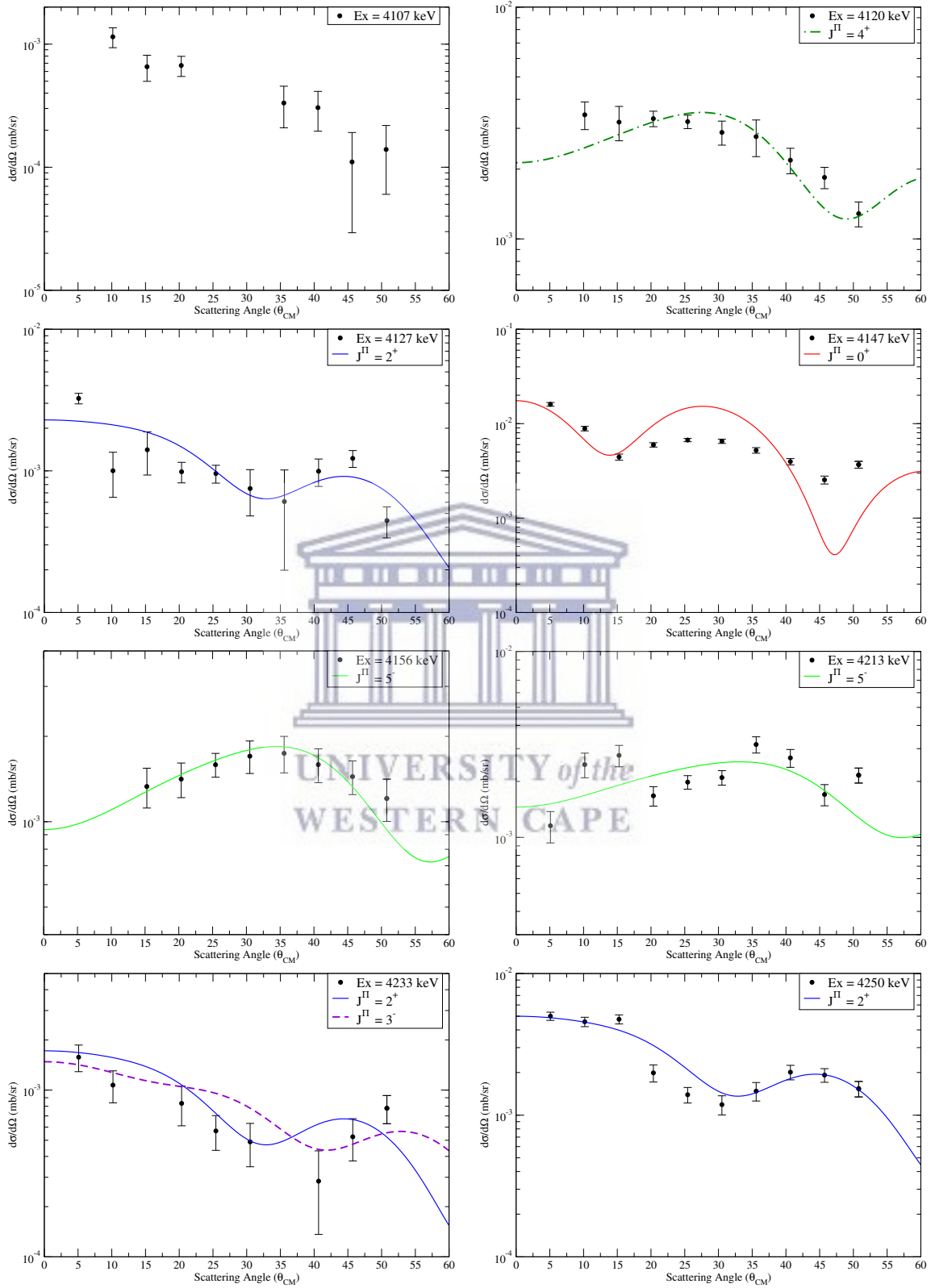


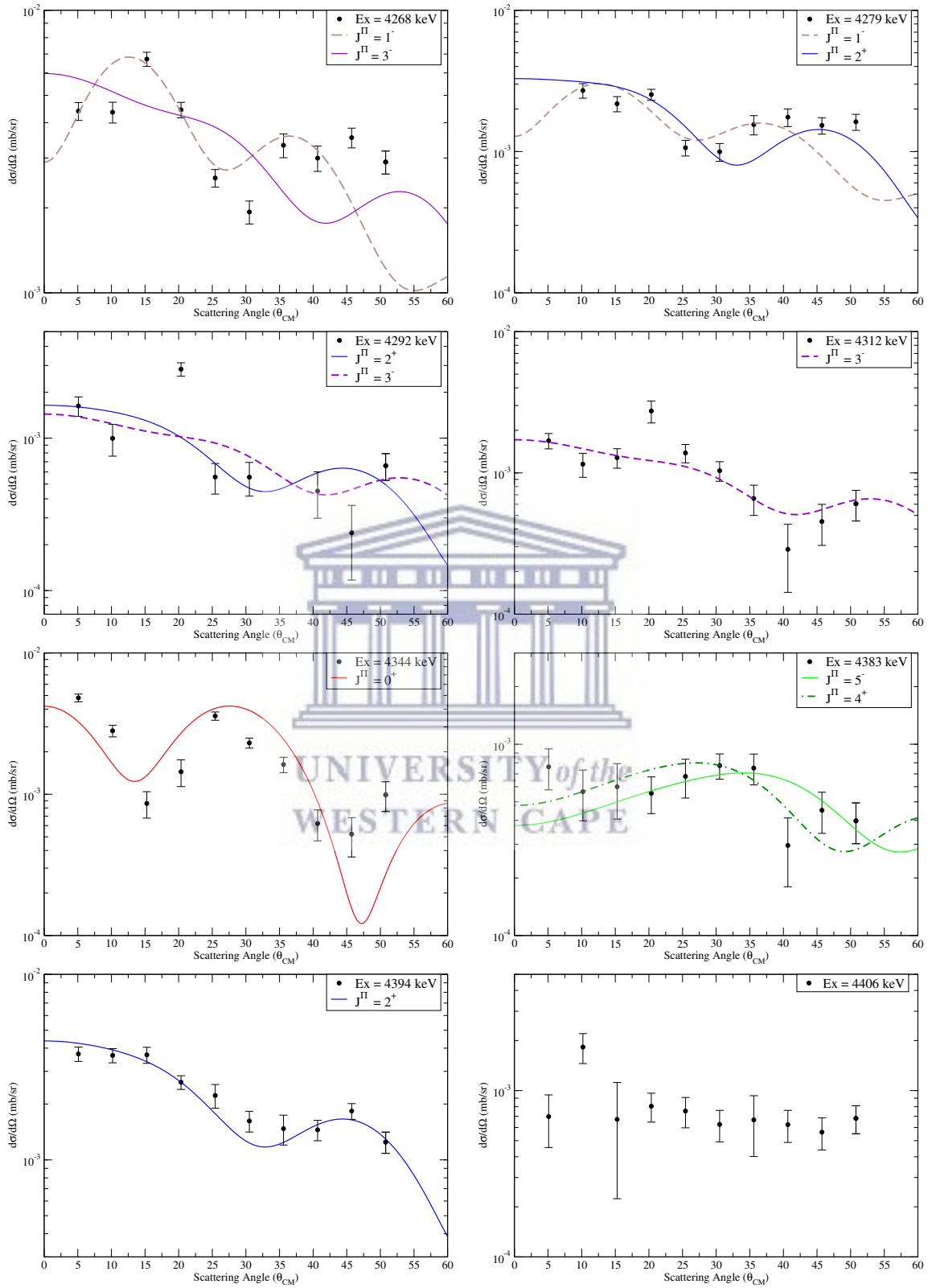


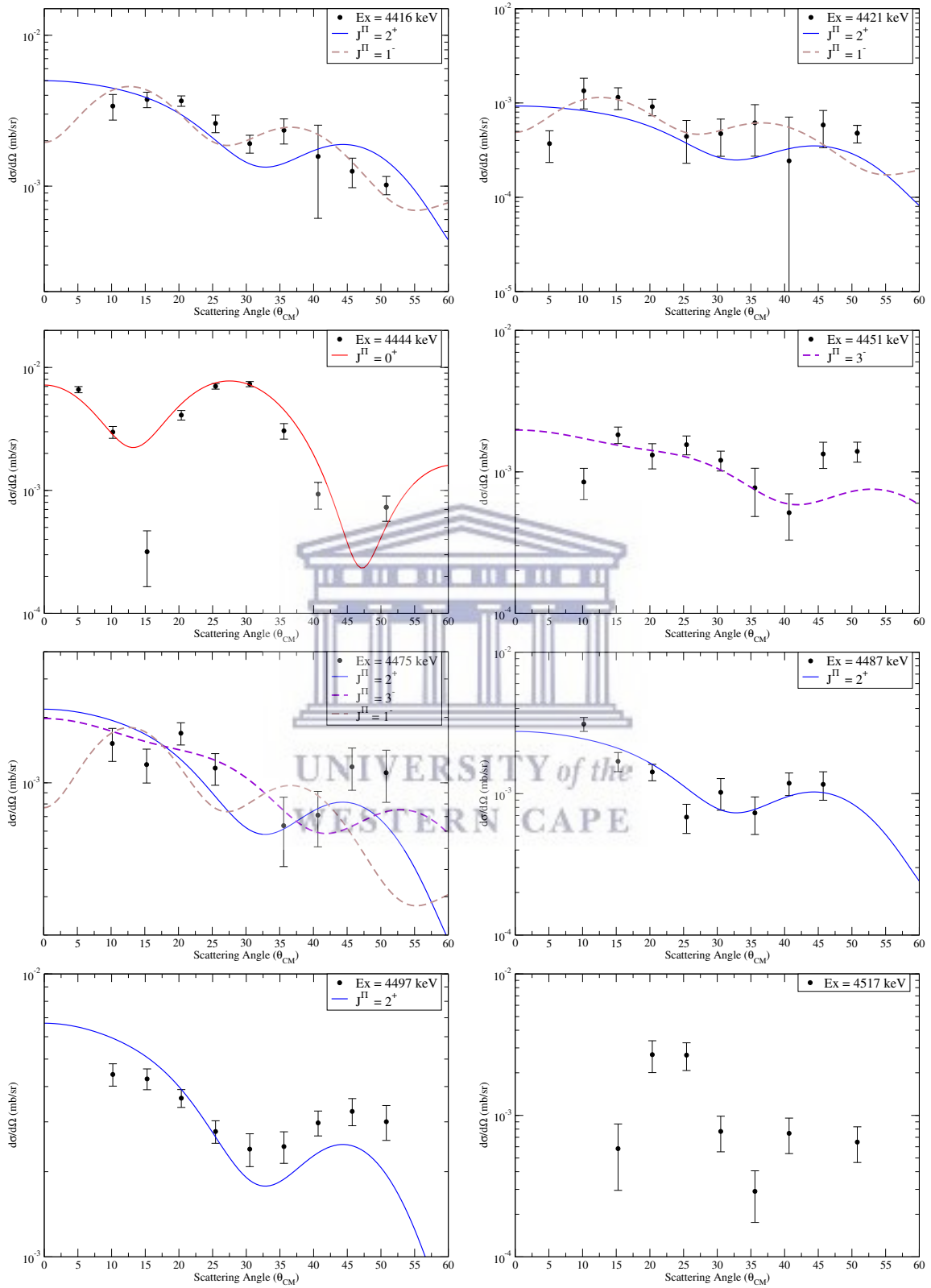


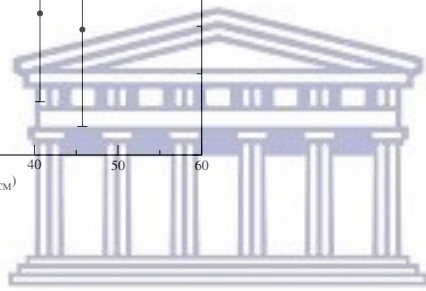
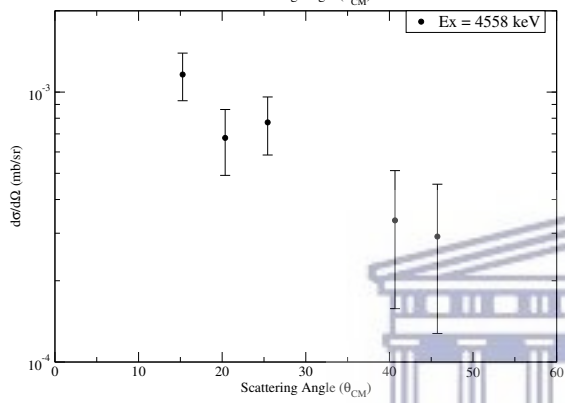
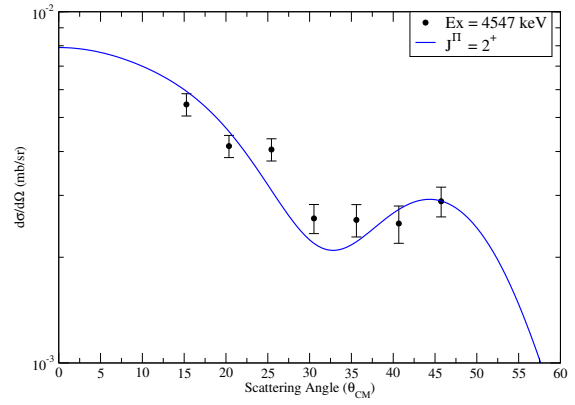
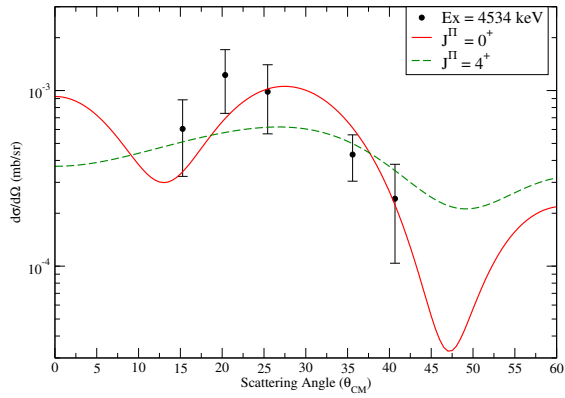








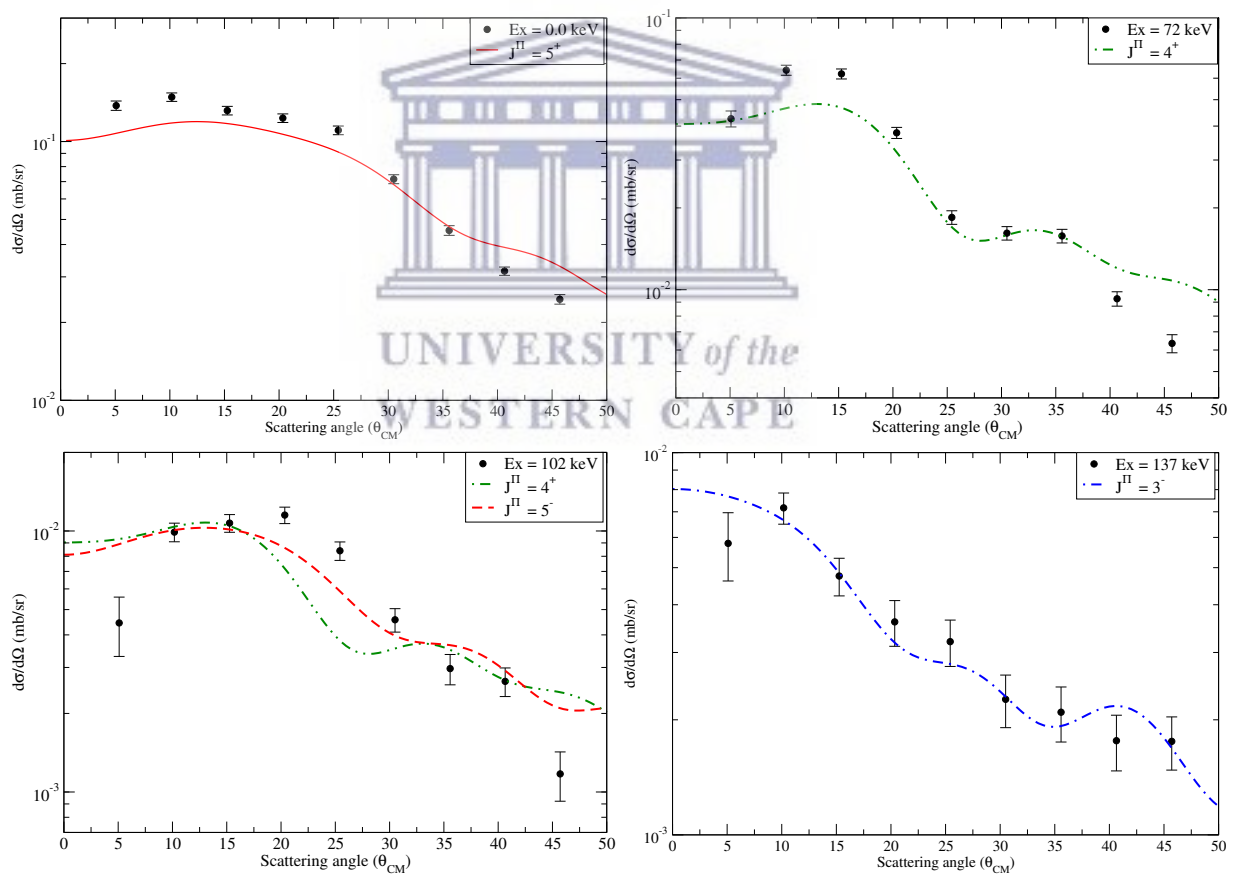


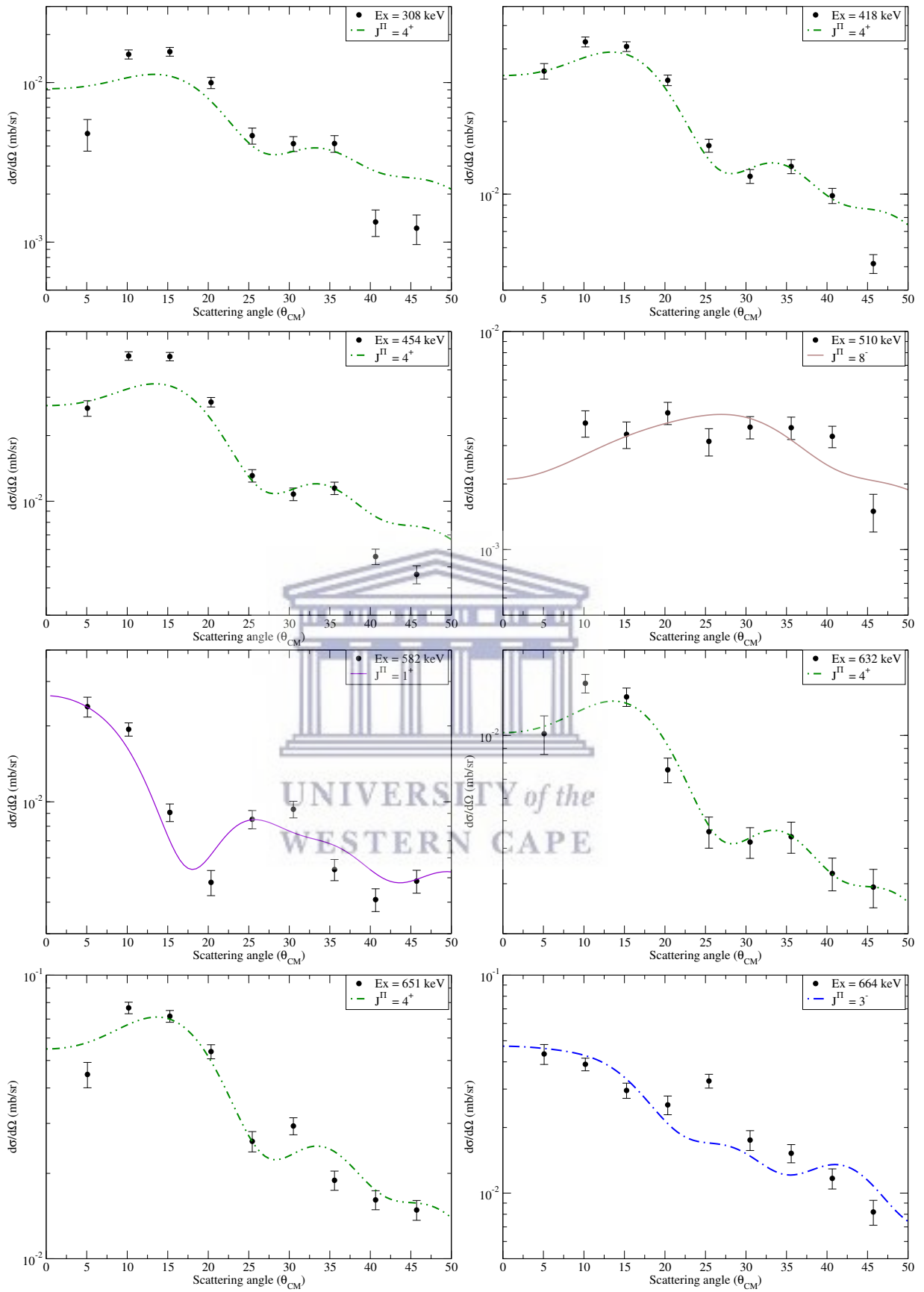


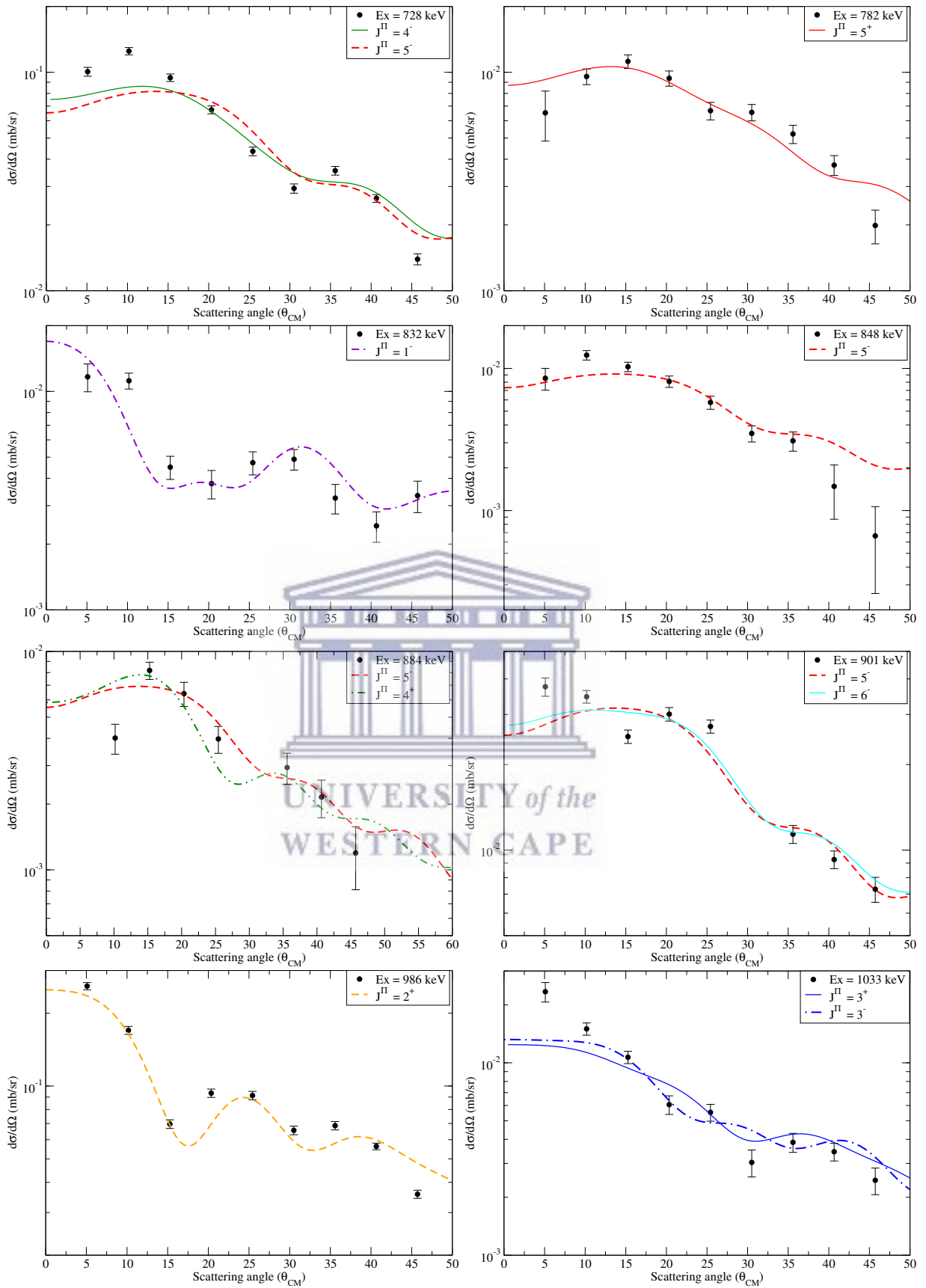
UNIVERSITY of the
 WESTERN CAPE

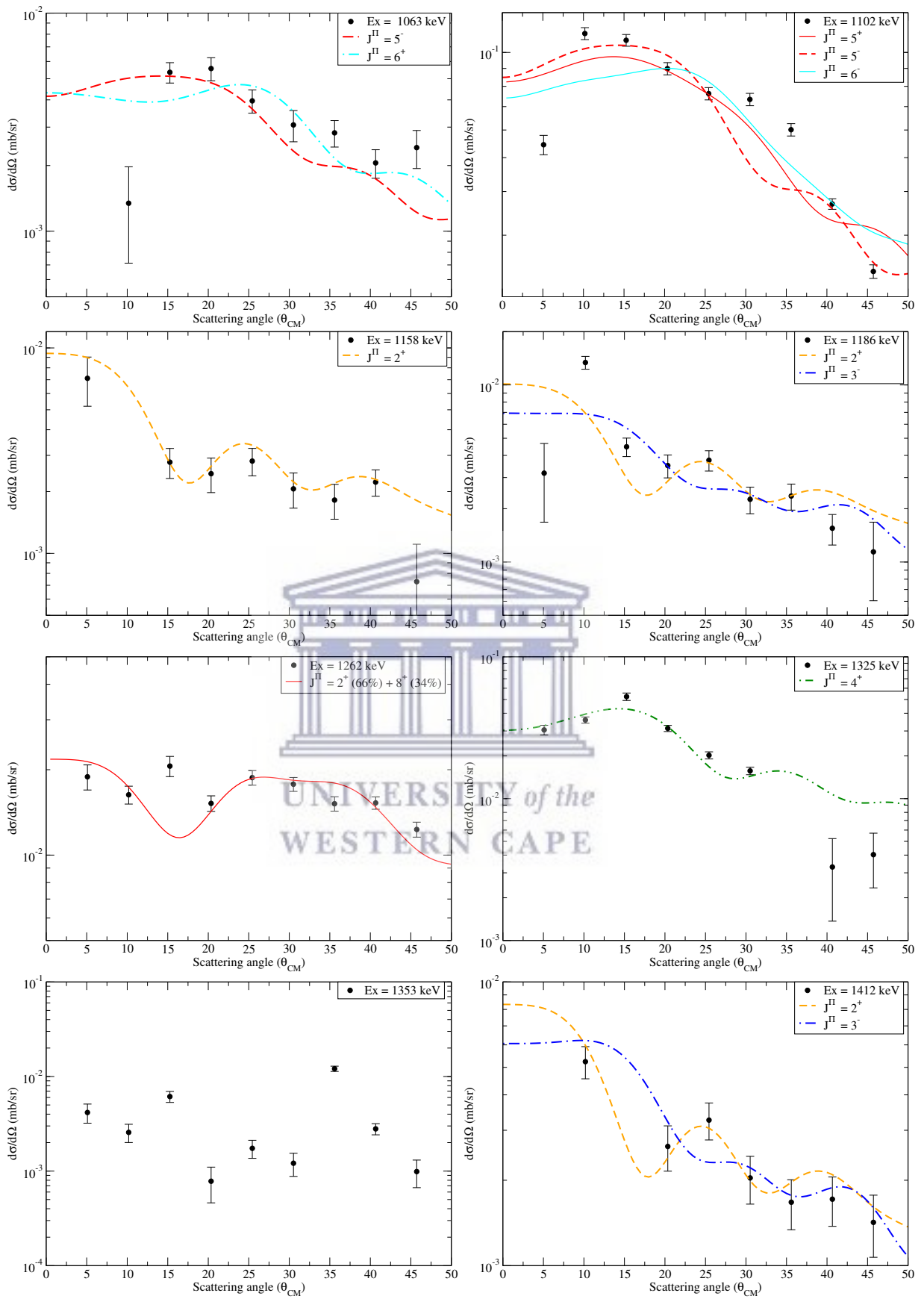
D | $^{138}\text{Ba}(d, \alpha)^{136}\text{Cs}$ Angular distributions

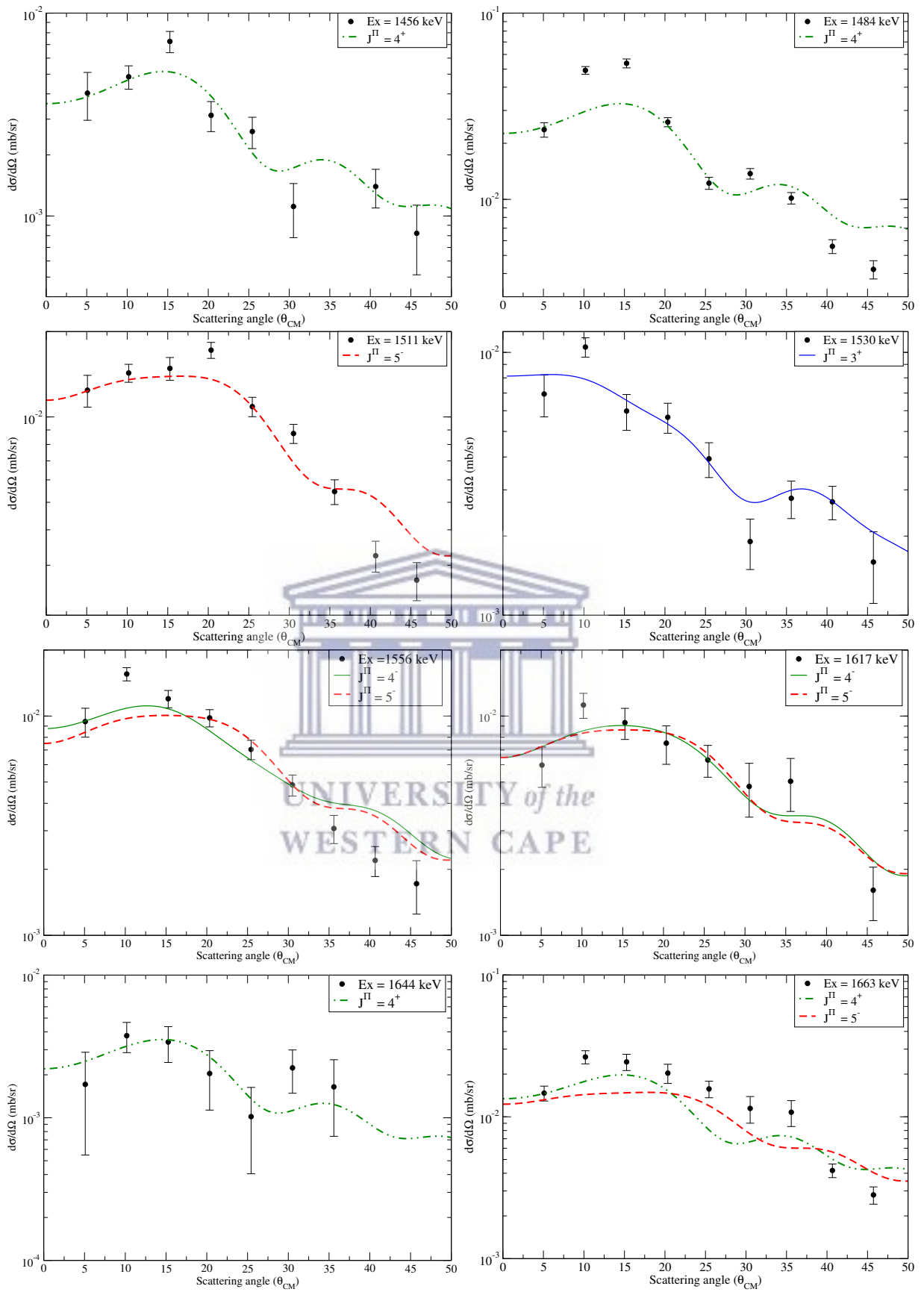
In this Appendix we show all the experimental and DWBA angular distributions for the states populated in the $^{138}\text{Ba}(d, \alpha)^{136}\text{Cs}$ reaction. All natural parity states here are shown as discontinues lines while the unnatural parity states are full solid lines. The deuteron optical model parameter set by An and Cai [178] and alpha optical model parameter set by Burnett *et al.* [184] are used in DWUCK4 [93].

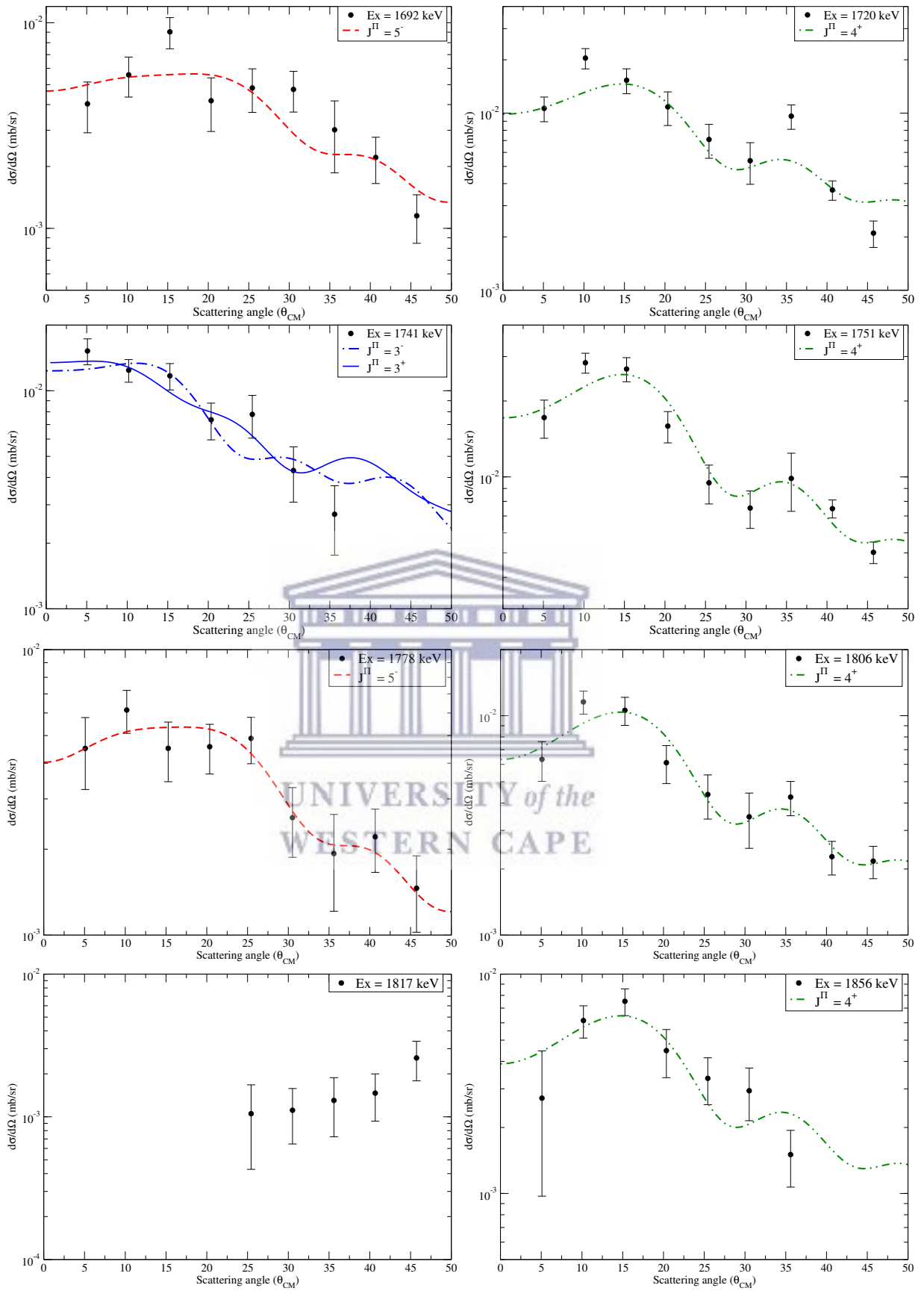


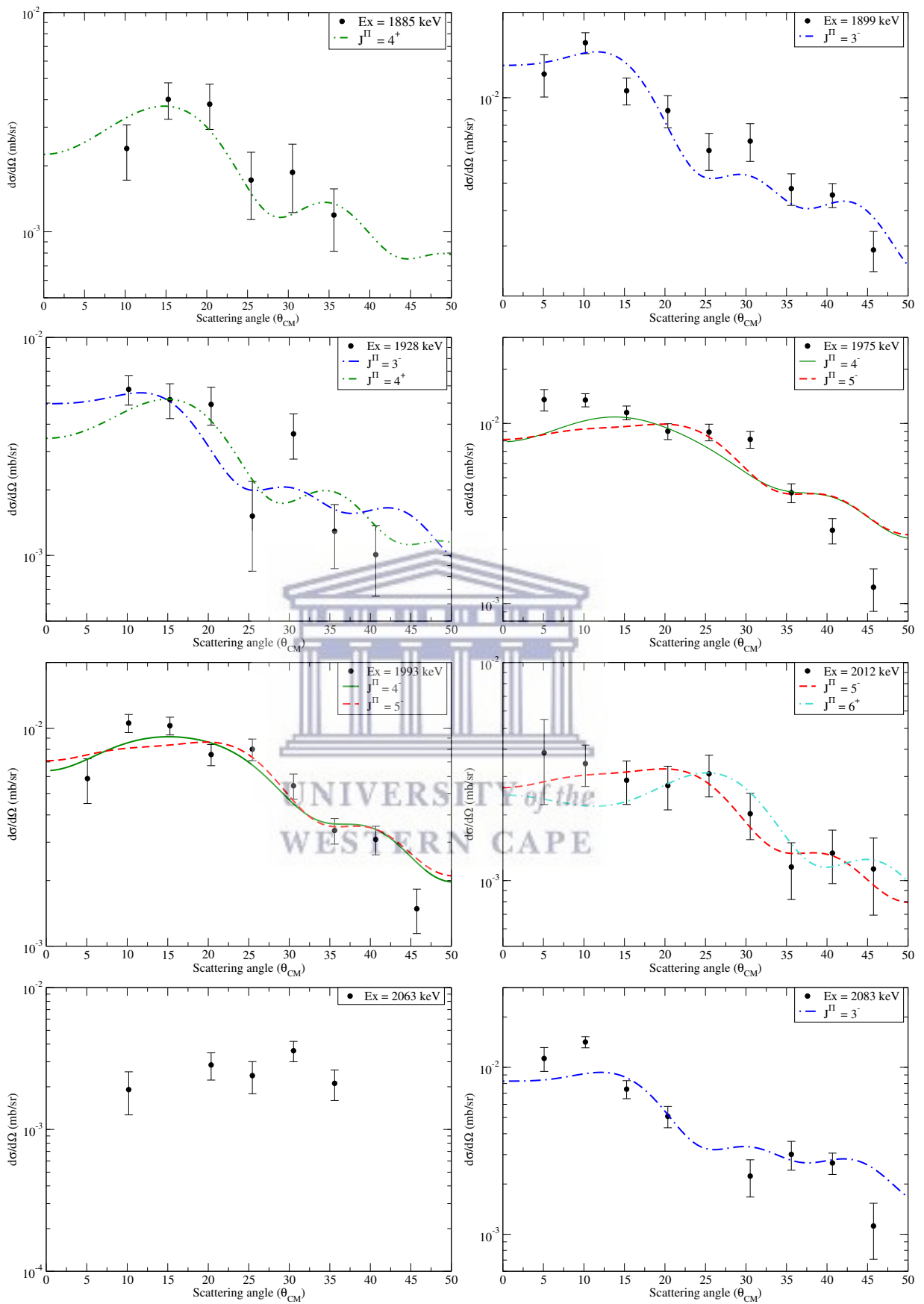


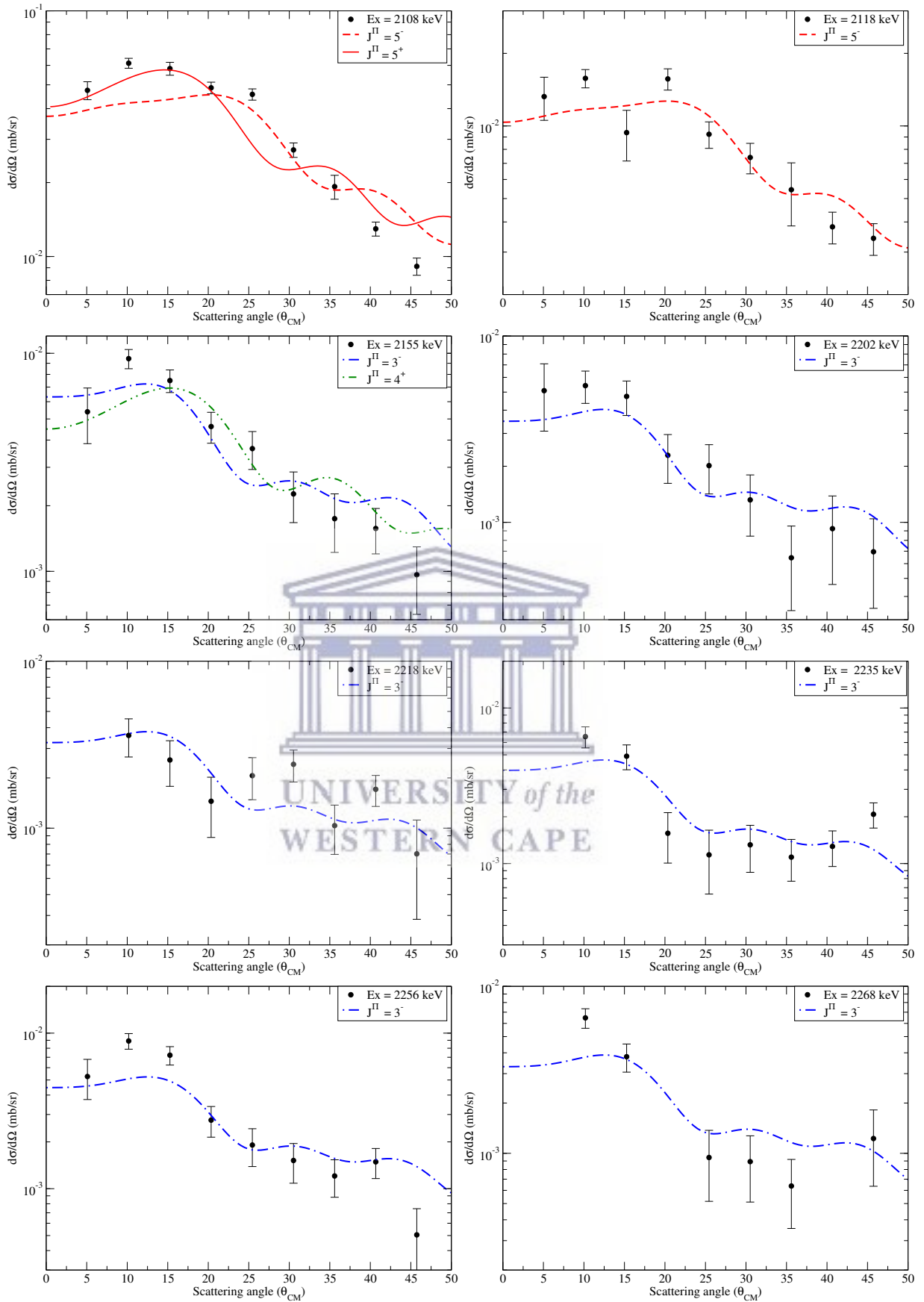


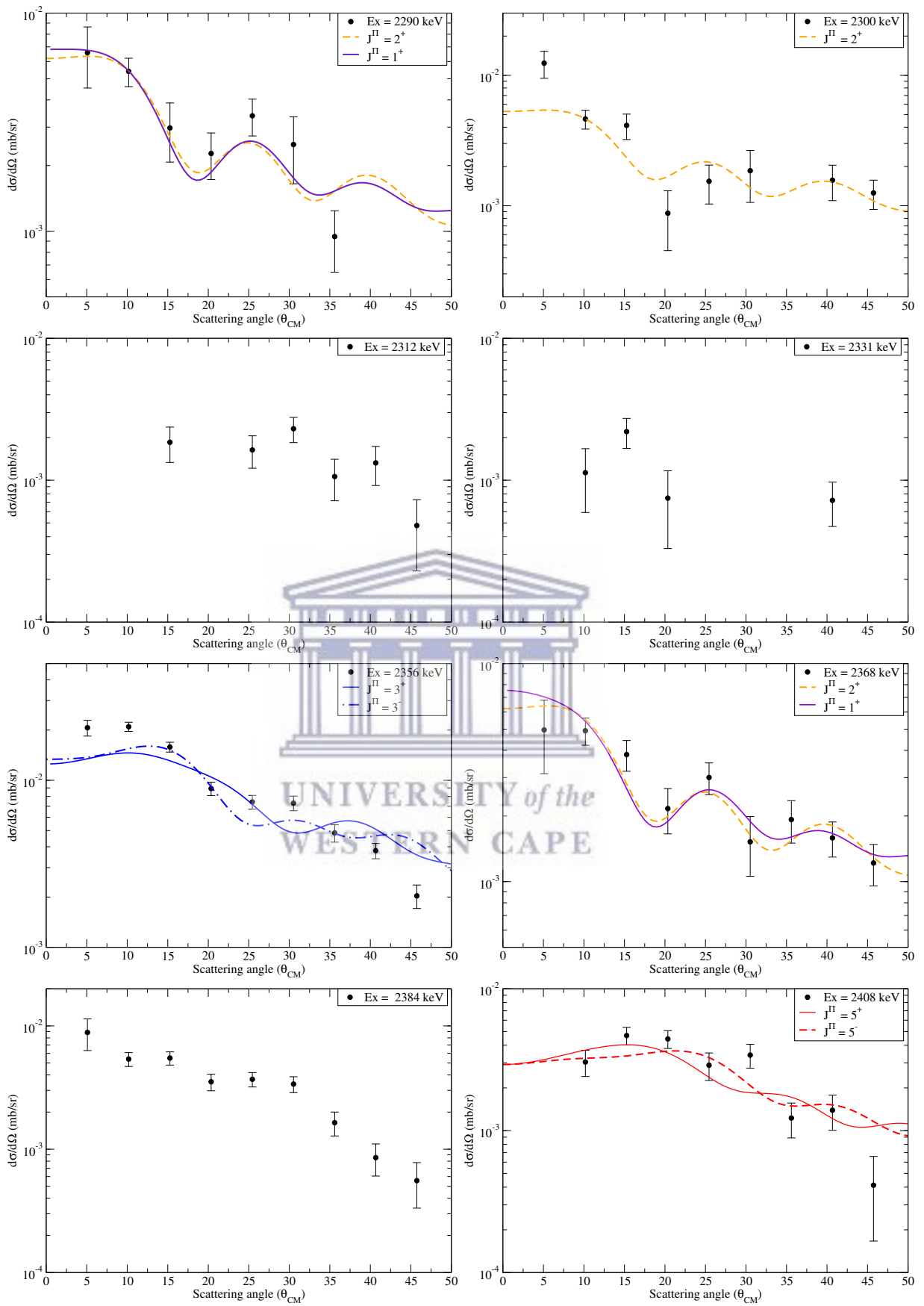


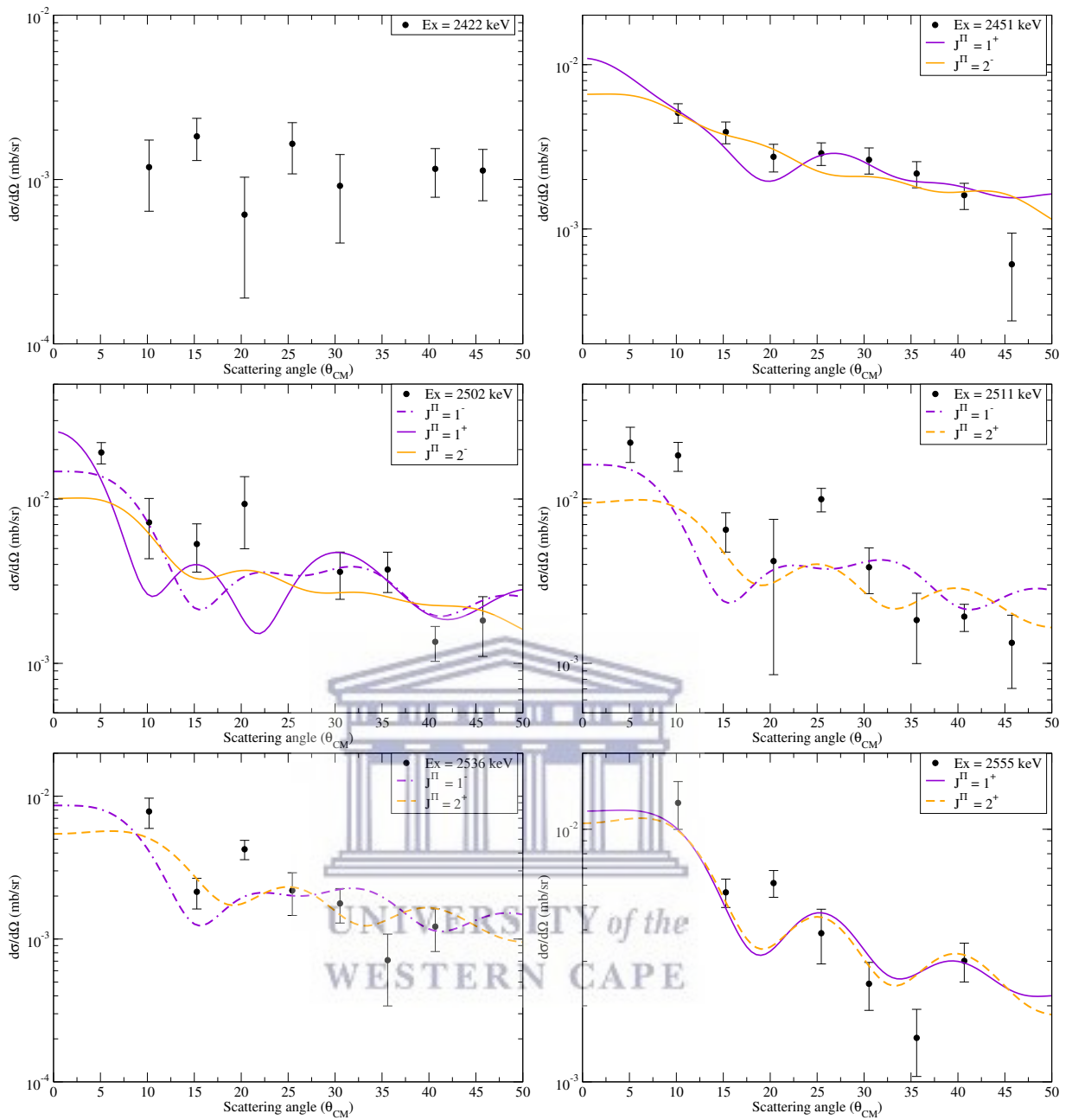












Bibliography

- [1] S. Bilenky, *Introduction to the Physics of Massive and Mixed Neutrinos, Lect. Notes Phys. 817*. Springer, Berlin Heidelberg, 2010.
- [2] D. J. Griffiths, *Introduction to Elementary Particles*. John Wiley & Sons., 1987.
- [3] E. M. Henley and A. Garcia, *Subatomic Physics, 3rd Edition*. World Scientific Publishing, 2007.
- [4] J. D. Bjorken and S. D. Drell, *Relativistic Quantum Mechanics*. New York : McGraw-Hill, 1964.
- [5] F. Halzen and A. D. Martin, *Quarks and leptons : an introductory course in modern particle physics*. 1984.
- [6] C. S. Wu, E. Ambler, R. W. Hayward, D. D. Hoppes, and R. P. Hudson, “Experimental Test of Parity Conservation in Beta Decay,” *Phys. Rev.*, vol. 105, pp. 1413–1415, Feb 1957.
- [7] R. Davis, “A review of the homestake solar neutrino experiment,” *Progress in Particle and Nuclear Physics*, vol. 32, pp. 13 – 32, 1994.
- [8] A. McDonald, “Evidence for Neutrino Oscillations I: Solar and Reactor Neutrinos,” *Nuclear Physics A*, vol. 751, pp. 53 – 66, 2005.
- [9] Y. Fukuda and (Super-Kamiokande Collaboration), “Evidence for Oscillation of Atmospheric Neutrinos,” *Phys. Rev. Lett.*, vol. 81, pp. 1562–1567, Aug 1998.

- [10] W. W. Christopher and (Super-Kamiokande collaboration), *The Super-Kamiokande Experiment*, pp. 19–43.
- [11] J. N. Bahcall, “Gallium solar neutrino experiments: Absorption cross sections, neutrino spectra, and predicted event rates,” *Phys. Rev. C*, vol. 56, pp. 3391–3409, Dec 1997.
- [12] J. N. Abdurashitov and (SAGE Collaboration), “Measurement of the solar neutrino capture rate with gallium metal. III. Results for the 2002–2007 data-taking period,” *Phys. Rev. C*, vol. 80, p. 015807, Jul 2009.
- [13] M. H. Ahn, others, and (K2K Collaboration), “Measurement of neutrino oscillation by the K2K experiment,” *Phys. Rev. D*, vol. 74, p. 072003, Oct 2006.
- [14] A. de Gouvea *et al.*, “Working Group Report: Neutrinos,” in *Proceedings, 2013 Community Summer Study on the Future of U.S. Particle Physics: Snowmass on the Mississippi (CSS2013): Minneapolis, MN, USA, July 29-August 6, 2013*, 2013.
- [15] W. C. Haxton and G. J. Stephenson, “Double beta decay,” *Progress in Particle and Nuclear Physics*, vol. 12, pp. 409 – 479, 1984.
- [16] J. W. F. Valle, “Neutrino physics overview,” *Journal of Physics: Conference Series*, vol. 53, no. 1, p. 473, 2006.
- [17] J. D. Vergados, H. Ejiri, and F. Šimkovic, “Theory of neutrinoless double-beta decay,” *Reports on Progress in Physics*, vol. 75, no. 10, p. 106301, 2012.
- [18] P. Vogel, “Nuclear structure and double beta decay,” *Journal of Physics G: Nuclear and Particle Physics*, vol. 39, no. 12, p. 124002, 2012.
- [19] F. T. Avignone, S. R. Elliott, and J. Engel, “Double beta decay, Majorana neutrinos, and neutrino mass,” *Rev. Mod. Phys.*, vol. 80, pp. 481–516, Apr 2008.
- [20] S. Dell’Oro, S. Marcocci, M. Viel, and F. Vissani, “Neutrinoless Double Beta Decay: 2015 Review,” *Advances in High Energy Physics*, vol. 2016, p. 2162659, 2016.

- [21] Heinrich Päs and Werner Rodejohann, “Neutrinoless double beta decay,” *New Journal of Physics*, vol. 17, no. 11, p. 115010, 2015.
- [22] F. F. Deppisch, M. Hirsch, and H. Päs, “Neutrinoless double-beta decay and physics beyond the standard model,” *Journal of Physics G: Nuclear and Particle Physics*, vol. 39, no. 12, p. 124007, 2012.
- [23] R. N. Mohapatra and G. Senjanović, “Neutrino Mass and Spontaneous Parity Non-conservation,” *Phys. Rev. Lett.*, vol. 44, pp. 912–915, Apr 1980.
- [24] J. Vergados, “The neutrinoless double beta decay from a modern perspective,” *Physics Reports*, vol. 361, no. 1, pp. 1 – 56, 2002.
- [25] J. Schechter and J. W. F. Valle, “Neutrinoless double- β decay in $SU(2)\times U(1)$ theories,” *Phys. Rev. D*, vol. 25, pp. 2951–2954, Jun 1982.
- [26] J. Engel and J. Menéndez, “Status and future of nuclear matrix elements for neutrinoless double-beta decay: a review,” *Reports on Progress in Physics*, vol. 80, no. 4, p. 046301, 2017.
- [27] V. A. Rodin, A. Faessler, F. Šimkovic, and P. Vogel, “Uncertainty in the $0\nu\beta\beta$ decay nuclear matrix elements,” *Phys. Rev. C*, vol. 68, p. 044302, Oct 2003.
- [28] F. Šimkovic, A. Faessler, H. Mütter, V. Rodin, and M. Stauf, “ $0\nu\beta\beta$ -decay nuclear matrix elements with self-consistent short-range correlations,” *Phys. Rev. C*, vol. 79, p. 055501, May 2009.
- [29] J. Hyvärinen and J. Suhonen, “Nuclear matrix elements for $0\nu\beta\beta$ decays with light or heavy Majorana-neutrino exchange,” *Phys. Rev. C*, vol. 91, p. 024613, Feb 2015.
- [30] F. Šimkovic, V. Rodin, A. Faessler, and P. Vogel, “ $0\nu\beta\beta$ and $2\nu\beta\beta$ nuclear matrix elements, quasiparticle random-phase approximation, and isospin symmetry restoration,” *Phys. Rev. C*, vol. 87, p. 045501, Apr 2013.

- [31] M. T. Mustonen and J. Engel, “Large-scale calculations of the double- β decay of ^{76}Ge , ^{130}Te , ^{136}Xe , and ^{150}Nd in the deformed self-consistent Skyrme quasiparticle random-phase approximation,” *Phys. Rev. C*, vol. 87, p. 064302, Jun 2013.
- [32] E. Caurier, J. Menéndez, F. Nowacki, and A. Poves, “Influence of Pairing on the Nuclear Matrix Elements of the Neutrinoless $\beta\beta$ Decays,” *Phys. Rev. Lett.*, vol. 100, p. 052503, Feb 2008.
- [33] J. Menéndez, A. Poves, E. Caurier, and F. Nowacki, “Disassembling the nuclear matrix elements of the neutrinoless $\beta\beta$ decay,” *Nuclear Physics A*, vol. 818, no. 3, pp. 139 – 151, 2009.
- [34] P. K. Rath, R. Chandra, K. Chaturvedi, P. K. Raina, and J. G. Hirsch, “Uncertainties in nuclear transition matrix elements for neutrinoless $\beta\beta$ decay within the projected-Hartree-Fock-Bogoliubov model,” *Phys. Rev. C*, vol. 82, p. 064310, Dec 2010.
- [35] J. Barea and F. Iachello, “Neutrinoless double- β decay in the microscopic interacting boson model,” *Phys. Rev. C*, vol. 79, p. 044301, Apr 2009.
- [36] T. R. Rodríguez and G. Martínez-Pinedo, “Energy density functional study of nuclear matrix elements for neutrinoless $\beta\beta$ decay,” *Phys. Rev. Lett.*, vol. 105, p. 252503, Dec 2010.
- [37] E. Caurier, G. Martínez-Pinedo, F. Nowacki, A. Poves, and A. P. Zuker, “The shell model as a unified view of nuclear structure,” *Rev. Mod. Phys.*, vol. 77, pp. 427–488, Jun 2005.
- [38] B. Brown, “The nuclear shell model towards the drip lines,” *Progress in Particle and Nuclear Physics*, vol. 47, no. 2, pp. 517 – 599, 2001.
- [39] G. Martínez-Pinedo, A. Poves, E. Caurier, and A. P. Zuker, “Effective g_A in the pf shell,” *Phys. Rev. C*, vol. 53, pp. R2602–R2605, Jun 1996.

- [40] B. H. Wildenthal, M. S. Curtin, and B. A. Brown, “Predicted features of the beta decay of neutron-rich sd-shell nuclei,” *Phys. Rev. C*, vol. 28, pp. 1343–1366, Sep 1983.
- [41] O. Civitarese and J. Suhonen, “Nuclear matrix elements for double beta decay in the QRPA approach: A critical review,” *Journal of Physics: Conference Series*, vol. 173, no. 1, p. 012012, 2009.
- [42] V. Rodin, A. Faessler, F. Simkovic, and P. Vogel, “Assessment of uncertainties in QRPA $0\nu\beta\beta$ -decay nuclear matrix elements,” *Nuclear Physics A*, vol. 766, pp. 107 – 131, 2006.
- [43] D. Cha, “ $\sigma\tau_+$ strength in nuclei,” *Phys. Rev. C*, vol. 27, pp. 2269–2281, May 1983.
- [44] P. Vogel and M. R. Zirnbauer, “Suppression of the two-neutrino double-beta decay by nuclear-structure effects,” *Phys. Rev. Lett.*, vol. 57, pp. 3148–3151, Dec 1986.
- [45] H. Ejiri, “Double Beta Decays and Neutrino Masses,” *Journal of the Physical Society of Japan*, vol. 74, no. 8, pp. 2101–2127, 2005.
- [46] H. Ejiri, “Nuclear spin isospin responses for low-energy neutrinos,” *Physics Reports*, vol. 338, no. 3, pp. 265 – 351, 2000.
- [47] F. Simkovic, L. Pacearescu, and A. Faessler, “Two-neutrino double beta decay of ^{76}Ge within deformed QRPA,” *Nuclear Physics A*, vol. 733, no. 3, pp. 321–350, 2004.
- [48] Frekers, D. and Alanssari, M., “Charge-exchange reactions and the quest for resolution,” *Eur. Phys. J. A*, vol. 54, no. 10, p. 177, 2018.
- [49] H. Dohmann *et al.*, “The $(d, ^2\text{He})$ reaction on ^{96}Mo and the double- β decay matrix elements for ^{96}Zr ,” *Phys. Rev. C*, vol. 78, p. 041602, Oct 2008.
- [50] S. Rakers *et al.*, “Low-lying GT^+ strength in ^{116}In from a $(d, ^2\text{He})$ reaction experiment and its implications for ^{116}Cd double β decay,” *Phys. Rev. C*, vol. 71, p. 054313, May 2005.

- [51] H. Akimune *et al.*, “GT strengths studied by ($^3\text{He},t$) reactions and nuclear matrix elements for double beta decays,” *Physics Letters B*, vol. 394, no. 1, pp. 23 – 28, 1997.
- [52] E.-W. Grewe *et al.*, “($^3\text{He},t$) reaction on the double β decay nucleus ^{48}Ca and the importance of nuclear matrix elements,” *Phys. Rev. C*, vol. 76, p. 054307, Nov 2007.
- [53] E.-W. Grewe *et al.*, “The ($d, ^2\text{He}$) reaction on ^{76}Se and the double- β -decay matrix elements for $A = 76$,” *Phys. Rev. C*, vol. 78, p. 044301, Oct 2008.
- [54] R. A. Sen’kov, M. Horoi, and B. A. Brown, “Neutrinoless double- β decay of ^{82}Se in the shell model: Beyond the closure approximation,” *Phys. Rev. C*, vol. 89, p. 054304, May 2014.
- [55] J. Suhonen and O. Civitarese, “Review of the properties of the $0\nu\beta^-\beta^-$ nuclear matrix elements,” *Journal of Physics G: Nuclear and Particle Physics*, vol. 39, no. 12, p. 124005, 2012.
- [56] M. Horoi and S. Stoica, “Shell model analysis of the neutrinoless double- β decay of ^{48}Ca ,” *Phys. Rev. C*, vol. 81, p. 024321, Feb 2010.
- [57] J. Barea, J. Kotila, and F. Iachello, “Nuclear matrix elements for double- β decay,” *Phys. Rev. C*, vol. 87, p. 014315, Jan 2013.
- [58] R. A. Sen’kov and M. Horoi, “Neutrinoless double- β decay of ^{48}Ca in the shell model: Closure versus nonclosure approximation,” *Phys. Rev. C*, vol. 88, p. 064312, Dec 2013.
- [59] R. A. Sen’kov and M. Horoi, “Accurate shell-model nuclear matrix elements for neutrinoless double- β decay,” *Phys. Rev. C*, vol. 90, p. 051301, 2014.
- [60] S. J. Freeman and J. P. Schiffer, “Constraining the $0\nu 2\beta$ matrix elements by nuclear structure observables,” *Journal of Physics G: Nuclear and Particle Physics*, vol. 39, no. 12, p. 124004, 2012.

- [61] R. Álvarez-Rodríguez *et al.*, “Deformed quasiparticle random phase approximation formalism for single- and two-neutrino double β decay,” *Phys. Rev. C*, vol. 70, p. 064309, 2004.
- [62] Caurier, E., Nowacki, F., and Poves, A., “Nuclear-structure aspects of the neutrinoless decays,” *Eur. Phys. J. A*, vol. 36, no. 2, pp. 195–200, 2008.
- [63] J. Menéndez, A. Poves, E. Caurier, and F. Nowacki, “Occupancies of individual orbits, and the nuclear matrix element of the ^{76}Ge neutrinoless $\beta\beta$ decay,” *Phys. Rev. C*, vol. 80, p. 048501, Oct 2009.
- [64] J. Suhonen and O. Civitarese, “Effects of orbital occupancies on the neutrinoless $\beta\beta$ matrix element of ^{76}Ge ,” *Physics Letters B*, vol. 668, no. 4, pp. 277 – 281, 2008.
- [65] J. Suhonen and O. Civitarese, “Effects of orbital occupancies and spin-orbit partners on $0\nu\beta\beta$ -decay rates,” *Nuclear Physics A*, vol. 847, no. 3, pp. 207 – 232, 2010.
- [66] A. Gando *et al.*, “Search for Majorana Neutrinos Near the Inverted Mass Hierarchy Region with KamLAND-Zen,” *Phys. Rev. Lett.*, vol. 117, p. 082503, Aug 2016.
- [67] J. Shirai *et al.*, “Results and future plans for the KamLAND-Zen experiment,” *Journal of Physics: Conference Series*, vol. 888, no. 1, p. 012031, 2017.
- [68] J. Shirai, “KamLAND-Zen: Status and Future,” *Nuclear Physics B - Proceedings Supplements*, vol. 237-238, pp. 28 – 30, 2013. Proceedings of the Neutrino Oscillation Workshop.
- [69] J. B. Albert *et al.*, “Search for Majorana neutrinos with the first two years of EXO-200 data,” *Nature*, vol. 510, pp. 229–234, 2014.
- [70] M. Auger *et al.*, “The EXO-200 detector, part I: detector design and construction,” *Journal of Instrumentation*, vol. 7, no. 05, p. P05010, 2012.
- [71] C. Alduino *et al.*, “First Results from CUORE: A Search for Lepton Number Violation via $0\nu\beta\beta$ Decay of ^{130}Te ,” *Phys. Rev. Lett.*, vol. 120, p. 132501, Mar 2018.

- [72] C. E. Aalseth *et al.*, “Search for neutrinoless double- β decay in ^{76}Ge with the majorana demonstrator,” *Phys. Rev. Lett.*, vol. 120, p. 132502, Mar 2018.
- [73] M. Agostini *et al.*, “Improved Limit on Neutrinoless Double- β Decay of ^{76}Ge from GERDA Phase II,” *Phys. Rev. Lett.*, vol. 120, p. 132503, Mar 2018.
- [74] O. Azzolini *et al.*, “First Result on the Neutrinoless Double- β Decay of ^{82}Se with CUPID-0,” *Phys. Rev. Lett.*, vol. 120, p. 232502, Jun 2018.
- [75] E. Andreotti *et al.*, “ ^{130}Te neutrinoless double-beta decay with CUORICINO,” *Astroparticle Physics*, vol. 34, no. 11, pp. 822 – 831, 2011.
- [76] J. Argyriades *et al.*, “Measurement of the two neutrino double beta decay half-life of Zr-96 with the NEMO-3 detector,” *Nuclear Physics A*, vol. 847, no. 3, pp. 168 – 179, 2010.
- [77] R. Arnold *et al.*, “Measurement of the double-beta decay half-life and search for the neutrinoless double-beta decay of ^{48}Ca with the NEMO-3 detector,” *Phys. Rev. D*, vol. 93, p. 112008, Jun 2016.
- [78] D. Waters *et al.*, “Latest Results from NEMO-3 & Status of the SuperNEMO Experiment,” *Journal of Physics: Conference Series*, vol. 888, no. 1, p. 012033, 2017.
- [79] N. Ackerman *et al.*, “Observation of Two-Neutrino Double-Beta Decay in ^{136}Xe with the EXO-200 Detector,” *Phys. Rev. Lett.*, vol. 107, p. 212501, Nov 2011.
- [80] J. B. Albert *et al.*, “Improved measurement of the $2\nu\beta\beta$ half-life of ^{136}Xe with the EXO-200 detector,” *Phys. Rev. C*, vol. 89, p. 015502, Jan 2014.
- [81] J. Albert *et al.*, “Search for Neutrinoless Double-Beta Decay with the Upgraded EXO-200 Detector,” *Phys. Rev. Lett.*, vol. 120, p. 072701, Feb 2018.
- [82] L. Yang *et al.*, “Status and Prospects for the EXO-200 and nEXO Experiments,” *Journal of Physics: Conference Series*, vol. 888, no. 1, p. 012032, 2017.

- [83] J. B. Albert *et al.*, “Sensitivity and discovery potential of the proposed nEXO experiment to neutrinoless double- β decay,” *Phys. Rev. C*, vol. 97, p. 065503, Jun 2018.
- [84] K. Eguchi *et al.*, “First Results from KamLAND: Evidence for Reactor Antineutrino Disappearance,” *Phys. Rev. Lett.*, vol. 90, p. 021802, Jan 2003.
- [85] A. A. Sonzogni *Nuclear Data Sheets*, vol. 95, p. 837, 2002.
- [86] P. Puppe *et al.*, “High-resolution ($^3\text{He},t$) reaction on the double- β decaying nucleus ^{136}Xe ,” *Phys. Rev. C*, vol. 84, p. 051305, Nov 2011.
- [87] K. Wimmer *et al.*, “Identification of the slow $E3$ transition $^{136}\text{Cs}^m \rightarrow ^{136}\text{Cs}$ with conversion electrons,” *Phys. Rev. C*, vol. 84, p. 014329, Jul 2011.
- [88] J. Hyvärinen and J. Suhonen, “Analysis of the Intermediate-State Contributions to Neutrinoless Double β - Decays,” *Advances in High Energy Physics*, vol. 2016, no. 4714829, 2016.
- [89] G. R. Satchler, *Introduction to Nuclear Reactions*. The Macmillan Press Ltd., 1980.
- [90] H. Paetz gen. Schieck, *Nuclear Reactions: An Introduction*. Lecture Notes in Physics, Springer, Berlin, Heidelberg, 2014.
- [91] N. K. Glendenning, “Nuclear Spectroscopy with Two-Nucleon Transfer Reactions,” *Phys. Rev.*, vol. 137, pp. B102–B113, Jan 1965.
- [92] P. E. Hodgson, “The nuclear optical model,” *Reports on Progress in Physics*, vol. 34, no. 2, p. 765, 1971.
- [93] P. Kunz, “DWUCK4 DWBA Program, University of Colorado,” 1978.
- [94] N. K. Glendenning, *Direct Nuclear Reactions*. Academic Press, Inc., 1983.
- [95] A. R. Edmonds, *Angular Momentum in Quantum Mechanics*. Princeton University Press, 1957.

- [96] R. W. Nielsen, “Nuclear Reactions: Mechanism and Spectroscopy. Volume II,” 2016.
- [97] I. S. Towner and J. Hardy, “Direct two-nucleon transfer reactions and their interpretation in terms of the nuclear shell model,” *Advances in Physics*, vol. 18, no. 74, pp. 401–488, 1969.
- [98] R. A. Broglia and V. Zelevinsky, *Fifty Years of Nuclear BCS*. World Scientific, 2013.
- [99] R. A. Broglia, O. Hansen, and C. Riedel, *Two-Neutron Transfer Reactions and the Pairing Model*, pp. 287–457. Boston, MA: Springer US, 1973.
- [100] P. Debenham and N. M. Hintz, “Excited Rotational Band in ”Spherical” ^{150}Sm ,” *Phys. Rev. Lett.*, vol. 25, pp. 44–46, Jul 1970.
- [101] W. McLatchie, J. Kitching, and W. Darcey, “The reaction $^{154}\text{Sm}(p,t)^{152}\text{Sm}$ and further evidence for shape coexistence in ^{152}Sm ,” *Physics Letters B*, vol. 30, no. 8, pp. 529 – 530, 1969.
- [102] A. Bohr, B. R. Mottelson, and D. Pines, “Possible Analogy between the Excitation Spectra of Nuclei and Those of the Superconducting Metallic State,” *Phys. Rev.*, vol. 110, pp. 936–938, May 1958.
- [103] J. Bardeen, L. N. Cooper, and J. R. Schrieffer, “Theory of Superconductivity,” *Phys. Rev.*, vol. 108, pp. 1175–1204, Dec 1957.
- [104] D. Bes, R. Broglia, O. Hansen, and O. Nathan, “Isovector pairing vibrations,” *Physics Reports*, vol. 34, no. 1, pp. 1 – 53, 1977.
- [105] D. J. Dean and M. Hjorth-Jensen, “Pairing in nuclear systems: from neutron stars to finite nuclei,” *Rev. Mod. Phys.*, vol. 75, pp. 607–656, Apr 2003.
- [106] W. v. Oertzen and A. Vitturi, “Pairing correlations of nucleons and multi-nucleon transfer between heavy nuclei,” *Reports on Progress in Physics*, vol. 64, no. 10, p. 1247, 2001.

- [107] W. von Oertzen, *Fifty Years of Nuclear BCS*, ch. Enhanced Two Nucleon Transfer Due to Pairing Correlations, pp. 405–418.
- [108] A. Poves, *Fifty Years of Nuclear BCS*, ch. Neutrinoless Double Beta Decay Pairing Matters, pp. 297–308.
- [109] V. Rodin, A. Faessler, F. Imkovic, and P. Vogel, “Assessment of uncertainties in QRPA $0\nu\beta\beta$ -decay nuclear matrix elements,” *Nuclear Physics A*, vol. 766, pp. 107–131, 2006.
- [110] I. Talmi, “Coupling schemes in nuclei,” *La Rivista del Nuovo Cimento (1971-1977)*, vol. 3, pp. 85–102, Jan 1973.
- [111] J. P. Schiffer *et al.*, “Nuclear Structure Relevant to Neutrinoless Double β Decay: ^{76}Ge and ^{76}Se ,” *Phys. Rev. Lett.*, vol. 100, p. 112501, Mar 2008.
- [112] B. P. Kay *et al.*, “Nuclear structure relevant to neutrinoless double β decay: The valence protons in ^{76}Ge and ^{76}Se ,” *Phys. Rev. C*, vol. 79, p. 021301, Feb 2009.
- [113] T. Bloxham *et al.*, “Pair correlations in the neutrinoless double- β decay candidate ^{130}Te ,” *Phys. Rev. C*, vol. 82, p. 027308, Aug 2010.
- [114] J. S. Thomas *et al.*, “Neutron pair correlations in $A = 100$ nuclei involved in neutrinoless double- β decay,” *Phys. Rev. C*, vol. 86, p. 047304, Oct 2012.
- [115] B. P. Kay *et al.*, “Valence neutron properties relevant to the neutrinoless double- β decay of ^{130}Te ,” *Phys. Rev. C*, vol. 87, p. 011302, Jan 2013.
- [116] A. Roberts *et al.*, “Proton pair correlations and the neutrinoless double- β decay of ^{76}Ge ,” *Phys. Rev. C*, vol. 87, p. 051305, May 2013.
- [117] J. P. Entwisle *et al.*, “Change of nuclear configurations in the neutrinoless double- β decay of $^{130}\text{Te} \rightarrow ^{130}\text{Xe}$ and $^{136}\text{Xe} \rightarrow ^{136}\text{Ba}$,” *Phys. Rev. C*, vol. 93, p. 064312, Jun 2016.

- [118] S. V. Szwece *et al.*, “Rearrangement of valence neutrons in the neutrinoless double- β decay of ^{136}Xe ,” *Phys. Rev. C*, vol. 94, p. 054314, Nov 2016.
- [119] S. J. Freeman *et al.*, “Experimental study of the rearrangements of valence protons and neutrons amongst single-particle orbits during double- β decay in ^{100}Mo ,” *Phys. Rev. C*, vol. 96, p. 054325, Nov 2017.
- [120] S. J. Freeman *et al.*, “Pair correlations in nuclei involved in neutrinoless double beta decay: Ge76 and Se76,” *Physical Review C - Nuclear Physics*, vol. 75, no. 5, pp. 1–4, 2007.
- [121] A. L. Goodman, “On the $Z = 64$ shell closure,” *Nuclear Physics A*, vol. 331, no. 2, pp. 401 – 406, 1979.
- [122] M. A. Rahman and M. S. Chowdhury, “Nuclear structure of ^{102}Mo ,” *Phys. Rev. C*, vol. 73, p. 054311, May 2006.
- [123] S. Takeda *et al.*, “ $^{100}\text{Mo}(t, p)^{102}\text{Mo}$ Reaction at 15.8 MeV,” *Journal of the Physical Society of Japan*, vol. 34, no. 5, pp. 1115–1122, 1973.
- [124] H. Fielding, R. Anderson, D. Lind, C. Zafiratos, and W. Alford, “Two-proton transfer near $Z = 40$,” *Nuclear Physics A*, vol. 269, no. 1, pp. 125 – 137, 1976.
- [125] P. Debenham and N. M. Hintz, “The (p, t) reaction on even isotopes of Sm,” *Nuclear Physics A*, vol. 195, no. 2, pp. 385 – 414, 1972.
- [126] J. Bjerregaard, O. Hansen, O. Nathan, and S. Hinds, “The (t, p) reaction with the even isotopes of Sm,” *Nuclear Physics*, vol. 86, no. 1, pp. 145 – 166, 1966.
- [127] R. Chapman, W. McLatchie, and J. Kitching, “The (t, p) reaction on the even isotopes of neodymium,” *Nuclear Physics A*, vol. 186, no. 3, pp. 603 – 619, 1972.
- [128] K. Yagi, Y. Aoki, J. Kawa, and K. Sato, “Strong $L = 0$ and 2 transitions in (p, t) reactions in even-mass Nd isotopes,” *Physics Letters B*, vol. 29, no. 10, pp. 647 – 648, 1969.

- [129] E. A. Mccutchan, “Nuclear Data Sheets for $A = 136$,” *Nuclear Data Sheets*, vol. 152, p. 331, 2018.
- [130] H. Kusakari *et al.*, “Quasi-gamma bands in even-mass Xe AND Ba nuclei,” *Nuclear Physics A*, vol. 242, no. 1, pp. 13 – 29, 1975.
- [131] H. Kusakari, K. Kitao, S. Kono, and Y. Ishizaki, “Study of even-mass Ba nuclei by the (p, t) reaction,” *Nuclear Physics A*, vol. 341, no. 2, pp. 206 – 218, 1980.
- [132] R. Casten and P. V. Brentano, “An extensive region of O(6)-like nuclei near $A = 130$,” *Physics Letters B*, vol. 152, no. 1, pp. 22 – 28, 1985.
- [133] R. F. Casten and N. V. Zamfir, “Evidence for a Possible E(5) Symmetry in ^{134}Ba ,” *Phys. Rev. Lett.*, vol. 85, pp. 3584–3586, Oct 2000.
- [134] S. Pascu *et al.*, “Structure investigation with the (p, t) reaction on $^{132,134}\text{Ba}$ nuclei,” *Phys. Rev. C*, vol. 81, p. 014304, Jan 2010.
- [135] S. Pascu *et al.*, “Investigation of the ^{128}Ba nucleus with the (p, t) reaction,” *Phys. Rev. C*, vol. 79, p. 064323, Jun 2009.
- [136] G. Suliman *et al.*, “Study of the ^{130}Ba nucleus with the (p, t) reaction,” *The European Physical Journal A*, vol. 36, pp. 243–250, Jun 2008.
- [137] G. Cata-Danil *et al.*, “Monopole transfer strength to $^{132,134}\text{Ba}$ in (p, t) reactions and the interacting boson approximation,” *Phys. Rev. C*, vol. 54, pp. 2059–2062, Oct 1996.
- [138] M. Gerçeklioğlu, “Transfer strengths to the 0^+ states excited by (p, t) reactions in $^{130,132,134}\text{Ba}$,” *Phys. Rev. C*, vol. 82, p. 024306, Aug 2010.
- [139] E. Flynn, J. Cizewski, R. E. Brown, and J. Sunier, “ $^{136,138}\text{Ba}(t, p)$ and the systematics of neutron pairing vibrations at $N = 82$,” *Physics Letters B*, vol. 98, no. 3, pp. 166 – 168, 1981.

- [140] W. Alford *et al.*, “The (3He, n) reaction on N = 82 targets and even isotopes of neodymium,” *Nuclear Physics A*, vol. 321, no. 1, pp. 45 – 61, 1979.
- [141] R. Hertenberger *et al.*, “The Stern-Gerlach polarized ion source for the Munich MP-tandem laboratory, a bright source for unpolarized hydrogen and helium ion beams as well,” *Nuclear Instruments and Methods in Physics Research Section A: Accelerators, Spectrometers, Detectors and Associated Equipment*, vol. 536, no. 3, pp. 266 – 272, 2005.
- [142] M. Löffler, H. Scheerer, and H. Vonach, “The ion optical properties of the Munich Q3D-spectrograph investigated by means of a special experimental ray tracing method,” *Nuclear Instruments and Methods*, vol. 111, no. 1, pp. 1 – 12, 1973.
- [143] R. Hertenberger *et al.*, “A light ion focal plane detector for the Q3D magnetic spectrograph with periodic cathode readout,” *Nuclear Instruments and Methods in Physics Research Section A: Accelerators, Spectrometers, Detectors and Associated Equipment*, vol. 258, no. 2, pp. 201 – 208, 1987.
- [144] J. Ott *et al.*, “A position sensitive cathode strip detector with single strip readout,” *Nuclear Instruments and Methods in Physics Research Section A: Accelerators, Spectrometers, Detectors and Associated Equipment*, vol. 367, no. 1, pp. 280 – 284, 1995. Proceedings of the 7th International Wire Chamber Conference.
- [145] H.-F. Wirth *et al.*, “New Q3D Focal Plane Detector with Cathode-strip Readout Became Operational,”
- [146] W. H. Press, S. A. Teukolsky, W. T. Vetterling, and B. P. Flannery, *Numerical Recipes in FORTRAN (2nd Ed.): The Art of Scientific Computing*. New York, NY, USA: Cambridge University Press, 1992.
- [147] S. Triambak, *The isobaric multiplet mass equation and ft value of the $0^+ \rightarrow 0^+$ Fermi transition in ^{32}Ar : two tests of isospin symmetry breaking*. PhD thesis, University of Notre Dame, Indiana, USA, 2007.

- [148] A. Sonzogni, “Nuclear Data Sheets for $A = 134$,” *Nuclear Data Sheets*, vol. 103, no. 1, pp. 1 – 182, 2004.
- [149] C. M. Baglin, “Nuclear Data Sheets for $A = 92$,” *Nuclear Data Sheets*, vol. 113, no. 10, pp. 2187 – 2389, 2012.
- [150] E. Browne, “Nuclear Data Sheets for $A = 90$,” *Nuclear Data Sheets*, vol. 82, no. 3, pp. 379 – 546, 1997.
- [151] J. F. Ziegler, M. D. Ziegler, and J. P. Biersack, “SRIM - The stopping and range of ions in matter (2010),” *Nuclear Instruments and Methods in Physics Research B*, vol. 268, pp. 1818–1823, June 2010.
- [152] N. J. Mukwevho, “Second $T = 3/2$ state in ${}^9\text{B}$ and the isobaric multiplet mass equation,” Master’s thesis, University of the Western Cape, the Republic of South Africa, 2018.
- [153] N. J. Mukwevho *et al.*, “Second $T = 3/2$ state in ${}^9\text{B}$ and the isobaric multiplet mass equation,” *Phys. Rev. C*, vol. 98, p. 051302, Nov 2018.
- [154] F. D. Becchetti and G. W. Greenlees, “Nucleon-Nucleus Optical-Model Parameters, $A > 40$, $E < 50$ MeV,” *Phys. Rev.*, vol. 182, pp. 1190–1209, Jun 1969.
- [155] A. Koning and J. Delaroche, “Local and global nucleon optical models from 1 keV to 200 MeV,” *Nuclear Physics A*, vol. 713, no. 3, pp. 231 – 310, 2003.
- [156] R. L. Varner *et al.*, “A global nucleon optical model potential,” *Physics Reports*, vol. 201, no. 2, pp. 57 – 119, 1991.
- [157] J. J. H. Menet, E. E. Gross, J. J. Malanify, and A. Zucker, “Total-Reaction-Cross-Section Measurements for 30-60-MeV Protons and the Imaginary Optical Potential,” *Phys. Rev. C*, vol. 4, pp. 1114–1129, Oct 1971.
- [158] R. L. Walter and P. P. Guss *Rad. Effects*, vol. 95, p. 73, 1986.

- [159] X. Li, C. Liang, and C. Cai, “Global triton optical model potential,” *Nuclear Physics A*, vol. 789, no. 1, pp. 103 – 113, 2007.
- [160] F. Jr. and G.W.Greenlees *Ann. Rept. J.H. Willians Lab, Univ. Minnesota*, 1969.
- [161] W. Gelletly, J. A. Moragues, M. A. J. Mariscotti, and W. R. Kane, “ $^{135}\text{Ba}(n, \gamma)$ Reaction and Level Structure of ^{136}Ba ,” *Phys. Rev.*, vol. 181, pp. 1682–1696, May 1969.
- [162] G. M. Julian and T. E. Fessler, “Decay of ^{136}La and ^{134}La ,” *Phys. Rev.*, vol. 172, pp. 1208–1213, Aug 1968.
- [163] F. Becvar, J. Vrzal, J. Liptak, and J. Urbanec *J.N.I.R Report No. P3-3695, Dubna (unpublished)*, 1968.
- [164] Bečvář, F. and Lipták, J. and Urbanec, J. and Vrzal, J., “Investigation of γ -rays from neutron capture on ba and pr,” *Czechoslovak Journal of Physics B*, vol. 19, pp. 899–910, Jul 1969.
- [165] G. Scharff-Goldhaber and J. Weneser, “System of Even-Even Nuclei,” *Phys. Rev.*, vol. 98, pp. 212–214, Apr 1955.
- [166] I. Diószegi, C. Maráczy, and A. Veres, “Low-spin levels in ^{136}Ba studied via the $(n, n'\gamma)$ reaction,” *Nuclear Physics A*, vol. 438, no. 2, pp. 395 – 412, 1985.
- [167] P. D. Kunz, “CHUCK3 DWBA Program, University of Colorado,” *Unpublished*.
- [168] R. E. Chrien, G. W. Cole, J. L. Holm, and O. A. Wasson, “Neutron-resonance capture gamma rays in ^{136}Ba ,” *Phys. Rev. C*, vol. 9, pp. 1622 – 1632, Apr 1974.
- [169] M. M. Al-Hamidi *et al.*, “Investigation of ^{136}Ba γ -Transitions in the $(n, n'\gamma)$ Reaction,” *Phys. Atomic Nuclei*, vol. 57, 1994.
- [170] R. Massarczyk *et al.*, “Electromagnetic dipole strength of ^{136}Ba below the neutron separation energy,” *Phys. Rev. C*, vol. 86, p. 014319, Jul 2012.

- [171] S. Mukhopadhyay *et al.*, “Multiphonon states in ^{136}Ba ,” *Phys. Rev. C*, vol. 78, p. 034317, Sep 2008.
- [172] F. R. Metzger, “Nuclear resonance fluorescence in ^{136}Ba ,” *Phys. Rev. C*, vol. 18, pp. 2138–2144, Nov 1978.
- [173] N. Pietralla *et al.*, “Isovector quadrupole excitations in the valence shell of the vibrator nucleus ^{136}Ba : Evidence from photon scattering experiments,” *Phys. Rev. C*, vol. 58, pp. 796–800, Aug 1998.
- [174] M. A. Islam, T. J. Kennett, and W. V. Prestwich, “M1 and E2 strength functions of barium from thermal neutron capture,” *Phys. Rev. C*, vol. 42, pp. 207–220, Jul 1990.
- [175] T. Shizuma *et al.*, “A new isomer in ^{136}Ba populated by deep inelastic collisions,” *The European Physical Journal A - Hadrons and Nuclei*, vol. 20, pp. 207–210, May 2004.
- [176] J. J. Valiente-Dobón *et al.*, “ ^{136}Ba studied via deep-inelastic collisions: Identification of the $(\nu h_{112})_{10+}^{-2}$ isomer,” *Phys. Rev. C*, vol. 69, p. 024316, Feb 2004.
- [177] M. Wang *et al.*, “The AME2016 atomic mass evaluation (II). Tables, graphs and references,” *Chinese Physics C*, vol. 41, no. 3, p. 030003, 2017.
- [178] H. An and C. Cai, “Global deuteron optical model potential for the energy range up to 183 MeV,” *Phys. Rev. C*, vol. 73, p. 054605, May 2006.
- [179] Y. Han, Y. Shi, and Q. Shen, “Deuteron global optical model potential for energies up to 200 MeV,” *Phys. Rev. C*, vol. 74, p. 044615, Oct 2006.
- [180] J. Bojowald *et al.*, “Elastic deuteron scattering and optical model parameters at energies up to 100 MeV,” *Phys. Rev. C*, vol. 38, pp. 1153–1163, Sep 1988.
- [181] C. M. Perey and F. G. Perey, “Deuteron Optical-Model Analysis in the Range of 11 to 27 MeV,” *Phys. Rev.*, vol. 132, pp. 755–773, Oct 1963.

- [182] V. Zerkin and B. Pritychenko, “The experimental nuclear reaction data (exfor): Extended computer database and web retrieval system,” *Nuclear Instruments and Methods in Physics Research Section A: Accelerators, Spectrometers, Detectors and Associated Equipment*, vol. 888, pp. 31 – 43, 2018.
- [183] M. Avrigeanu, A. Plompen, and V. Avrigeanu, “Optical model potentials for α -particles scattering around the Coulomb barrier on A100 nuclei,” vol. 723, pp. 104–126, 07 2003.
- [184] S. M. Burnett *et al.*, “Octupole vibrational states in the even-mass barium isotopes,” *Nuclear Physics A*, vol. 442, no. 2, pp. 289 – 299, 1985.
- [185] L. McFadden and G. R. Satchler, “Optical-model analysis of the scattering of 24.7 MeV alpha particles,” *Nuclear Physics*, vol. 84, no. 1, pp. 177 – 200, 1966.
- [186] P. Mohr, “Total reaction cross section σ_{reac} of α -induced reactions from elastic scattering: The example $^{140}\text{Ce}(\alpha,\alpha)^{140}\text{Ce}$,” *Phys. Rev. C*, vol. 87, p. 035802, Mar 2013.
- [187] A. Palumbo *et al.*, “Systematic study of the α -optical potential via elastic scattering near the $Z = 50$ region for p -process nuclei,” *Phys. Rev. C*, vol. 85, p. 035808, Mar 2012.
- [188] M. Avrigeanu and V. Avrigeanu, “ α -particle nuclear surface absorption below the Coulomb barrier in heavy nuclei,” *Phys. Rev. C*, vol. 82, p. 014606, Jul 2010.
- [189] W. W. Daehnick and Y. S. Park, “Spectroscopy of $1f - 2p$ Nuclei with Direct (d, α) and (d, p) Reactions. I. Cu^{66} and Ni^{61} ,” *Phys. Rev.*, vol. 180, pp. 1062–1081, Apr 1969.
- [190] J. Dickens, R. Drisko, F. Perey, and G. Satchler, “Local energy approximation for finite-range in stripping reactions,” *Physics Letters*, vol. 15, no. 4, pp. 337 – 339, 1965.

- [191] F. Perey and D. Saxon, “The local energy approximation to nonlocality and finite range effects,” *Physics Letters*, vol. 10, no. 1, pp. 107 – 109, 1964.
- [192] R. M. DelVecchio and W. W. Daehnick, “Systematic Distorted-Wave Born-Approximation Predictions for Two-Nucleon Transfers: Applications to (d, α) Experiments,” *Phys. Rev. C*, vol. 6, pp. 2095–2108, Dec 1972.
- [193] H.-F. Wirth *et al.*, “One- and two-nucleon transfer reactions to ^{196}Au ,” *Phys. Rev. C*, vol. 70, p. 014610, Jul 2004.
- [194] P. J. Iano and N. Austern, “Deuteron Stripping on Deformed Nuclei,” *Phys. Rev.*, vol. 151, pp. 853–874, Nov 1966.
- [195] F. Cappuzzello and others., “The numen project: Nuclear matrix elements for neutrinoless double beta decay,” *The European Physical Journal A*, vol. 54, p. 72, May 2018.
- [196] Pote, G., Idini, A., Barranco, F., Vigezzi, E., and Broglia, R.A., “Reaction mechanism of two-neutron transfer in dwba,” *EPJ Web of Conferences*, vol. 17, p. 01004, 2011.
- [197] O. Tanimura, R. Wolf, R. Kaps, and U. Mosel, “Exact first- and second-order distorted-wave born methods,” *Physics Letters B*, vol. 132, no. 4, pp. 249 – 254, 1983.
- [198] G. Potel, F. Barranco, E. Vigezzi, and R. A. Broglia, “Evidence for phonon mediated pairing interaction in the halo of the nucleus ^{11}Li ,” *Phys. Rev. Lett.*, vol. 105, p. 172502, Oct 2010.
- [199] G. Potel, A. Idini, F. Barranco, E. Vigezzi, and R. A. Broglia, “Cooper pair transfer in nuclei,” *Reports on Progress in Physics*, vol. 76, p. 106301, oct 2013.
- [200] I. J. Thompson, “Coupled reaction channels calculations in nuclear physics,” *Computer Physics Reports*, vol. 7, no. 4, pp. 167 – 212, 1988.

- [201] B. Brown and W. Rae, “The Shell-Model Code NuShellX@MSU,” *Nuclear Data Sheets*, vol. 120, pp. 115 – 118, 2014.
- [202] R. E. Philips and S. T. Thornton, *A FORTRAN program for relativistic kinematic calculations in two-body nuclear reactions*. Technical report, Oak Ridge National Lab., Tenn., 1967.

